MATERIALS FOR ADAPTIVE STRUCTURAL ACOUSTIC CONTROL

Period February 1, 1994 to January 31, 1995

Annual Report

VOLUME III

OFFICE OF NAVAL RESEARCH
Contract No.: N00014-92-J-1510

APPROVED FOR PUBLIC RELEASE — DISTRIBUTION UNLIMITED

Reproduction in whole or in part is permitted
for any purpose of the United States Government

L. Eric Cross

PENNSTATE

1855

THE MATERIALS RESEARCH LABORATORY
UNIVERSITY PARK, PA

REPORT DOCUMENTATION PAGE

Form Approved
OMB No. 0704-0188

1. AGENCY USE ONLY (Leave blank)	2. REPORT DATE	3. REPORT TYPE AND DATES COVERED
	4/6/95	ANNUAL REPORT 02/1/94 TO 01/31/95

4. TITLE AND SUBTITLE

MATERIALS FOR ADAPTIVE STRUCTURAL ACOUSTIC CONTROL

5. FUNDING NUMBERS

6. AUTHOR(S)

L. ERIC CROSS

7. PERFORMING ORGANIZATION NAME(S) AND ADDRESS(ES)

MATERIALS RESEARCH LABORATORY
THE PENNSYLVANIA STATE UNIVERSITY
UNIVERSITY PARK, PA 16802

8. PERFORMING ORGANIZATION REPORT NUMBER

9. SPONSORING/MONITORING AGENCY NAME(S) AND ADDRESS(ES)

OFFICE OF NAVAL RESEARCH
CODE 1513:NRJ
800 NORTH QUINCY STREET
ARLINGTON, VA 22217

GERALD T. SMITH
OFFICE OF NAVAL RESEARCH RES. REP.
536 SOUTH CLARK STREET, RM 286
CHICAGO, ILLINOIS 60606-1588

10. SPONSORING/MONITORING AGENCY REPORT NUMBER

11. SUPPLEMENTARY NOTES

12a. DISTRIBUTION/AVAILABILITY STATEMENT

12b. DISTRIBUTION CODE

13. ABSTRACT *(Maximum 200 words)*

SEE FOLLOWING TWO PAGES

14. SUBJECT TERMS

15. NUMBER OF PAGES

16. PRICE CODE

17. SECURITY CLASSIFICATION OF REPORT	18. SECURITY CLASSIFICATION OF THIS PAGE	19. SECURITY CLASSIFICATION OF ABSTRACT	20. LIMITATION OF ABSTRACT

GENERAL INSTRUCTIONS FOR COMPLETING SF 298

The Report Documentation Page (RDP) is used in announcing and cataloging reports. It is important that this information be consistent with the rest of the report, particularly the cover and title page. Instructions for filling in each block of the form follow. It is important to ***stay within the lines*** to meet ***optical scanning requirements***.

Block 1. Agency Use Only *(Leave blank)*.

Block 2. Report Date. Full publication date including day, month, and year, if available (e.g. 1 Jan 88). Must cite at least the year.

Block 3. Type of Report and Dates Covered. State whether report is interim, final, etc. If applicable, enter inclusive report dates (e.g. 10 Jun 87 - 30 Jun 88).

Block 4. Title and Subtitle. A title is taken from the part of the report that provides the most meaningful and complete information. When a report is prepared in more than one volume, repeat the primary title, add volume number, and include subtitle for the specific volume. On classified documents enter the title classification in parentheses.

Block 5. Funding Numbers. To include contract and grant numbers; may include program element number(s), project number(s), task number(s), and work unit number(s). Use the following labels:

C	- Contract	PR	- Project
G	- Grant	TA	- Task
PE	- Program Element	WU	- Work Unit Accession No.

Block 6. Author(s). Name(s) of person(s) responsible for writing the report, performing the research, or credited with the content of the report. If editor or compiler, this should follow the name(s).

Block 7. Performing Organization Name(s) and Address(es). Self-explanatory.

Block 8. Performing Organization Report Number. Enter the unique alphanumeric report number(s) assigned by the organization performing the report.

Block 9. Sponsoring/Monitoring Agency Name(s) and Address(es). Self-explanatory.

Block 10. Sponsoring/Monitoring Agency Report Number. *(If known)*

Block 11. Supplementary Notes. Enter information not included elsewhere such as: Prepared in cooperation with...; Trans. of...; To be published in.... When a report is revised, include a statement whether the new report supersedes or supplements the older report.

Block 12a. Distribution/Availability Statement. Denotes public availability or limitations. Cite any availability to the public. Enter additional limitations or special markings in all capitals (e.g. NOFORN, REL, ITAR).

- **DOD** - See DoDD 5230.24, "Distribution Statements on Technical Documents."
- **DOE** - See authorities.
- **NASA** - See Handbook NHB 2200.2.
- **NTIS** - Leave blank.

Block 12b. Distribution Code.

- **DOD** - Leave blank.
- **DOE** - Enter DOE distribution categories from the Standard Distribution for Unclassified Scientific and Technical Reports.
- **NASA** - Leave blank.
- **NTIS** - Leave blank.

Block 13. Abstract. Include a brief *(Maximum 200 words)* factual summary of the most significant information contained in the report.

Block 14. Subject Terms. Keywords or phrases identifying major subjects in the report.

Block 15. Number of Pages. Enter the total number of pages.

Block 16. Price Code. Enter appropriate price code *(NTIS only)*.

Blocks 17. - 19. Security Classifications. Self-explanatory. Enter U.S. Security Classification in accordance with U.S. Security Regulations (i.e., UNCLASSIFIED). If form contains classified information, stamp classification on the top and bottom of the page.

Block 20. Limitation of Abstract. This block must be completed to assign a limitation to the abstract. Enter either UL (unlimited) or SAR (same as report). An entry in this block is necessary if the abstract is to be limited. If blank, the abstract is assumed to be unlimited.

DISCLAIMER NOTICE

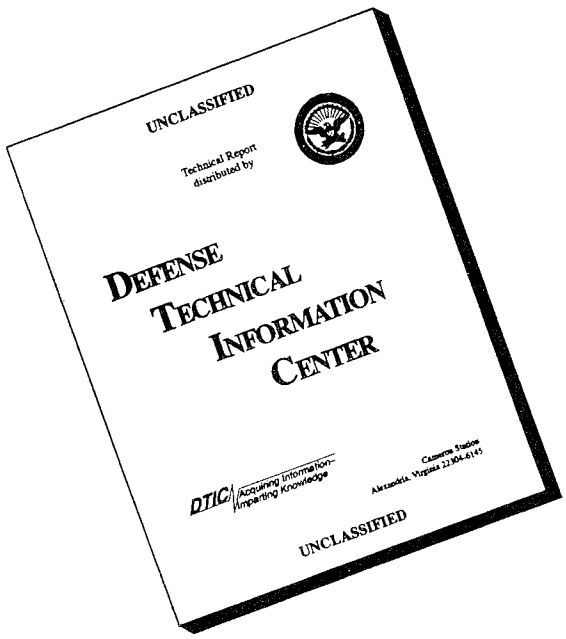

THIS DOCUMENT IS BEST QUALITY AVAILABLE. THE COPY FURNISHED TO DTIC CONTAINED A SIGNIFICANT NUMBER OF PAGES WHICH DO NOT REPRODUCE LEGIBLY.

ABSTRACT

The objectives of this ONR sponsored University Research Initiative (URI) entitled "Materials for Adaptive Structural Acoustic Control" concern both basic fundamental studies and highly applied development of the piezoelectric and electrostrictive ferroelectric ceramics which carry both the sensing and actuation functions for adaptive control. The report documents work over the third year of this five year program. For convenience and continuity, the activities are grouped under the headings" General Summary Papers, Materials Studies, Composite Sensors, Actuator Studies, Integration Issues, Processing Studies, Thin Film Ferroelectrics, and the Abstracts of graduating students on the program.

The first general papers illustrate the educational role undertaken by MRL faculty both in the basic understanding of ferroics, and in the philosophy of their application in 'smart' systems. It is interesting that through work pioneered on earlier ONR programs in MRL, it is now possible to measure both direct and converse electrostrictive response in simple solids, and to thus explore models to explain the signs and magnitudes of these striction constants. The relaxor ferroelectrics have been a topic of study for more than 30 years in the laboratory, but recent breakthroughs have revolutionized the level of understanding and opened a vista for further potential application of size (scale) effects in ferroics. Electrical control of shape memory has been achieved in a number of electro-ferroic solids, but full exploitation will need more complete understanding of both ferroelectric and ferroelastic:ferroelectric domain wall processes. Photostriction, the combination of photovoltaic and piezoelectric effects in ceramics promises an interesting range of new device possibilities.

In material studies, the elegant work on lanthanum modified lead titanate has now been fully written up, and the vital role of strain coupling in the onset of diffuse response underscored. New experimental methods have been applied to separating and measuring intrinsic and extrinsic components of response in PZT ceramics and to the measurement of microwave properties in these high K systems. Soft, intermediate, and hard modified lead zirconate and PZT composition have been under study for new and more interesting morphotropic phase boundaries which could be fabricated in single crystal form. Both optical birefringence and Raman studies are being used to explore domain and phase changes.

In sensing studies, the focus has been maintained upon flextensional (Moonie) structures and the enhanced performance which new end cap designs are affording. The polyvinylidene fluoride/trifluoethylene piezoelectrics are themselves an interesting composite system where the lower symmetry demands more complete characterization. The 1:3 rod and tube type composites have many performance advantages and trade-offs which will ensure wider scale application now that economical assembly techniques are at hand.

For actuation, the flextensional (Moonie) offers a number of advantages which merit further study. Both material and multilayer device related fatigue and destruction mechanisms are under study, and modes to control and alleviate microcracking and space change degradation are examined. More detailed studies of the photostriction effects and their control by doping effects in PZTs have also been accomplished.

Integration studies have continued to explore the components which must be co-processed in the smart material or adaptive assemblage. Examples are the thick film conductors in copper or silver/palladium, the 0:3 high density piezoelectric polymer composites and the filter functions required to eliminate cross talk in the wiring system.

Processing studies are essential to the fabrication of the very wide range of materials demanded by all elements of the program. Relaxor materials have formed the focus for many processing activities but more recently the needs for high strain actuation are refocusing interest on phase switching antiferroelectric:ferroelectric compositions in the high lead zirconate PLZTs and PSnZTs with mounting evidence for multiple ferroelectric phases appearing under high fields.

Thin film papers have been selected from the extensive work in MRL on ferroelectric films because of their relevance to transduction in piezoelectric or phase switching compositions.

MATERIALS FOR ADAPTIVE STRUCTURAL ACOUSTIC CONTROL

Period February 1, 1994 to January 31, 1995

Annual Report

VOLUME III

OFFICE OF NAVAL RESEARCH
Contract No.: N00014-92-J-1510

APPROVED FOR PUBLIC RELEASE — DISTRIBUTION UNLIMITED

L. Eric Cross

PENNSTATE

1855

THE MATERIALS RESEARCH LABORATORY
UNIVERSITY PARK, PA

TABLE OF CONTENTS

APPENDICES

VOLUME I

General Summary Papers

1. Newnham, R.E., S. Trolier-McKinstry and J.R. Giniewicz, "Piezoelectric, Pyroelectric and Ferroic Crystals, *J. Mater. Educ.* **15**, 189-223 (1993).

2. Newnham R.E., "Electroceramics in the 1990s and Beyond, *Euroceramics II*, Vol. 3, Deutsche Keramische Gesellschaft Köln, Germany, 1771-1782 (1994).

3. Newnham, R.E. and V. Sundar, "Anisotropy in Electrostriction and Elasticity," *J. Mat. Sci. Lett.* **13**, 799-801, Chapman and Hall, London, England (1994).

General Summary Papers (continued) –Volume I

4. Cross, L.E., "Relaxor Ferroelectrics: An Overview," *Ferroelectrics* **151**, 305-320 (1994).

5. Cross, L.E., Boundary Conditions for Shape Memory in Ceramic Material Systems, *J. Intelligent Material Systems on Structures* **6**, 55 (1994).

6. Uchino, K. and S.Y. Chu, "Photostriction and Its Applications," Proc. Amer. Ceram. Soc. Pac. Rim Conf., *Ferroic Materials*, 287-293 (1994).

7. Kumar, S., A.S. Bhalla and L.E. Cross, "Smart Ceramics for Broadband Vibration Control," *J. Intelligent Materials Systems and Structures* **5**(5), 673 (1994).

8. Kumar, S., A.S. Bhalla and L.E. Cross, "Smart Ferroelectrics for Acoustic and Vibration Control," *J. Intelligent Materials Systems and Structures* **5**(5), 678 (1994).

Materials Studies

9. Rossetti, G., L.E. Cross and J.P. Cline, "Structural Aspects of the Ferroelectric Phase Transition in Lanthanum-Substituted Lead Titanate," *J. of Mat. Sci.* **30**(1), 24-34 (1995).

10. Rossetti, G.A., Jr., M.A. Rodriguez, A. Navrotsky, L.E. Cross and R.E. Newnham, "Structure of the Defect Perovskite $[Pb_{0.85}La_{0.10}]TiO_3$ between 10 and 1023K," *J.Appl. Phys.***77**(4), 1683 (1994)

11. Zhang, Q.M., H. Wang, N. Kim and L.E. Cross, "Direct Evaluation of Domain-Wall and Intrinsic Contributions to the Dielectric and Piezoelectric Response and Their Temperature Dependence on Lead Zirconate-Titanate Ceramics," *J. Appl. Phys.* **75**(1), 454-9 (1994).

12. Li, Shaoping, A.S. Bhalla, R.E. Newnham, L.E. Cross and C.-Y. Huang, "90° Domain Reversal in $Pb(Zr_xTi_{1-x})O_3$ Ceramics," *J. Mater. Sci.* **29**(5), 1290-4 (1994).

13. Li, S., J. Sheen, S.-J. Jang, A.S. Bhalla, R.E. Newnham and L.E. Cross, "Modified Lumped Parameter Method for Measurements of Dielectric Susceptibility in Ferroelectrics," *Jpn. J. Appl. Phys.*, Part 1 33(6A), 3617-21 (1994).

14. Troilo, L.M., D. Damjanovic and R.E. Newnham, "Modified Lead Titanate Ceramics with a Relatively Large Dielectric Constant for Hydrophone Applications," *J. Am. Cer. Soc.* **77**(3), 857-59 (March 1994).

15. Subbarao, E.C., V. Srikanth, W. Cao and L.E. Cross, "Domain Switching and Microcracking During Poling of Lead Zirconate Titanate Ceramics," *Ferroelectrics* **145**, 771-781 (1993).

16. Jiang, Q.Y., E.C. Subbarao and L.E. Cross, "Dielectric Properties of Single Grain in PLZT Ferroelectric Ceramics," *Ferroelectrics Lett.* **17**, 41-46 (1994).

Materials Studies (continued) –Volume I

17. Wang, J.F., J. Gineiwicz and A.S. Bhalla, "Soft Piezoelectric $(1-x)Pb(Sc_{0.5}Ta_{0.5})O_{3-x}PbTiO_3$ Ceramics with High Coupling Factors and Low Qm," *Ferroelectrics Lett.* **16**, 113-118 (1993).

18. Alberta, E.F., A.S. Bhalla and T. Takenaka, "The Complex Piezoelectric, Elastic, and Dielectric Coefficients for a Lead Zirconate-Based Ceramic Under Electrical Bias," *Ferroelectrics* **154**, 11 (1994).

VOLUME II

19. Alberta, E.F., A.S. Bhalla and T. Takenaka, "The Piezoelectric, Elastic and Dielectric Constants for Ceramics in the Solid Solution $(x)PbZrO_3-(1-x-z)PbZn_{1/3}Nb_{2/3}O_3$ - (z) $PbTiO_3$," *Ferroelectrics* (in press).

20. Alberta, E.F and A.S. Bhalla, "An Evaluation of Lead-Zirconate Based Ceramics For Use In Non-Volatile Ferroelectric Memory Devices," *Proceedings of the 9th Annual International Symposium on the Applications of Ferroelectrics* (1994).

21. Alberta, E.F. and A.S. Bhalla, "Dielectric and Piezoelectric Properties of Ceramics in the Lead Indium Niobate Lead Scandium Tantalate Solid Solution System," *Proceedings of the 9th Annual International Symposium on the Applications of Ferroelectrics* (1994).

22. Jin, B.-M., A.S. Bhalla, J.-B. Kim and J.-N. Kim, "Dielectric Response of $Li_{0.4}K_{0.6}NbO_3$ Crystal in the Frequency Domain," *J. Mat. Sci. Mat. Electronics* **4**, 225-228 (1993).

23. Jin, B.-M., A.S. Bhalla, B.-C. Choi and J.-N. Kim, "Dielectric Anomalies in $Li_{0.4}K_{0.6}NbO_3$ Crystals," *Physica Sta. Solidi.* **140**, 239-245 (1993).

24. Oh, K.Y., K. Uchino and L.E. Cross, "Optical Study of Domains in $Ba(Ti,Sn)O_3$ Ceramics," *J. Amer. Ceram. Soc.* **77**(11), 2809-16 (1994).

25. Idink, H., V. Srikanth, W.B. White and E.C. Subbarao, "Raman Study of Low Temperature Phase Transitions in Bismuth Titanate, $Bi_4Ti_3O_{12}$," *J. Appl. Phys.* **76**(3), 1819-1823 (1994).

Composite Sensors

26. Newnham, R.E. and K.A. Markowski, "Composite Sensors and Actuators," Submitted for Proceedings of the Japan-U.S. Workshop on Functional Fronts in Advanced Ceramics, Tsukuba, Japan, December 6-8, 1994.

27. Dogan, A., S. Yoshikawa, K. Uchino and R.E. Newnham, "The Effect of Geometry on the Characteristics of the Moonie Transducer and Reliability Issues," *Proceedings of the IEEE Ultrasonics Symposium* **2**, 935-939 (1994).

28. Xu, Q.C., A. Dogan, J. Tressler, S. Yoshikawa and R.E. Newnham, "Ceramic-Metal Composite Actuator," *Ferroelectrics Special Issue on Piezoelectric and Electrostrictive Actuators* **160** (1994).

Composite Sensors (continued) –Volume II

29. Onitsuka, K., A. Dogan, Q.C. Xu, S. Yoshikawa and R.E. Newnham, "Design Optimization for Metal-Ceramic Composite Actuator, 'Moonie'," *Ferroelectrics* **156**, 37-42 (1994).

30. Tressler, J.F., Q.C. Xu, S. Yoshikawa, K. Uchino and R.E. Newnham, "Composite Flextensional Transducers of Sensing and Actuation," *Ferroelectrics* **156**, 67-72 (August 1994).

31. Meyer, R., H. Weitzing, Q.C. Xu, Q.M. Zhang, R.E. Newnham and J.K. Cochran, "Lead Zirconate Hollow-Sphere Transducers," *J. Am. Ceram. Soc.* **77**(6), 1669-72 (1994).

32. Wang, H., Q.M. Zhang, L.E. Cross and A.O. Sykes, "Piezoelectric, Dielectric, and Elastic Properties of Poly (Vinylidene Fluoride/Trifluoroethylene)," *J. Appl. Phys.* **74**(5), 3394-3398 (1993).

33. Wang, H., Q.M. Zhang and L.E. Cross, "Piezoelectric Relaxation of P(VDF-TrFE) Copolymer," *Ferroelectrics* **159**, 218-286 (1994).

34. Zhang, Q.M., W. Cao, H. Wang and L.E. Cross., "Characterization of the Performance of 1-3 Type Piezocomposites for Low-Frequency Applications," *J. Appl. Phys.* **73**(3), 1403-1410 (1993).

35. Zhang, Q.M., H. Wang and L.E. Cross, "Piezoelectric Tubes and 1-3 Tubular Composites as Tunable Actuators and Sensors," *Proc. SPIE-Int. Soc. Opt. Eng. (1993)*, 1916 (Smart Materials), 244-54.

36. Zhang, Q.M., H. Wang and L.E. Cross, "Piezoelectric Tubes and Tubular Composites for Actuator and Sensor Applications," *J. Mater. Sci.* **28**(14), 3962-3968 (1993).

Actuator Studies

37. Newnham, R.E., A. Dogan, Q.C. Xu and S. Yoshikawa, "Flextensional 'Moonie' Actuators," *IEEE 1993 Ultrasonics Symposium Proc.*, Baltimore, Maryland, Vol. 1, 509-514 (Oct. 31-Nov. 3, 1993).

38. Dogan, A., Q. Xu, K. Onitsuka, S. Yoshikawa, K. Uchino and R.E. Newnham, "High Displacement Ceramic Metal Composite Actuators (Moonies)," *Ferroelectrics* **156**, 1 (1994).

39. Uchino, K., "Manufacturing Technology of Multilayered Transducers," *Proc. Amer. Ceram. Soc.* (in press).

40. Furuta, A. and K. Uchino, "Destruction Mechanism of Multilayer Ceramic Actuators: Case of Antiferroelectrics," *Ferroelectrics* **160**, 277-285 (1994).

41. Aburatani, H., S. Harada, K. Uchino, A. Furuta and Y. Fuda, "Destruction Mechanisms in Ceramic Multilayer Actuators," *Jpn. J. Appl. Phys.* **33**, 3091-3094 (1994).

Actuator Studies (continued) –Volume II

42. Uchino, K. and H. Aburatani, "Destruction Detection Techniques for Safety Piezoelectric Actuator Systems," *Proc. 2nd Int'l Conf. Intelligent Mater.*, pp. 1248-56 (1994).

VOLUME III

43. Takahashi, S., S. Hirose and K. Uchino, "Stability of PZT Piezoelectric Ceramics Under Vibration-Level Change," *J. Amer. Ceram. Soc.* **77**(9), 2429-32 (1994).

44. Jiang, Q.Y., E.C. Subbarao and L.E. Cross., "Effect of Composition and Temperature on Electric Fatigue of La-Doped Lead Zirconate Titanate Ceramics," *J. Appl. Phys.* **75**(11), 7433-7443 (1994).

45. Srikanth, V. and E.C. Subbarao, "Acoustic Emission Study of Phase Relations in Low Y_2O_3 Portions of ZrO_2-Y_2O_3 System," *J. Mater. Sci.* **29**, 3363-3371 (1994).

46. Chu, S.Y., Z. Ye and K. Uchino, "Impurity Doping Effect on Photostriction in PLZT Ceramics," *J. Adv. Performance Mater.* **1**, 129-143 (1994)..

47. Chu, S.Y., Z. Ye and K. Uchino, "Photovoltaic Effect for the Linearly Polarized Light in (Pb,La)(Zr,Ti)O_3 Ceramics," *Smart Mater. Struct.* **3**, 114-117 (1994).

48. Chu, S.Y., M.L. Mulvihill, Z. Ye and K. Uchino, "Bulk Photovoltaic Effect for the Linearly Polarized Light in $Pb(Zn_{1/3}Nb_{2/3})O_3$ Single Crystals," *Jpn. J. Appl. Phys.* **34** (Part 1, No. 2A) (1995).

49. Mulvihill, M.L., L.E. Cross and K. Uchino, "Low Temperature Dynamic Observation of Relaxor Ferroelectric Domain in Lead Zinc Niobate," *J. Amer. Ceram. Soc.* (in press).

50. Uchino, K., "Electrooptic Ceramics and Their Display Applications," *Ceramics International* (in press).

51. Lee, D., J. Yuk, N. Lee and K. Uchino, "Humidity-Sensitive Properties of Nb_2O_5-Doped Pb(Zr,Ti)O_3," *Sensor and Mater.* **5**(4), 231-240 (1994).

52. Lee, N.Y., N. Usuki, H. Aburatani, Y. Ito and K. Uchino, "Pb/Ti Ratio of RF-Magnetron Sputtered $PbTiO_3$ Thin Films," *Jpn. J. Appl. Phys.* (accepted).

Integration Issues

53. Dougherty, J.P. and Y. Chen, "Tailoring Materials for Smart Applications," Invited Paper, *Proc. 1994 Intl. Conf. on Intelligent Materials*, June 5-8, 1994, Williamsburg VA.

54. Hackenberger, W.S., T.R. Shrout, J.P. Dougherty and R.F. Speyer, "The Effect of Differential Shrinkage on the Sintering and Microstructural Development of Low-Temperature Co-Firable Multilayer Substrates," *Proc. SAMPE/ISHM 7th International Electronics Conference*, pp. 643-650, Parsippany, NJ, June 20-23, 1994

***Integration Issues** (continued)* –Volume III

55. Wang, S.F., J.P. Dougherty, W. Huebner, and J.G. Pepin, "Silver-Palladium Thick Film Conductors," published as the feature article in *Journal of the American Ceramic Society* **77**(12), 3051-72 (December 1994).

56. Sample, D.R., P.W. Brown and J.P. Dougherty, "The Microstructural Evolution of Copper Thick Films Observed by Environmental Scanning Microscopy," *J. American Ceramic Society* (in press).

VOLUME IV

57. Fiallo, H.H., J.P. Dougherty, S.J. Jang, R.E. Newnham and L. Carpenter, "Transmission Properties of Metal-Semiconductor-Relaxor Microstrip Lines", *IEEE Trans. Microwave Theory & Techniques* **42**(7), 1176-1182, (July 1994).

58. Dougherty, J.P., M. Megherhi, and H.H. Fiallo, "Integrated Filters and Over Voltage Protection in Multilayer Ceramic Packaging Materials," *Proc. Eighth Cimtec World Ceramics Conference*, Florence, June 29-July 4, 1994.

Processing Studies

59. Miller, D.V., C.A. Randall, A.S. Bhalla, R.E. Newnham and J.H. Adair, "Electrorheological Properties of $BaTiO_3$ Suspensions," *Ferroelectrics Lett.* **15**, 141-151 (1993).

60. Fielding, J.T., Jr., T.R. Shrout and S.J. Jang, "Increased Operating Temperature Range in La-Modified $Pb(Mg_{1/3}Nb_{2/3}O_3$-$PbTiO_3$ Relaxor Ferroelectric-Based Transducers," *Proc. 9th ISAF*, State College, PA (August 1994).

61. Fielding, J.T., Jr., S.J. Jang and T.R. Shrout, "Field-Induced Piezoelectric Materials for 100 kHz-10 MHz Transducer Applications," *Proc. 9th ISAF*, State College, PA (August 1994).

62. Brodeur, Russell P., Kamau wa Gachigi, Philip M. Pruna and Thomas R. Shrout, "Ultra-High Strain Ceramics with Multiple Field-Induced Phase Transitions," *J. Am. Ceram. Soc.* **77**(11), 3042 (1994).

63. Yoshikawa, S., N. Kim, T. Shrout, Q. Zhang, P. Moses and L.E. Cross, "Field-Induced Lead Zirconate Titanate Stannate Antiferroelectric-to-Ferroelectric Phase Switching Ceramics," *Proc. 9th ISAF*, State College, PA (August 1994).

64. Gururaja et al., "Electrostrictive Ultrasonic Probe Having Expanded Operating Temperature Range," United States Patent, Patent Number: 5,345,139, Date of Patent: September 6, 1994.

65. Yoon, K.H., Y.S. Cho, D.K. Kang, K. Uchino and K.Y. Oh, "Effect of Eutectic Lithium Sulphate-Sodium Sulphate Flux on the Synthesis of Lead Magnesium Niobate," *Ferroelectrics* **160**, 255-264 (1994).

Thin Film Ferroelectrics –Volume IV

66. Brooks, K.G., J. Chen, K.R. Udayakumar and L.E. Cross, "Electric Field Forced Phase Switching in La-Modified Lead Zirconate Titanate Stannate Thin Films," *J. Appl. Phys.* **75**(3), 1699-704 (1994).

67. Ghosh, P.K., A.S. Bhalla and L.E. Cross, "Surface Morphology of r.f. Sputtered Bismuth Titanate Thin Films," *J. Materials Science* **29**, 4659-4662 (1994).

68. Lee, N.Y., T. Sekine, Y. Ito and K. Uchino, "Deposition Profile of RF-Magnetron-Sputtered $BaTiO_3$ Thin Films," *Jpn. J. Appl. Phys.* **33** (Part 1, No. 3A), 1484-88 (1994).

Graduating Students in the Program

69. Dogan, Aydin. PhD Thesis (Abstract), Materials Program. Flextensional "Moonie and Cymbal" Actuators. December 1994.

70. Wang, Hong. PhD Thesis (Abstract), Materials Program. Electromechanical Effects in Polymeric Materials. August 1994.

71. Tressler, James F. Master of Science (Abstract), Ceramic Science. Smart Ceramic-Metal Composites for Active Vibration Control. December 1993.

ACTUATOR STUDIES

(continued)

APPENDIX 43

journal

J. Am. Ceram. Soc., 77 [9] 2429–32 (1994)

Stability of PZT Piezoelectric Ceramics under Vibration Level Change

Sadayuki Takahashi†

NEC Corporation, Miyazaki, Kawasaki-shi 216, Japan

Seiji Hirose†

Yamagata University, Yonezawa-shi, Yamagata 992, Japan

Kenji Uchino*

The Pennsylvania State University, Materials Research Laboratory, University Park, Pennsylvania 16802

Stability of the piezoelectric properties with changing vibration level was studied in lead zirconate–titanate (PZT) ceramics by using the constant-current/velocity driving method. The changes of Young's modulus Y_0^E and mechanical loss factor Q_m^{-1} are a function of the square of effective vibration velocity v_0. The nonlinear proportional constants of the above functions indicate the degree of stability under vibration level change. The stability of PZT estimated by these constants coincides with the results obtained through the heat generation study.

I. Introduction

Applications of piezoelectric materials for actuators have been vigorously studied in recent years.[1,2] A very large mechanical output power is required for these applications, and lead zirconate–titanate (PZT) based ceramics are usually used for these actuator devices. In order to obtain a great output power, the ceramics must be driven at a high vibration level. This causes heat generation as well as a drastic change in piezoelectric properties.[3–6] Since the measuring method to determine piezoelectric characteristics at high vibration levels was not established previously, only a few studies were made by one of the authors[7] concerning materials durable at high vibration levels.

Recently, Hirose *et al.*[8,9] have succeeded in establishing a method for measuring vibration level characteristics continuously from low to high levels. The vibration level characteristics for PZT have been measured using this method.[10,11] The results suggest that the piezoelectric properties vary with vibration level and that heat generation of the material increases drastically when the vibration level exceeds a certain value. Moreover, these behaviors are markedly dependent on the material compositions.

This paper deals with the stability of the piezoelectric properties under vibration level change in various PZT ceramics. The results are very useful for designing high-power piezoelectric devices such as actuators and are also useful for developing materials capable of withstanding high power drive.

II. Experimental Procedure

(1) Specimens

The vibration level characteristics in the PZT-based ceramics depend strongly on both the basic composition and the dopant. The following two PZT composition series, designated A and B, were used here:

A: $Pb(Zr_{0.54}Ti_{0.46})O_3$ + metal oxide,

where metal oxide was 0.5 wt% of Nb_2O_5, 0.5 wt% of Fe_2O_3, or none.

B: $Pb(Zr_xTi_{1-x})O_3$ + y wt% Fe_2O_3,

where $0.58 \geq x \geq 0.48$ and $1.0 \geq y \geq 0$.

Rectangular plate vibrators with l = 43 mm, w = 7 mm, and t = 1 mm, shown in Fig. 1, were used for all the measurements. Electric poling was carried out along the thickness direction.

(2) Measurements

The fundamental length expansion vibration mode was excited by the constant current/velocity driving circuit. Resonant frequency f_0, mechanical quality factor Q_m, motional admittance Y_{m0}, and damped admittance Y_d were measured as a function of effective vibration velocity v_0.

Figure 2 shows the electric equivalent circuit for the vibrator in the vicinity of the resonant frequency. The following equations describe the relations between the circuit component constants and the above measured values:

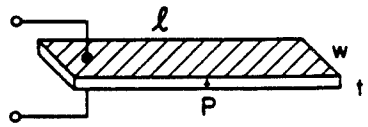

Fig. 1. Shape and size of the piezoelectric vibrator used in the experiments.

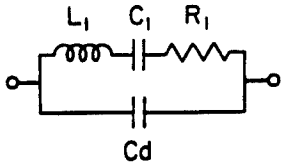

Fig. 2. Electric equivalent circuit for the piezoelectric vibrator around its resonant frequency.

D. E. Bonnema—contributing editor

Manuscript No. 193585. Received May 16, 1994; approved July 5, 1994.

*Member, American Ceramic Society.

†Present address: The Pennsylvania State University, MRL, University Park, PA 16802.

$$f_0 = \frac{1}{2\pi\sqrt{L_1C_1}} \qquad Q_m = \frac{2\pi f_0 L_1}{R_1} \tag{1}$$

$$Y_{m0} = \frac{1}{R_1} \qquad Y_d = 2\pi f C_d$$

Subsequently, Young's modulus Y_0^E, relative permittivity ε_{33}^T, and electromechanical coupling factor k_{31} can be calculated by

$$Y_0^E = \frac{\rho f^2}{\pi^2 L_1 C_1} \tag{2}$$

$$\varepsilon_{33}^T = \frac{tC_d}{lw\varepsilon_0(1 - k_{31}^2)}$$

$$k_{31}^2 = \frac{1}{1 + \left(\frac{8C_d}{\pi^2 C_1}\right)}$$

where ρ and ε_0 are the density and the permittivity of free space, respectively. Therefore, the values of Y_0^E, ε_{33}^T, and k_{31} can be determined by measuring f_0, Q_m, Y_{m0}, and Y_d.

The effective vibration velocity v_0 is represented by the maximum vibration amplitude ξ_m as follows:

$$v_0 = \sqrt{2}\pi f_0 \xi_m \tag{3}$$

where ξ_m was observed using the optical displacement sensor.

III. Results and Discussions

(1) A-series PZT

The vibration level characteristics for resonant frequency f_0, permittivity ε_{33}^T, electromechanical coupling factor k_{31}, and mechanical quality factor Q_m for the A-series PZT ($Pb(Zr_{0.54}Ti_{0.46})O_3$ + metal oxide) are shown in Figs. 3(a), (b), (c), and (d), respectively. The values of f_0 and Q_m decrease with increasing v_0, whereas ε_{33}^T and k_{31} increase. These behaviors are markedly affected by the dopant. All properties in the Nb-doped PZT begin to change from a relatively low vibration level in comparison with the case in the Fe-doped PZT. The undoped is somewhere in between.

In Figs. 4(a) and (b), 5(a) and (b) $\Delta Y_0^E/(Y_0^E)_0$, $\Delta\varepsilon_{33}^T/(\varepsilon_{33}^T)_0$, $\Delta k_{31}/(k_{31})_0$ and $\Delta Q_m^{-1}/(Q_m^{-1})_0$ are plotted as a function of v_0 on a logarithmic scale. The results suggest that the fractional change $\Delta A/A_0$ of any property (A: Y_0^E, ε_{33}^T, k_{31}, Q_m^{-1}) can be expressed by the following empirical formula:

$$\frac{\Delta A}{A_0} = \alpha v_0^\beta \tag{4}$$

where β is a nonlinear power constant which is insensitive to materials. On the other hand, α, the nonlinear proportional constant, can indicate the material's stability with changing vibration level: the smaller the α is, the more stable the material is.

The α and β values determined experimentally are summarized in Table I. The value of β is approximately 2 except k_{31}. Since the average stored elastic energy density $\bar{u}$ for the vibrator is given by[12]

$$\bar{u} = \frac{1}{2}\rho v_0^2 \tag{5}$$

Equation (4) can be rewritten as follows:

$$\frac{\Delta A}{A_0} = \alpha'\bar{u} \tag{6}$$

where $\alpha = (1/2)\rho\alpha'$. Therefore, Y_0^E, ε_{33}^T, and Q_m^{-1} become proportional to the average stored elastic energy density.

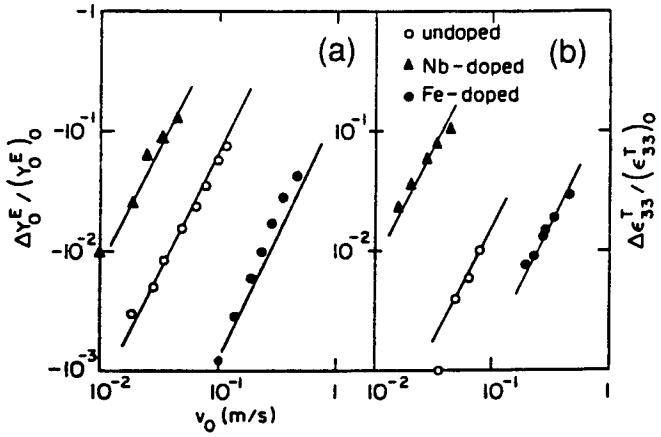

Fig. 4. Vibration level characteristics of fractional changes of (a) Young's modulus $\Delta Y_0^E/(Y_0^E)_0$ and (b) permittivity $\Delta\varepsilon_{33}^T/(\varepsilon_{33}^T)_0$ in undoped, Nb-doped, and Fe-doped $Pb(Zr_{0.54}Ti_{0.46})O_3$ ceramics.

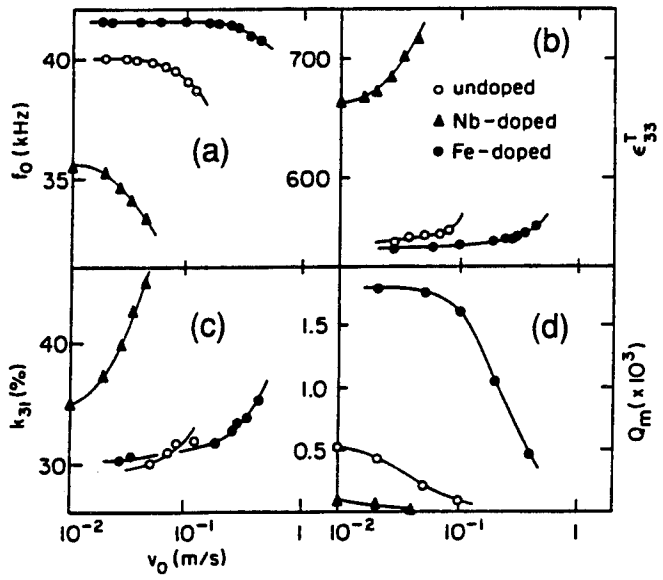

Fig. 3. Vibration level characteristics of (a) resonant frequency f_0 (b) permittivity ε_{33}^T, (c) electromechanical coupling factor k_{31}, and (d) mechanical quality factor Q_m in undoped, Nb-doped, and Fe-doped $Pb(Zr_{0.54}Ti_{0.46})O_3$ ceramics.

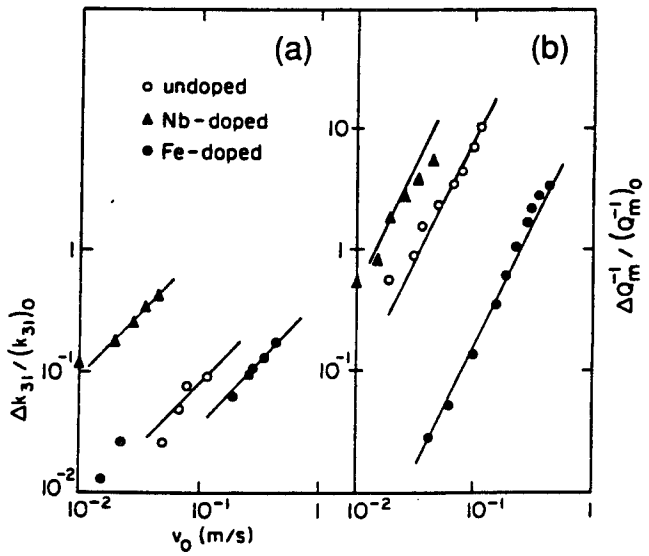

Fig. 5. Vibration level characteristics of fractional changes of (a) coupling factor $\Delta k_{31}/(k_{31})_0$ and (b) mechanical loss factor $\Delta Q_m^{-1}/(Q_m^{-1})_0$ in undoped, Nb-doped, and Fe-doped $Pb(Zr_{0.54}Ti_{0.46})O_3$ ceramics.

In comparison to the undoped PZT, the value of α is large for the Nb-doped PZT and small for the Fe-doped one. This means that the Fe-doped PZT is the most stable among the three compositions. The result coincides well with the previous heat generation study.[10,11]

(2) *B-series PZT*

The dependence of $\Delta Y_0^E/(Y_0^E)_0$ and $\Delta Q_m^{-1}/(Q_m^{-1})_0$ on v_0 is plotted for $Pb(Zr_xTi_{1-x})O_3$ + 0.5 wt% Fe_2O_3 ($0.58 \geq 0.48$) and $Pb(Zr_{0.52}Ti_{0.48})O_3$ + y wt% Fe_2O_3 ($1.0 \geq y \geq 0$) in Figs. 6(a), (b), and 7(a), (b), respectively. It is clear that Eq. (4) with $\beta = 2$ is also valid over wide x and y ranges.

Figure 8 shows nonlinear proportional constant change for Young's modulus (α_Y) and mechanical loss factor ($\alpha_{Q^{-1}}$) with zirconium molar concentration x. Both the $|\alpha_Y|$ and $\alpha_{Q^{-1}}$ exhibit minimum values near $x = 0.52$, which is close to the morphotropic phase boundary (MPB).

In Fig. 9, $|\alpha_Y|$ and $\alpha_{Q^{-1}}$ are shown as a function of Fe doping concentration y. Both the $|\alpha_Y|$ and $\alpha_{Q^{-1}}$ decrease with increasing y and appear to be approximately constant for $y \geq 0.6$.

These results also coincide well with those of previous studies concerning heat generation.[10,11] Consequently, the nonlinear proportional constant may be a good indicator for the stability of the piezoelectric properties under a giant vibration level. It was found difficult, however, to apply Eq. (4) for ε_{33}^T and k_{31} in B-series PZT.

Table I. Nonlinear Proportional Constant α and Nonlinear Power Constant β Determined Experimentally for Undoped, Nb-Doped, and Fe-Doped $Pb(Zr_{0.54}Ti_{0.46})O_3$ Ceramics

Characteristics	Dopant	α	β
Y_0^E	Nb-doped	-7.7×10	2
	Undoped	-5.8	2
	Fe-doped	-1.3×10^{-1}	2
ε_{33}^T	Nb-doped	5.0×10	2
	Undoped	1.2	2
	Fe-doped	1.7×10^{-1}	2
k_{31}	Nb-doped	9.4	1
	Undoped	7.6×10^{-1}	1
	Fe-doped	3.5×10^{-1}	1
Q_m^{-1}	Nb-doped	4.6×10^3	2
	Undoped	8.5×10^2	2
	Fe-doped	1.7×10	2

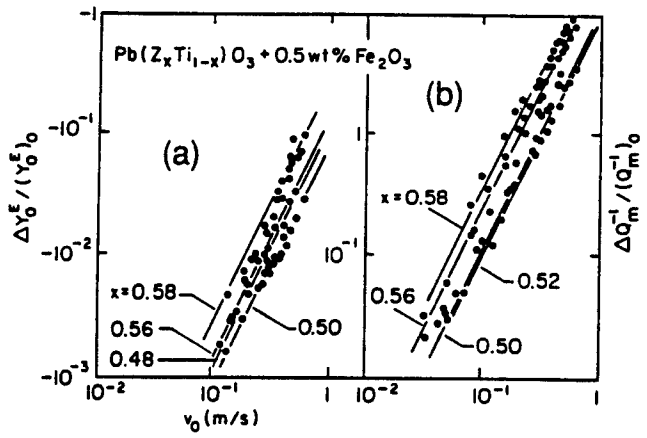

Fig. 6. Vibration level characteristics of fractional changes of (a) Young's modulus $\Delta Y_0^E/(Y_0^E)_0$ and (b) mechanical loss factor $\Delta Q_m^{-1}/(Q_m^{-1})_0$ in $Pb(Zr_xTi_{1-x})O_3$ + 0.5 wt% Fe_2O_3 ceramics.

IV. Conclusion

The vibration level characteristics of piezoelectric properties were measured in various PZT ceramics using the constant-current/velocity driving method. The stability under a high vibration level was discussed. The fractional changes both for Young's modulus and mechanical loss factor are a function of the square of the effective vibration velocity. In addition, the nonlinear proportional constant is found to be a good indicator for the stability of materials.

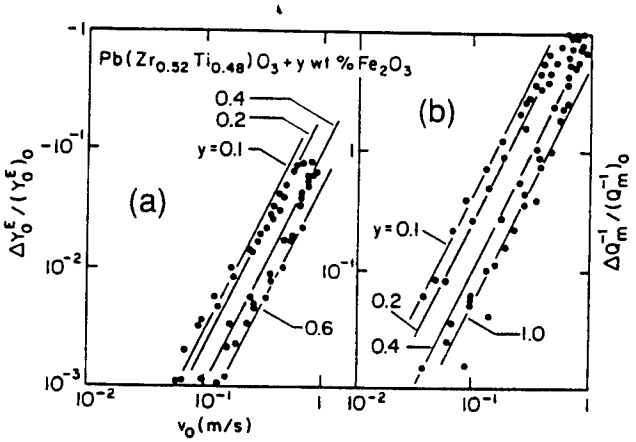

Fig. 7. Vibration level characteristics of fractional changes of (a) Young's modulus $\Delta Y_0^E/(Y_0^E)_0$ and (b) mechanical loss factor $\Delta Q_m^{-1}/(Q_m^{-1})_0$ in $Pb(Zr_{0.52}Ti_{0.48})O_3$ + y wt% Fe_2O_3 ceramics.

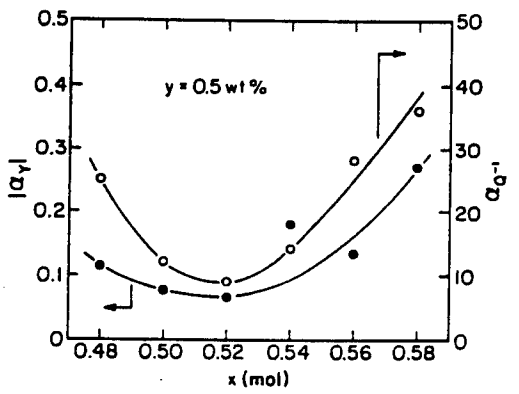

Fig. 8. Nonlinear proportional constants α_Y and $\alpha_{Q^{-1}}$ for $Pb(Zr_xTi_{1-x})O_3$ + 0.5 wt% Fe_2O_3 ceramics as a function of zirconium molar concentration x.

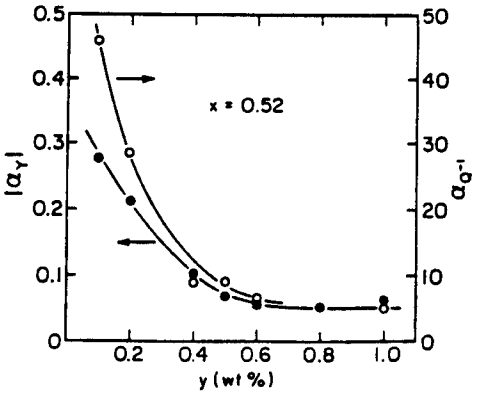

Fig. 9. Nonlinear proportional constants α_Y and $\alpha_{Q^{-1}}$ for $Pb(Zr_{0.52}Ti_{0.48})O_3$ + y wt% Fe_2O_3 ceramics as a function of y.

References

[1]K. Uchino, *Piezoelectric/Electrostrictive Actuators* (in Jpn.). Morikita-Syuppan, Tokyo, Japan, 1991.

[2]S. Takahashi, "Multilayer Piezo-Ceramic Actuators and Their Applications," *Ferroelectric Ceramics*. Edited by N. Setter and E. L. Colla. Birkhauser Verlag, Basel, Switzerland, 1993.

[3]R. A. Gdula, "High-Field Losses of Adulterated Lead Zirconate–Titanate Piezoelectric Ceramics," *J. Am. Ceram. Soc.*, **51** [12] 683–87 (1968).

[4]J. H. Belding and M. G. McLaren, "Behavior of Modified Lead Zirconate–Titanate Piezoelectric Ceramics," *Am. Ceram. Soc. Bull.*, **49** [12] 1025–29 (1970).

[5]H. J. Hagemann, "Loss Mechanisms and Domain Stabilization in Doped $BaTiO_3$," *J. Phys. C: Solid State Phys.*, **11**, 3333–44 (1978).

[6]K. Lubitz and W. Wersing, "Automatic Performance Testing of Piezoelectric Ceramics for Power Transducers," *Ferroelectrics*, **40**, 237–44 (1982).

[7]K. Uchino, H. Negishi, and T. Hirose, "Drive Voltage Dependence of Electromechanical Resonance in PLZT Piezoelectric Ceramics," *Jpn. J. Appl. Phys.*, **28** [Suppl. 28-2] 47 (1989).

[8]S. Hirose and H. Shimizu, "A Method for Automatic Measurement of Ultrasonic-Transducer Constants Using Micro-Computer Control" (in Jpn.); pp. 729–30 in Preprints of the Spring Meeting of the Acoustical Society of Japan (Tokyo, Japan, March 1990). The Acoustical Society of Japan, Tokyo, Japan, 1990.

[9]S. Hirose, Y. Yamayoshi, M. Taga, and H. Shimizu, "A Method for Measuring the Vibration Level Dependence of Impedance-Type Equivalent Circuit Constants," *Jpn. J. Appl. Phys.*, **30** [Suppl. 30-1] 1117–19 (1991).

[10]S. Takahashi and S. Hirose, "Vibration Level Characteristics of Lead-Zirconate–Titanate Ceramics," *Jpn. J. Appl. Phys.*, **31** [Pt. 1, No. 9B] 3055–57 (1992).

[11]S. Takahashi and S. Hirose, "Vibration-Level Characteristics for Iron-Doped Lead-Zirconate–Titanate Ceramics," *Jpn. J. Appl. Phys.*, **32** [Pt. 1, No. 5B] 2422–25 (1993).

[12]K. Nagai and M. Konno, *Electromechanical Vibrators and Their Applications* (in Jpn.); pp. 41–44. Corona-Sha, Tokyo, Japan, 1974.

APPENDIX 44

Effect of composition and temperature on electric fatigue of La-doped lead zirconate titanate ceramics

Q. Y. Jiang, E. C. Subbarao, and L. E. Cross
Materials Research Laboratory, The Pennsylvania State University, University Park, Pennsylvania 16802

(Received 1 September 1993; accepted for publication 24 February 1994)

Composition and temperature of ferroelectric La-doped lead zirconate titanate ceramics influence its electric fatigue behavior, defined as the degradation of the electrical properties under the action of an ac field applied for a long time. Compositions of rhombohedral symmetry exhibit little or no fatigue compared with those of tetragonal and orthorhombic symmetry. At temperatures higher than the dielectric maximum, no fatigue effect was detected. Compositions close to phase boundaries (FE-AFE, FE-FE, or FE-PE) display significant fatigue behavior. Electric fatigue arises from the pinning of domains by space charges or injected carriers or from microcracking. The former (which are charge related) is accompanied by smaller strains and is recoverable by thermal and electrical treatment, while the latter (arising from microcracking) arises from large incompatible stresses between grains and is a permanent damage. The understanding of the mechanism of electric fatigue gained in the present study provides guidelines for enhancing the long-term reliability of devices based on ferroic materials.

I. INTRODUCTION

Composition-temperature diagrams play an important role in the understanding of the behavior of materials. In the case of lanthanum-doped lead zirconate titanate (PLZT) ceramics, which constitute an important class of ferroelectric materials with applications spanning from high-strain electromechanical transducers to thin-film nonvolatile memory devices, such a composition-temperature diagram encompasses: (i) a variety of ferroic phases such as one or more ferroelectric (FE), antiferroelectric (AFE), and paraelectric (PE) phases separated from each other by phase boundaries; spatial composition fluctuations within a given sample, resulting in a ferroelectric relaxor type behavior, are also possible and (ii) a cubic perovskite structure with a range of subtle distortions giving rise to tetragonal (T) and rhombohedral (R) symmetries. Pure lead zirconate has monoclinic symmetry.

These features are displayed in the phase diagram for the PLZT system at room temperature (Fig. 1) in which the hatched region separating the FE-AFE and FE-PE phases denotes a region where a diffuse, metastable ferroelectric phase can be induced by a sufficiently large electric field. The addition of La to the basic lead zirconate titanate (PZT) system confers many beneficial effects such as increased squareness of the (P-E) hysteresis loop, decreased coercive field (E_c), enhanced dielectric and piezoelectric properties and larger electromechanical coupling coefficients, improved mechanical compliance and transparency.[1] A property exhibited by various PLZT compositions, which is of specific significance to the present study, is the variety of hysteresis loops. These include (a) ferroelectric (FE_T) square loop with a large E_c and a linear electro-optic behavior; (b) ferroelectric switchable square loop (FE_R) with high polarization and low E_c; (c) slim loop with no remanant polarization but high induced polarization when subjected to an electric field, also possessing a bifringence which is a quadratic function of the electric field, and a large electrostrictive effect; and (d) a double hysteresis loop, characteristic of AFE materials, near the AFE-FE phase boundary. Thus, a wide variety of ferroic behavior is exhibited by these materials, depending upon composition and crystal symmetry.

Another aspect of considerable importance to the present study is the fact that the crystal structure of some of these compositions is very sensitive to the electric field and stress,[2] for example, a thermally depoled state which is macroscopically cubic with micropolar regions[3] and electrically poled states with macrodomains having an orthorhombic symmetry at room temperature.[2,4,5]

To ensure the long-term reliability of a range of important devices based on these materials involving application of an ac field for a large number of cycles, a clear understanding of the physics underlying their behavior is necessary and is undertaken as a part of a comprehensive study of the fatigue behavior of PLZT ceramics[6] including the effect of surface treatment,[7] porosity,[8] grain size,[9] etc. The property studied is electric fatigue, which is the change in electrical properties (decrease of remanant polarization P_r, and increase of coercive field E_c under the influence of an ac field. A range of compositions in PLZT system was selected to cover ferroelectric, antiferroelectric, paraelectric, and relaxor ferroic behavior, spanning cubic, tetragonal, rhombohedral, and (induced) orthorhombic symmetries. For a given composition, electric fatigue at various temperatures was examined to elucidate the role of the type of ferroic behavior and crystal structure. For clarification of the arguments presented, two materials not belonging to the PLZT system were included in the study; these are the well-known relaxor ferroelectric of lead magnesium niobate (PMN) composition and a single crystal of ferroelectric triglycine sulfate (TGS) which has only 180° domain configuration.

There are three earlier studies of relevance to the present work. Taylor[10] studied the compositional dependence of the fatigue behavior of $Pb_{0.99}[(Zr_xSn_y)_{1-z}Ti_z]_{0.98}Nb_{0.02}O_3$ ternary composition and found minimum fatigue at $x=0.5$, $y=0.5$, and $z=0.14$ and maximum fatigue at $x=0.8$, $y=0.2$,

 0021-8979/94/75(11)/7433/11/$6.00

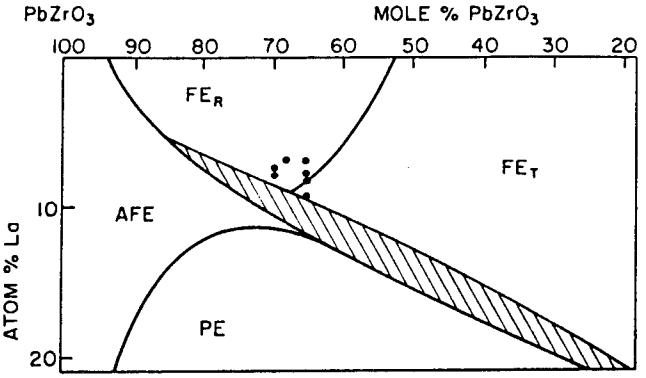

FIG. 1. Room-temperature phase diagram of PLZT ceramics with selected compositions (Ref. 1).

and $z=0.06$. These effects were attributed to the magnitude of the field-induced strain (due to domain reorientations), the larger strain leading to a greater decay. However, some of the samples of the present study on hot-pressed PLZT (7/68/32 and 7/65/35) with a small grain size have the same magnitude of strain as the most fatigued composition of Taylor, but without exhibiting any electric fatigue, suggesting that factors other than the magnitude of electrically induced strain need also to be considered. Freimen *et al.*[11] found that the critical fracture toughness K_{1C} (stress intensity factor) of PZT ceramics plotted as a function of % $PbTiO_3$ exhibited minima at the phase boundaries (AFE_O-$FE_R^{(LT)}$, $FE_R^{(LT)}$-$FE_R^{(HT)}$, and $FE_R^{(HT)}$-FE_T), especially at the morphotropic boundary between tetragonal and rhombohedral phases (Fig. 2). According to these authors, both domain twinning and microcracking could reduce and redistribute the stress and increase the fracture energy with a trade-off between twinning and microcracking giving rise to the observed minima and maxima in Fig. 2. It must be pointed out that the behavior of these materials under an applied ac electric field may not necessarily correspond to the fracture behavior under static mechanical stress.

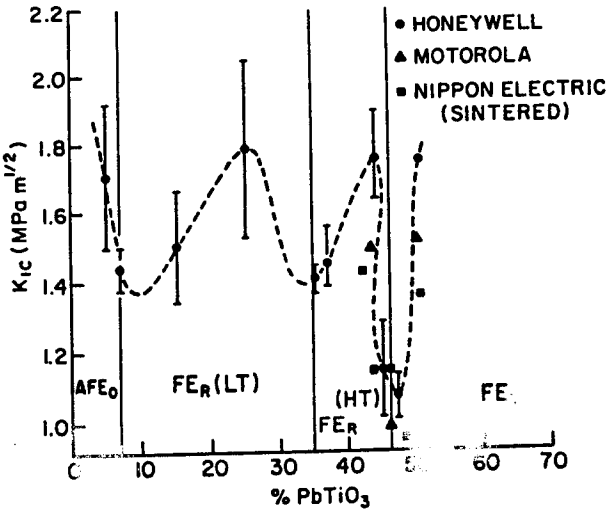

FIG. 2. Critical fracture toughness K_{1C} as a function of composition in PZT ceramic system. Vertical lines indicates the position of the phase boundaries at 25 °C (Ref. 11).

TABLE I. The grain size, temperature of maximum dielectric constant, and ac frequency for fatigue study of PLZT ceramic with different compositions.

Composition	Grain size (μm)	T_m (°C)	f (Hz)
7/65/35	1[a], 5	140	100
8/65/35	5	100	100
8.4/65/35	7	92	40
9.5/65/35	7	55	160
7/68/32	5	130	200
7.6/70/30	7	90	60
7.9/70/30	7	82	100

[a]Sintered; rest are hot pressed.

The only study of the effect of temperature on fatigue behavior of ferroelectrics is that of Stadler[12] who did not find any consistent fatigue behavior in $BaTiO_3$ single crystals in the temperature range of −195 °C and room temperature.

II. EXPERIMENT

There are two ferroelectric (rhombohedral and tetragonal) phases and an antiferroelectric and a paraelectric phase present at room temperature in the PLZT system (Fig. 1). The compositions (La/Zr/Ti) for the present study were selected to include the ferroelectric rhombohedral phase (7/68/32, 7/65/35, 7.6/70/30), the vicinity of the rhombohedral-tetragonal phase boundary (8/65/35, 8.4/65/35), the vicinity of the FE-AFE mixed region (7.9/70/30), and the FE-PE mixed region (9.5/65/35), as marked in Fig. 1.

Schulze, Biggers, and Cross[13] have shown that there is no difference in the phases obtained by conventional sintering and hot pressing processes. In order to obtain dense, pore-free, transparent ceramics, all compositions except 7/65/35 were hot pressed at 1200 °C under a pressure of 200 kg/cm^2 for 20 h (Table I). The average grain size was 5–7 μm in these samples (Table I). The composition 7/65/35 was prepared both by hot pressing and solid-state sintering route at 1300±20 °C. The surfaces of the ceramic sample were ground with 3 μm abrasive and carefully cleaned using an improved procedure[7] to avoid fatigue induced by surface contamination, and finally electroded with sputtered gold.

The properties studied were the remanant polarization P_r and coercive field E_c, calculated from the P-E hysteresis loops obtained using a conventional Sawyer–Tower circuit and recorded on a Nicolet 214 digital oscilloscope. The frequency of the applied ac field for fatigue study is also listed in Table I. The shape of the hysteresis loops provides important data on the nature of the ferroic behavior.

In order to study the effect of crystal structure and ferroic nature on electric fatigue, fatigue studies were carried out at temperatures below and above the temperature corresponding to maximum dielectric constant (T_m, listed in Table I for each composition, which decreases with increasing La content). In most cases, room-temperature studies are also included.

The surfaces and fractured faces of the fatigued samples were observed by scanning electron microscope (SEM),

while changes in the bulk of the sample were studied by using an optical microscope, taking advantage of the transparency of the hot-pressed samples. The gold electrodes were removed before optical microscopic examination. The growth of the cracks can be deduced by focusing the optical microscope at different heights of the sample disk.

III. RESULTS

A. Compositional dependence

1. Fatigue in PLZT x/65/35 compositions

Fatigue tests were carried out on hot-pressed PLZT samples with compositions of the same Zr/Ti ratio, x/65/35, for $x=7$, 8, 8.4, and 9.5. The location of each composition is marked in the phase diagram (Fig. 1). The composition 7/65/35 is in the rhombohedral phase and has stable square hysteresis loop; 8/65/35 and 8.4/65/35 are near the morphotropic phase boundary region and have unstable square hysteresis loops which are very sensitive to the measuring frequencies at room temperature; 9.5/65/35 is near the mixed ferroelectric-paraelectric phase region and has a slim hysteresis loop at room temperature. The fatigue experiments were carried out at room temperature for all compositions except that the composition 9.5/65/35 was studied at -140 °C because of the absence of the square hysteresis loop at room temperature. Figure 3 shows that fatigue did not occur for 7/65/35, but occurred in the other three compositions and proceeded significantly for 8/65/35 and 8.4/65/35. The P_r and P_m (which is not shown here) decreased and E_c increased with the increase of the switching cycles in the three fatigued specimens. The variation of E_c is nearly a mirror image of that of P_r. Figure 4 shows the hysteresis loops for each composition before and after fatigue tests; it is noted that the most fatigued two compositions have initial distorted hysteresis loops.

All the fatigued samples did not recover after thermal treatment at 300 °C for 2 h; the permanent damage usually indicates the microcracking mechanism.[9] The optical micrographs of the fatigued specimens through transmitted light after the removal of the gold electrodes are shown in Fig. 5 for the composition 8/65/35. The sample was partially electroded and the center circle was the switched region in Fig. 5(a). A macrocrack was found which started from the edge of the electrode and extended to the unelectroded region [bottom left-hand corner of Fig. 5(a)], while macrocracks were not observed inside the switched region. The opaque ring in Fig. 5(a) observed after fatigue test indicates a microstructure change, with the center area still remaining transparent and undamaged. Further observation under higher-magnification of part of the opaque ring is shown in Figs. 5(b), 5(c), and 5(d) when the picture was focused near the bottom face of the sample (b), in the middle level (half above the bottom) (c), and near the top surface (d). Three features were noticed under the optical microscope: (1) the microcraking was completely inside the switched region; (2) the mode of the microcracking was intergranular; (3) the microcracks started from the electrode edges near the surface and propagated toward the other face, with the propagation paths of the cracks being a combination of the horizontal and vertical directions. A unique character of the microcracking is noticed in this sample, i.e., in the microcracked region, all the grains break up to give a sandlike appearance. Since very few ceramics are transparent, this type of cracking has rarely been observed in such a direct striking way.

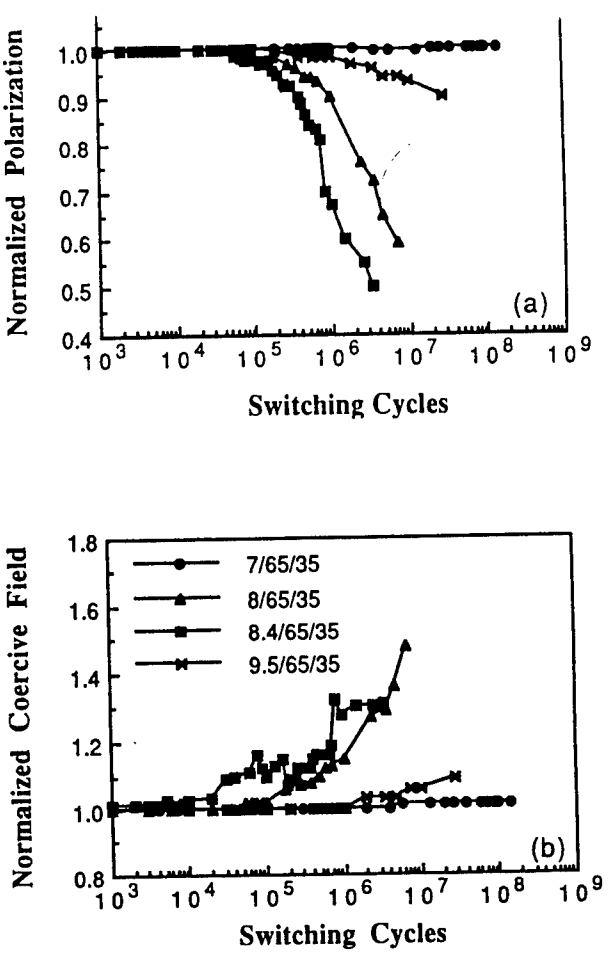

FIG. 3. The normalized remanant polarizations and coercive fields as a function of the switching cycles for hot-pressed PLZT ceramics with compositions x/65/35.

Microcracking was more severe for 8.4/65/35, and started both from edges and from surface as observed by scanning electron microscopy (SEM) (Fig. 6). In Fig. 6(a) macrocracks can be seen on the fractured cross section of the fatigued sample near the surface; after wiping off part of the gold electrode on the surface, it is found that some of the grains were partially pulled out as shown in Fig. 6(b). The fatigued sample became partially opaque; the opaque regions were parallel to the surfaces and close to the high voltage terminal face. After removal of the discolored region (half of the thickness) by grinding, the sample recovered nearly to its original state, and Table II lists the changes of its P_r and E_c.

2. Fatigue in PLZT x/70/30 compositions

PLZT 7.6/70/30 and 7.9/70/30 are close to the phase boundary between ferroelectric rhombohedral phase and antiferroelectric phase (Fig. 1); their T_m and the ac frequencies for fatigue tests are listed in Table I. The results of their

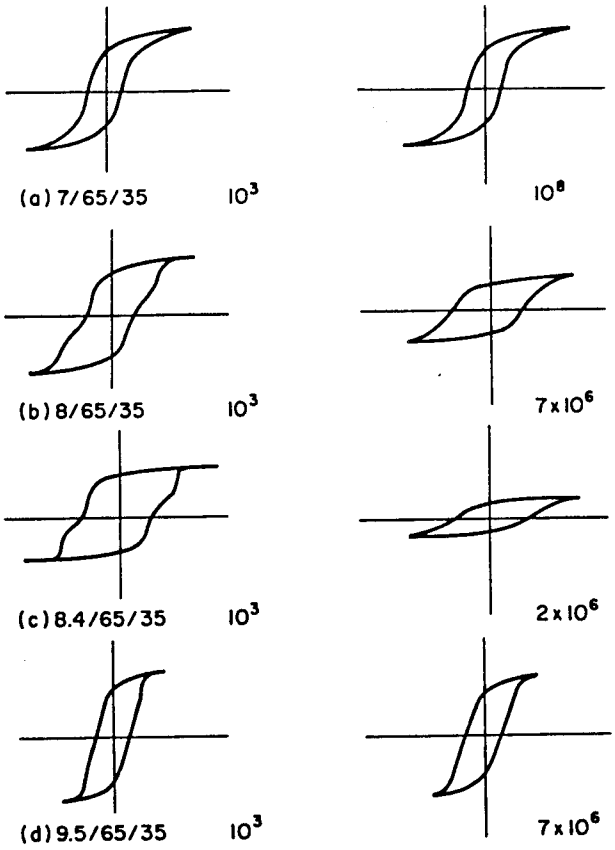

FIG. 4. Hysteresis loop curves recorded during fatigue tests for hot-pressed PLZT ceramics with compositions x/65/35.

fatigue tests together with that of composition 7/68/32 [Fig. 7(a)] show that fatigue occurred in both compositions and more severely in composition 7.6/70/30. Figure 7(b) shows the hysteresis loops for each composition measured at the beginning and the end of the fatigue tests, where composition 7.9/70/30 showed double hysteresis loops.

It is noticed that the three compositions (8/65/35, 8.4/65/35, and 7.6/70/30) which fatigued most severely have similar hysteresis loops as can be seen in Figs. 4 and 7(b). The same cracking pattern as occurred in 8.4/65/35 and 8/65/35 samples was also observed by optical microscope in fatigued 7.6/70/30 samples (not shown here).

Although the grain sizes of those compositions ranged from 5 to 7 μm, the rates of the fatigue for the severely fatigued compositions (8.4/65/35, 7 μm; 8/65/35, 5 μm; 7.6/70/30, 7 μm) were obviously higher than that of 7/68/32 composition with 10 μm grain size.[9] Therefore, there is no doubt about the compositional effect on the fatigue behavior, and the mechanism of the composition effect will be discussed later.

3. Fatigue in antiferroelectric ceramics

The lanthanum-doped lead zirconate titanate stannate antiferroelectric ceramic system was studied extensively by Berlincourt, Krueger, and Jaffe,[14] among others. The composition used in our study is $Pb_{0.97}La_{0.02}(Zr_{0.53}Ti_{0.12}Sn_{0.35})O_6$ which is in the antiferroelectric tetragonal phase close to the phase boundary of antiferroelectric tetragonal and ferroelectric rhombohedral phases, and its coercive field is 25 kV/cm at low frequency. The samples were fabricated by conventional sintering method. The average grain size is 6 μm and the sizes of pores range from 1 to 30 μm.

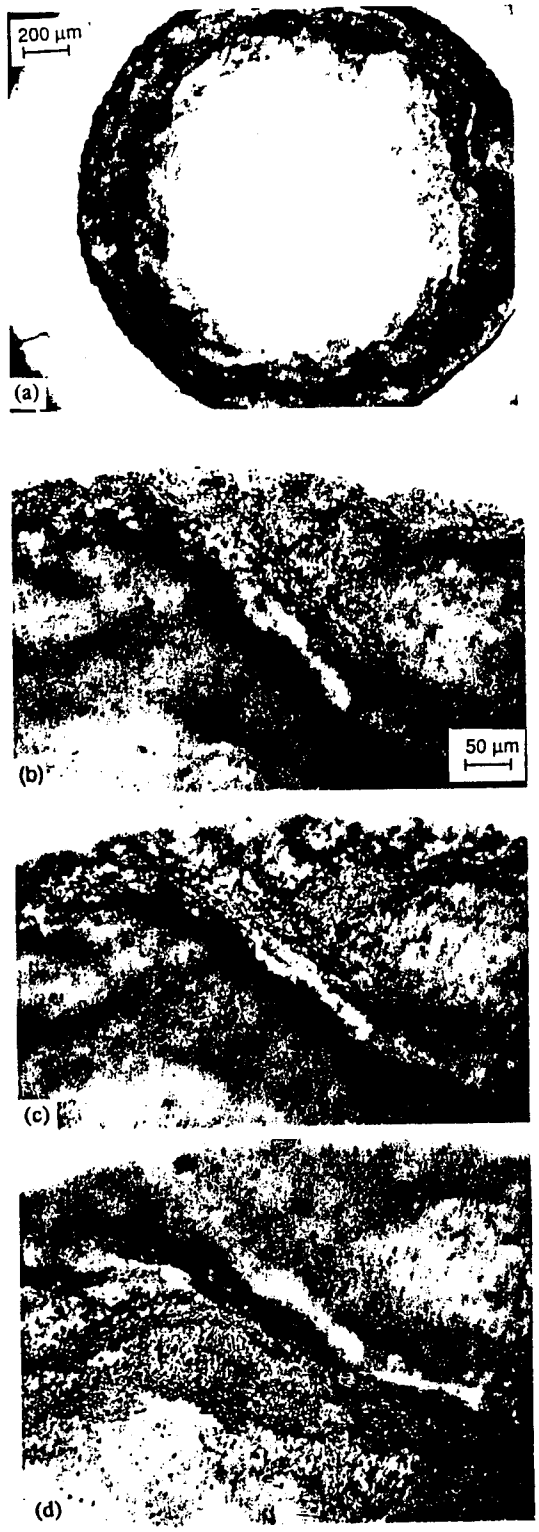

FIG. 5. Microstructure of the fatigued PLZT 8/65/35 sample observed by optical microscope with transmitted light: (a) show the total fatigued area (within circle); (b), (c), and (d) further observation under higher magnification for part of the opaque ring in (a), when the picture was focused near the bottom face of the sample (b), in the middle level (half above the bottom) (c), and near the top surface (d).

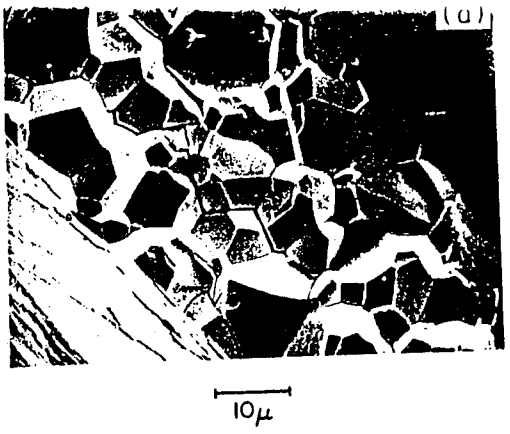

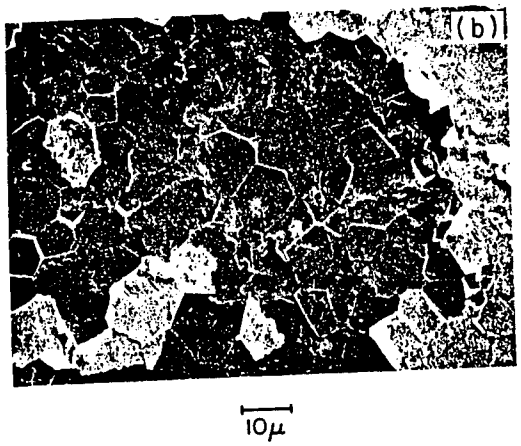

FIG. 6. Fractured cross section of a fatigued PLZT 8.4/65/35 sample observed by SEM: (a) fractured cross section and (b) microstructure changes of the surface beneath the electrode.

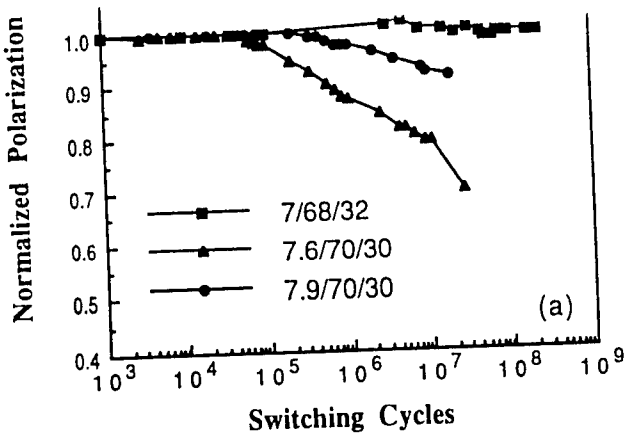

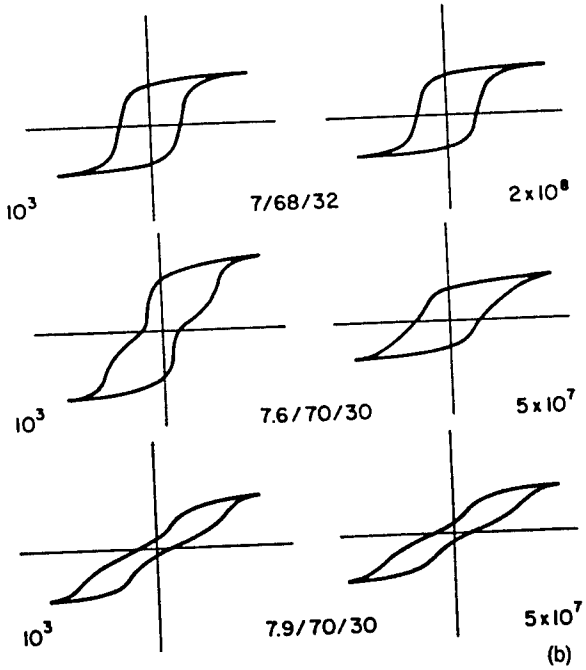

FIG. 7. (a) The normalized remanant polarization as a function of the switching cycles; (b) hysteresis loop curves recorded during fatigue tests for hot pressed PLZT ceramic of three compositions.

The fatigue study carried out at 600 Hz up to 10^9 switching cycles shows that the polarization decreased slowly with the switching cycles, and the coercive field was stable until 10^8 switching cycles, then increased slowly with continuous switching [Fig. 8(a)]. The double hysteresis loops recorded at 10^4 and 10^9 switching cycles [Fig. 8(b)] show no significant changes in the shapes of the loops.

4. Fatigue in triglycine sulfate single crystal

Triglycine sulfate (TGS) single crystal, $(NH_2CH_2COOH)_3 \cdot H_2SO_4$, has monoclinic symmetry; its Curie temperature is 49 °C. Ferroelectricity is found along the direction of the twofold polar axis, monoclinic *b* axis (Jona and Shirane[15]). TGS is water soluble and undeteriorated surfaces are difficult to obtain during sample preparation. Thus, the samples used in the present experiments were prepared by cleavage of the crystal planes which are perpendicular to the *b* axis, resulting in very clean and undamaged surfaces. The thicknesses of the samples ranged from 1 to 2 mm.

TABLE II. The changes of the polarization and coercive field of the PLZT 8.4/65/35 sample due to fatigue and its recovery.

	P_r (μC/cm^2)	E_c (kV/cm)
After 10 switching cycles	27.9	3.1
After 10^6 switching cycles	10.7	4.7
After removal of discolored region	24.7	3.4

The fatigue experiment was carried out at a frequency of 900 Hz, using silver paint as electrode. The results show that fatigue did not occur even after 10^8 switching cycles [Fig. 9(a)]. The hysteresis loops at 10^3 and 10^8 are shown in Fig. 9(b), the coercive field at 900 Hz is 0.35 kV/cm. Stability of the ferroelectricity under ac field switching in TGS single crystal could be due to the fact that only 180° domain configuration exists in the crystal; this is further discussed in the following subsection.

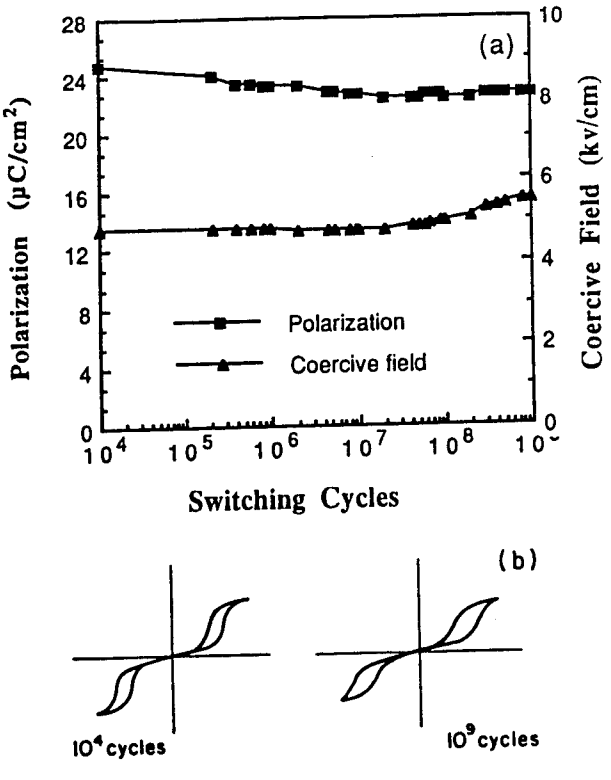

FIG. 8. (a) The normalized polarization and coercive field as a function of switching cycles; (b) hysteresis loop curves recorded during fatigue experiment for antiferroelectric $Pb_{0.97}La_{0.02}(Zr_{0.53}Ti_{0.12}Sn_{0.35})O_3$ ceramic.

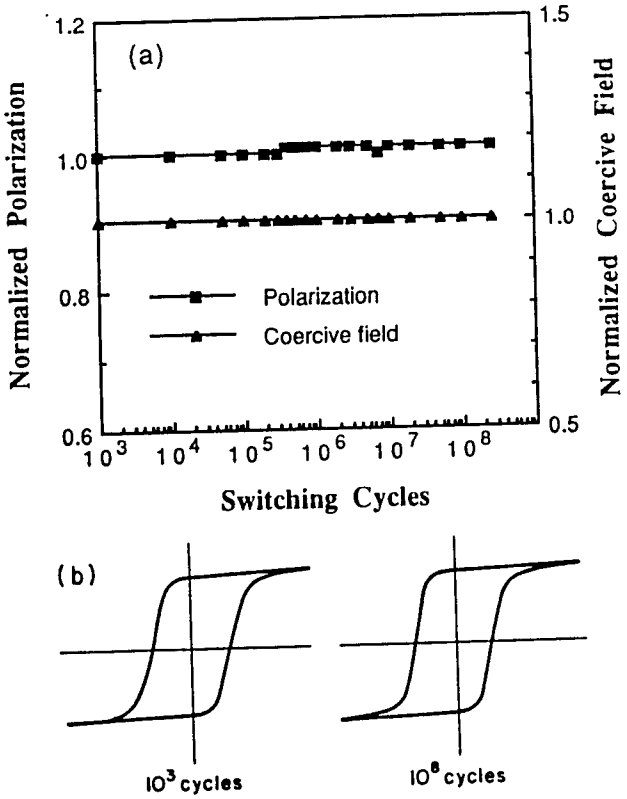

FIG. 9. (a) The normalized remanant polarization and coercive field as function of the switching cycles for TGS single crystal; (b) its hysteresis loop curves recorded during fatigue test (P_r=2.5 μC/cm^2, E_c=0.35 kV/cm).

B. Temperature dependence

1. Fatigue behavior of PLZT ceramics

Compositions of PLZT 7/65/35 (T_m=140 °C) made by conventional sintering and hot-pressed 9.5/65/35 were studied for temperature effects. Figure 10(a) shows the results of fatigue tests for sintered PLZT 7/65/35 at 30, 87, 118, 152, and 167 °C temperatures, the maximum field and the frequency for all different temperatures were kept constant (11 kV/cm and 400 Hz). The corresponding hysteresis loops recorded before and after fatigue tests are shown in Fig. 11(a) for each temperature except at 167 °C at which the loops were straight lines and did not change with switching cycles. In Fig. 10(a), the fatigue rates decrease as temperature increases. It was expected that when temperature is higher than T_m, the fatigue should stop since above T_m the majority of the structure is transformed to the paraelectric phase. However, fatigue still occurred at 152 °C (12 °C higher than T_m) with a much slower rate and finally at 167 °C (27 °C higher than T_m), fatigue was no longer observed. The P_m decreases with the increase of temperature (Table III). In Fig. 11(a) the remanant polarization decreases with increasing temperature and did not completely disappear until the temperature was higher than T_m. Constrictive neck (double) hysteresis loops were not observed as temperature increases which often occur in the compositions near phase boundaries. The mechanism of fatigue in composition of sintered 7/65/35 is mainly due to domain pinning by space charges.[8] How temperature affects the space-charge pinning will be discussed later.

The composition 9.5/65/35 was chosen to study the low-temperature behavior because it has lower T_m (55 °C) and the square hysteresis loops occurred only at very low temperatures. Fatigue experiments were carried out at three temperatures, −140, 25, and 105 °C with the frequencies of 160, 50, and 100 Hz, respectively; the results are shown in Figs. 10(b) and 11(b). It is surprising to find that the fatigue at −140 °C (with large polarization and square loop) proceeded much more slowly than that at 25 °C with slim loop. The P_m and the P_r at −140 °C were 37.5 and 27.7 μc/cm^2 and higher than the P_m (23 μC/cm^2) at 25 °C; this is different from the situation in sintered 7/65/35 composition. When temperatures were high enough both the samples did not fatigue any more; although the remanant polarizations approach zero and hysteresis loops become slim, fatigue still occurred (as long as temperature is below T_m). It can be concluded from these results that when ferroelectric ceramics are in paraelectric phase (at a temperature about 30 °C higher than the T_m), fatigue does not occur either in sintered or hot pressed PLZT ceramics.

Fatigued 9.5/65/35 samples did not recover after thermal treatment. Fatigue that occurred in these samples is due to microcracking since its grain size (7 μm) is larger than the critical size and the observations under optical microscope with transmitted light on 9.5/65/35 sample fatigued at 25 °C revealed not only microcracking but also macrocracking, which propagated severely as shown in Fig. 12(a). In the 9.5/65/35 sample fatigued at −140 °C only some sandlike grains were observed by optical microscope with transmitted light [Fig. 12(b)]; the cracking at low temperature was much less severe than that of the sample fatigued at 25 °C. The different cracking behaviors will be discussed later.

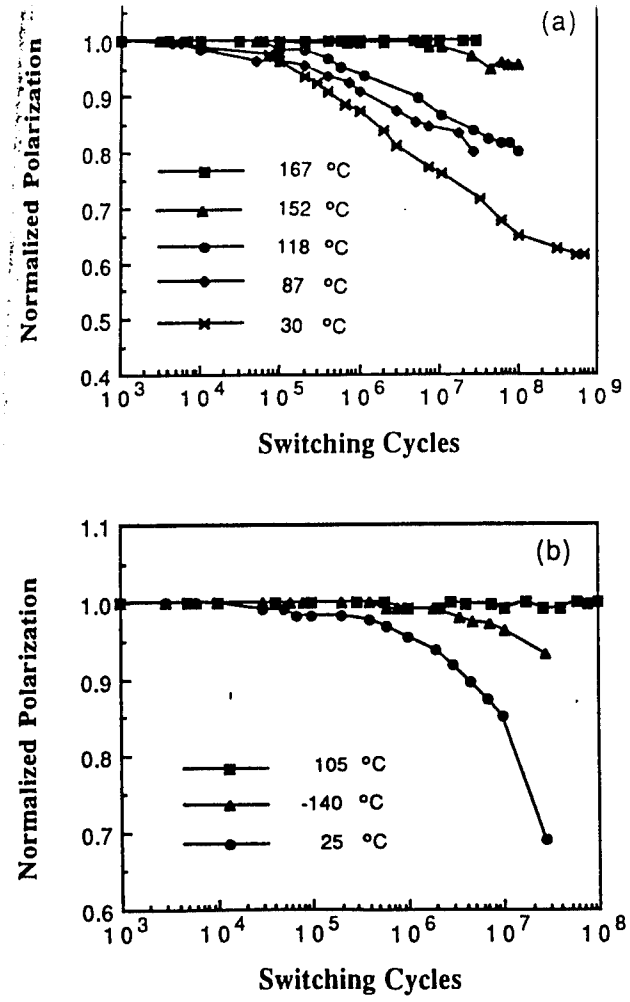

FIG. 10. The normalized polarization as a function of the switching cycles for (a) sintered PLZT 7/65/35 ceramic and (b) hot-pressed PLZT 9.5/65/35, at different temperatures.

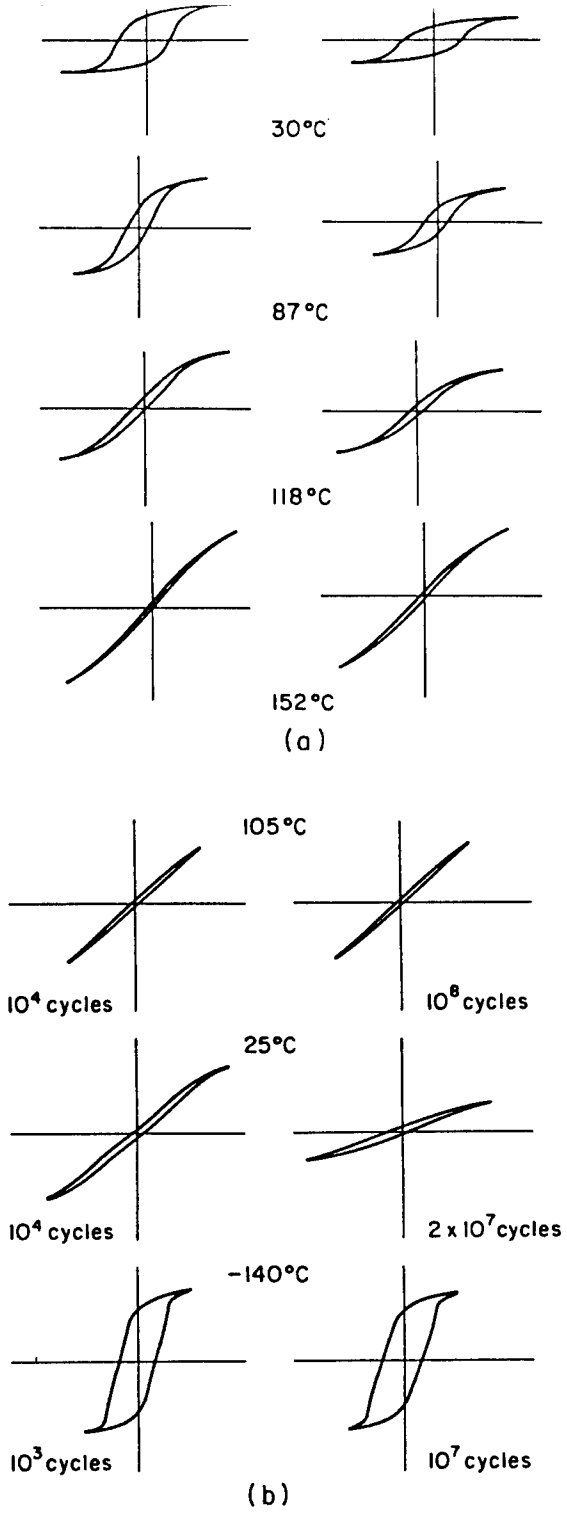

FIG. 11. Hysteresis loop curves recorded during fatigue tests (a) at four temperatures for sintered PLZT 7/65/35 ceramic and (b) at three temperatures for hot-pressed 9.5/65/35 PLZT ceramic.

2. Fatigue behavior of PMN ceramics

PMN ceramic specimens with average grain size 5 μm were made by conventional sintering method and have a low T_m, about -15 °C. Fatigue did not occur at 25 °C up to 10^9 switching cycles, and at -140 °C the P_m and P_r, which had initial values of 32.0 μm/cm^2 and 18.4 μC/cm^2, started decreasing after 10^6 switching cycles, with the E_c almost unchanged. Figure 13(a) shows the changes of polarization with switching cycles at 25 and -140 °C. Fatigue in PMN at low temperature proceeded much more slowly than that in sintered PLZT sample whose hysteresis loop at room temperature had the same shape as that of PMN at -140 °C. After 10^8 switching cycles at -140 °C the polarization only dropped by 10% of the initial value. When the sample temperature returned to room temperature, the P_m measured again was the same as that measured before the fatigue experiment; thus fatigue at low temperature in PMN did not cause permanent damage. Fatigue in this case was caused by domain pinning, and not by microcracking, since it is impossible to heal microcracks at room temperature. In addition, these samples were sintered by conventional method and had low density (97%); their fatigue mechanism should be the same as in sintered PLZT and PZT samples.[8]

Fatigue experiments were also carried out on hot-pressed PMN doped with 1% lanthanum at room temperature and -140 °C. After 10^9 switching cycles under applied ac field, the P_m and P_r did not decrease and E_c was unchanged.

TABLE III. The maximum polarization of sintered PLZT 7/65/35 ceramic at different temperatures.

T (°C)	37	87	118	152	167
P_m (μC/cm^2)	28.0	26.0	21.5	15.0	12.6

Figure 13(b) shows the Pr as a function of switching cycles at both 25 and −140 °C. The grain size of hot-pressed PMN was 2 μm and below critical grain size; like the hot-pressed PLZT 7/68/32 and 7/65/35 ceramic with small grain size, fatigue did not occur in hot-pressed PMN ceramic with grain size less than 5 μm. It shows once again that high density is a necessary requirement to avoid the onset of fatigue.

IV. DISCUSSION

A. Compositional effect

The results given in previous sections have clearly revealed that fatigue behavior is sensitive to the composition and temperature. It is noticed that the compositions of PLZT with pure rhombohedral phase did not fatigue, while the compositions located near phase boundaries fatigued; thus, fatigue behavior could be actually affected by crystal structure and/or domain structure.

Both the compositions 7/65/35 and 7/68/32 which did not fatigue belong to rhombohedral phase under applied field; no phase changes occurred during ac switching processes as shown in Figs. 4 and 7(b) exhibiting normal ferroelectric loops without any distortion. Switching by electric field takes place more easily in ferroelectric rhombohedral phase (FE_R) than in ferroelectric tetragonal and orthorhombic phases (FE_T,FE_O), since the E_c value of FE_R compositions of PLZT is about half the E_c of FE_T compositions of PLZT.[1] This indicates that for rhombohedral structure internal stresses are smaller during the switching process than those for tetragonal and orthorhombic phases. This can be further proved by $BaTiO_3$ single crystal in which the E_c for orthorhombic phase at $-90_{(+)}$ °C is 1.45 kV/cm while for rhombohedral phase of the same crystal at almost same temperature $-90_{(-)}$ °C the E_c is 0.9 kV/cm (Jona and Shirane[15]). Stadler[12] found that none of $BaTiO_3$ crystals tested at −195 °C (rhombohedral phase) suffered any change in switching charge after 4×10^8 cycles and the charge switched at room temperature (tetragonal phase) dropped to less than half its original value after 4×10^7 cycles. The rhombohedral crystal structure is derived from cubic structure by shear deformation. Since the shear elastic modulus is only half of the normal elastic modulus, the energy needed for shear deformation is less than for normal deformation, and the internal stress resulting from the shear deformation should also be smaller than that due to the normal deformation. The internal stresses in PLZT ceramics for several compositions with different crystal structures have been studied quantitatively by Okazaki[16] using the microindentation method; he found that the internal stress in FE_R is smaller than that in FE_T, and increases with increasing c/a ratio in tetragonal compositions. From the above discussion it is clear that the ease of switching by electric field and smaller internal stress in FE_R is the main reasons for the absence of electric fatigue and microcracks in 7/65/35 and 7/68/32 PLZT compositions in our study.

PLZT 8/65/35 and 8.4/65/35 and 7.6/70/30, which are the three compositions exhibiting severe fatigue, have similar constricted neck hysteresis loops as can be seen in Figs. 4 and 7(b). All three compositions are located in the cubic matrix region before poling, and change to orthorhombic after poling,[4] indicating field-induced phase transformation at room temperature, while the 7/65/35 and 7/68/32 compositions sustain their rhombohedral phase structures after poling. The occurrence of the necks in the hysteresis loops of 8/65/35, 8.4/65/35, and 7.6/70/30 compositions also indicates the transformation of macrodomain states with orthorhombic symmetry to microdomain states in cubic matrix; this transformation can be further proved by the measurement of the electric-field dependence of transmittance of the PLZT sample at different temperatures (Yin *et al.*[17]). Their results showed that when the hysteresis loops have square shapes without necks at low temperature (−10 °C), the maximum transmittance is very low (<6%) in the switching process; once the necks occurred (at 7 and 13 °C the maximum transmittance can reach above 80% twice in one switching cycle, which indicates that the cubic matrix state can recur in the switching process. Therefore, the structure changes from cubic matrix with microdomains to orthorhombic macrodomain state twice in one cycle in the sample with a constricted neck hysteresis loop. The changes of crystal and domain structure could result in large internal strain fluctuations and internal stresses which cause microcracking and failure. This may explain the occurrence of severe fatigue in these three samples.

The hysteresis loops for the composition 7.9/70/30 are pseudoantiferroelectric type, with very small remanant polarization and remanant strain [Fig. 7(b)]. The field-forced phase change returns to the original state before the field drops to zero, and no macrodomains are left to be switched to microdomains by the reversal field; this could greatly reduce the internal stresses, and result in less fatigue in composition 7.9/70/30 than in the other three compositions discussed above.

In true antiferroelectric materials (AFE) the switching of the polarization has a different mechanism; no spontaneous polarization exists in AFE, and the orientations of the dipoles are alternately aligned in opposite directions. The field-forced ferroelectric phase is stable only under high field, and at low fields FE returns to the AFE state. Fatigue in the antiferroelectric sample (Fig. 8) is much less severe, which is possibly due to the fact that in the switching process of the AFE to FE, the polarization direction changes only by 180 °C with consequent smaller internal stresses than in switching the spontaneous polarization of the ferroelectrics by 90°. The slow fatigue observed in AFE samples may be partially contributed by space-charge pinning,[8] since the samples were made by conventional sintering method, which gives rise to voids and pores.

It is not surprising that fatigue did not occur in TGS single crystals, because there are only 180° domains in this crystal. In switching process, only some atoms or atom

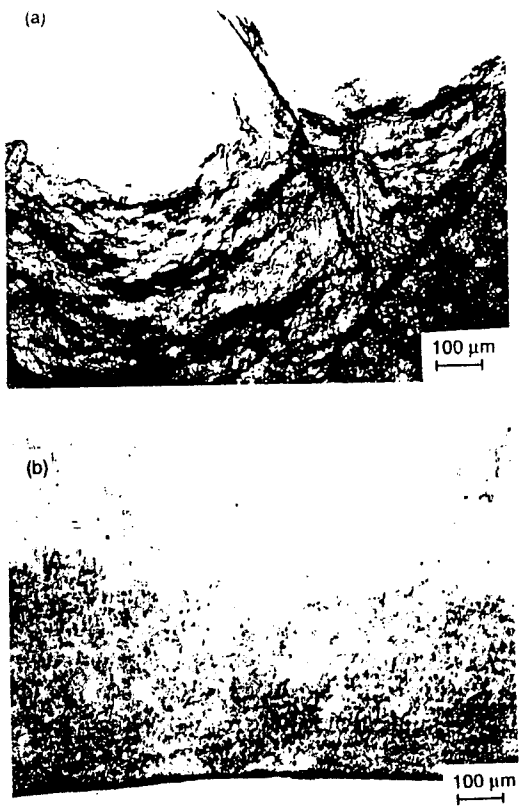

FIG. 12. Cracks observed in fatigued hot-pressed 9.5/65/35 ceramics by optical microscope with transmitted light: (a) Fatigued at room temperature and (b) fatigued at −140 °C.

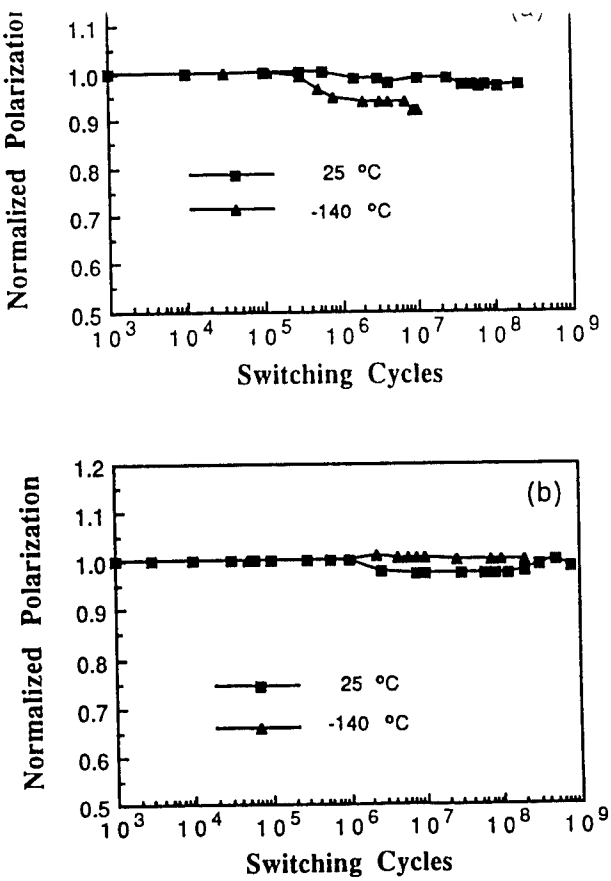

FIG. 13. Polarization as a function of the switching cycles for (a) sintered PMN and (b) hot-pressed 1% La-doped PMN.

groups of TGS rotate under the applied field, with no change in the crystal structure; therefore, the internal stresses involved in switching process should be quite small. Further, defects in high-quality TGS organic crystals are rare; hence domain pinning occurs only with difficulty.

B. Temperature effect

Since the main mechanism of fatigue in sintered PLZT 7/65/35 is domain and defect pinning by space charges, the explanation of the temperature dependence of fatigue should consider both domain states and space-charge mobility at different temperatures. As temperature increases, the maximum polarization decreases (Table III) and the remanant polarization decreases faster [Fig. 11(a)], since fewer domain walls are available for pinning. At higher temperatures near T_m, the samples are highly polarizable under the applied field, and the domains or defects which have been pinned by space charges could be depinned by the ac field; Stewart and Cosentino[18] found that fatigued soft PZT sample could be restored to nearly its original condition by heating the sample to 150 °C and then applying 60 Hz excitation. The change in the mobility of the space charge with temperature may have a much lesser effect on fatigue compared with the changes of the polarization. So, it can be concluded that the lower fatigue rates at higher temperatures could primarily be contributed by the decrease of the polarization in PLZT 7/65/35 sintered ceramics.

The disappearance of fatigue at 167 °C [Fig. 10(a)] can be easily explained; the sample was almost completely in paraelectric phase (27 °C higher than T_m), the spontaneous polarization disappeared and domains no longer existed. A slow fatigue observed at 152 °C could be due to the fact that relaxor materials have diffuse phase transformations because of the coexistence of ferroelectric and paraelectric phases arising from the inhomogeneous compositional fluctuations, and the polar regions can exist at temperatures somewhat above T_m (Cross[3]); in addition, the applied field can force some of the nonpolar regions into the polar region; under long-time continuous ac switching some of the polar regions could be stabilized by space charge or injected carriers, with a slow decrease of the switchable polarization.

The decrease of the polarization can not explain the temperature dependence of fatigue in hot-pressed 9.5/65/35 samples [Fig. 10(b)], which showed greater fatigue at 25 °C than at −140 °C, since the main fatigue mechanism of hot-pressed high-density (>99%) PLZT ceramics is microcracking and differs from that of sintered low-density (92%–97%) PLZT samples.[8] The phase relations in x/65/35 PLZT at different temperatures deduced from x-ray, dielectric, and piezoelectric measurements by O'Bryan[5] show that the PLZT 9.5/65/35 at 25 °C has a pseudocubic structure and is placed in the AFE (pseudocubic region), based on the existence of a double hysteresis loop. However, a double hysteresis loop

can also be due to the field-induced ferroelectric phase at temperatures near T_c or T_m as in the case of $BaTiO_3$ crystal, or the field-forced transformation of microdomains to macrodomains;[19] in addition, the superlattice crystal structure associated with AFE phase in $PbZrO_3$ was not observed in this phase region.[5] Fatigue due to microcracking at 25 °C could be caused by the nonuniform deformation of mismatched grains and concentration of stresses near the electrode edges. Although at this temperature the remanant polarization is small and the piezoelectric contribution can be neglected, the electrostriction is quite large in this composition (relaxor ceramic) at room temperature. The electrostrictive coefficients Q_{11} and Q_{12} measured by Meng, Kumar, and Cross[20] for PLZT 9.5/65/35 are 21.0×10^{-3} and -9.1×10^{-3} m^4/C^2, respectively. The initial polarization of the sample used in the fatigue experiment at 25 °C was 23.0 $\mu C/cm^2$ under an applied field of 22 kV/cm, and the longitudinal strain calculated from Q_{11} and P_m is 11×10^{-4} which is of the same order as the piezoelectric strains. This high strain and the large grain size (7 μm) resulted in microcracking.

At 105 °C, a temperature 50 °C higher than T_m of 9.5/65/35 composition, the sample is in paraelectric phase. As the polarization is only half of the value at 25 °C, so the strain is only one-fourth of that at 25 °C; in addition, the local microstructure stresses which exist below T_c due to the phase transformation from cubic to ferroelectric phase are released. Hence, the microcracking (fatigue) did not occur at this high temperature.

The occurrence of fatigue at low temperature (−140 °C) is more complicated [Fig. 10(b)]; both the P_m and P_r are quite high and the field-induced strain could be larger than that at room temperature. The different structures at 25 and −140 °C may explain this fatigue behavior. At −140 °C, the sample should be in the ferroelectric rhombohedral phase which has smaller internal stresses than other ferroelectric phases. The square hysteresis loops without necks [Fig. 11(b)] indicate that the crystal structure was stable at low temperature under an applied field. Therefore, the field applied to the sample at low temperature mainly caused the switching of the spontaneous polarization and did not cause a change of the crystal structure, while it is known[3] that at room temperature the applied field could induce the transformation of nonpolar regions to polar states and produce unstable lattice distortions, resulting in microstructure stresses which enhance microcracking and increase the rate of fatigue. The slow fatigue at low temperature may also be related to the change in the mechanical strength of the sample; since the lattices contract with the decrease of temperature, producing compressive internal stresses in the sample, the fracture strength could be higher at low temperatures. The occurrence of slow fatigue could be attributed to the large grain size which results in microcracking.

Fatigue behavior in PMN ceramic system is similar to that in PLZT ceramics. The conventionally sintered samples with a grain size of 5 μm showed fatigue at low temperature (−140 °C) with a rather slow rate. The cause of the fatigue is believed to be domain and defect pinning since after the sample was reheated to room temperature (40 °C higher than T_m), the initial state was recovered without permanent damage. The slower fatigue rate in the PMN sample than in sintered PLZT 7/65/35 could arise from three reasons: (1) The density of the sintered PMN ceramic is higher than that of sintered PLZT 7/65/35 ceramic; less pores and defects are available to provide space charges;[8] (2) PMN is a stoichiometric compound, and has fewer intrinsic defects (which can be pinned by space charge or injected carriers) and cleaner grain boundaries; (3) the mobility of the space charge may be less at low temperature.

Hot-pressed PMN (1% La) did not fatigue at low temperature, which is attributed to its high density and small grain size. At room temperature, fatigue did not occur in both the PMN samples because both were in paraelectric phase.

V. CONCLUSIONS

Evidence has been presented to establish the relationship between fatigue behavior and composition in the PLZT system. In the x/65/35 compositions, fatigue increased from nil at $x=7$ through $x=9.5$, 8 to most severe for $x=8.4$. The two compositions ($x=8.4$ and 8) with severe fatigue rates had exhibited constricted hysteresis loops before the fatigue experiment. The fatigue rate of 7.6/70/30 PLZT composition was greater than that of 7.9/70/30. On the other hand, antiferroelectric (modified PLZT) composition as well as single-crystal triglycine sulfate (TGS) did not show any significant fatigue effect, which is attributed to the fact that polarization changes under applied ac field involve only 180° domain switching in these cases.

Temperature was also found to influence the fatigue rates of these materials. At temperatures higher than T_c or T_m (by 30–50 °C), no fatigue effects were observed and this was attributed to the absence of domains and spontaneous polarization in the paraelectric state. At other temperatures, the fatigue rate depends upon the ease of domain switches, and associated strains.

Both the compositional and temperature dependence of fatigue behavior translate into the influence of the crystal symmetry and ferroic state of the material under the action of applied ac field for long periods. Among the ferroelectric phases, the rhombohedral symmetry, with its small internal stress associated with the shear distortion of the cubic lattice, has the least fatigue rate compared to that of the ferroelectrics with tetragonal and orthorhombic symmetries. Antiferroelectric materials and ferroelectric TGS crystal exhibit little or no fatigue effect, since polarization changes only by 180° in these materials with no accompanying strain. On the other hand, the samples close to the phase boundaries (due to composition, temperature, or electric field) undergo most severe fatigue behavior and this is attributed to easy polarization changes and consequent large lattice distortions. Electric fatigue can be due to either domain pinning by space charges or injected charge carriers or intergranular microcracking resulting from incompatible stresses between grains. The former is recoverable by thermal and electrical treatment, while the latter (microcracking) is a permanent damage.

The conclusions drawn from the present study provide guidelines for enhancing the long-term reliability of devices based on ferroic ceramics.

The authors are grateful to the Office of Naval Research for financial support.

[1]G. H. Haertling, Ferroelectrics **75**, 25 (1987).
[2]E. T. Keve and K. L. Bye, J. Appl. Phys. **46**, 810 (1975).
[3]L. E. Cross, Ferroelectrics **76**, 241 (1987).
[4]E. T. Keve, Ferroelectrics **10**, 169 (1976).
[5]H. M. O'Bryan, Jr., J. Am. Ceram. Soc. **56**, 385 (1973).
[6]Q. Y. Jiang, Ph.D. thesis, Pennsylvania State University, 1992.
[7]Q. Y. Jiang, W. Cao, and L. E. Cross, J. Am. Ceram. Soc. (to be published).
[8]Q. Y. Jiang and L. E. Cross, J. Mater. Sci. (to be published).
[9]Q. Y. Jiang, E. C. Subbarao, and L. E. Cross (unpublished).
[10]G. W. Taylor, J. Appl. Phys. **38**, 4697 (1967).
[11]S. W. Freiman, L. Chuck, J. J. Mecholsky, J. J., D. L. Shellman, and L. J. Hasselman, and F. Lange (Plenum, New York, 1986), p. 175.
[12]H. L. Stadler, J. Appl. Phys. **29**, 743 (1958).
[13]W. A. Schulze, J. V. Biggers, and L. E. Cross, J. Am. Ceram. Soc. **61**, 46 (1978).
[14]D. Berlincourt, H. H. A. Krueger, and B. Jaffe, J. Phys. Chem. Solids **25**, 659 (1964).
[15]F. Jona and G. Shirane, *Ferroelectric Crystals* (Macmillan, New York, 1962), pp. 28 and 119.
[16]K. Okazaki, J. Am. Ceram. Soc. **63**, 1150 (1983).
[17]Z. W. Yin, X. M. He, C. Li, Z. Wei, and H. Ni, J. Chin. Silicate Soc. **11**, 410 (1983).
[18]W. C. Stewart and L. S. Cosentino, Ferroelectrics **1**, 149 (1970).
[19]X. Yao, Z. Chen, and L. E. Cross, J. Appl. Phys. **54**, 3399 (1983).
[20]Z. Y. Meng, U. Kumar, and L. E. Cross, J. Am. Ceram. Soc. **68**, 459 (1985).

APPENDIX 45

JOURNAL OF MATERIALS SCIENCE 29 (1994) 3363–3371

Acoustic emission study of phase relations in low-Y_2O_3 portion of ZrO_2–Y_2O_3 system

V. SRIKANTH, E. C. SUBBARAO*
Materials Research Laboratory, The Pennsylvania State University, University Park, PA 16802, USA

The (metastable) tetragonal phase in 3–4 mol% Y_2O_3–ZrO_2 alloys undergoes a transition to the monoclinic form in the 200–300 °C temperature range. Microcracking due to the volume change at this transition has been detected in these compositions by sharp acoustic emission during heating. The phase change was confirmed by X-ray diffraction, dilatometry and scanning electron microscopy. The monoclinic $\rightleftharpoons$ tetragonal transition in ZrO_2–1 mol% Y_2O_3 alloy at 850–750 °C and the same phase change in 2, 3, 4 and 6 mol% Y_2O_3 compositions at the eutectoid temperature of about 560 °C was also clearly signalled by the acoustic emission counts during heating and cooling. There was no significant acoustic emission activity on heating and cooling the 9 and 12 mol% Y_2O_3 compositions, which are cubic. The acoustic emission data thus confirm the phase relations in the 1–12 mol% Y_2O_3 region, established by conventional methods such as differential thermal analysis, dilatometry and X-ray diffraction.

1. Introduction

Since the discovery of high fracture toughness in zirconia alloys containing a metastable tetragonal phase by Garvie *et al.* [1], there has been intense study of the parameters governing this property. Toughened zirconia finds many applications, e.g. as extrusion dies. The presence of the metastable tetragonal phase which transforms to the monoclinic form is the key factor for the toughening process. Toughened zirconia alloys with small amounts of Y_2O_3 are among the prime candidates as toughened ceramics due to the relative ease of retaining the tetragonal phase at room temperature [2–4]. The amount of the tetragonal phase retained was found to depend on density [3], critical grain size [3, 4] (which in turn depends upon Y_2O_3 content), the temperature from which the sample is cooled [2] and the rate of cooling. For example, higher density, smaller than critical grain size, heating in the tetragonal phase field and rapid cooling rate favour the retention of the tetragonal phase. Both thermodynamic and kinetic factors were discussed in connection with transformation toughening [5]. The decrease in fracture toughness of partially stabilized zirconia annealed at > 1000 °C has been attributed to coarsening of tetragonal grains beyond the critical size [6–8]. On the other hand, annealing at low temperatures (200–300 °C) was also found to drastically decrease the strength and fracture toughness of zirconia–yttria alloys [9–26]. The amount of monoclinic phase was observed to increase rapidly when annealed in the 150–200 °C region and decrease sharply when annealed above 300–400 °C. Thus a maximum amount of the monoclinic phase is detected by annealing around 250 ± 50 °C. The exact annealing temperature for maximum monoclinic phase depends upon the initial sintering temperature [2, 10–18], the amount of Y_2O_3 [10–18, 21–24], the presence of moisture [19–24, 27, 28], time [10–23], the gaseous environment [29] and grain size [2, 10–18, 28]. The conversion of the tetragonal phase into the monoclinic form starts at the surface and proceeds to the interior [2, 10–18, 21–23, 29, 30]. Various additives [10–18, 25, 26, 29, 30], e.g. Al_2O_3 and CeO_2, are shown to prevent or inhibit this phase transformation, presumably due to the presence of second-phase particles at the grain boundaries providing a constraint. Alternately, surface modification methods have also been suggested [31, 32]. The phase composition (m, t, c) in all these studies was established by X-ray diffraction intensities [33, 34]. Since the monoclinic phase has a larger volume than the tetragonal phase, the t → m transformation causes microcracks, [9–18, 21–23, 26, 30] which are detected by scanning electron microscopy [3, 10–18].

Microcracking in ceramics due to phase changes (e.g. ferroelectric $PbTiO_3$ [35], superconducting $YBa_2Cu_3O_{7-x}$ [36]) or anisotropic axial thermal expansion (e.g. $Ca_{1-x}Sr_xP_6O_{24}$ [37], Al_2TiO_5 [38, 39]) can be easily detected by acoustic emission techniques. The t–m phase transformation in pure zirconia was studied by the acoustic emission method as a sintered sample and loose powder were cooled [40]. One of the objectives of the present work is to detect the microcracking accompanying the t → m transition during low-temperature annealing by the acoustic emission method as samples are heated in the 100–450 °C range.

* Permanent address: Tata Research Development and Design Centre, 1 Mangadas Road, Pune 411 050, India.

0022–2461

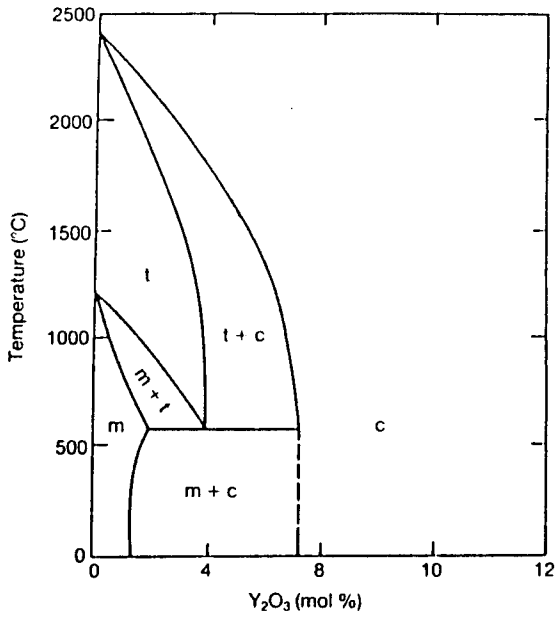

Figure 1 Low-yttria portion of the ZrO_2–Y_2O_3 phase diagram [4, 41, 42].

The phase diagram for the system ZrO_2–Y_2O_3 has been extensively investigated and an exhaustive review is presented by Yoshimura [41]. In the low-Y_2O_3 region, a number of investigations were carried out [42–45] and a generally agreed phase equilibrium diagram, proposed by Srivastava *et al.* [42], is shown in Fig. 1. At room temperature, one has monoclinic solid solution, m_{ss} + c_{ss} and c_{ss} with increasing Y_2O_3 content. The t → m transition of ZrO_2 is lowered from 1170 °C to a eutectoid temperature at about 565 °C at a composition of about 3.5 to 4.0 mol% Y_2O_3. These phase relations are established by conventional methods employing differential thermal analysis, quenching, and X-ray diffraction. The fact that the tetragonal phase can be retained metastably at room temperature under certain circumstances has already been mentioned, but is not shown in Fig. 1. One of the objectives of the present work is to detect the phase transitions in ZrO_2–Y_2O_3 compositions with 1–12 mol% Y_2O_3 during heating (up to 1000 °C) and cooling by acoustic emission methods, and to substantiate the results obtained by dilatometry, X-ray diffraction and scanning electron microscopy.

Thus, acoustic emission methods are employed in the present work to detect (i) microcracking during low-temperature ageing due to the t–m transition in ZrO_2 alloys with 3–4 mol% Y_2O_3 and (ii) phase transitions during heating and cooling of 1–12 mol% Y_2O_3 compositions.

2. Experimental procedure

Zirconia and yttria with the characteristics given in Table I were mixed in appropriate amounts to make 1, 2, 3, 4, 6, 9 and 12 mol% Y_2O_3 compositions in a ball mill in polyethylene containers using ethyl alcohol as wetting agent and 1/2 in. (13 mm) diameter zirconia balls as grinding medium. The slurry was dried in an air oven at 80 °C for 24 h. The dried powders were calcined at 1500 °C. Later the calcined powder was pressed into pellets and pellets were sintered at 1700 °C for 4 h. The heating and cooling rates were 10 °C min^{-1}. X-ray diffraction study was carried out on powders using CuK_α radiation at 2° min^{-1} scanning speed. The phase identification was based primarily on the $(\bar{1}\,1\,1)$ and (1 1 1) reflections at $d = 0.318$ and 0.286 nm for the monoclinic, (1 1 1) at $d = 0.296$ nm for the tetragonal and (1 1 1) at $d = 0.295$ nm for the cubic phase.

TABLE I Characteristics of zirconia and yttria powders used

Zirconium oxide[a]	
L.O.I at 650 °C	0.48%
$ZrO_2 + HfO_2$[b]	99.7%
SiO_2	0.03%
Fe_2O_3	< 0.015%
Na_2O	< 0.02%
CaO	< 0.02%
Cl	0.02%
SO_4	0.06%
Surface area (BET Method)	19 $m^2 g^{-1}$
Particle size (Sedigraph)	50% > 0.5 μm
Yttrium oxide	
Lu	< 50 p.p.m.
Gd	< 50 p.p.m.
Tm	< 50 p.p.m.
Yb	< 50 p.p.m.
Er	< 50 p.p.m.
Tb	< 50 p.p.m.
Dy	< 50 p.p.m.
Sm	< 50 p.p.m.
Ho	< 50 p.p.m.
Nd	< 100 p.p.m.
Si	< 100 p.p.m.
Fe	< 100 p.p.m.
Mg	< 100 p.p.m.
Ca	< 100 p.p.m.
Al	< 100 p.p.m.
Particle size	2–3 μm

[a] Typical average values from chemical analysis.
[b] ~ 2–3% HfO_2

For dilatometric measurements sintered pellets were cut into 25 mm × 5 mm × 5 mm. The samples and the two opposite faces of the specimen were polished flat and parallel. The heating rate was 10 °C min^{-1} and the cooling rate 2 °C min^{-1} in dilatometric runs (Harrop Industries model TD-716). Most of the measurements involved heating to 1000 °C and cooling to near room temperature. Some samples were cycled between room temperature and 1000 °C and room temperature and 450 °C to observe the transformation behaviour in detail.

For the acoustic emission study a sintered sample about 3 mm × 5 mm × 20 mm was attached with a high-temperature cement to a 30 cm long alumina rod which served as a waveguide. The other end of the alumina rod was joined to a transducer using a water-soluble ultrasonic couplant. The sample was placed inside a tube furnace and a Chromel–Alumel thermocouple positioned near the sample monitored the temperature. The furnace temperature was increased at 10 °C min^{-1} up to a temperature ranging from 450

to 900 °C. The maximum temperature was maintained for 10 min, followed by cooling at 10 °C min^{-1} to 500 °C and at 2 °C min^{-1} to 100 °C. The transducer employed had a centre frequency of 500 kHz (in a range of 300 to 700 kHz). The electrical signal output from the transducer was amplified, filtered and processed through a train of instrumentation consisting of an amplifier, discriminator, totalizer and rate-meter modules to obtain data for total AE counts and the count rate (counts per 5 °C). The discriminator triggered a pulse whenever the amplifier output exceeded a certain adjustable threshold. The details of the system used here are described elsewhere [36, 37].

The fractured surfaces of as-sintered samples and after the dilatometric runs were observed on an ISI 60 scanning electron microscope.

3. Results and discussion

Two main aspects are presented here: (i) the metastable t → m phase transition at about 250 °C and (ii) phase relations in the ZrO_2–Y_2O_3 system from 1 to 12 mol% Y_2O_3. In both cases the discussion is based on data from X-ray diffraction, dilatometry and acoustic emission, supplemented in some cases by scanning electron micrographs. Of these, acoustic emission is a novel technique to be employed for the study of phase relations in the ZrO_2–Y_2O_3 system.

3.1. Metastable tetragonal → monoclinic phase transition

The X-ray diffraction patterns of sintered samples with 3, 4 and 6 mol% Y_2O_3 are shown in Fig. 2. The monoclinic phase decreases as the cubic phase content increases with increasing Y_2O_3 content. The relative amount of the metastable tetragonal phase is large in 3 and 4 mol% Y_2O_3 compositions and is essentially absent in the 6 mol% Y_2O_3 composition, in agreement with earlier reports. The thermal expansion behaviour of 3 and 4 mol% Y_2O_3 samples was determined by dilatometry up to 1000 °C in repeated cycles of heating and cooling. The data for ZrO_2–3 mol% Y_2O_3 are shown in Fig. 3 for two cycles of heating up to 1000 °C. During the first heating, there is an abrupt large expansion at about 250 °C, followed by very little expansion between 300 and 500 °C, beyond which there is a large contraction at about 550 °C and finally normal expansion beyond 600 °C. During cooling of this sample, the usual contraction down to about 400 °C is followed by a sudden large expansion, finally displaying a small contraction at temperatures below 200 °C. During the second cycle of heating there is a small expansion up to about 500 °C, then a sudden contraction, followed by the usual gradual expansion. Thus, during the second heating, the behaviour is similar to that in the first heating except for the absence of the sudden expansion at about 250 °C. The behaviour during cooling is nearly identical in the two cycles.

Similar data for a ZrO_2–4 mol% Y_2O_3 sample for three cycles of heating to 1000 °C and cooling are shown in Fig. 4. The behaviour of this sample is essentially the same as that of the 3 mol% Y_2O_3 sample and the data for the second and third cycles of heating and cooling reproduce well. These results are interpreted in terms of the presence of some amount of metastable tetragonal phase in these samples, which transforms to the (stable) monoclinic phase at about 250 °C accompanied by a large expansion. The contraction at about 550 °C on heating and expansion at about 400 °C on cooling represent the m → t → m transformations.

In order to gain further insight into this metastable t → m transformation at about 250 °C, the 4 mol% Y_2O_3 sample was studied up to 450 °C (with no

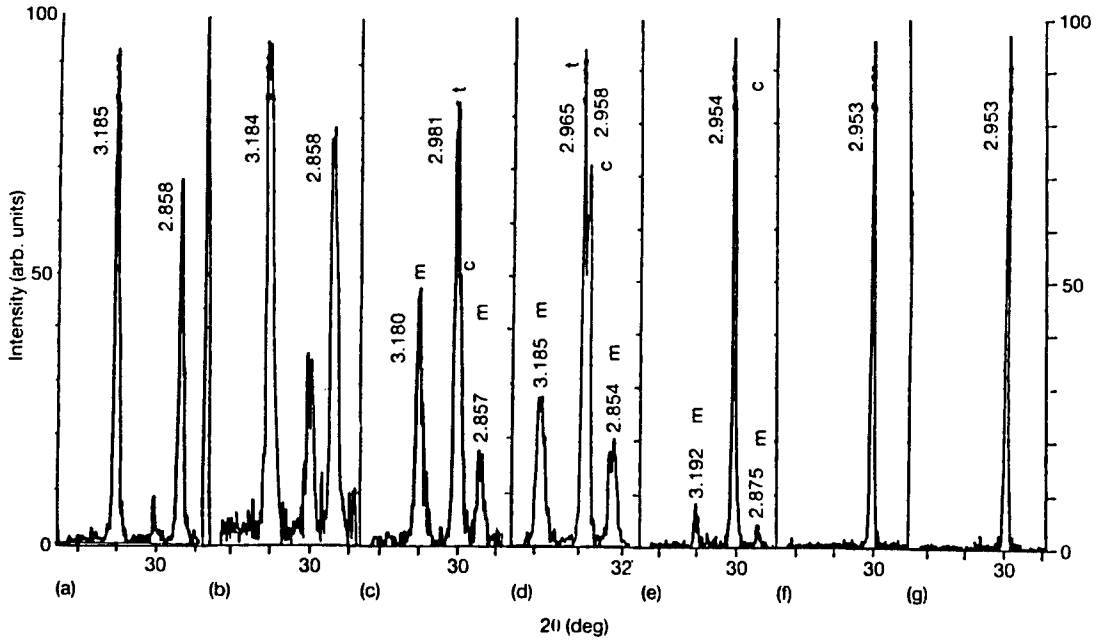

Figure 2 Portion of the X-ray diffraction patterns of (a) 1, (b) 2, (c) 3, (d) 4, (e) 6, (f) 9 and (g) 12 mol% Y_2O_3–ZrO_2 sintered compositions.

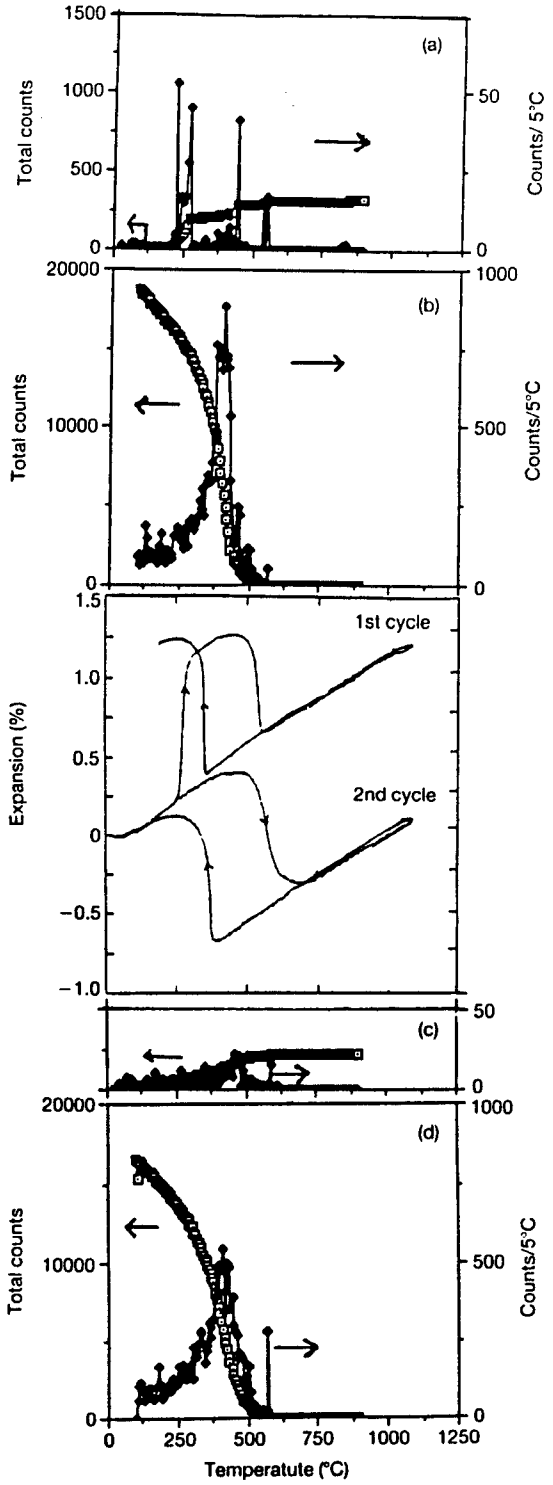

Figure 3 Thermal expansion behaviour of ZrO_2-3 mol% Y_2O_3 sample during two cycles of heating to 1000 °C and cooling (centre). The corresponding acoustic emission data (total counts and counts per 5 °C) in the first ((a) heating, (b) cooling) and second ((c) heating), (d) cooling) cycles are also shown: (⊡) total counts, (◆) counts per 5 °C.

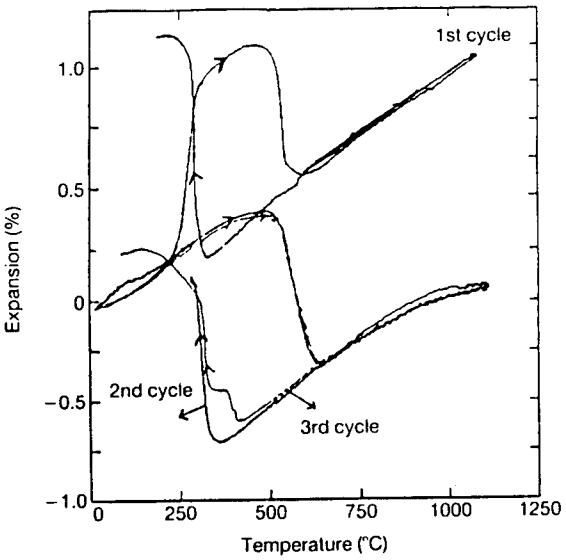

Figure 4 Thermal expansion behaviour of ZrO_2 4 mol% Y_2O_3 sample during three cycles of heating to 1000 °C, followed by cooling.

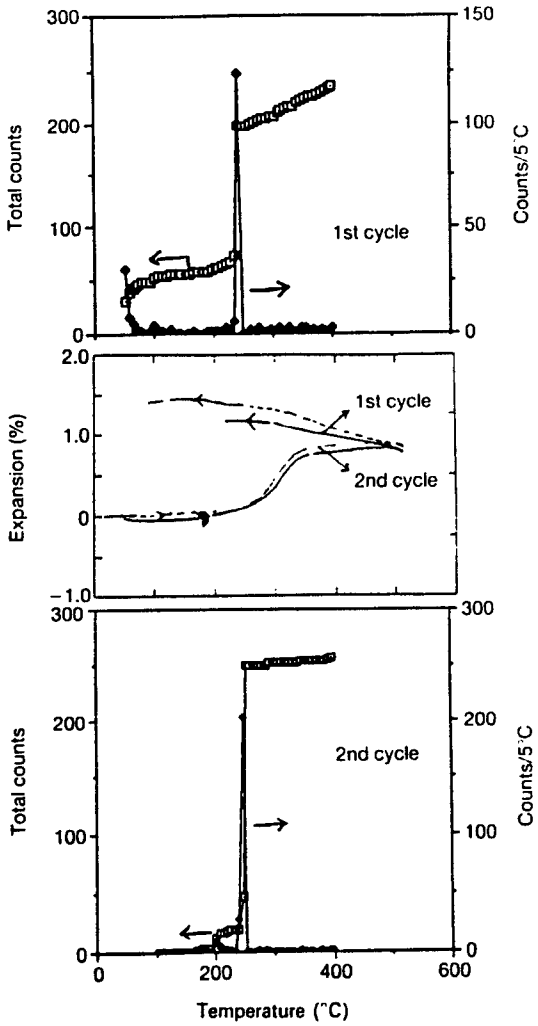

Figure 5 Thermal expansion behaviour of ZrO_2-4 mol% Y_2O_3 sample during two cycles of heating to 450 °C, followed by cooling. The corresponding acoustic emission data during heating in the two cycles are also shown: (⊡) total counts, (◆) counts per 5 °C.

holding time at the peak temperature) in two consecutive heating and cooling cycles (Fig. 5). The sample expands in the temperature range 250–350 °C, as noted before. On cooling from 450 °C, no dimensional anomalies are observed. Apparently, the

metastable tetragonal phase converts only partially into the monoclinic phase during the first heating up to 450 °C at the fast heating rate (10 °C min^{-1}) employed with no holding time at peak temperature. As a result, further transformation into the monoclinic phase takes place during the second heating cycle. It has been reported that annealing for about 20 h at 200 °C is necessary to obtain maximum conversion to the monoclinic phase in the 3 and 4 mol% Y_2O_3 samples. [10–18]. The present results are substantiated by the decrease of the X-ray diffraction intensity of the tetragonal reflection at 0.2965 nm of this sample after the first dilatometric experiment up to 450 °C, and its disappearance after the dilatometric experiment up to 1000 °C (Fig. 6), compared to that in the as-sintered condition. The X-ray diffraction intensity of the monoclinic phase increases relative to the tetragonal phase in the order: as-sintered, heated to 450 °C, and heated to 1000 °C. This clearly indicates that the monoclinic phase arises from conversion of the tetragonal phase and not from the cubic phase, in agreement with the results of Sato and Shimada [10].

These results are fully consistent with earlier reports [9–26] on the ageing or degradation of ZrO_2 samples with 3–4 mol% Y_2O_3 in the 200–400 °C temperature range due to conversion of the metastable tetragonal phase into the monoclinic form. The accompanying dimensional change is reported to cause microcracking [9–18, 21–23, 26, 30], which in turn results in a strength decrease. The presence of microcracks is plausible but is not easy to detect by microscopic techniques, though some indication of microcracks has been reported [3, 10–18]. In the present work, the acoustic emission method was employed for the detection of microcracks as these two samples were heated and cooled. The data (total counts and counts for 5 °C intervals) for the 3 mol% Y_2O_3 sample heated to and cooled from 1000 °C for two cycles are included in Fig. 3. The prominent acoustic emission activity in the 200–350 °C region detected during the first heating (Fig. 3a) is absent during the second heating (Fig. 3c), confirming that when the metastable $t \rightarrow m$ transformation is present extensive microcracking takes place due to the associated sudden dimensional change. The absence of similar activity in this temperature range during cooling (Fig. 3b and d) is consistent with this explanation.

Further confirmation of microcracking due to volume change associated with the metastable $t \rightarrow m$ phase change is obtained from acoustic emission data on heating the 3 mol% Y_2O_3 sample to 400 °C in two consecutive heating–cooling cycles (Fig. 7). Clearly there is a sudden, intense microcracking taking place around 250 °C during heating (Fig. 7a and c) which is absent during cooling (Fig. 7b and d). Further, the acoustic emission activity is less intense during the second heating to 400 °C (Fig. 7c) compared to that in the first cycle of heating (Fig. 7a), suggesting that much more of the metastable tetragonal phase present transforms to the monoclinic phase during the first

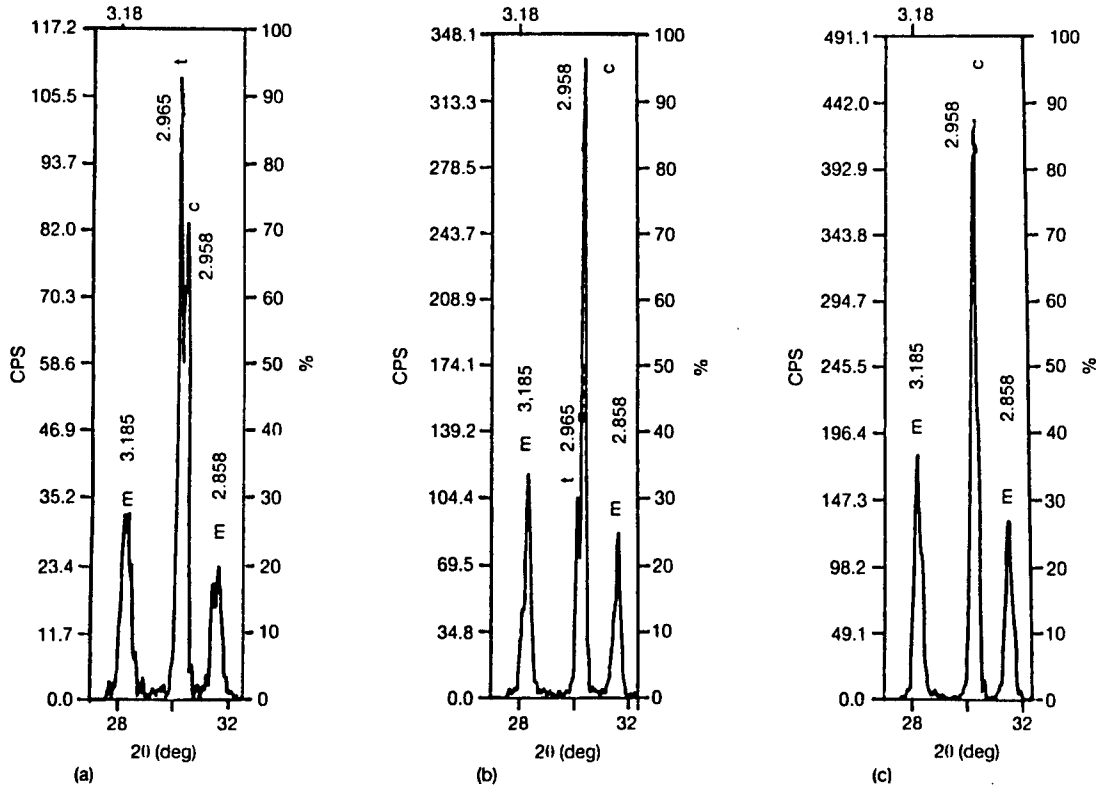

Figure 6 Portion of the X-ray diffraction patterns of ZrO_2–4 mol% Y_2O_3 sample (a) as sintered and after dilatometric runs up to (b) 450 °C and (c) 1000 °C.

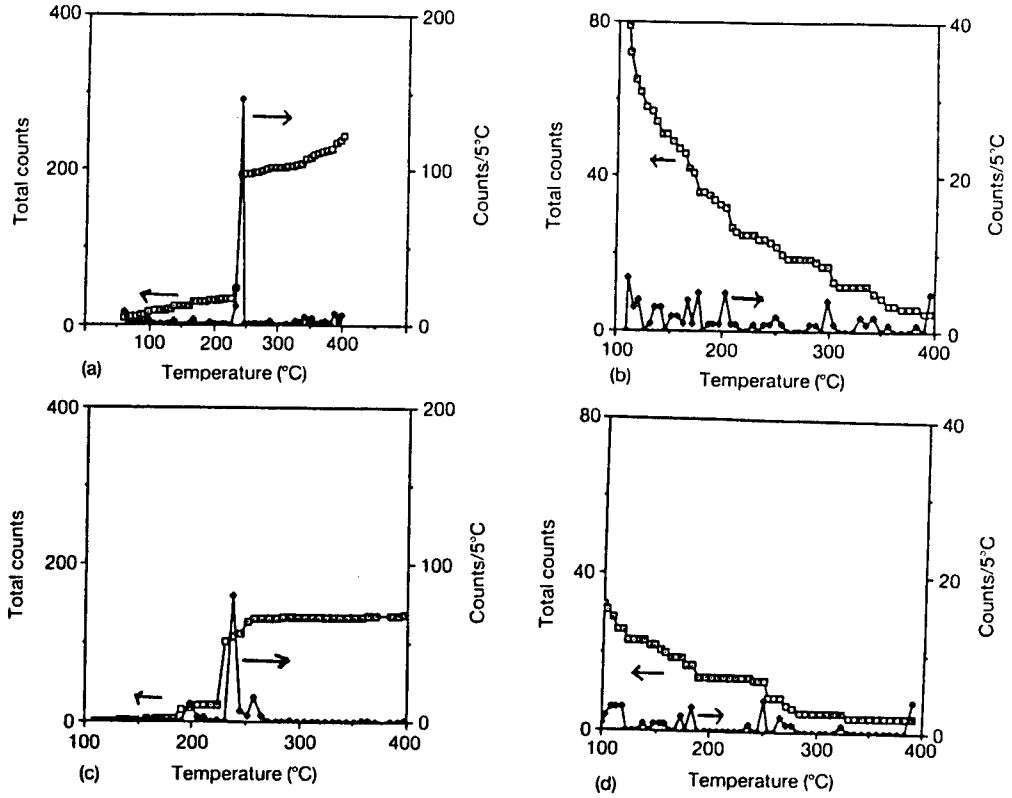

Figure 7 Acoustic emission data of ZrO_2–3 mol% Y_2O_3 sample (a, c) during heating to 400 °C and (b, d) cooling in two consecutive heating and cooling cycles: (⊡) total counts, (◆) counts per 5 °C.

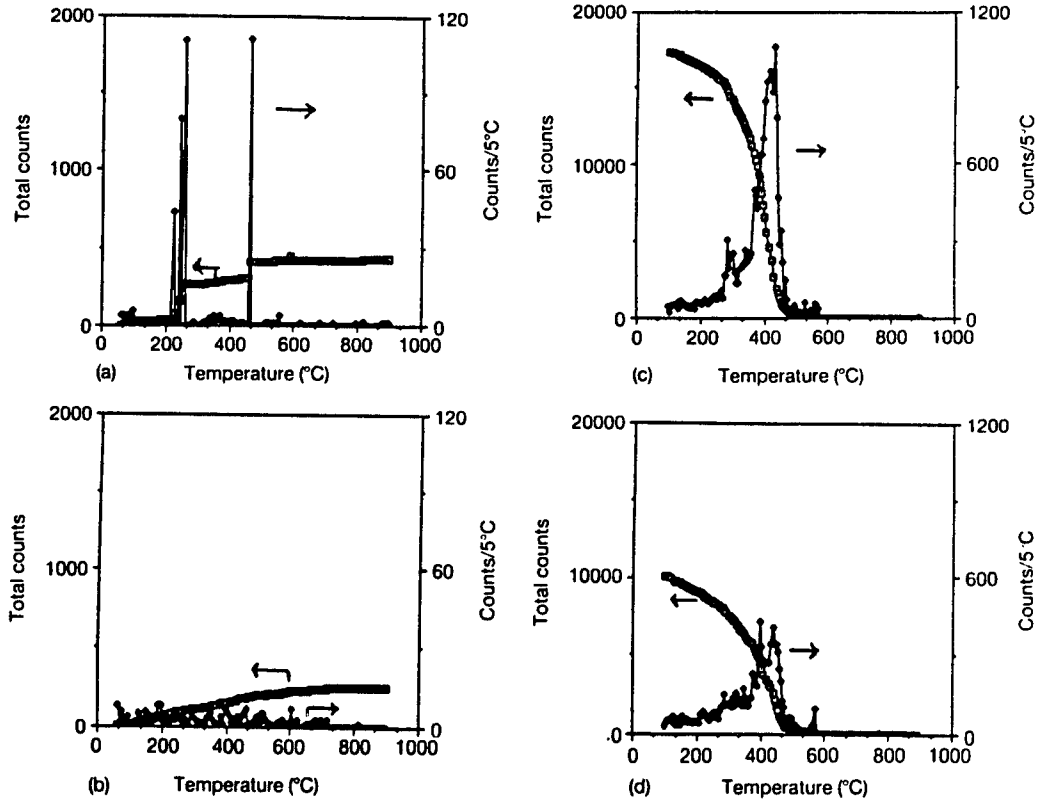

Figure 8 Acoustic emission data of ZrO_2–4 mol% Y_2O_3 sample (a, b) during heating to 900 °C and (c, d) cooling in two consecutive heating and cooling cycles: (⊡) total counts, (◆) counts per 5 °C. Refer to Fig. 4 for corresponding thermal expansion data.

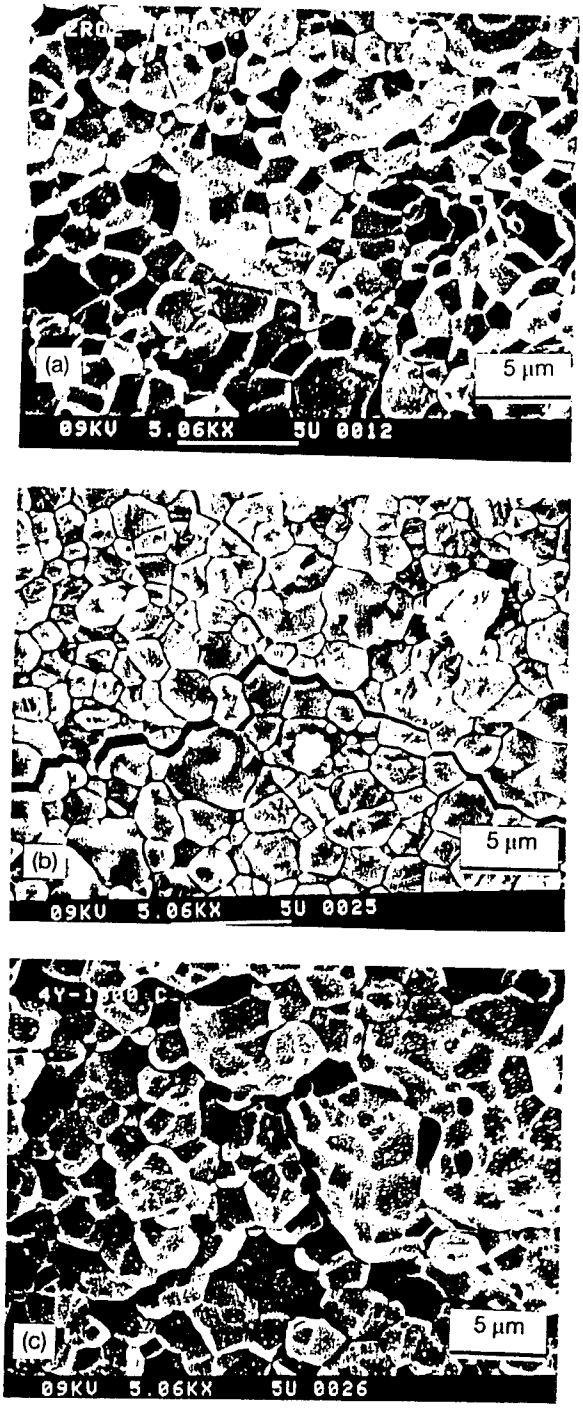

Figure 9 Scanning electron micrographs of ZrO_2–4 mol% Y_2O_3 sample (a) as sintered and after dilatometric runs up to (b) 450 °C and (c) 1000 °C.

cycle compared to the transformation of the smaller amount of the remaining metastable tetragonal phase during the second cycle of heating.

Similar data on two cycles of heating the 4 mol% Y_2O_3 sample to 400 °C are shown in Fig. 5a and c together with the corresponding dilatometric data (Fig. 5b), which indicate that the temperature of maximum acoustic emission activity coincides with the temperature of the start of the sudden dimensional expansion. As in the case of the 3 mol% Y_2O_3 sample, there was also no significant acoustic emission activity during cooling of the 4 mol% Y_2O_3 sample (not shown). The acoustic emission results on heating a 4 mol% Y_2O_3 sample to 1000 °C for the first time show intense acoustic emission activity at about 250 °C (Fig. 8a) and no significant acoustic emission counts at 250 °C during the second heating (Fig. 8b) as well as during the cooling cycles (Fig. 8c and d). Thus the acoustic emission data from several experiments on 3 and 4 mol% Y_2O_3 samples are similar.

Scanning electron micrographs of the ZrO_2–4 mol% Y_2O_3 sample after dilatometric measurement up to 450 °C show extensive intergranular microcracking (Fig. 9b) which is absent in the same sample in the as-sintered condition (Fig. 9a). The sample after a dilatometric experiment up to 1000 °C shows much less microcracking (Fig. 9c) than after cooling from 450 °C, suggesting that considerable healing of the microcracks generated on heating to low temperatures ($\leqslant$ 450 °C) has taken place by heating to and cooling from 1000 °C. The volume expansion accompanying the t → m phase change during cooling possibly contributes to the crack healing process.

3.2. Phase relations in the low-Y_2O_3 portion of the ZrO_2–Y_2O_3 system

The phase diagram of the low-Y_2O_3 portion of the ZrO_2–Y_2O_3 system, due to Srivastava *et al.* [42], is shown in Fig. 1, which is in agreement with other published phase diagrams [41, 43–45] except for the fact that the metastable tetragonal phase observed in a limited range of compositions is not shown here. In the present study, ZrO_2 compositions with 1–12 mol% Y_2O_3 were studied via X-ray diffraction, dilatometry and acoustic emission on heating and cooling. The X-ray diffraction data, shown in Fig. 2, were used to estimate the relative amounts of the monoclinic, (metastable) tetragonal and cubic phases (Table II). The sample with 1 mol% Y_2O_3 shows essentially monoclinic ZrO_2 solid solution. The amount of the monoclinic phase decreases gradually with increasing Y_2O_3 content till only a small amount of it is present in the 6 mol% Y_2O_3, and it is completely absent in the 9 and 12 mol% Y_2O_3 samples. The cubic phase increases with Y_2O_3 content such that 9 and 12 mol% Y_2O_3 compositions show pure cubic phase. As discussed earlier, 2, 3 and 4 mol% Y_2O_3 samples show some amount of metastable tetragonal phase in the as-sintered condition. The average grain size (1.5–2.0 μm) of these samples is above the reported critical grain size for the tetragonal phase [4] and therefore partial conversion to monoclinic phase has taken place, resulting in a mixture of m, t and c phases (Table II).

The thermal expansion behaviour of 1 and 2 mol% Y_2O_3 samples is depicted in Fig. 10 and of 6, 9 and 12 mol% Y_2O_3 samples in Fig. 11. Similar data for 3 and 4 mol% Y_2O_3 are already given in Figs 3 and 4.

The sintered samples of all these compositions were examined by acoustic emission during heating and

TABLE II Properties of sintered ZrO_2–Y_2O_3 compositions

Y_2O_3 (mol %)	α of cubic phase (10^{-6} C^{-1})	Density (g cm^{-3})	Grain size (μm)	Phase composition (%)			AE data (°C)	
				m	t	c	m → t	t → m
1		5.213	2.1	95	5	–	846	710
2		5.198	1.98	70	15	15	600	565
3	12.5	5.192	1.875	33	42	25	565	565
4	10.7	5.094	1.51	24	43	33	565	565
6	11.68	5.112		13	–	87	565	565
9	12.1	5.189		–	–	100		
12	11.98	5.012		–	–	100		

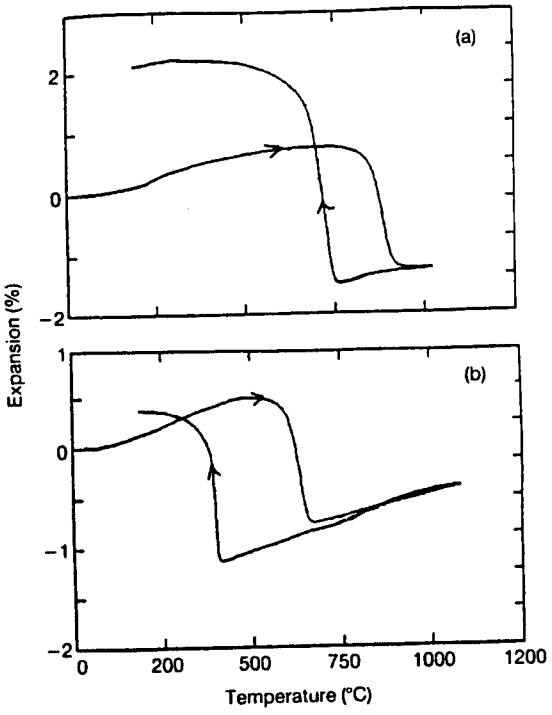

Figure 10 Thermal expansion behaviour of (a) 1 and (b) 2 mol% Y_2O_3 compositions.

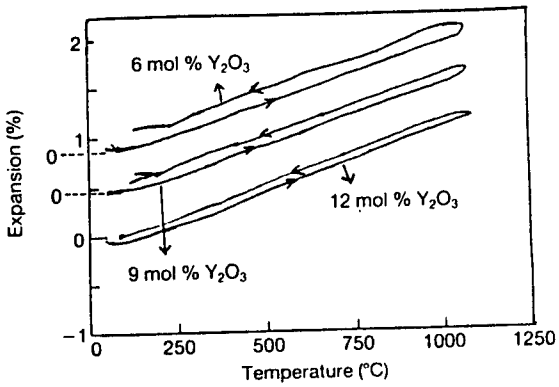

Figure 11 Thermal expansion behaviour of 6, 9, and 12 mol% Y_2O_3 compositions. The zero point of the expansion plot has been offset for the three samples.

cooling. The temperatures corresponding to the m → t and t → m phase transitions from the acoustic emission data for the compositions with 1–6 mol% Y_2O_3 are summarized in Table II. These transition temperatures are in reasonable agreement with Fig. 1. The acoustic emission data for 1 mol% Y_2O_3 shows intense acoustic emission activity at 835–840 °C on heating (Fig. 12a) and occurs at 708 °C and below on

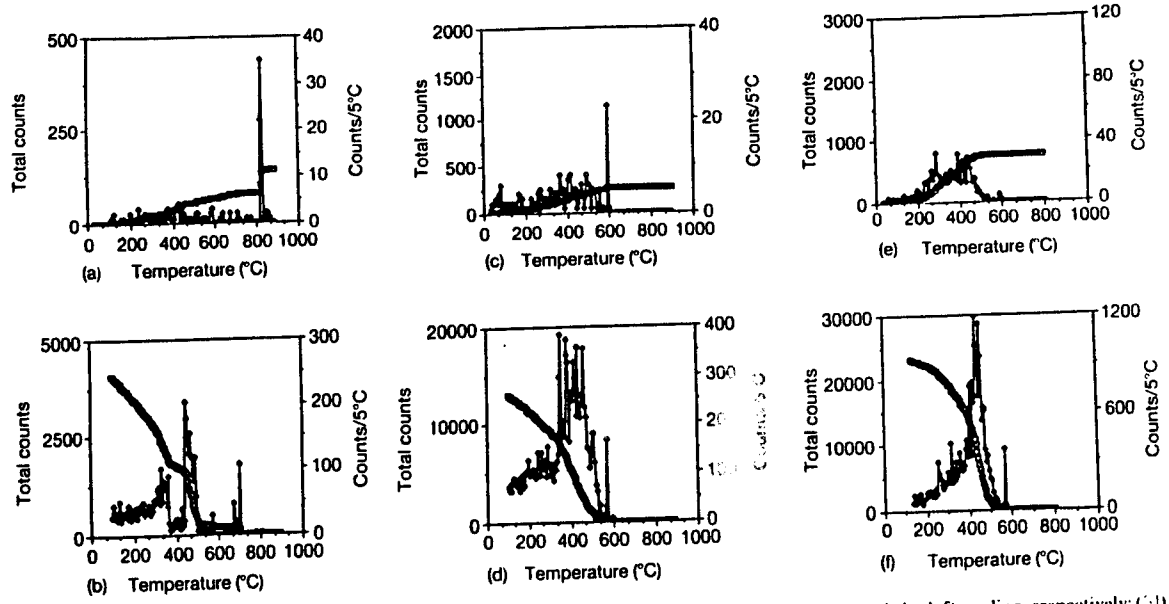

Figure 12 Acoustic emission data of 1, 2 and 6 mol% Y_2O_3 samples (a, c, e) during heating to 900 °C and (b, d, f) cooling, respectively: (◇) total counts, (◆) counts per 5 °C.

cooling (Fig. 12b), which appears to correspond to m → t and t → m transitions, respectively (Table II). In the case of 2 (Fig. 12c and d), 3, 4 (Figs 3 and 7) and 6 mol% Y_2O_3 (Fig. 12e and f), intense acoustic emission activity starts at 570 ± 5 °C on heating and cooling (Table II). Interestingly, this temperature coincides with the eutectoid temperature reported by Srivastava *et al.* [42]. No significant acoustic emission activity was observed on heating and cooling of samples with 9 and 12 mol% Y_2O_3, and this is consistent with the fact that they are purely cubic phases undergoing no phase changes.

The acoustic emission data thus are in agreement with the phase relationships in this system established by quenching, X-ray diffraction and other conventional methods.

4. Conclusions

The acoustic emission technique is shown to be a sensitive tool to determine phase transitions and microcracking in ZrO_2–Y_2O_3 ceramics. Using this method, the microcracking resulting from the volume change at the metastable tetragonal transition at about 250 °C in ZrO_2 alloys with 3 and 4 mol% Y_2O_3 has been clearly established. The onset of acoustic emission activity at the m → t and t → m transitions and at the eutectoid transformation at about 565 °C confirms the established phase relations in the low-Y_2O_3 portion of the ZrO_2–Y_2O_3 system. The acoustic emission results are corroborated by dilatometry, X-ray diffraction and scanning electron microscopy.

Acknowledgement

The authors are grateful to the Ben Franklin Technology Center of Central and Northern Pennsylvania for financial support under Project No. 90C. 1016R-1.

References

1. R. C. GARVIE, R. H. J. HANNINK and R. T. PASCOE, *Nature* **258** (1975) 703.
2. T. K. GUPTA, J. H. BECHTOLD, R. C. KUZNICKI, L. H. CADOFF and B. R. ROSSING, *J. Mater. Sci.* **12** (1977) 2421.
3. T. K. GUPTA, F. F. LANGE and J. H. BECHTOLD, *ibid.* **13** (1978) 1464.
4. F. F. LANGE, *ibid.* **17** (1982) 240.
5. *Idem, ibid.* **17** (1982) 225.
6. D. C. PORTER and A. H. HEUER, *J. Amer. Ceram. Soc.* **62** (1979) 298.
7. R. H. J. HANNING, K. A. JOHNSON, R. T. PASCOE and R. C. GARVIE, *Adv. Ceram.* **3** (1981) 116.
8. R. H. J. HANNING, *J. Mater. Sci.* **18** (1983) 457.
9. K. KOBAYASHI, H. KUWAJIMA and T. MASAKI, *Solid State Ionics* **3/4** (1981) 489.
10. T. SATO and M. SHIMADA, *J. Amer. Ceram. Soc.* **67** (1984) C212.
11. M. MATSUI, T. SOMA and I. ODA, *Adv. Ceram.* **12** (1984) 371.
12. K. TSUKUMA, Y. KUBOTA and T. TSUKIDATE, *ibid.* **12** (1984) 382.
13. M. WATANABE, S. IIO and I. FUKUURA, *ibid.* **12** (1984) 391.
14. K. NAKAJIMA, K. KOBAYASHI and Y. MURATA, *ibid.* **12** (1984) 399.
15. H. S. LU and S. Y. CHEN, *J. Amer. Ceram. Soc.* **70** (1987) 537.
16. R. E. LEE and A. H. HEUER, *ibid.* **71** (1988) 694.
17. M. RUHLE and A. H. HEUER, *Adv. Ceram.* **12** (1984) 14.
18. M. L. McCARTNEY and M. RUHLE, *Acta Metall.* **37** (1989) 1859.
19. T. SATO, S. OHTAKI, T. ENDO and M. SHIMADA, *J. Amer. Ceram. Soc.* **68** (1985) C320.
20. T. SATO, S. OHTAKI and M. SHIMADA, *J. Mater. Sci.* **20** (1985) 1466.
21. T. SATO and M. SHIMADA, *J. Amer. Ceram. Soc.* **68** (1985) 356.
22. *Idem, J. Mater. Sci.* **20** (1985) 3988.
23. M. YOSHIMURA, T. NOMA, K. KAWABATA and S. SOMIYA, *J. Mater. Sci. Lett.* **6** (1987) 465.
24. F. F. LANGE, G. L. DUNLOP and B. I. DAVIS, *J. Amer. Ceram. Soc.* **69** (1986) 237.
25. H. TUSUBAKINO, R. NOZATO and M. HAMAMOTO, *ibid.* **74** (1991) 440.
26. M. T. HERNANDEZ, J. R. JURADO, P. DURAN and J. L. G. FIERRO, *ibid.* **74** (1991) 1254.
27. Y. MURASE and E. KATO, *ibid.* **66** (1983) 196.
28. A. J. A. WINNUBST and A. J. BURGGRAAF, *Adv. Ceram.* **24** (1988) 39.
29. S. ITO, M. WATANABE, K. KURODA, H. SAKA and T. IMURA, *ibid.* **24** (1988) 49.
30. T. SATO, S. OHTAKI, T. ENDO and M. SHIMADA, *ibid.* **24** (1988) 29.
31. H. SCHUBERT, N. CLAUSSEN and M. RUHLE, *Proc. Br. Ceram. Soc.* **34** (1984) 157.
32. P. J. WHALEN, F. REIDINGER and R. E. ANTRIM, *J. Amer. Ceram. Soc.* **72** (1989) 319.
33. T. TORAYA, M. YOSHIMURA and S. SOMIYA, *ibid.* **67** (1984) C119.
34. R. C. GARVIE and P. S. NICHOLSON, *ibid.* **55** (1972) 303.
35. V. SRIKANTH and E. C. SUBBARAO, *Acta Metal.* **40** (1992) 109.
36. E. C. SUBBARAO and V. SRIKANTH, *Physica C* **171** (1990) 449.
37. V. SRIKANTH, E. C. SUBBARAO, D. K. AGRAWAL, C-Y HUANG, R. ROY and G. V. RAO, *J. Amer. Ceram. Soc.* **74** (1991) 365.
38. R. E. WRIGHT, *ibid.* **55** (1972) 54.
39. Y. OHYA, Z. NAKAGAWA and K. HAMANO, *ibid.* **70** (1987) C184.
40. D. R. CLARKE and A. ARORA, *Adv. Ceram.* **12** (1984) 54.
41. M. YOSHIMURA, *Ceram. Bull.* **67** (1988) 1950.
42. K. K. SRIVASTAVA, R. N. PATIL, C. B. CHOUDHARY, K. V. G. K. GOKHALE and E. C. SUBBARAO, *Trans. J. Bri. Ceram. Soc.* **73** (1974) 85.
43. H. G. SCOTT, *J. Mater. Sci.* **10** (1975) 152.
44. C. PASCUAL and P. DURAN, *J. Amer. Ceram. Soc.* **66** (1983) 23.
45. R. RUH, K. S. MAZDIYASNI, P. G. VALENTINE and H. O. RIELSTEIN, *ibid.* **67** (1984) C190.

Received 28 October 1991
and accepted 24 March 1992

APPENDIX 46

Advanced Performance Materials, 1, 129–143 (1994)

Impurity Doping Effect on Photostriction in PLZT Ceramics

SHENG-YUAN CHU, ZHOU YE AND KENJI UCHINO
International Center for Actuators and Transducers, Materials Research Laboratory, The Pennsylvania State University, University Park, PA 16802

Abstract. Photostriction is the superposition of a photovoltaic and piezoelectric effects. In this study, photostrictive effects in the perovskite (Pb, La) (Zr, Ti)O_3 were investigated as a function of B-site impurity doping. Donor doping was found to reduce both the grain size and room-temperature dielectric constant, influencing photovoltaic response. WO_3 and Ta_2O_5 doping increase the photovoltaic response, but do not significantly affect the piezoelectric effect in this material. Maximum photostriction is obtained for samples with 0.4 at% WO_3 doped or 1 at% Ta_2O_5 doped PLZT

Keywords: doping effect, photostriction effect, photovoltaic effect, PLZT

Introduction

The photovoltaic effect is observed in certain ferroelectrics, wherein a constant electromotive force is induced with application of near-ultraviolet radiation [1]–[3]. This effect was explained by Fridkin et al. in 1974 [4], by Glass et al. [2] and by Brody et al. [5], and probably originated from an excitation of electrons from asymmetric impurity potentials. The main features of the bulk photovoltaic effect are summarized as follows:

1) This effect appears in poled uniform single crystals or ceramics with noncentrosymmetry and is entirely different in nature from the P-N junction effect observed in semiconductors.
2) Constant photo-current and -voltage are generated in the spontaneous polarization direction under uniform illumination in the ferroelectric phase and disappears in the paraelectric phase.
3) The magnitude of the induced voltage is proportional to crystal length in the polarization direction and is much greater than the band gap energy of the crystal.

The expected photostriction effects as a superimposed phenomenon of photovoltaic and piezoelectric effects have been reported in our previous papers [6, 7], and potential applications in photo-driven remote control devices have been proposed [8, 9]. For practical applications, larger strain and quicker response are desired, and materials development and device design are focused on these objectives. One of the authors has firstly pointed out that the PLZT exhibits superior photostrictive effect, and effects of impurity doping in PLZT has also been investigated preliminarily [7].

In this paper, the photostriction effect in PLZT (3/52/48) ceramics is investigated in detail as a function of impurity doping. The effect of doping on grain size and room-temperature dielectric constant are also examined, because the grain size affects the photovoltaic effect [6], and the photovoltage may change with the dielectric constant for the constant photo-induced charge.

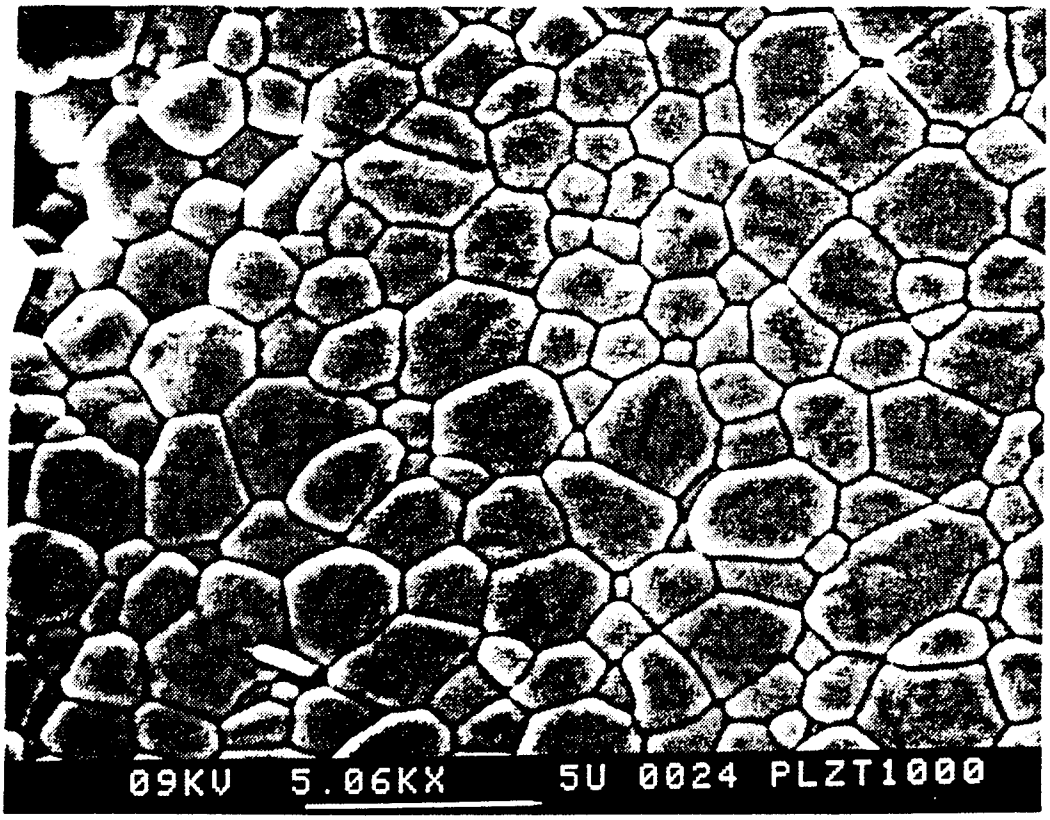

(a)

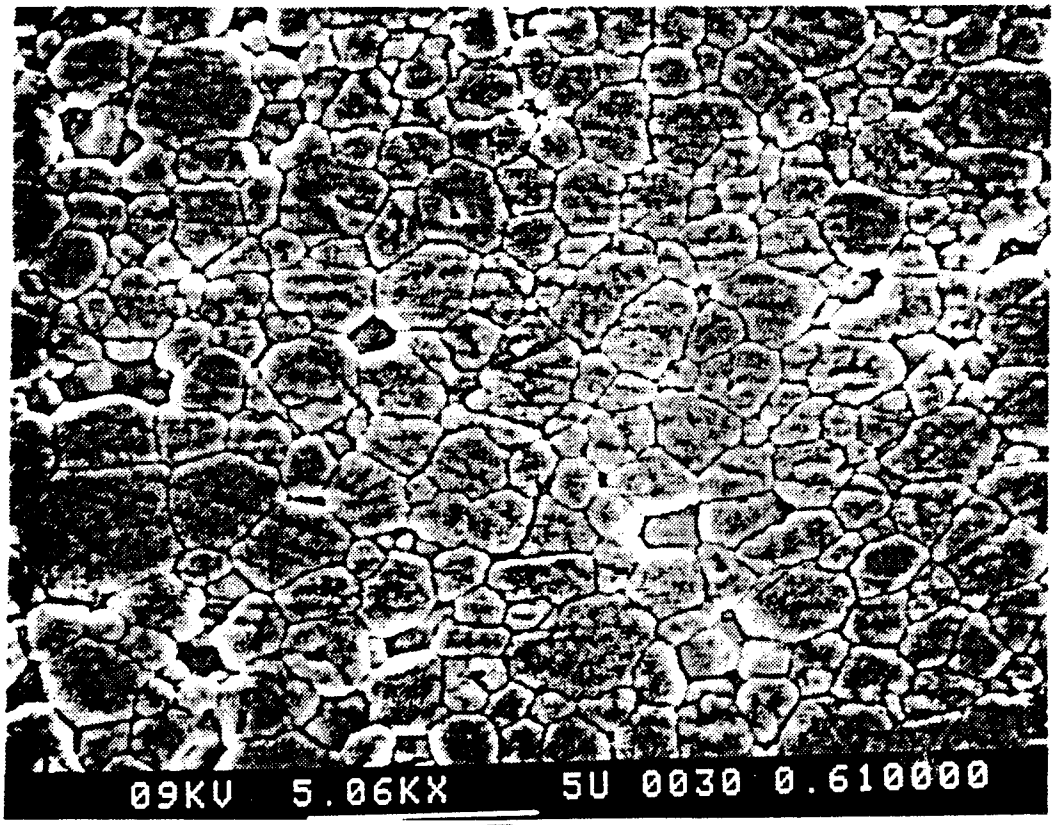

(b)

Figure 1. SEM photomicrographs of thermally-etched samples of (a) PLZT, (b) PLZT-WO_3 and (c) PLZT-Ta_2O_5.

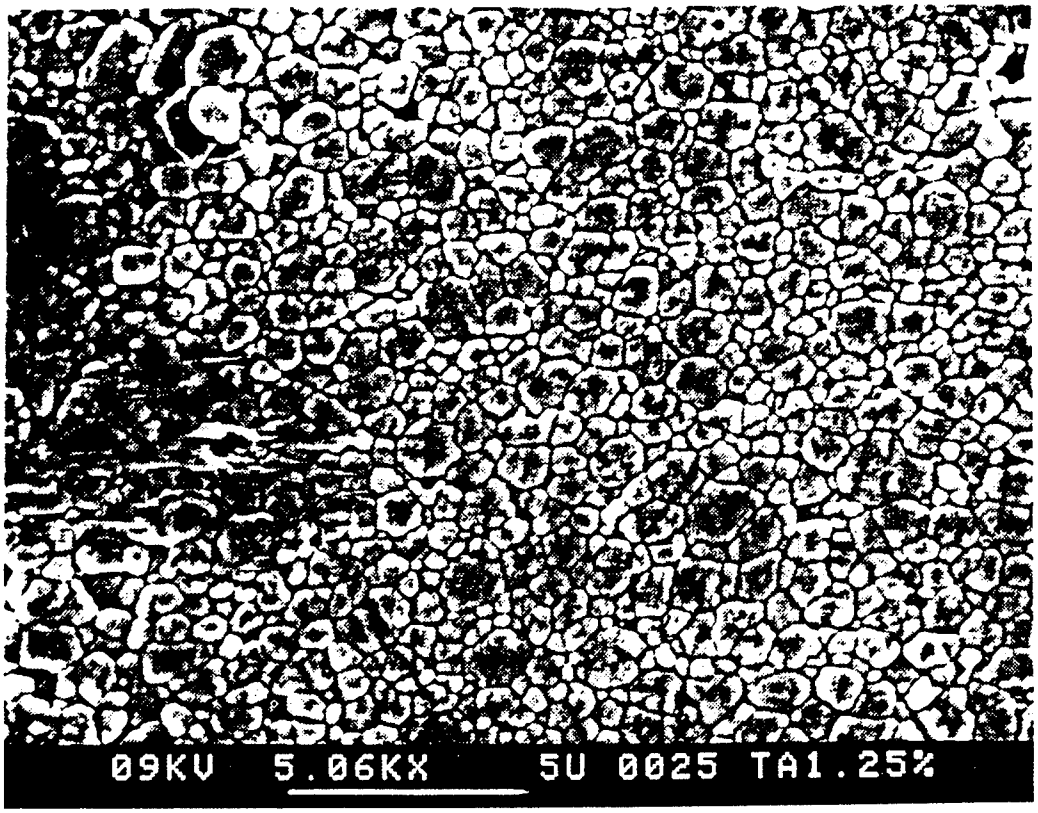

(c)

Sample preparation

PLZT $(x/y/z)$ samples were prepared in accordance with the following composition formula:

$$Pb_{1-y}La_y(Zr_{1-x}Ti_x)_{1-\frac{y}{4}}O_3.$$

PLZT (3/52/48) was selected due to its optimum photostriction ($x_{ph} = d_{33}E_{ph}$) within the PLZT system [6].

The ceramic powder was prepared by a conventional mixed oxide technique. $PbCO_3$, La_2O_3, ZrO_2, TiO_2 and dopant were weighed in the appropriate proportions and mixed in a ball mill for 2 days using ethanol and zirconia grinding media. 0.5 wt% excess $PbCO_3$ was added to compensate for weight loss during calcination and sintering. The slurry was dried, then calcined in a closed crucible at 950°C for 10 hrs. The calcined powder was ball-milled again for 48 hrs. The samples were sintered in sealed alumina crucibles at 1270°C/ 2 hrs. A PbO rich atmosphere was maintained with lead zirconate powder to minimize lead loss during sintering. An x-ray diffractometer did not monitor any secondary phases other than the perovskite structure. Sintered samples were electroded with silver paste. Finally, each sample was cut and poled in silicone oil at 120°C under a 15 kV/cm electric field.

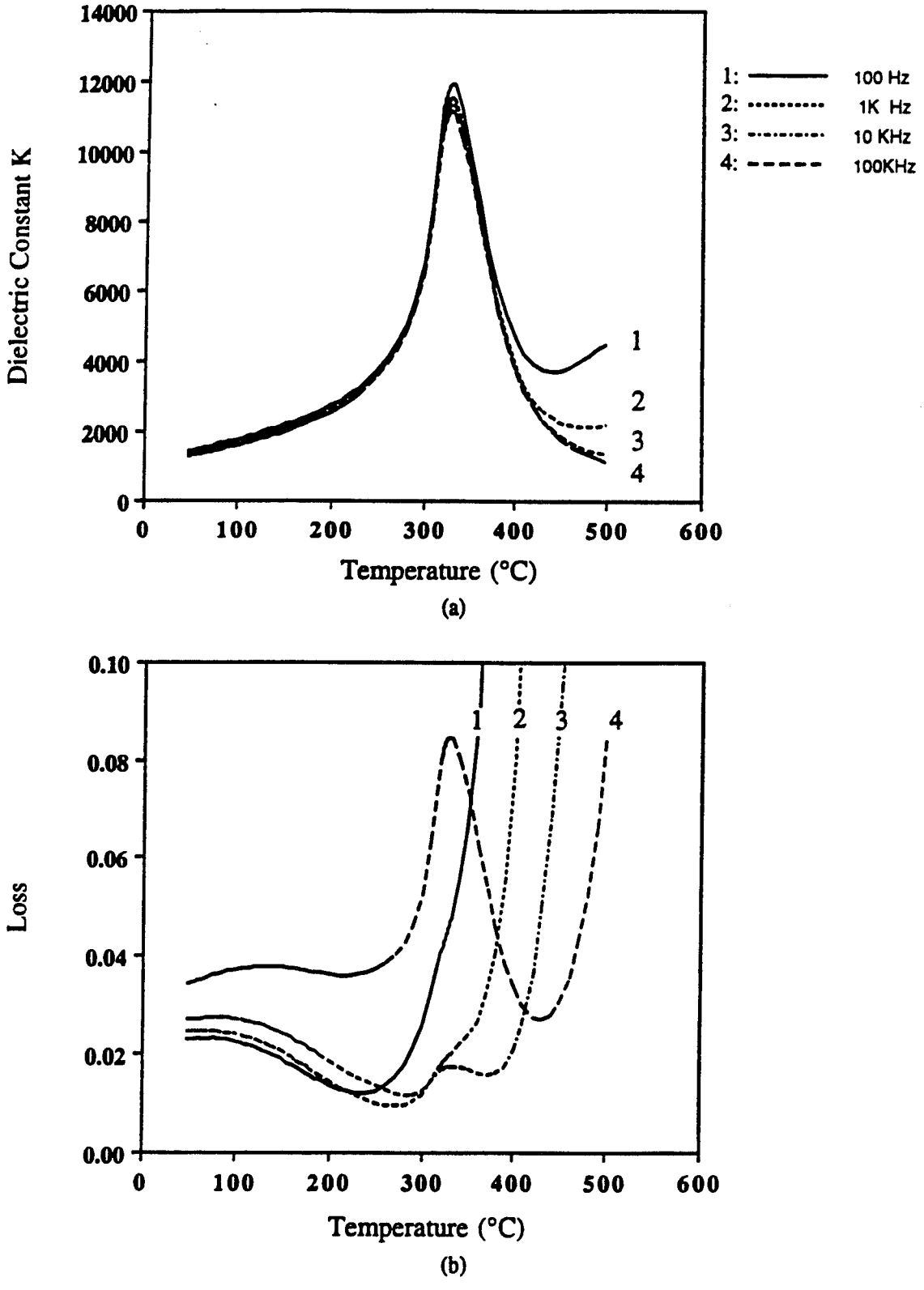

Figure 2. Dielectric constant and loss vs. temperature for PLZT-WO_3 (0.4 at%).

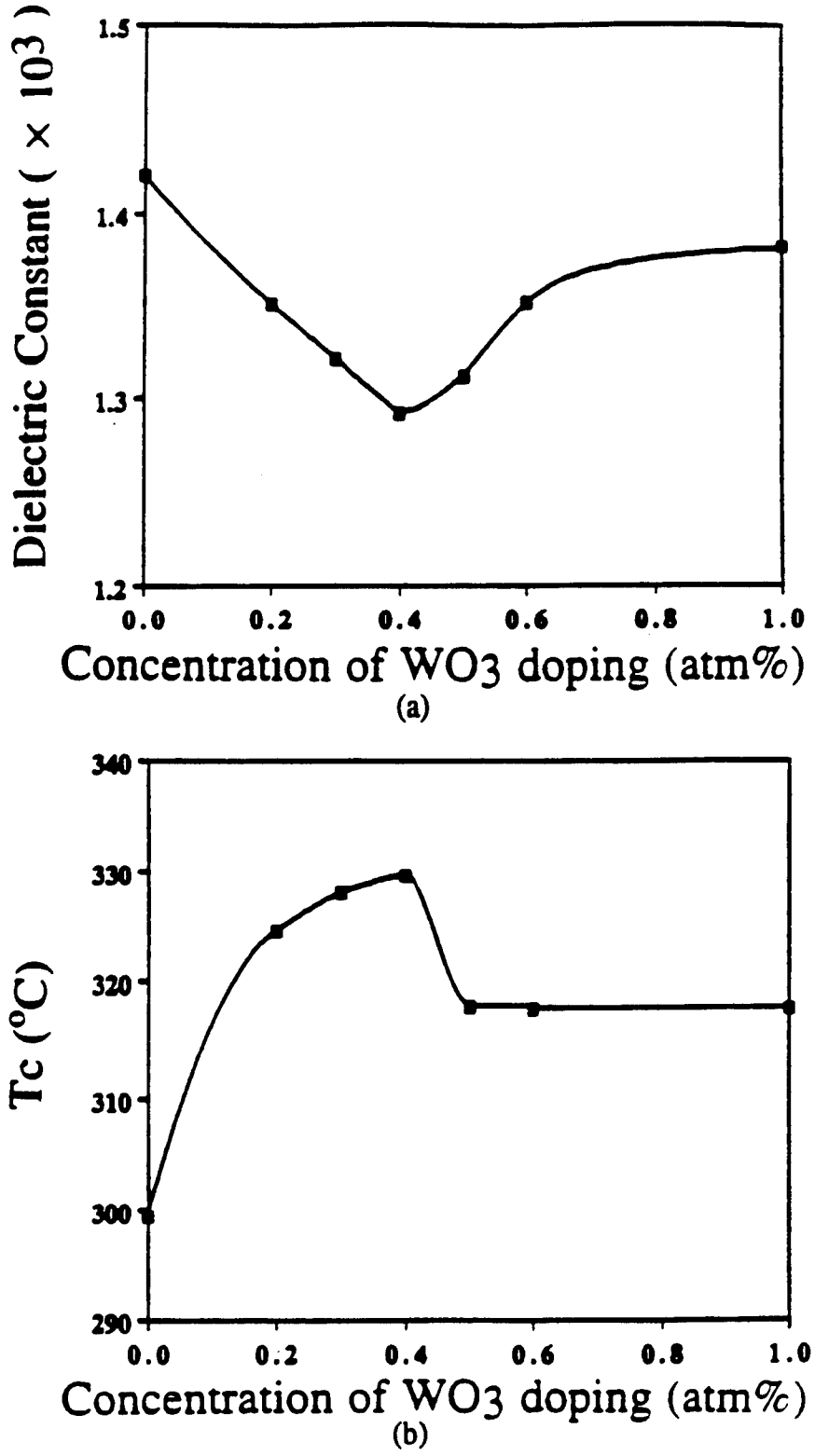

Figure 3. Room-temperature dielectric constant (a) and Curie temperature (b) vs. WO_3 doping level.

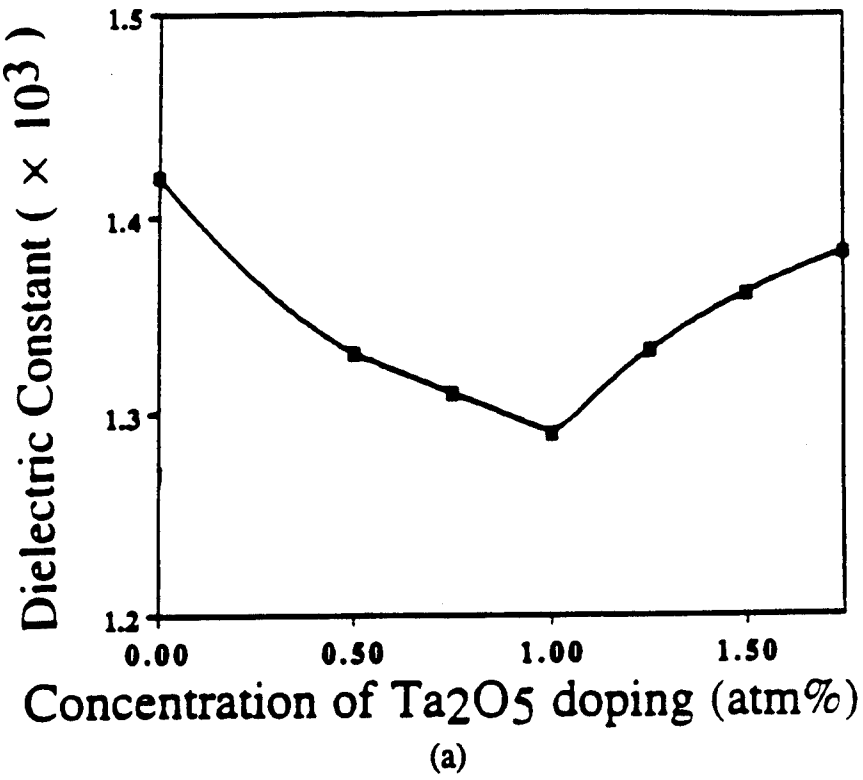

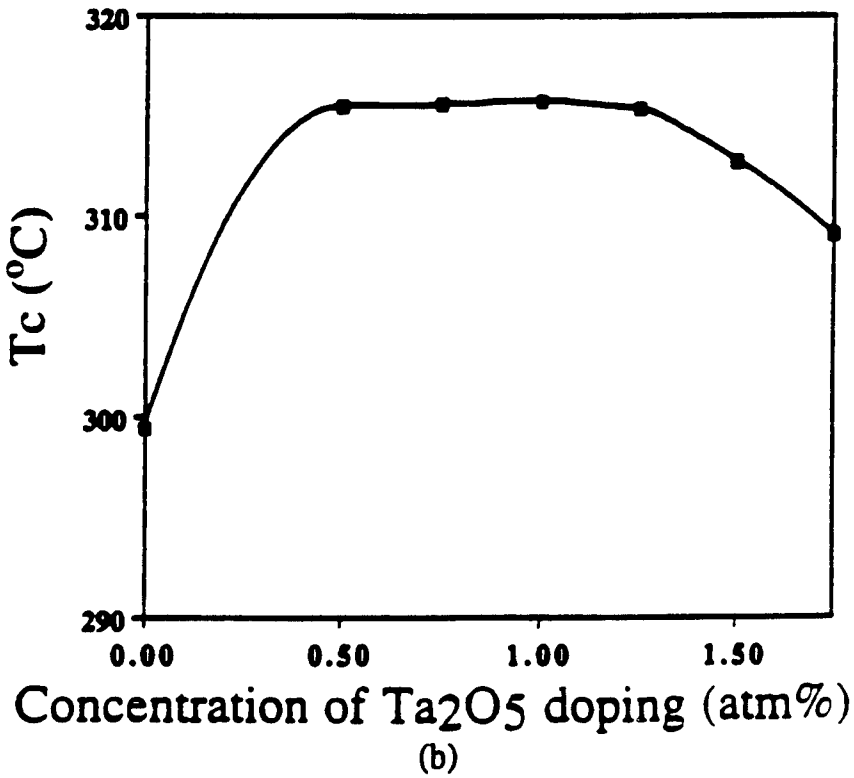

Figure 4. Room-temperature dielectric constant (a) and Curie temperature (b) vs. Ta_2O_5 doping level.

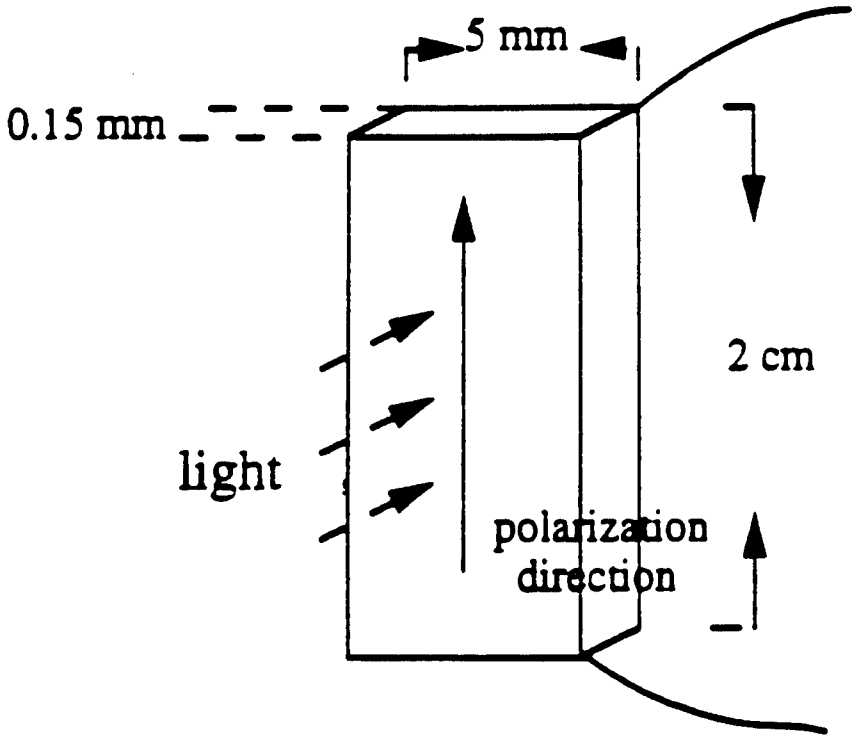

Figure 5. Sample configuration for photovoltaic effect measurements.

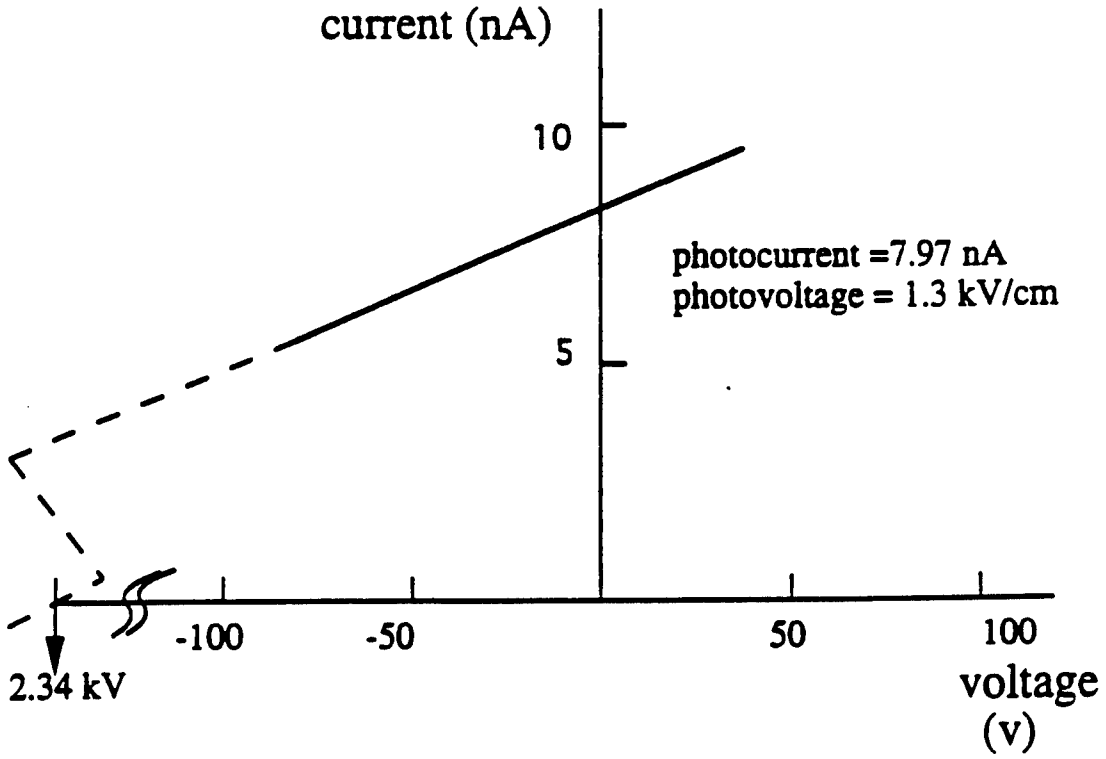

Figure 6. Photocurrent measured as a function of applied voltage for a 0.4% WO_3 doped PLZT sample. Light intensity is 4 mW/cm^2.

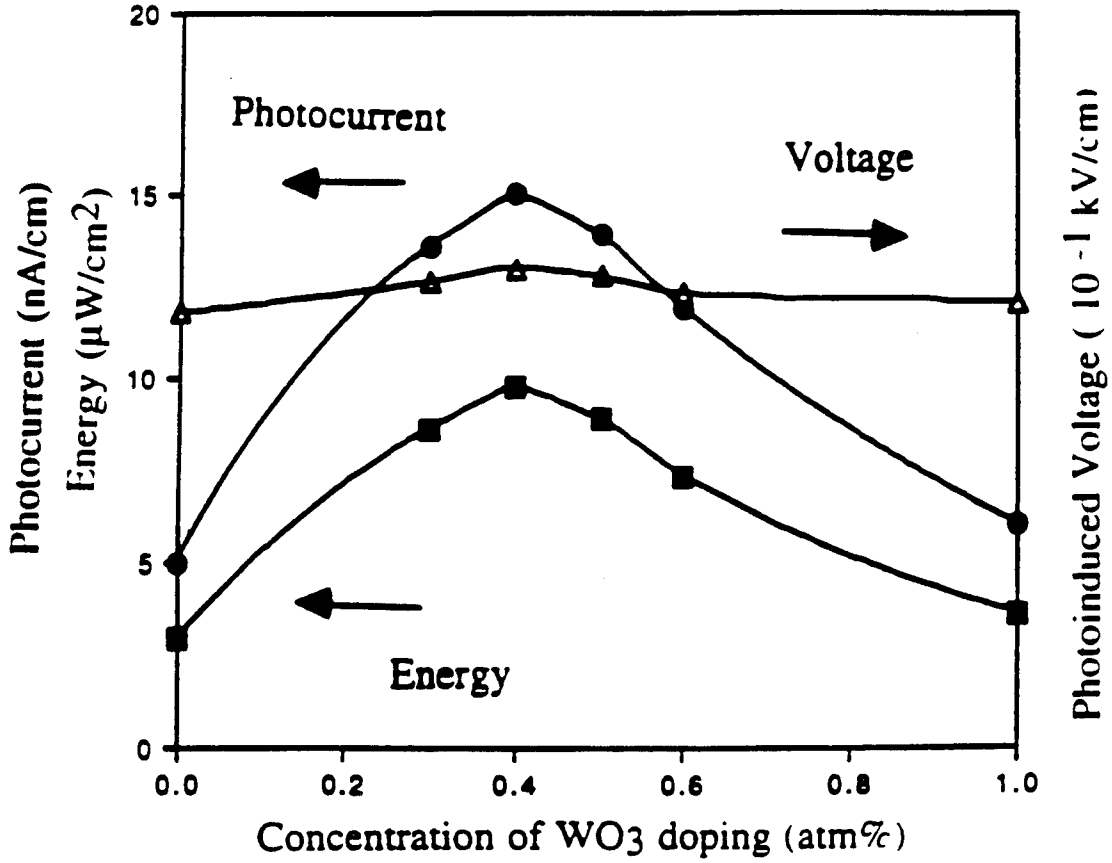

Figure 7. Photovoltaic current, voltage and potential power as a function of dopant concentration in WO_3 doped PLZT.

SEM observation

Figures 1(a), 1(b) and 1(c) show the thermally etched PLZT, PLZT-WO_3 and PLZT-Ta_2O_5 scanning electron microscope (SEM) photomicrographs, respectively. Pure PLZT has the largest grain size; however, it is difficult to determine grain size differences between WO_3 doped and Ta_2O_5 doped samples with different concentration. No additional phase was observed around the grain boundaries.

Dielectric measurements

Samples for dielectric measurements were polished using SiC powders to about 10 mm in diameter and 1 mm in thickness and electroded with sputtered platinum (Pt). Figure 2 shows dielectric constant and loss tan δ behavior as functions of temperature and frequency for 0.4 at% WO_3 doped PLZT. Figure 3(a) shows the change in room-temperature dielectric constant (at 10 kHz) with dopant concentration for WO_3 (0–1.0 at%), and Figure 3(b) shows the dielectric constant maximum temperature, which almost coincides with the Curie temperature (T_c), as a function of WO_3 doping. Consequently, the dielectric constant is

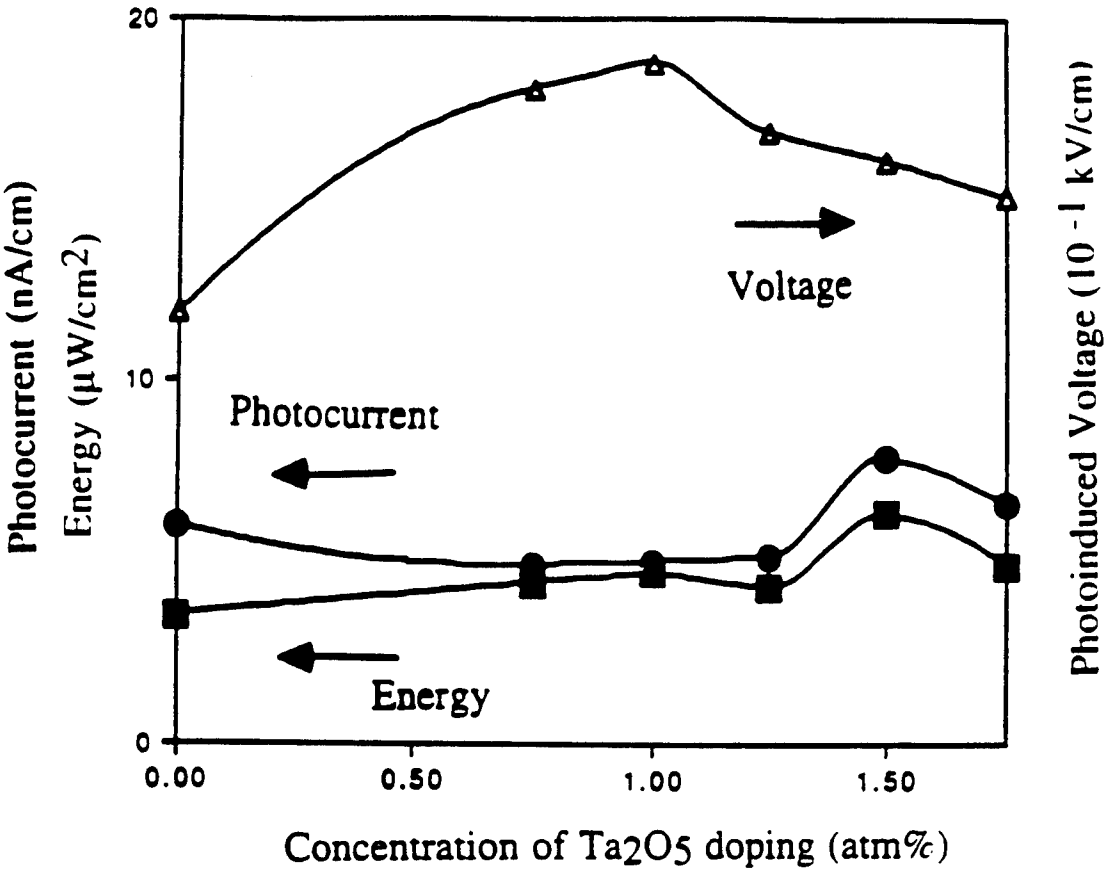

Figure 8. Photovoltaic current, voltage and potential power as a function of dopant concentration of Ta_2O_5 doped PLZT.

minimum at 0.4 atm% WO_3 doping. From Figure 3, it is evident that WO_3 increases T_c and 0.4 at% WO_3 doping shows the maximum Curie temperature.

Figures 4(a) and 4(b) show the changes in the room-temperature dielectric constant (10 kHz) and Curie temperature with Ta_2O_5 doping, respectively. In the case of Ta_2O_5 doping, the maximum Curie temperature and the minimum dielectric constant are obtained at 1.0 at% Ta_2O_5.

We can conclude that a slight donor doping reduces the grain size and shifts the Curie temperature to the higher temperature, as reported by T. Yamamoto et al. [10]. The correlation of these data with the photostriction will be discussed later.

Photovoltaic effect measurements

PLZT (3/52/48) doped with various concentrations of WO_3 and Ta_2O_5 were used for this study. Sample size for this measurement was $20 \times 4 \times 0.15$ mm^3: the 4×0.15 mm^2 surface was electroded with silver paste and silver wires were attached. The configuration of the sample is shown in Figure 5. Radiation from a high-pressure mercury lamp (Ushio

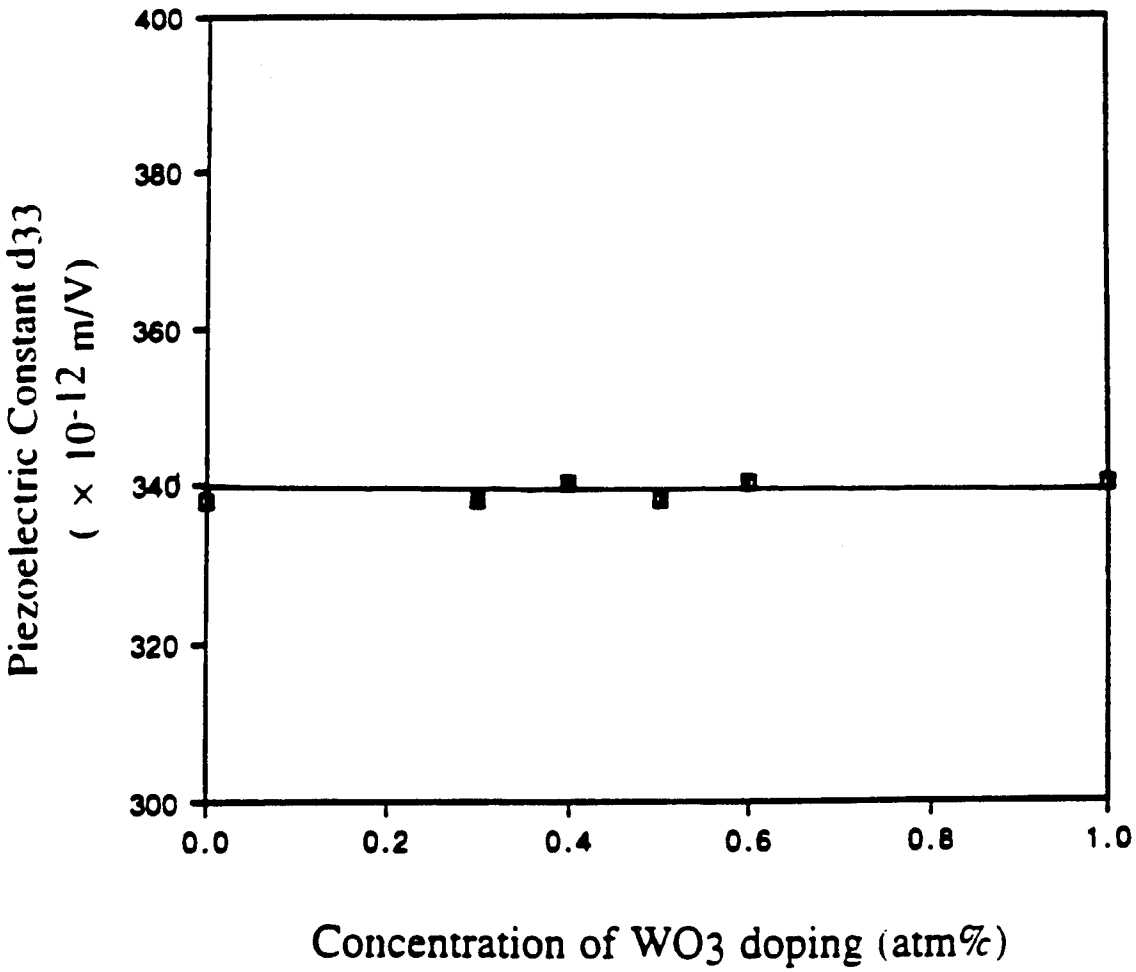

Figure 9. Piezoelectric coefficient (d_{33}) as a function of WO_3 doping.

Electric USH-500D) was passed through a UV bandpass filter (Oriel Co., No. 59811), an IR blocking filter (Oriel Co., No. 59060), and a fused quartz optical focusing lens. The light was almost monochromated to 370 mm, and the intensity was 4 mW/cm^2. Slight temperature increase about 10°C was observed on the sample.

The photovoltaic voltage reaches 1 kV/mm, and the current is on the order of nA. The induced current was measured with a high-input-impedance (200 TΩ) electrometer (Keithley 617) as a function of the external voltage over a range −100 V to + 100 V. The photovoltaic voltage and the current are defined as the maximum open-circuit voltage and short-circuit current, respectively [7]. Upon exposure to UV radiation, a weak pyroelectric current was initially observed, even with the IR blocking filter, and a steady-state photovoltaic current was achieved after several seconds. Measurements were made after the crystals had thermally equilibrated with the radiation to avoid contribution from the pyroelectric effect. The photovoltaic voltage and the current were determined from the intercepts of the horizontal and the vertical axes, respectively. A typical curve is shown in Figure 6 for PLZT doped with 0.4 at% WO_3.

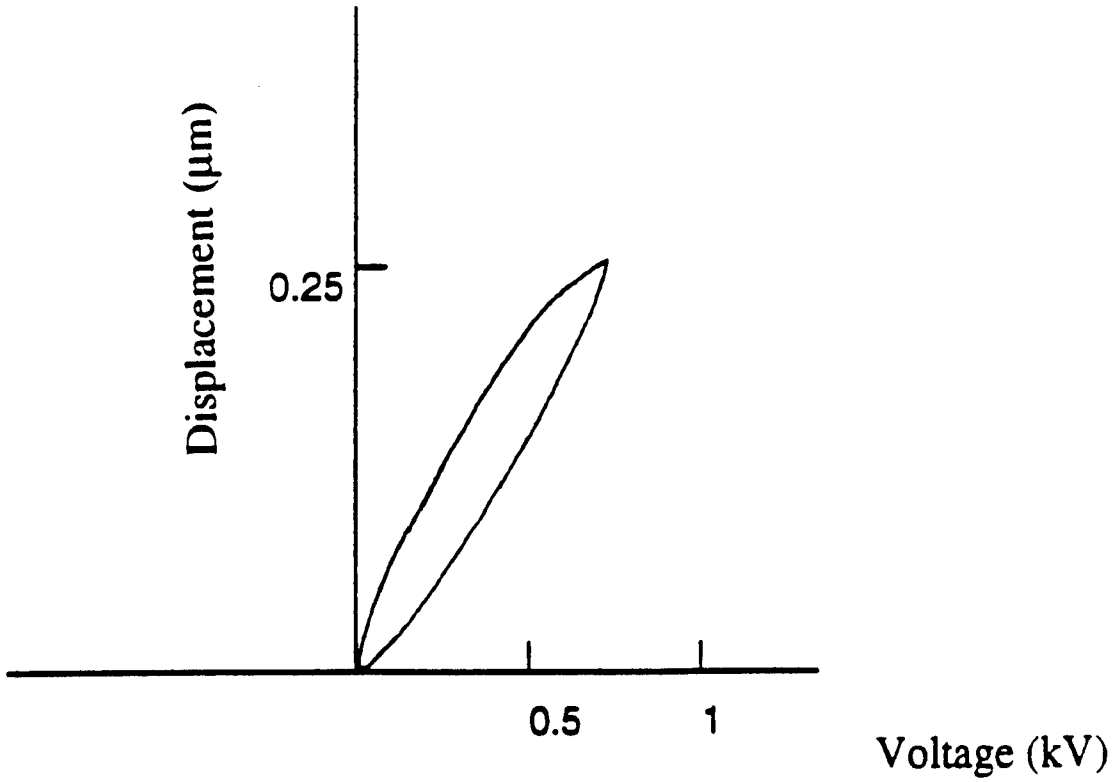

Figure 10. Induced displacement as a function of applied electric field for 0.4% WO_3 doped PLZT. ($t = 0.45$ mm).

Figures 7 and 8 show the photovoltaic current, photovoltaic voltage and stored energy ($P = (1/2)I\max \times V\max$) in PLZT doped with WO_3 and with Ta_2O_5, respectively. Photovoltaic current and voltage show a peak at 0.4 at% for the WO_3 samples, while photovoltaic current and photovoltage show a peak at 1.5 at% and 1 at% for the Ta_2O_5 samples, respectively. It was found that higher photovoltaic current and potential power can be obtained in WO_3 doped samples, while the higher photovoltage can be obtained in Ta_2O_5 doped samples. Notice that the strain magnitude increases as the photovoltaic voltage increases; and with increasing photo-current, there is an increase in the overall response.

Field-induced strain measurements

Since photostriction x_{ph} is defined in terms of the photovoltaic voltage E_{ph} and the piezoelectric coefficient d_{33} as

$$x_{ph} = d_{33}E_{ph}, \tag{1}$$

it is increased by increasing the photovoltaic voltage and/or the piezoelectric coefficient.

Samples for induced strain measurements were of the same configurations as for dielectric measurements, except they are electroded with sputtered silver (Ag) and poled in silicone oil at 120°C under a 20 kV/cm electric field. After poling, d_{33} measurements were made using a Berlincourt d_{33} meter (Channel Products, Inc.) at 100 Hz. The measured d_{33}

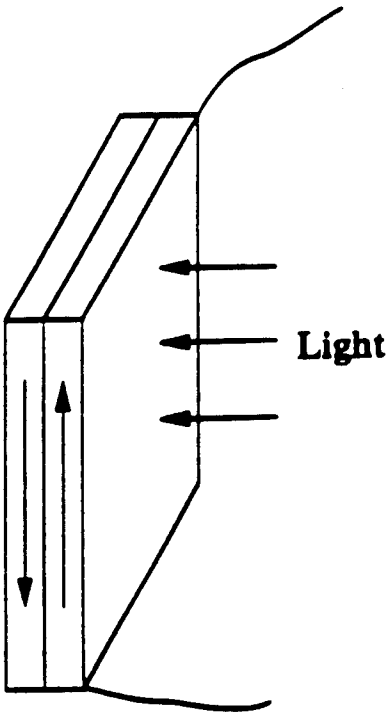

(a)

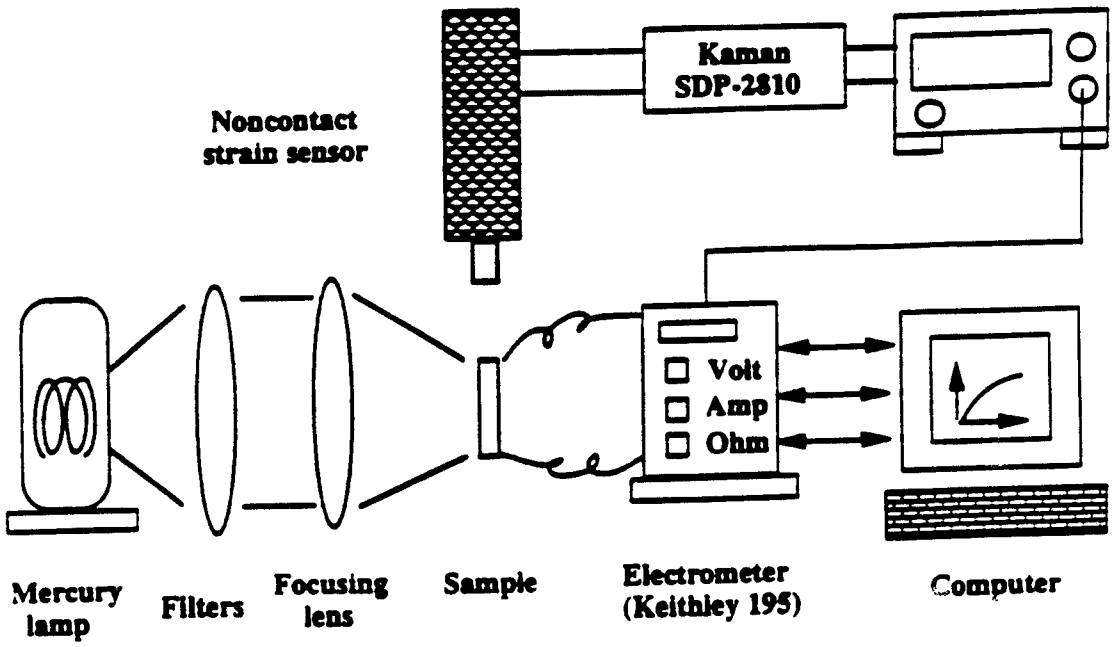

(b)

Figure 11. Co: ıration of bimorph sample (a), and experimental setup (b) for photostrictive-effect measurement.

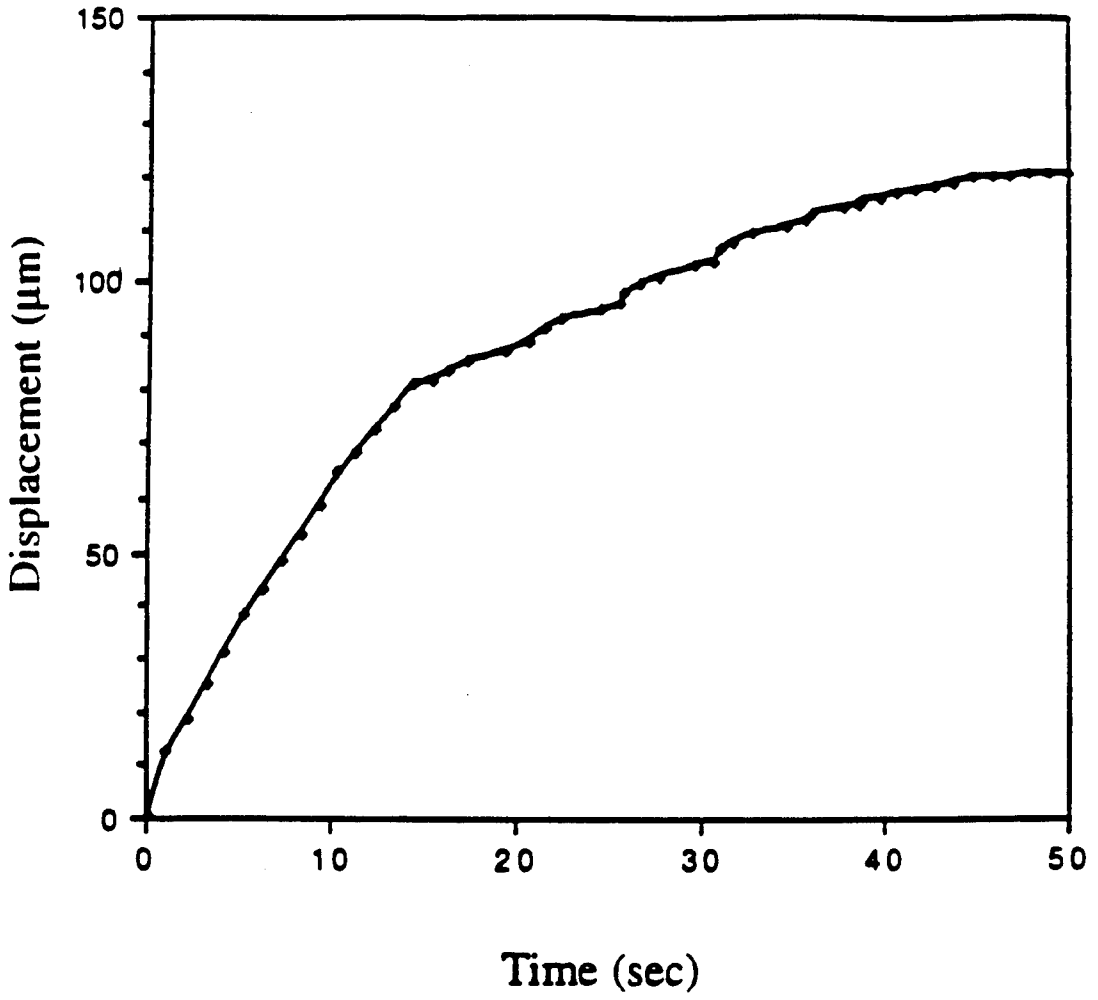

Figure 12. Bimorph deflection of device for 0.4% WO_3 doped PLZT device.

values were about the same for all samples (330×10^{-12} m/V) as seen in Figure 9 for WO_3-doped samples.

The field-induced displacement was also measured (see Figure 10). The average d_{33} constant obtained from the slope is 350×10^{-12} m/V, in good agreement with the Berlincourt meter data.

In spite of impurity doping, the value of the piezoelectric coefficient remains constant, indicating that photostriction is proportional to the photovoltaic voltage for these compositions.

Photostrictive effect measurements

A bimorph design consisting of two oppositely-poled ceramic plates (5 mm × 20 mm × 0.15 mm in size) was used for photostrictive-effect measurements. The configuration of the samples is shown in Figure 11(a). The displacement at the tip of this photostrictive bi-

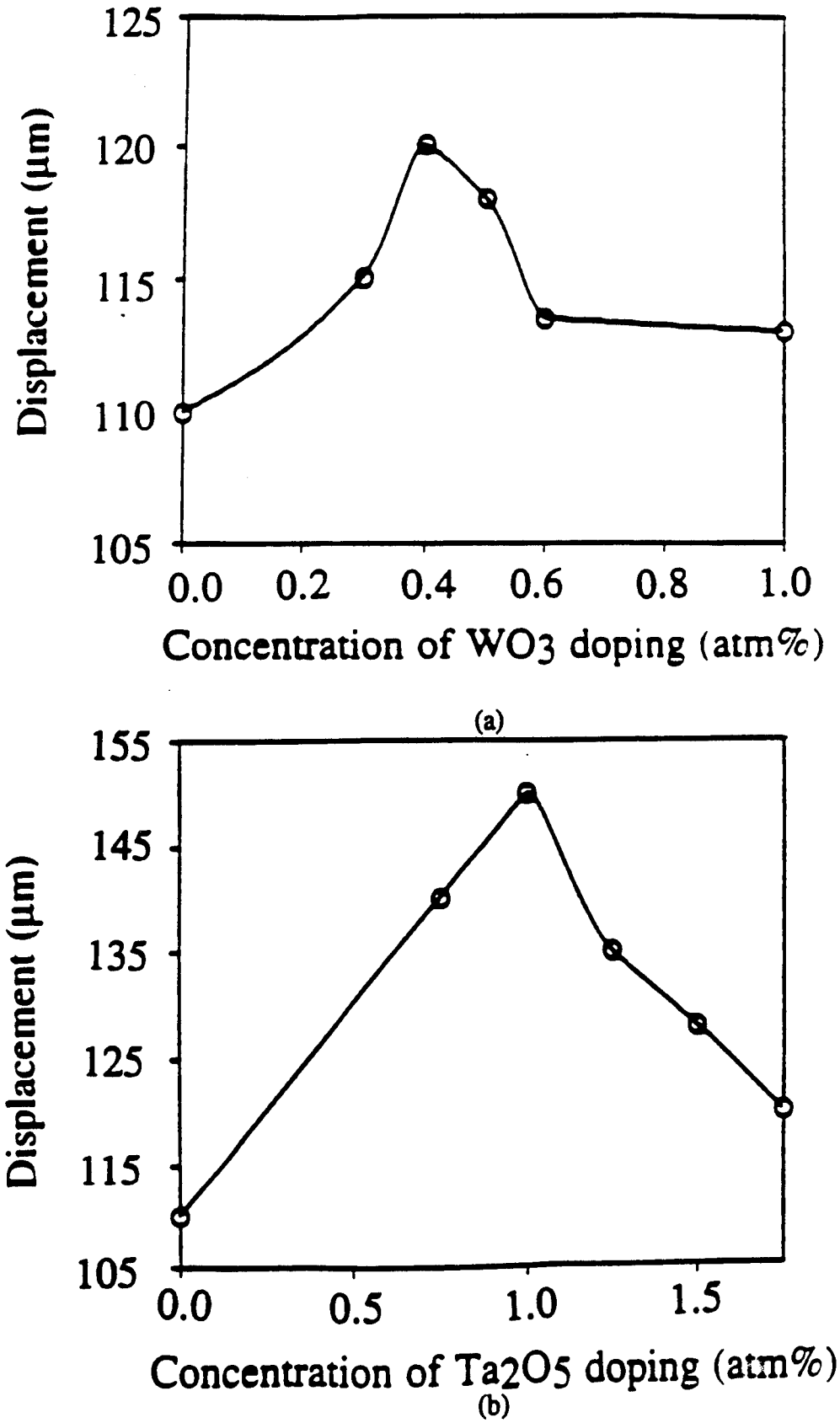

Figure 13. Light-induced displacement as functions of WO_3 and Ta_2O_5 doping.

morph was measured with a noncontact position sensor (Kaman Instrumentation Systems, SDP-2810.). The setup for photostrictive effect measurements is shown in Figure 11(b). The photostrictive effect in 0.4% WO_3 doped PLZT is shown in Figure 12. The displacement reached 50 μm in several seconds and saturated at 120 μm under a light intensity of 4 mW/cm^2. Figures 13(a) and 13(b) show the light-induced tip displacement as functions of WO_3 or Ta_2O_5 doping, respectively.

Conclusion

Donor doping was found to reduce the grain size and increase the Curie temperature, leading to the larger crystal distortion and the larger photo-current. The dielectric constant decrease enhances the larger photo-voltage. On the other hand, slight doping with WO_3 or Ta_2O_5 does not contribute to the piezoelectric effect, consequently, photostriction is mainly governed by the photovoltaic effect. The maximum photocurrent is obtained for 0.4 at% WO_3 doping and the maximum photovoltage is obtained for 1 at% Ta_2O_5 doping.

The tip displacement of a 20 mm long photostrictive bimorph can reach more than 100 μm in a couple of seconds, a great improvement over pure PLZT, and will be applicable to photo-acoustic devices.

Acknowledgment

This work is supported by Army Research Laboratory (ARL), No. DAALO3-92-G-0244. The authors would also thank Dr. Russell Brodeur for his critical review.

References

1. Fridkin, V.M. 1979. Photoferroelectrics: *Solid State Sciences*, Vol. 9.
2. Glass, A.M., von der Linde, D., Austin, D.H., and Negran, T.H. 1975. *J. Elec. Mat.*, Vol. 4, No. 5, 915–943.
3. Fridkin, V.M. and Povov, B.N. 1978. *Sov. Phys. Usp.* 21(12), 981–991.
4. Fridkin, V.M., Grekov, A.A., Ionov, P.V., Rodin, A.I., Savchenko, E.A., and Mikhailina, K.A. 1974. *Ferroelectrics*, Vol. 8. 433–435.
5. Brody, P.S. and Growne, F. 1975. *J. Elec. Mat.*, Vol. 4, No. 5, 955–971.
6. Sada, T., Inoue, M., and Uchino. K. 1987. *J. Ceram. Soc. Jpn.*, Vol. 5, 545.
7. Tanimura, M. and Uchino, K. 1988. Sensors and Materials, 1, 47–56.
8. Tanimura, M., Uchino, K., and Hikita, K. 1989. *Jpn. J. Appl. Phys.*, 28 (Suppl. 28-2), 170–172.
9. Uchino. K. 1989. *J. Rob. Mech.*, 1(2), 124–127.
10. Yamamoto, T. and Okazaki. K. 1990. Seventh International Symposium on the Application of Ferroelectrics.

APPENDIX 47

Smart Mater. Struct. 3 (1994) 114–117. Printed in the UK

Photovoltaic effect for the linearly polarized light in (Pb,La)(Zr,Ti)O_3 ceramics

Sheng-Yuan Chu, Zhou Ye and Kengi Uchino

International Center for Actuators and Transducers, Materials Research Laboratory, The Pennsylvania State University, University Park, PA 16802, USA

Received 10 February 1994, accepted for publication 2 May 1994

Abstract. The bulk photovoltaic effect in non-centrosymmetric crystals is caused by asymmetric generation, recombination or scattering of excited non-equilibrium electronic carriers. In this paper, photovoltaic effects in (Pb,La)(Zr,Ti)O_3-based ceramics have been investigated using linearly polarized light. Angular dependence of the photovoltaic voltage and current on the polarization direction of the light was observed in doped (Pb,La)(Zr,Ti)O_3 ceramics. A phenomenological model was proposed to fit the experimental results from which the photovoltaic coefficients were calculated.

1. Introduction

The photovoltaic effect is observed in certain ferroelectrics, wherein a constant electromotive force is induced with application of near-ultraviolet radiation [1–3]. This effect was explained by Fridkin *et al* in 1974 [4], by Glass *et al* [2] and by Brody and Growne [5], and probably originated from an excitation of electrons from asymmetric impurity potentials. The main features of the bulk photovoltaic effect are summarized as follows:

(1) This effect appears in poled uniform single crystals or ceramics with non-centrosymmetry and is entirely different in nature from the P–N junction effect observed in semiconductors.

(2) Constant photocurrent and photovoltage are generated in the spontaneous polarization direction under uniform illumination in the ferroelectric phase and disappear in the para-electric phase.

(3) The magnitude of the induced voltage is proportional to the crystal length in the polarization direction and is much greater than the band-gap energy of the crystal.

So far, most studies have been made on single crystals to clarify the origin of the effect. However, our research group has been focusing on polycrystalline samples such as $PbTiO_3$-based [6, 7] and Pb(Zr,Ti)O_3-based ceramics [8, 9] from a practical application point of view. We have developed a high photovoltage ($\approx$ 1 kV mm^{-1}) generator with relatively quick response ($\approx$ 1 s) in the (Pb,La)(Zr,Ti)O_3 (PLZT) system. Moreover, by superimposing the photovoltaic effect on the inherent piezoelectricity of these compounds, practical photostrictive materials have been realized [10, 11]. A bimorph-type photostrictive element can exhibit a several-hundreds-μm tip deflection under violet light illumination. This actuator is applicable to remote-control devices such as photo-driven relays [10] and micro walking robots [12].

In this paper, the bulk photovoltaic effect in bulk PLZT (3/52/48) ceramics has been investigated by illuminating with linearly polarized light, and the angular dependence of the photovoltaic voltage and current on the polarized-light direction has been determined. This measurement is important particularly when the photostrictor is utilized as a photoacoustic device in conjunction with optical polarizers.

2. Sample preparation

PLZT ($x/y/z$) samples were prepared in accordance with the following composition formula:

$$Pb_{1-y}La_y(Zr_{1-x}Ti_x)_{1-y/4}O_3.$$

Since the photostriction figure of merit is evaluated by the product of the photovoltaic voltage and the piezoelectric coefficient ($x_{ph} = d_{33} \times E_{ph}$) PLZT (3/52/48) was selected due to its optimum photostrictive response within the PLZT system [9].

The ceramic powder was prepared by a conventional mixed-oxide technique. $PbCO_3$, La_2O_3, ZrO_2, TiO_2 and dopant were weighed in the appropriate proportions and mixed in a ball mill for 2 days using ethanol and zirconia grinding media. 0.5 wt.% excess $PbCO_3$ was added to compensate for weight loss during calcination and sintering. The slurry was dried, then calcined in a closed

0964-1726/94/020114+04$19.50

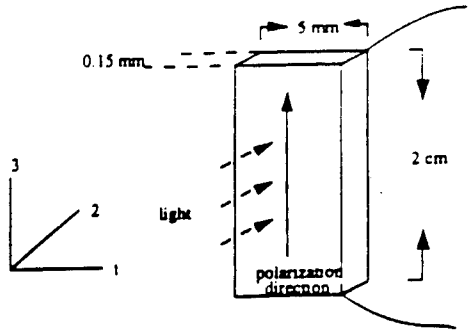

Figure 1. Sample configuration for photovoltaic-effect measurements.

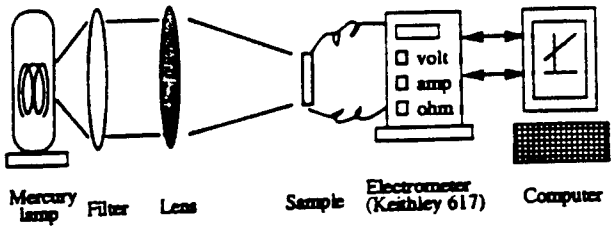

Figure 2. Experimental set-up for photovoltaic-effect measurements.

crucible at 950 °C for 10 h. The calcined powder was ball-milled again for 48 h. The samples were sintered in sealed alumina crucibles at 1270 °C/2 h. A PbO-rich atmosphere was maintained with lead zirconate powder to minimize lead loss during sintering. Sintered samples were electroded with silver paste. Finally, each sample was cut and poled in silicone oil at 120 °C under a 15 kV cm^{-1} electric field.

3. Photovoltaic effect measurements

PLZT (3/52/48) doped with various concentrations of WO_3 and Ta_2O_5 was used for this study. The sample size was $20 \times 4 \times 0.15$ mm^3: the 4×0.15 mm^2 surface was electroded with silver paste and silver wires were attached. The configuration of the sample is shown in figure 1. Radiation from a high-pressure mercury lamp (Ushio Electric USH-500D) was passed through a UV bandpass filter (Oriel Co., No.59811), an IR blocking filter (Oriel Co., No.59060), and an optical focusing lens. The experimental set-up is shown in figure 2. A wavelength peak around 370 nm, where the maximum photovoltaic effect of PLZT is obtained, was applied to the sample.

The photovoltaic voltage reaches 1 kV mm^{-1}, and the current is of the order of nA. The induced current was measured with a high-input-impedance (200 TΩ) electrometer (Keithley 617) as a function of the external voltage over a range −100 V to +100 V. The photovoltaic voltage and the current are defined as the maximum open-circuit voltage and short-circuit current respectively [10]. Upon exposure to UV radiation, a weak pyroelectric current was initially observed even with the IR blocking filter, and a steady-state photoelectric current was achieved after several

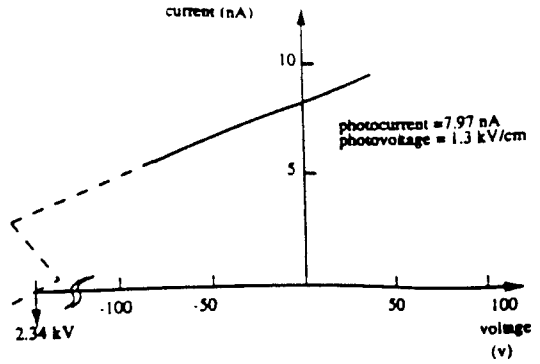

Figure 3. Photocurrent measured as a function of applied voltage for a 0.4% WO_3-doped PLZT sample.

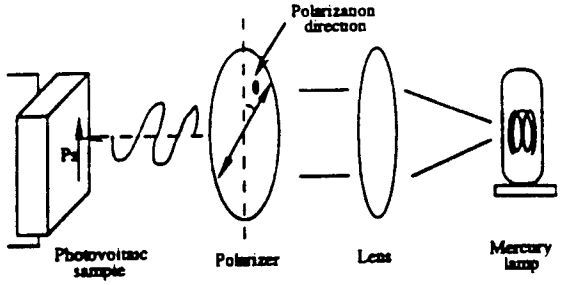

Figure 4. Experimental set-up for light-polarization-dependence measurements.

seconds. Measurements were made after the crystals had thermally equilibrated with the radiation to avoid any contribution from the pyroelectric effect. The photovoltaic voltage and the current were determined from the intercepts of the horizontal and the vertical axes, respectively. A typical curve is shown in figure 3 for PLZT doped with 0.4 at.% WO_3.

4. Angular dependence of the photovoltaic voltage and current

A polarizer was put between the focusing lens and the sample to monitor the angular dependence of the photovoltaic effect under linearly polarized light, as shown in figure 4. The angle θ was measured with respect to the origin of the remnant polarization direction. Figure 5 shows the experimental dependence of the photovoltaic current J and the corresponding voltage V on the light-polarization direction. Both the photovoltage and photocurrent provide the maximum values at $\theta = 0$, 180°, and the minimum at $\theta = 90°$. It was observed that the photocurrent and photovoltage deviations with respect to the change of light-polarization direction are 2% and 14% respectively, for the WO_3-doped samples, regardless of the absolute values of current and voltage. This is the first observation of angular dependence of the photovoltaic effect in ceramic samples, although this dependence was reported for single-crystal samples [13, 14].

The photovoltaic current density J_i can be described by the third-rank tensor α_{ijk} [15] as

$$J_i = \alpha_{ijk} E_j E_k^*. \qquad (1)$$

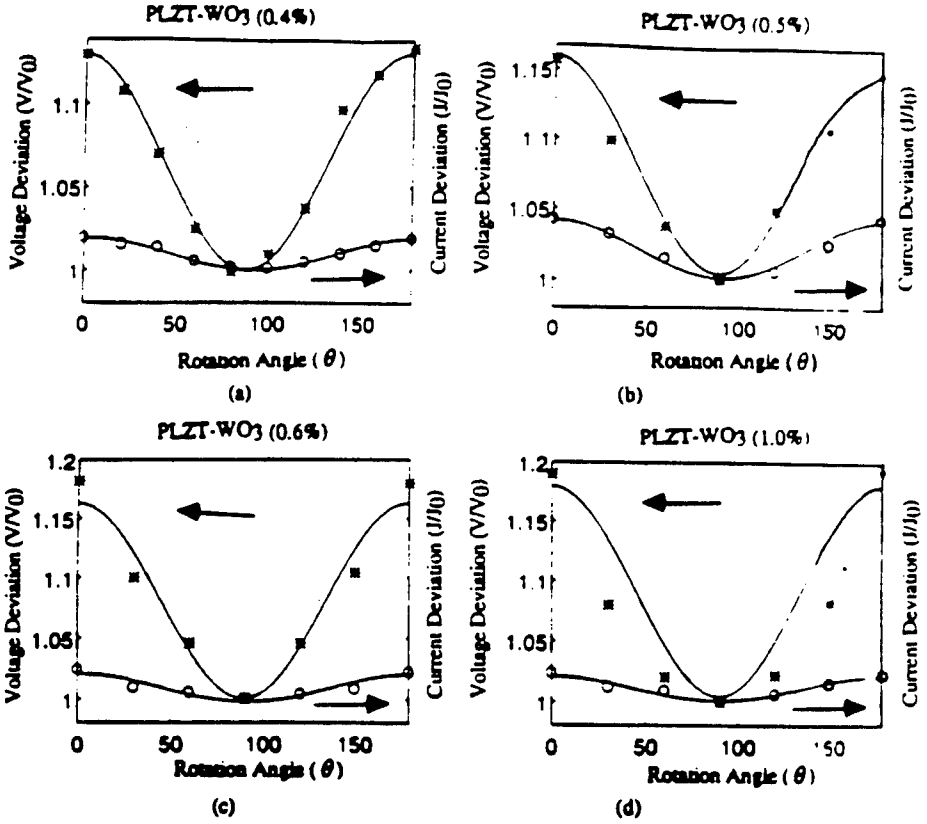

Figure 5. Dependence of the normalized photovoltaic current and photovoltage on the direction of the light-polarization plane and the light for various WO_3-doped PLZT samples. (*a*) 0.4%, (*b*) 0.5%, (*c*) 0.6%, and (*d*) 1%. Solid curves are the theoretically fitted curves.

Table 1. α_{31} and α_{33} coefficients of WO_3 and Ta_2O_5 doped PLZT.

	WO_3 at.%				Ta_2O_5 at.%			
	0.4	0.5	0.6	1	1	1.25	1.5	1.75
α_{31} (10^{-6}) (A W^{-1})	12.487	6.844	6.31	4.49	4.2	4.23	6.57	5.83
α_{33} (10^{-6}) (A W^{-1})	12.787	7.13	6.46	4.55	4.46	4.46	6.955	6.05
α_{33}/α_{31}	1.024	1.042	1.024	1.013	1.062	1.054	1.059	1.038

When a homogeneous ferro- or piezoelectric crystal is illuminated uniformly with linearly polarized light, a photovoltaic current J_i arises in it. The sign and the magnitude of the current depend on the orientation of the light-polarization vector with projections E_j and E_k. E_k^* is the conjugate vector of E_k.

Having the electrodes opened, the photovoltaic current J_i gives rise to the photovoltage

$$V_i = J_i l/(\sigma_d + \sigma_{ph}) \tag{2}$$

where σ_d and σ_{ph} are the dark conductivity and photoconductivity, respectively, and l is the distance between the electrodes. The value of V_i exceeds the energy gap of the ferro- or piezoelectric crystal by several orders of magnitude, (i.e. $V \gg E_g$) [1].

From the non-zero α_{ijk} for poled ceramics (Curie Group ∞m) the expression for J_z (the direction of linearly polarized light propagation is shown in figure 5) is obtained from equation (1):

$$J_z = \alpha_{31} I + (\alpha_{33} - \alpha_{31}) I \cos^2\theta \tag{3}$$

where I is the incident light intensity and $E_2 E_2^*/\sin^2\theta = E_3 E_3^*/\cos^2\theta = I$ (refer to figure 1). The experimental dependence $J_z(\theta)$ is in good agreement with equation (3). The solid curves in figure 5 are calculated from equation (3). The values of α_{31} and α_{33} are tabulated in table 1. Values of α_{31} and α_{33} are of the order of 10^{-6}, and α_{33} is larger than α_{31}. It is also noteworthy that systematic changes of α_{31} and α_{33} values are found with changes in dopant concentration. However, α_{33}/α_{31} remains essentially constant, and α_{33}/α_{31} is somewhat smaller in WO_3-doped than in Ta_2O_5-doped samples.

In order to determine the photovoltaic coefficient values ($k_{ijk} = (1/\alpha^*)\alpha_{ijk}$), the absorption coefficient (α^*) measurements are required.

5. Summary

The angular dependence of the photovoltaic current and the corresponding voltage on the light-polarization orientation with respect to the spontaneous polarization has been successfully observed in ceramic samples of PLZT. This angular dependence of the photovoltaic current is consistent with the symmetry of the poled ceramic. The difference between the peak–peak deviations in the current (2%) and voltage (14%) suggests a relatively large dependence of photoconductivity on light-polarization orientation.

References

[1] Fridkin V M 1979 *Photoferroelectrics (Springer Series on Solid State Sciences 9)* ed M Cardona, P Fulde and H-J Queisser (New York: Springer)

[2] Glass A M, von der Linde D, Austin D H and Negran T J 1975 *J. Electron. Mater.* **4** 915–43

[3] Fridkin V M and Povov B N 1978 *Sov. Phys. Usp.* **21** 981–91

[4] Fridkin V M, Grekov A A, Ionov P V, Rodin A I, Savchenko E A and Mikhailina K A 1974 *Ferroelectrics* **8** 433–5

[5] Brody P S and Crowne F 1975 *J. Electron. Mater.* **4** 955–71

[6] Uchino K, Miyazawa Y and Nomura S 1982 *Japan. J. Appl. Phys.* **21** 1671–4

[7] Uchino K, Miyazawa Y and Nomura S 1983 *Japan. J. Appl. Phys.* Suppl. **22–2** 102–5

[8] Uchino K and Aizawa M 1985 *Japan. J. Appl. Phys.* Suppl. **24–3** 139–41

[9] Uchino K, Aizawa M and Nomura S 1985 *Ferroelectrics* **64** 199–208

[10] Tanimura M and Uchino K 1988 *Sensors Mater.* **1** 47–56

[11] Tanimura M, Uchino K and Hikita K 1989 *Japan. J. Appl. Phys.* **28** Suppl. 28–2 170–2

[12] Uchino K 1989 *J. Robot. Mech.* **1** 124–7

[13] Koch W T H, Munser R, Ruppel W and Wurfel P 1976 *Ferroelectrics* **13** 305–7

[14] Fridkin V M and Sturman B I 1992 *The Photovoltaic and Photorefractive Effects in Noncentrosymmetric Materials* ed G W Taylor (Philadelphia, PA: Gordon and Breach)

[15] Fridkin V M, Grekov A A and Rodin A I 1982 *Ferroelectrics* **43** 99–108

APPENDIX 48

Bulk Photovoltaic Effect for the Linearly Polarized Light in $Pb(Zn_{1/3}Nb_{2/3})O_3$ Single Crystals

Sheng-Yuan CHU, Maureen L. MULVIHILL, Zhou YE and Kenji UCHINO
International Center for Actuators and Transducers, Materials Research Laboratory, The Pennsylvania State University, University Park, PA 16802, U.S.A.

(Received May 30, 1994; accepted for publication August 20, 1994)

The bulk photovoltaic effect in non-centrosymmetric crystals is caused by asymmetric generation, recombination or scattering of excited nonequilibrium electronic carriers. In this paper, the photovoltaic effect has been investigated in relaxor ferroelectric $Pb(Zn_{1/3}Nb_{2/3})O_3$ single crystals using linearly polarized light. Angular dependence of photovoltaic voltage and current on the polarization direction of light was observed in the crystal. A phenomenological model was proposed to fit the experimental results from which the photovoltaic coefficients were calculated.

KEYWORDS: bulk photovoltaic effect, $Pb(Zn_{1/3}Nb_{2/3})O_3$, relaxor, microdomain, photovoltaic coefficient

1. Introduction

The photovoltaic effect is observed in certain ferroelectrics, wherein a constant electromotive force is induced with application of near-ultraviolet radiation.[1-3] This effect was explained by Fridkin *et al.* in 1974.[4] Glass *et al.*[2] and Brody and Growne,[5] and probably originated from an excitation of electrons from asymmetric impurity potentials. The main features of the bulk photovoltaic effect are summarized below.

1) This effect appears in poled uniform single crystals or ceramics with noncentro-symmetry and is entirely different in nature from the P-N junction effect observed in semiconductors.
2) Constant photocurrent and -voltage are generated in the spontaneous polarization direction under uniform illumination in the ferroelectric phase and disappear in the paraelectric phase.
3) The magnitude of the induced voltage is proportional to the crystal length in the polarization direction and is much greater than the bandgap energy of the crystal.

Most of the studies have been made so far on normal ferroelectric single crystals with linearly polarized light, and significant angular dependence of the photovoltaic voltage and current on the polarization direction of the light with respect to the spontaneous polarization direction of the sample crystal has been reported.[1]

In this paper, the photovoltaic effect has been investigated in relaxor ferroelectric $Pb(Zn_{1/3}Nb_{2/3})O_3$ single crystals, where microdomains may have an effect on the photovoltaic phenomenon. $Pb(Zn_{1/3}Nb_{2/3})O_3$ is a well-known relaxor ferroelectric with a Curie temperature around 140°C, and a peculiar domain reversal mechanism which was also reported by us.[6]

2. Sample Preparation

The raw oxide powders PbO, ZnO and Nb_2O_5 were mixed in stoichiometric proportions. The ratio of flux, PbO, to composition used was 2:1. The powder was heated in a sealed platinum crucible to 1200°C, and cooled to 800°C at a rate of 2°C/h. Then they were cooled to room temperature. The crystals were removed from the flux by soaking in hot 25 vol% nitric acid.

Then, the $Pb(Zn_{1/3}Nb_{2/3})O_3$ single crystal was cut into a (111) plate. Sample size for this measurement was $1.55 \times 0.72 \times 0.56$ mm^3: the 1.55×0.72 mm^2 surface was electroded with silver paste. The crystal orientation of perovskite $\langle 111 \rangle$ was taken for the applied electrical field direction. Before photovoltaic-effect measurements, the sample was poled in silicone oil at 110°C under an electric field of 15 kV/cm for 10 min. The configuration of the sample is shown in Fig. 1.

3. Photovoltaic Effect Measurements

The experimental setup is shown in Fig. 2. Light from a high-pressure mercury lamp (Ushio Electric USH-500D) was passed through a UV band-pass filter (Oriel Co., No. 59811), an IR blocking filter (Oriel Co., No. 59060), and an optical focusing lens. A wavelength peak around 370 nm was then applied to the sample on the 1.55×0.56 mm^2 face.

For the unpoled $Pb(Zn_{1/3}Nb_{2/3})O_3$ crystal, the current was on the order of 10^{-12} A and the photovoltaic voltage was about 100 V/cm. However, after poling, the photocurrent and voltage increased to the order of 10^{-10} A and 1 kV/cm. Upon exposure to UV radiation, a weak pyroelectric current was initially observed even with the IR blocking filter, and a steady-state photoelectric current was achieved after 10 s. Figure 3 shows the transient response of current. The induced current was measured with a high-input-impedance (200 TΩ)

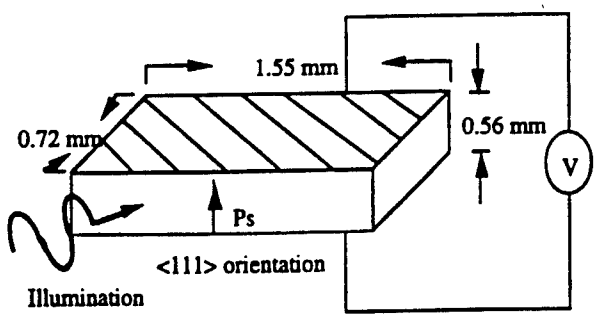

Fig. 1. Sample configuration for the photovoltaic-effect measurement.

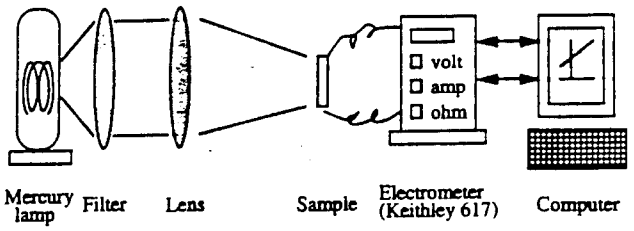

Fig. 2. Experimental setup for the photovoltaic-effect measurement.

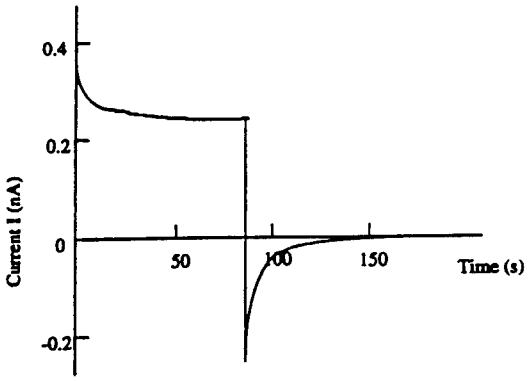

Fig. 3. Transient response of the current in a $Pb(Zn_{1/3}Nb_{2/3})O_3$ single-crystal sample.

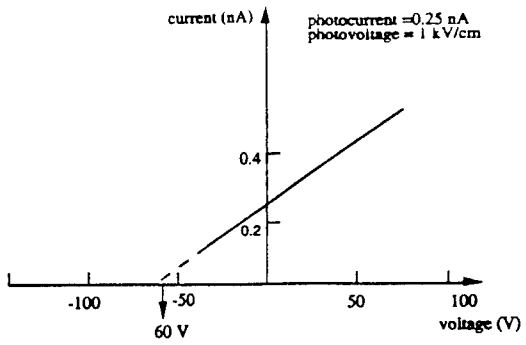

Fig. 4. Photocurrent measured as a function of applied voltage fo a $Pb(Zn_{1/3}Nb_{2/3})O_3$ single crystal.

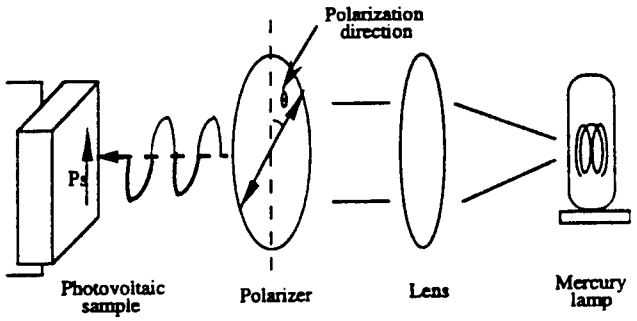

Fig. 5. Experimental setup for light-polarization-dependence measurements.

electrometer (Keithley 617) as a function of the external voltage over the range -100 V to $+100$ V. Measurements were made after the crystals reached thermal equilibrium with the radiation to avoid contribution from the pyroelectric effect. The photovoltaic voltage and the current are defined as the maximum open-circuit voltage and short-circuit current, respectively,[7] and were determined from the intercepts of the horizontal and vertical axes, respectively. A typical curve is shown in Fig. 4.

4. Angular Dependence of Photovoltaic Voltage and Current

A polarizer was placed between the focusing lens and the sample to monitor the angular dependence of the photovoltaic effect under linearly polarized light, as shown in Fig. 5. The angle θ was measured with respect to the origin of the remanent polarization direction. Figure 6 shows the experimental dependence of the photovoltaic current J and the corresponding voltage V on the light polarization direction under the illumination intensity of 1 mW/cm^2 for $\lambda=366$ nm. Both the photovoltage and photocurrent provide the maximum values at $\theta=0$ and 180°, and the minimum at $\theta=90°$. It was observed that the photocurrent and photovoltage deviations with respect to the change of light polarization direction are 16% and 11%, respectively, for the $Pb(Zn_{1/3}Nb_{2/3})O_3$ single-crystal samples, regardless of the absolute values of current and voltage.

To our knowledge, this is the first observation of an

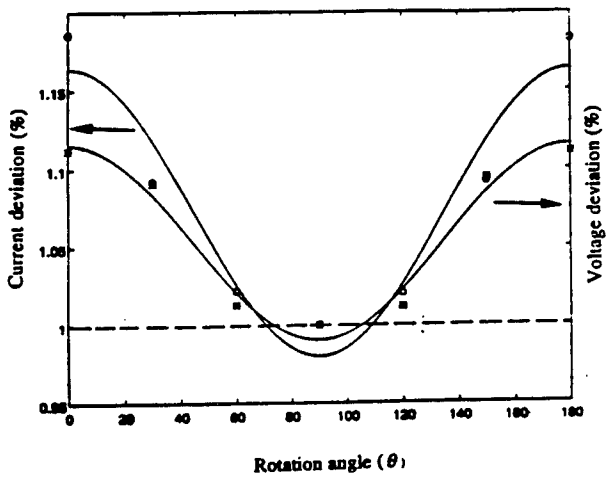

Fig. 6. Dependence of the normalized photovoltaic current and photovoltage on the direction of the light polarization plane with respect to the spontaneous polarization direction for a $Pb(Zn_{1/3}Nb_{2/3})O_3$ single crystal. Solid lines are the theoretically fitted curves. (○: photocurrent, *: photovoltage) Light power= 0.152 ± 0.001 mW.

angular dependence of the photovoltaic effect in a relaxor ferroelectric single crystal, although this dependence was reported for other normal ferroelectric single crystals.[8,9] Compared with normal ferroelectrics such as $LiNbO_3$[10] and SbSI,[11] the deviations in the photocurrent and voltage are relatively small, in a comparable magnitude of the polycrystalline samples

reported in our previous paper.[12] This may be attributed to the microdomain configuration in the relaxor $Pb(Zn_{1/3}Nb_{2/3})O_3$.

When a homogeneous ferro- or piezoelectric crystal is illuminated uniformly with linearly polarized light, a photovoltaic current J_i arises from it. The photovoltaic current density J_i can be described by the third-rank tensor α_{ijk}[13] as

$$J_i=\alpha_{ijk}E_jE_k^*. \quad (1)$$

The sign and the magnitude of the current depend on the orientation of the light polarization vector with projections E_j and E_k.

With the electrodes open, the photovoltaic current J_i gives rise to the photovoltage

$$V_i=J_il/(\sigma_d+\sigma_{ph}), \quad (2)$$

where σ_d and σ_{ph} are the dark and photoconductivity, respectively, and l is the distance between the electrodes. The value of V_i exceeds the energy gap of the ferro- or piezoelectric crystal by several orders of magnitude (i.e., $V \gg E_g$).[1]

From nonzero α_{ijk}'s for $Pb(Zn_{1/3}Nb_{2/3})O_3$ single crystals (Point Group 3m), the expression for J_z (the direction of linearly polarized light propagation is shown in Fig. 5) is obtained from eq. (1):

$$J_z=\alpha_{31}I+(\alpha_{33}-\alpha_{31})I\cos^2\theta \quad (3)$$

where I is the incident light intensity. The experimental dependence $J_z(\theta)$ is in good agreement with eq. (3). The solid lines in Fig. 6 are calculated from eq. (3). Values of α_{31} and α_{33} are then calculated as 2.1×10^{-7} A/W and 3.2×10^{-7} A/W, respectively.

In order to determine the photovoltaic coefficient values ($k_{ijk}=(1/\alpha^*)\alpha_{ijk}$), the absorption coefficient (α^*) measurements are required.

5. Conclusions

The angular dependence of the photovoltaic current and the corresponding voltage on the light polarization orientation with respect to the spontaneous polarization has been successfully observed in relaxor ferroelectric $Pb(Zn_{1/3}Nb_{2/3})O_3$ single crystals. This angular dependence of the photovoltaic current is consistent with the symmetry of the poled single crystal. The difference between the peak-to-peak deviations in the current (16%) and voltage (11%) is relatively small in comparison with the case of normal ferroelectrics. This may be attributed to the microdomain configuration in the relaxor $Pb(Zn_{1/3}Nb_{2/3})O_3$.

Acknowledgement

This work is supported by Army Research Office (ARO), No. DAALO3-92-G-0244.

1) V. M. Fridkin: *Photoferroelectrics*, eds. M. Cardona, P. Fulde and H.-J. Queisser (Solid State Sciences, New York, 1979) Vol. 9, Chap. 6. p. 85.
2) A. M. Glass, D. von der Linde, D. H. Austin and T. J. Negran: J. Electron. Mater. **4** (1975) L915.
3) V. M. Fridkin and B. N. Povov: Sov. Phys. Usp. **21** (1978) L981.
4) V. M. Fridkin, A. A. Grekov, P. V. Ionov, A. I. Rodin, E. A. Savchenko and K. A. Mikhailina: Ferroelectrics **8** (1974) L433.
5) P. S. Brody and F. Growne: J. Electron. Mater. **4** (1975) L955.
6) M. L. Mulvihill, L. E. Cross and K. Uchino: to be published in J. Am. Ceram. Soc.
7) M. Tanimura and K. Uchino: Sens. & Mater. **1** (1988) L47.
8) W. T. H. Koch, R. Munser, W. Ruppel and P. Wurfel: Ferroelectrics **13** (1976) L305.
9) V. M. Fridkin and B. I. Sturman: *The Photovoltaic and Photorefractive Effects in Noncentrosymmetric Materials*, ed. G. W. Taylor (Gordon and Breach Science Publishers, Philadelphia, 1992) Vol. 8, Chap. 3. p. 120.
10) V. M. Fridkin and R. M. Magomadov: Zh. Eksp. Teor. Fiz. Lett. **30** (1979).
11) V. M. Fridkin and A. I. Rodin: Phys. Status Solidi a **61** (1980) 123.
12) S.-Y. Chu, Z. Ye and K. Uchino: J. Smart Mater. & Struct. **3** (1994) 114.
13) V. M. Fridkin, A. A. Grekov and A. I. Rodin: Ferroelectrics **43** (1982) L99.

APPENDIX 49

LOW TEMPERATURE DYNAMIC OBSERVATION OF RELAXOR FERROELECTRIC DOMAINS IN LEAD ZINC NIOBATE

Maureen L. Mulvihill*♦, L. Eric Cross* and Kenji Uchino*
International Center for Actuators and Transducers (ICAT)
Materials Research Laboratory
The Pennsylvania State University
University Park, Pennsylvania 16802

ABSTRACT

Domain reorientation was examined in lead zinc niobate-lead titanate solid solution single crystals because of its contribution to electrically controlled change of shape and change of response in piezoelectric transducers and actuators. High resolution optical techniques were used to explore the build up of macro polar domains from micro polar regions in relaxor compositions. Domains changed from ambiguous spindle-like to sharp domains as $PbTiO_3$ content increased. The domain walls in the $Pb(Zn_{1/3}Nb_{2/3})O_3$-rich samples moved with a wave-like motion. The motion froze-in below -130°C or -30°C for field biased or non-biased samples respectively. The domains were observed as functions of temperature from 300°C to -185°C and electric field.

KEYWORDS: domains, relaxor ferroelectric, lead zinc niobate, actuators, piezoelectrics

INTRODUCTION

In the past ferroelectric domains have been observed statically by many methods, such as acid etching[1] and transmission electron microscopy (TEM)[2]. However, it has been very difficult to observe domain motion dynamically. In this study a high resolution optical technique was used to explore the build up of macro polar domains from micro polar regions in relaxor compositions, $Pb(Zn_{1/3}Nb_{2/3})O_3$ - $PbTiO_3$, as functions of temperature and applied electric field. It is important

****

Presented at the 95th Annual Meeting of the American Ceramic Society, Cincinnati, Ohio, April 20, 1993 (19-SXVIIP).
♦Received Third Place Award in Graduate Student Poster Competition at the 95th Annual Meeting of the American Ceramic Society, Cincinnati, Ohio.
Supported by the Office of Naval Research, under Grant No. N00014-91-J-4145.
*Member of the American Ceramic Society.

to study domain reorientation mechanisms because of their contributions to the electrically controlled change of shape and change of response in piezoelectric transducers and actuators.

Lead zinc niobate based single crystals were studied because of their wide use as high permittivity dielectrics in capacitor industries. $Pb(Zn_{1/3}Nb_{2/3})O_3$ (PZN) has a diffuse phase transition near 140°C.[3,4] It has a complex perovskite structure (rhombohedral symmetry) in which the Zn^{2+} and Nb^{5+} are in a disordered arrangement on the B-sites. The variations in the local composition, due to the disordered B-site ion arrangement, cause the phase transition to vary locally; therefore, a Curie region occurs rather than a Curie point. $PbTiO_3$ (PT) has a sharp transition at 490°C and a simple tetragonal perovskite structure. In PT, a Curie point occurs because there is no variation in local composition. $(1-x)Pb(Zn_{1/3}Nb_{2/3})O_3 - xPbTiO_3$ (PZN-PT) form a complete solid solution up to $x = 0.2$. PZN-PT has a room temperature morphotropic phase boundary (MPB) of $x = 0.1$ at 25°C between the rhombohedral and tetragonal phases as illustrated in Figure 1.[5]

EXPERIMENTAL PROCEDURE

Single crystals of PZN-PT were grown using the flux method with excess PbO.[6] The Laué X-Ray Technique was used to precisely determine the <011> and <111> directions. The crystals were then sliced parallel to the [011] plane, as shown in Figure 2. They were polished to a thickness of 100 μm and until a near-scratch free surface was achieved on both sides. The samples were gold sputtered leaving a 400 μm gap on the surface. Silver leads were attached to the sample with air dry silver paste. The samples were heat-treated to a temperature above 300°C to anneal out the ferroelastic domains produced during polishing. By annealing out the ferroelastic domains, the single crystals divided back into small micro domains.[7] Therefore, the growth of micro to macro domains could be observed.

Samples with 100 and 90.5 percent PZN (rhombohedral symmetry) were observed in this study as a function of temperature under cyclic applied electric field parallel to the <111> axis. The <111> direction is the polarization axis for crystals with rhombohedral symmetry.

A high resolution CCD (Charged Coupled Device) camera was attached to a Nikon Transmission Petrographic Microscope which was connected to a monitor and VCR (illustrated in Figure 3). The polarizing light microscope was used to observe the domains because of birefringence between the domains. It also allows possible magnifications up to 1300 times on the monitor. The temperature sample stage (Linkam Inc.) in conjunction with the deep focal point of the objective lenses allowed an electric field to be safely applied across the sample. The sample stage had the ability to cycle the temperature between 600 to -185°C with or without an electric field. The static and dynamic motion of the domains were instantaneously recorded by the VCR and observed on the monitor. The VCR records up to 30 frames per second.

EXPERIMENTAL RESULTS AND DISCUSSION

The variation of domain shape can be observed between rhombohedral domains (100 percent PZN) and a combination of rhombohedral and tetragonal domains (0.905PZN-0.095PT). The rhombohedral domains appear ambiguous spindle-like, whereas the tetragonal domains appear sharp stripe-like. These observations shown in Figures 4 through 7 are in good agreement with the previous work.[8,9] A 10 μm scale is indicated on each of the figures. For Figures 5 and 7, the electric field was applied from right to left as illustrated in Figure 2a along the <111>. For Figure 6 the electric field was applied also along the <111>, but in the figure it was from top to bottom, as illustrated in Figure 2b.

Domain Change with Temperature

Figures 4a through 4e show a series of domain change pictures taken from a 0.905/0.095 PZN-PT single crystal. The temperature was decreased from -8.4 to -27.4°C without applying an electric field. This sample proved that domain motion occurs even at low temperatures without being biased. A domain wall moved from the upper right corner (Figure 4a at -8.4°C) to lower left corner (Figure 4e at -27°C). More spindle-like domains developed at -20°C (Figure 4c) then combined to form a larger domain at lower temperatures, -27°C. For this composition, the domain motion froze-in near -30°C.

Domain Change with Electric Field

Figure 5 is a 100% PZN single crystal at a constant temperature of 28°C. Total domain reversal occurred after one cycle of an AC field with a maximum field of 5 kV/cm at 0.05 Hz. For crystals with rhombohedral symmetry, there exists domains with 71, 109 and 180 degree orientations between each other. Figure 5 represents a sample as the electric field switched the domains to another preferred domain orientation. Therefore, the domain walls returned to their original orientation after 1 cycle. The domains in the figures were saturated because the AC field up to 5 kV/cm was applied for several hours. It is very interesting that even at a very high electric field the domains did not go to a complete single domain state, but maintained a narrow stripe-like pattern with nearly constant width. This is a rather different phenomenon from the normal ferroelectric's case such as $BaTiO_3$. Note that the domain orientation returned to approximately the same position, shown in Figures 5a and 5d. This domain wall motion was closely related to the $Pb(Mg_{1/3}Nb_{2/3})O_3$ single crystal domains seen by Bokov and Myl'nikova.[3]

Domain Change with Applied Electric Field while Changing Temperature

The sample in Figure 6 is a 100% PZN single crystal in which the temperature was raised from -114 to -38°C with an AC applied field with a maximum of 7.5 kV/cm. Below -130°C, the domain motion was frozen; however, as temperature increased the domains began to move slowly. The domain motion appeared to nucleate in island regions on the crystal surface (illustrated in Figure 6a). As the temperature increased these regions grew, the domains switched across the entire crystal as shown in Figure 6d (-54°C). The switching speed increased as the temperature increased. The dramatic changes in the domain motion as a function of temperature can be seen in the center of Figures 6a through 6e. A slight temperature hysteresis also occurred between heating and cooling. The domain motion on cooling stopped at -130°C, but on heating began at -125°C.

Figure 7 is an example of a MPB composition 0.905/0.095 PZN-PT single crystal as temperature decreased from 191°C (paraelectric state) to -119°C (ferroelectric state). An AC-field of 10 kV/cm at 0.05 Hz was simultaneously applied. The domains (illustrated by birefringence changes) of the sample at 191°C (Figure 7a) were still changing even though it was above the Curie

Range for this sample. The large polar fluctuations in the paraelectric phase above the Curie Range permitted the alternating field to force a phase change from a paraelectric state with large mobile micropolar regions to a ferroelectric state in which a domain structure becomes apparent.[7] As the temperature decreased more spindle-like domains formed. Near room temperature the domain motion was more complicated because of the rhombohedral/tetragonal phase coexisting. The domain orientation had fourteen possible directions rather than eight or six for rhombohedral or tetragonal symmetry, respectively. It is notable that the domain shape also gradually changed because of the symmetry changes caused by the addition of PT. The shape transformed from ambiguous spindle-like domains to sharp domains as the PT increased. In this sample the domain motion freezing was observed also near -130°C.

SUMMARY

Domains in PZN-PT changed from small ambiguous spindle-like to sharp stripe-like domains as $PbTiO_3$ content increased. This difference may be partially due to the crystallographic structure change from rhombohedral to the tetragonal phase. The domain walls moved with a wave-like motion in pure PZN while keeping a narrow stripe-like domain pattern. The MPB composition of 0.905/0.095 PZN-PT has a more complicated domain wall motion than the other compositions since they can have both tetragonal and rhombohedral domains. The successive phase transitions from rhombohedral/tetragonal and tetragonal/cubic were also observed as the temperature increased. Domain motion freezing was successfully observed by microscopy. The freeze-in temperature for pure PZN was -130°C or -30°C for field-biased or non-biased samples, respectively. Quantitative analyses on the domain switching speed and the frozen island size will be reported in following papers.

REFERENCES

1 G. Arlt and P. Sasko, "Domain Configuration and Equilibrium Size of Domains in $BaTiO_3$ Ceramics," *J. Appl. Phys.* **51** [9] 4956 (1980).

2 C.A. Randall, D.J. Barber and R.W. Whatmore, "Ferroelectric Domain Configuration in a Modified PZT Ceramic," *J. Mat. Sci.*, **22** 925 (1987).

3 V.A. Bova and I.E. Myl'nikova, "Ferroelectric Properties of Monocrystals of New Perovskite Compounds," *Soviet Physics-Solid State,* **2** [11] 2428 (1961).

4 N.P. Khuchua, V.A. Bova and I.E. Myl'nikova, "Dielectric Properties of $Pb(Zn_{1/3}Nb_{2/3})O_3$, a Ferroelectric with an Indistinct Phase Transition," *Soviet Physics-Solid State,* **10** [1] 194 (1968).

5 J. Kuwanta, K. Uchino and S. Nomura, "Phase Transitions in $Pb(Zn_{1/3}Nb_{2/3})O_3$-$PbTiO_3$ System," *Ferroelectrics,* **37** 579 (1981).

6 Y. Yokomizu, T. Takahashi and S. Nomura, "Ferroelectric Properties of $Pb(Zn_{1/3}Nb_{2/3})O_3$,"*J.Phys.Soc.Jpn.* **28** [5] 1278 (1970).

7 J. Kuwanta, K. Uchino and S. Nomura, "Diffuse Phase Transition in Lead Zinc Niobate," *Ferroelectrics*, **22** 863 (1979).

8 K. Kato, K. Suzuki and K. Uchino, *J. Jpn. Ceram. Soc.*, **98** 840 (1990).

9 R. Ujiie and K. Uchino, "Dynamical Domain Observation in Relaxor Ferroelectrics," *IEEE Proceedings*, Hawaii (1990).

ACKNOWLEDGMENTS

The authors would like to thank Drs. R.P. Brodeur and C.A. Randall for their insightful discussions.

LIST OF FIGURES

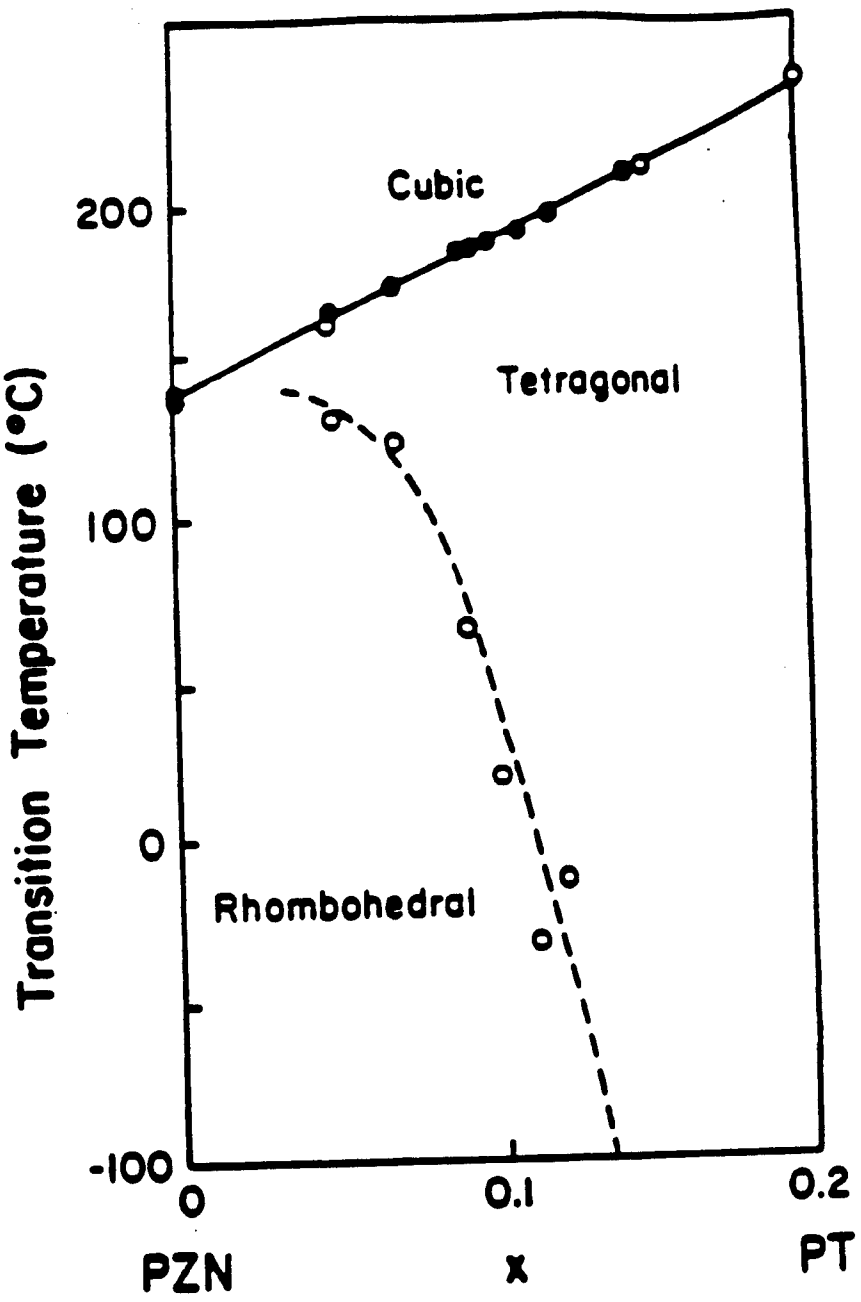

Figure 1: Phase diagram of the $Pb(Zn_{1/3}Nb_{2/3})O_3$-$PbTiO_3$ solid solution system taken from Kuwanta et al.[5]

2a.

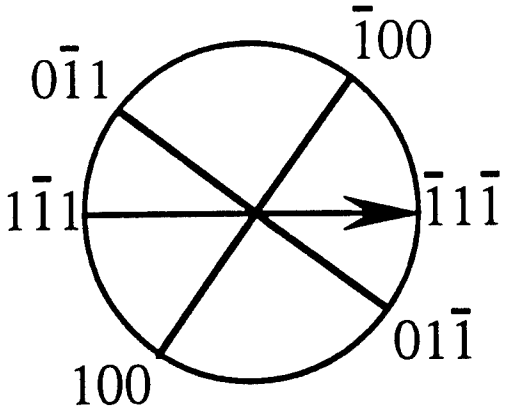

2b.

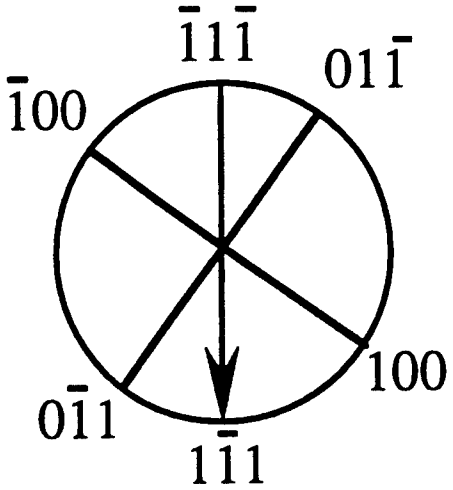

Figure 2: Illustration of the stereographic projection on the (011) plane. 2a) The <111> goes from right to left. 2b) The <111> goes from top to bottom.

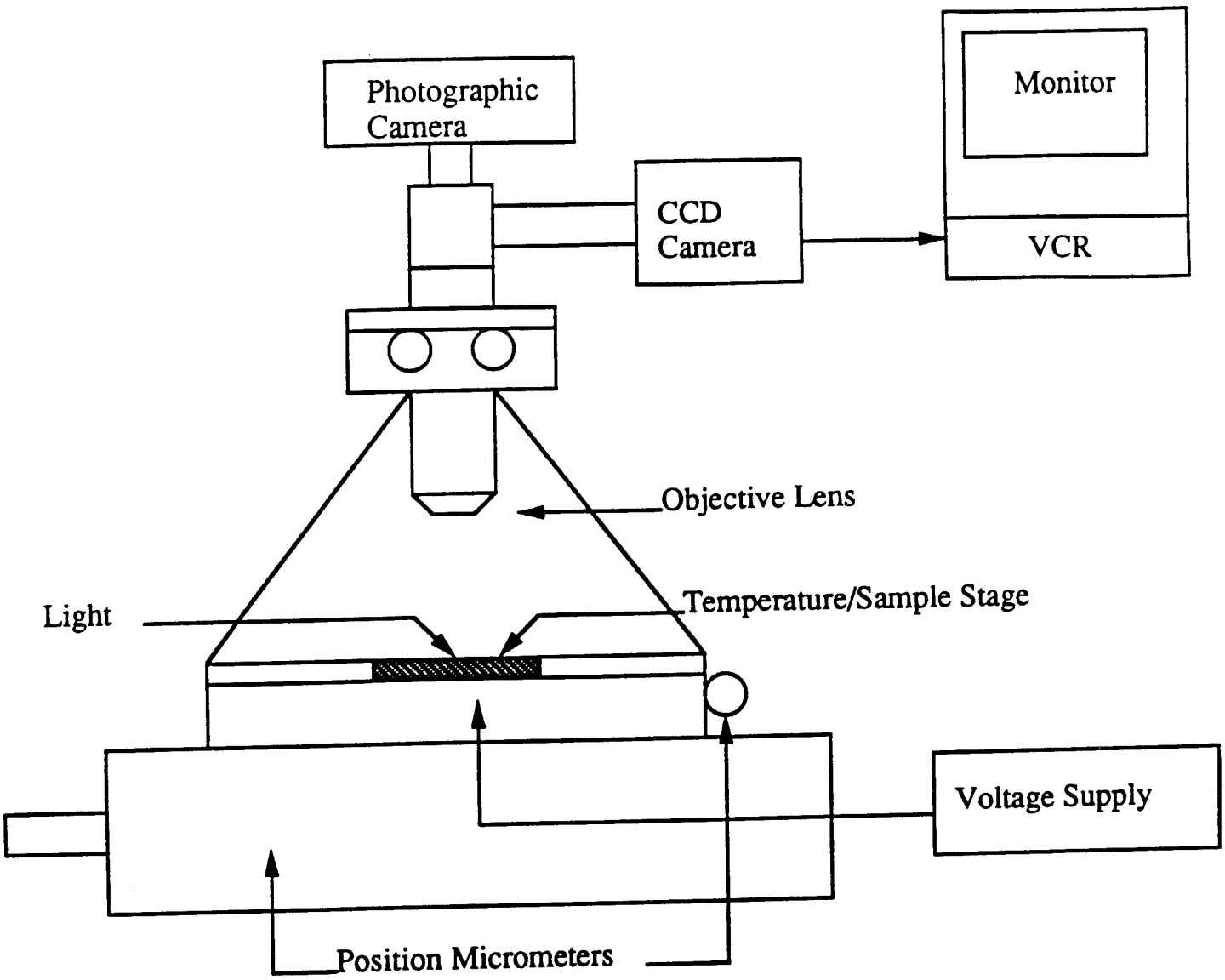

Figure 3: Illustrates the ICAT CCD Microscope System at the Materials Research Laboratory, Pennsylvania State University.

4a

4b

4c

4d

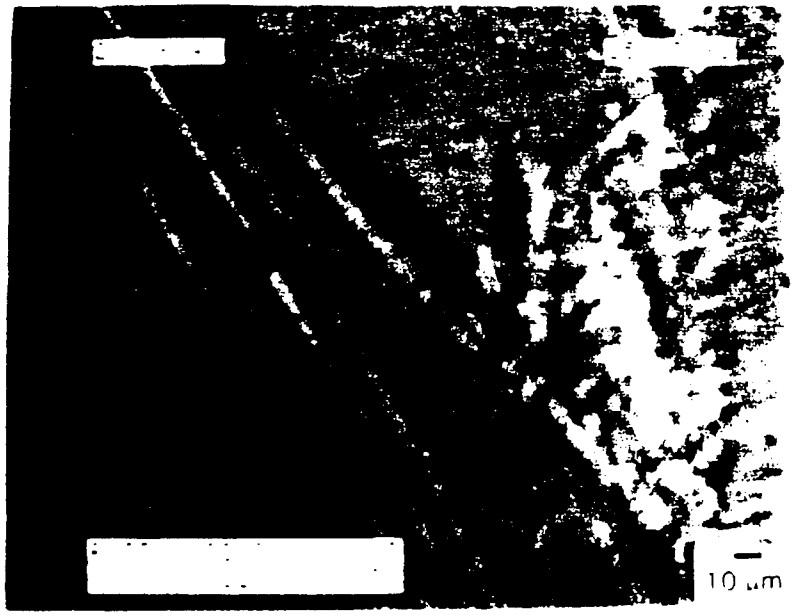

4e

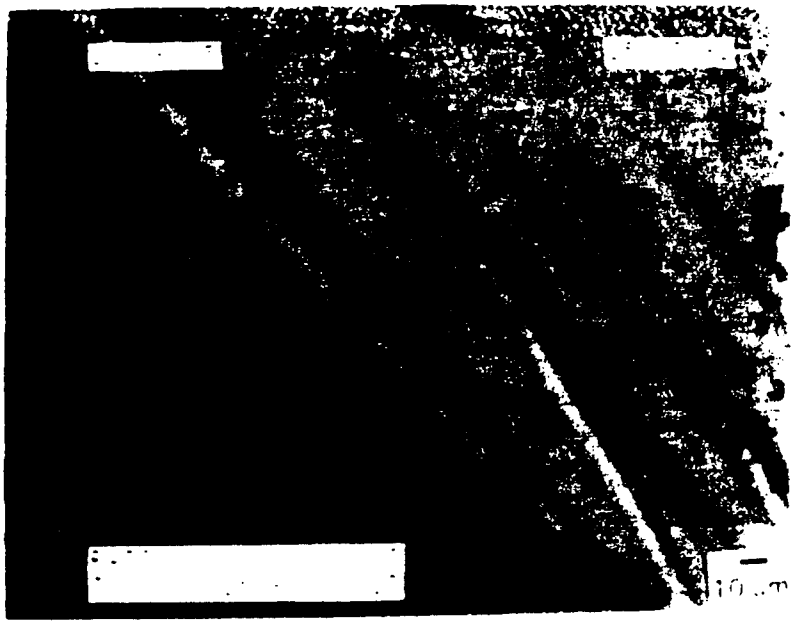

Figure 4: The domain change with temperature for a 0.905/0.095 PZN-PT composition. a) -8°C b) -17°C c) -20°C d) -22°C e) -25°C.

5a

5b

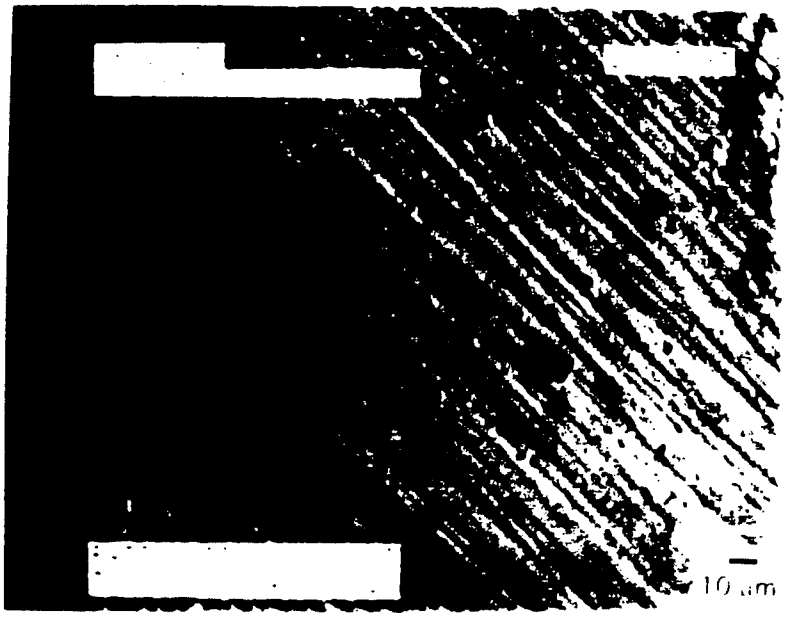

5c

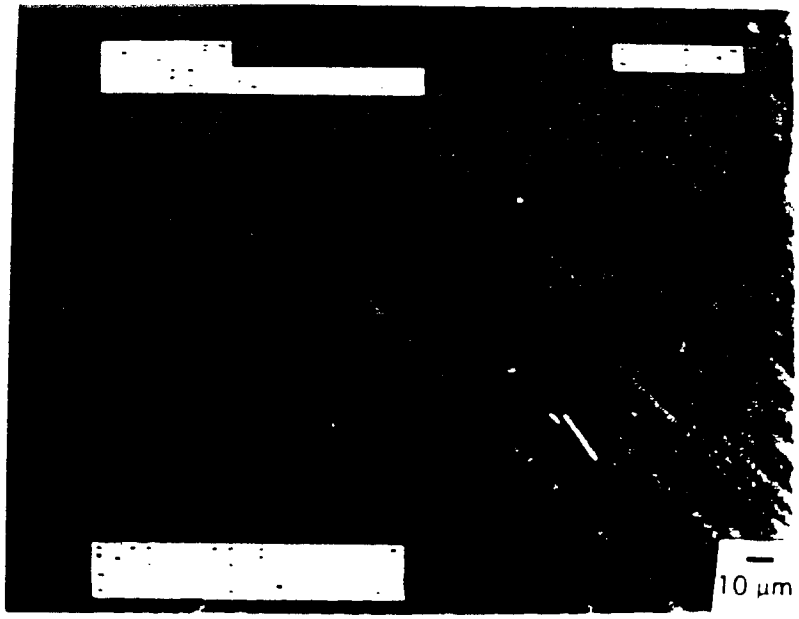

5d

Figure 5: The domain change with electric field at 28°C for a 100 percent PZN single crystal. a) -4.5kV/cm b) 2.5kV/cm c) 5kV/cm d) -4.5kV/cm.

(b)

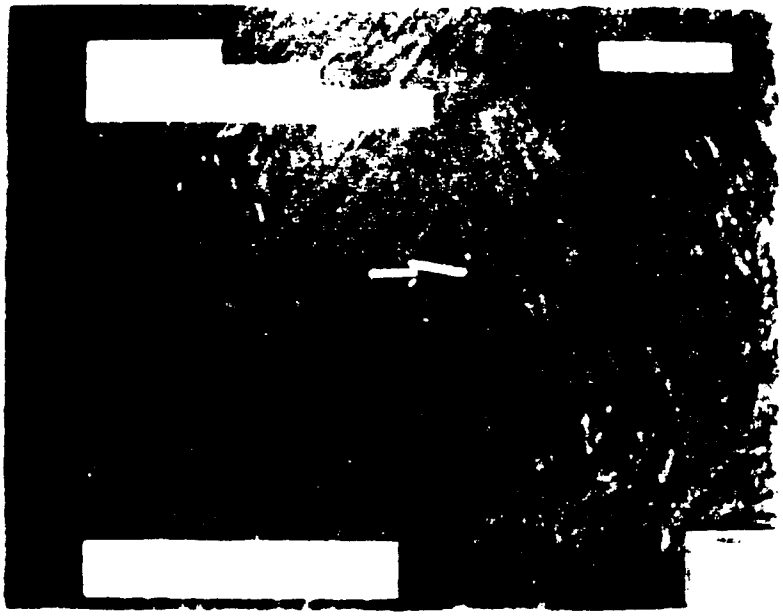

(c)

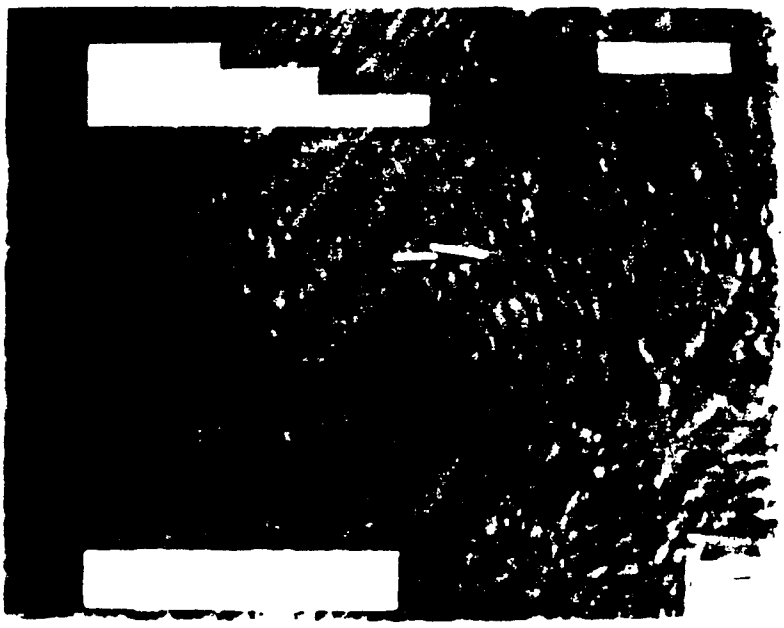

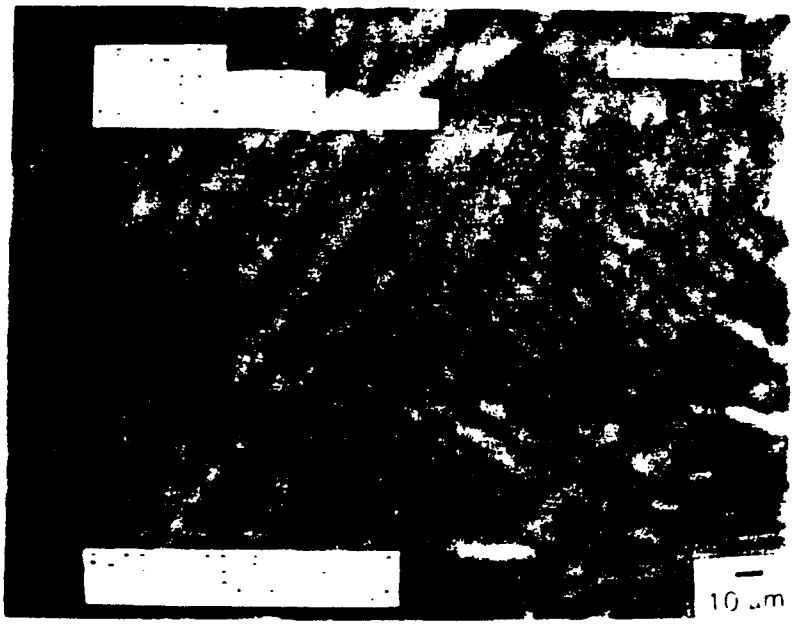

Figure 6: The domain change under an applied electric field of +/-7.5 kV/cm with changing temperature for a 100 percent PZN single crystal. a) -114°C b) -85°C c) -70°C d) -53°C e) -36°C.

7a

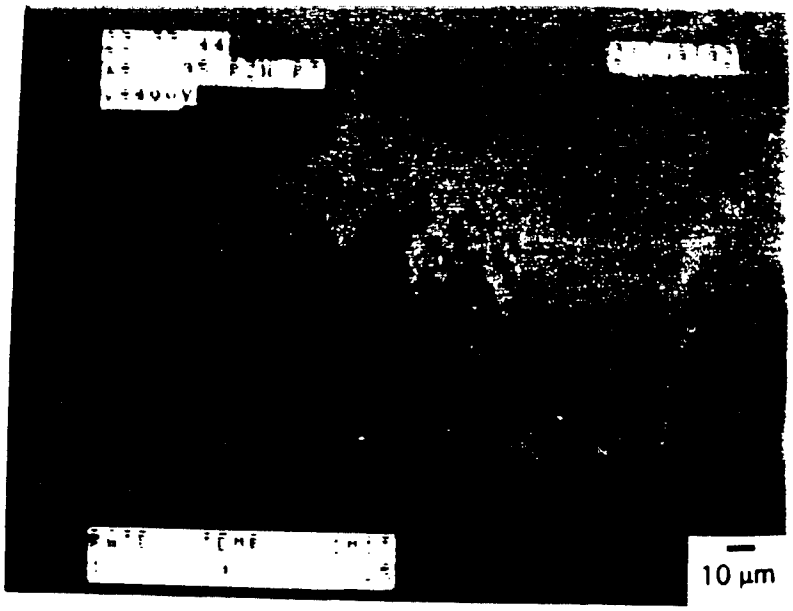

7b

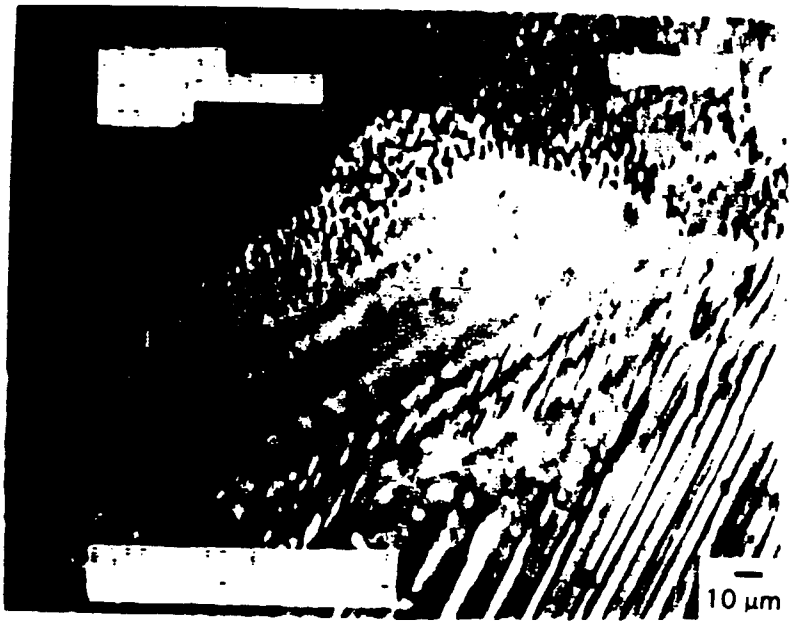

7c

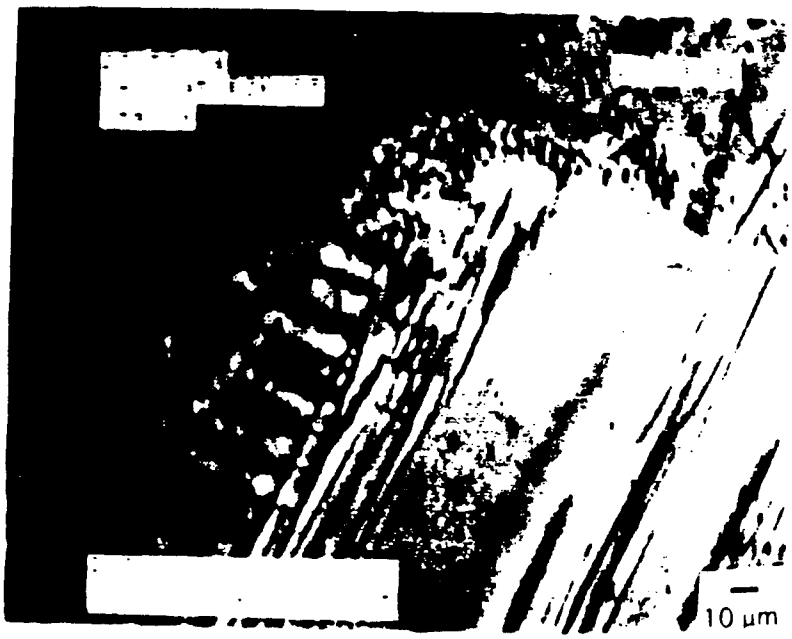

7d

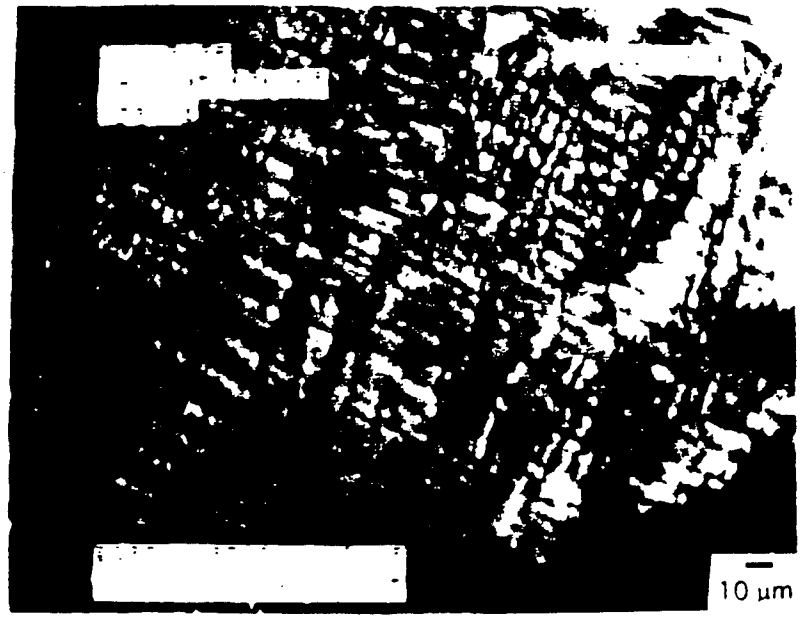

7e

Figure 7: The domain change under an applied electric field of +/-7.5 kV/cm with changing temperature for a 0.905/0.095 PZN-PT single crystal. a) 191°C b) 53°C c) -4°C d) -66°C e) -119°C.

APPENDIX 50

ELECTROOPTIC CERAMICS AND THEIR DISPLAY APPLICATIONS

Kenji UCHINO

International Center for Actuators and Transducers
Materials Research Laboratory
The Pennsylvania State University
University Park, PA 16802, USA

Relaxor ferroelectrics are remarked in non-linear optic applications because an extraordinarily large apparent "electrooptic Kerr effect" can be observed even in the so-called paraelectric state. This paper describes the fundamental electrooptic properties of perovskite-type polycrystalline and single crystals, $Pb(Zn_{1/3}Nb_{2/3})O_3$, $(Pb,La)(Zr,Ti)O_3$ and $Pb(Mg_{1/3}Nb_{2/3})O_3$-$PbTiO_3$, firstly. Then, a new type of two-dimensional light valve array for an image projector is introduced. A light shutter array with 10x10 pixels was fabricated by a sophisticated tape casting technique. Plate-through and separate electrodes are stacked alternately so as to make vertical addressing by an external electrode connecting separate electrodes and horizontal addressing by a plate-through electrode. The applicative feasibility to a high definition image projector was verified.

1. INTRODUCTION

The electrooptic effect, which is the refractive indices change with an external applied electric field, will provide very promising useful devices such as light valves, deflectors, displays etc. in the next optical communication age, in conjunction with solid state laser chips and optical fibers. Compared with liquid crystal devices, the ceramic electrooptic components, in general, possess advantages in response speed (μsec), particularly in falling time, durability for strong light illumination and contrast ratio (10^2) /gray scale (16 scales). On the other hand, the present ceramic components require relatively high drive voltage (1 kV) and production cost ($ 100). Therefore, the development of a simple mass-production process and designing of electrode configurations with a narrow gap, as well as the improvement of material properties, will be the key factors to the actual commercialization of the ceramic optical components.

Let us review the principle of a light shutter utilizing the second-order electrooptic effect (Kerr effect), initially. The birefringence Δn is induced in a crystal when an electric field E is applied:

$$\Delta n = - (1/2) R n^3 E^2, \qquad (1)$$

where $R (= R_{11} - R_{12})$ is the quadratic electrooptic coefficient and n is the original refractive index of the crystal. When this sample is placed between crossed polarizers arranged at the 45 direction with respect to the E direction, and light is transmitted transversely to the E field (Fig. 1), the output light intensity is represented by

$$I = I_0 A \sin^2[(R n^3 L / 2 \lambda) E^2], \qquad (2)$$

where I_0 is the incident light intensity, A an equipment constant, L the optical path length (i. e. the sample thickness), and λ is the wavelength of the light. The voltage required for the first intensity maximum is an essential device parameter and called the half-wavelength voltage.

This paper describes the fundamental electrooptic propertiesof relaxor ferroelectrics, firstly, searching the possibility of new electrooptic materials. Then, the experimental data are given in detail on the $Pb(Mg_{1/3}Nb_{2/3})O_3$-$PbTiO_3$ system. Finally, a new type of two-dimensional light valve array for an image projector is introdued, which can be mass-produced by a sophisticated tape casting technique. The drive voltage has been remarkably reduced, and FET's can be used directly for operation. This device will be a good candidate for the future high definition image projector.

2. CERAMIC ELECTROOPTIC MATERIALS

2.1. $Pb(Zn_{1/3}Nb_{2/3})O_3$

Relaxor ferroelectrics are remarked in non-linear optic applications because an extraordinarily large apparent "electrooptic Kerr effect" can be observed even in the so-called paraelectric state. Figure 2 shows the birefringence Δn versus electric field E relation of a $Pb(Zn_{1/3}Nb_{2/3})O_3$ single crystal in the paraelectric phase.[1] The single crystal sample was made by a flux method using excess PbO. The parabolic curve in the low field region tends to approach a straight line in the high field region.

A possible phenomenological analysis of this peculiar phenomenon is based on the model that the crystal is composed of the ferroelectric and paraelectric phases mixed together.[1] Suppose that the volume fraction of the paraelectric phase x(T) is given by the accumulated Gaussian distribution with respect to temperature, the birefringence Δn is estimated by the summation of linear and quadratic electrooptic effects:[2]

$$\Delta n = [1 - x(T)]\, n^3(r_{33} - r_{13})\, E/2 + x(T)\, n^3 R_{44}\, E^2/2, \qquad (3)$$

where n is the refractive index, and r and R represent electrooptic Pockels and Kerr coefficients, respectively. Even if the experimental data can be explained phenomenologically, the actual situation may not be so simple as this model: x(T) should be also a function of electric field E.

Another more realistic explanation is found in a microscopic domain reversal mechanism. $Pb(Zn_{1/3}Nb_{2/3})O_3$ exhibits very small spindle-like domains (5 μm) with ambiguous boundaries arranged perpendicularly to the external electric field. When the field above 0.5 kV/mm is applied, the ambiguous curve domain wall[illegible]oves simultaneously in a certain size region, so that each micro-domain should change synchronously like [illegible]operative phenomena (See Fig. 3).[3] It is noteworthy that the stripe period of the dark and bright doma[illegible](corresponding to up and down polarizations) will not be changed by the domain reversal, and that each domain area changes under an AC external field with zero net polarization at zero field. The relaxor crystal can be electrically-poled easily when an electric field is applied around the transition temperature, and depoled completely without any remanent polarization. This can explain large "apparent" secondary non-linear effects in physical properties such as electrostrictive and electrooptic Kerr phenomena, without exhibiting any hysteresis.

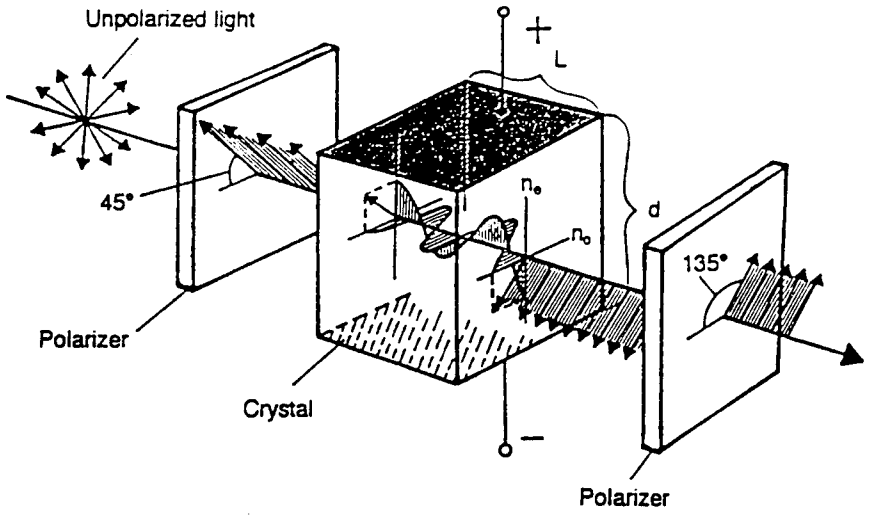

FIGURE 1
Fundamental construction of an electrooptic light shutter.

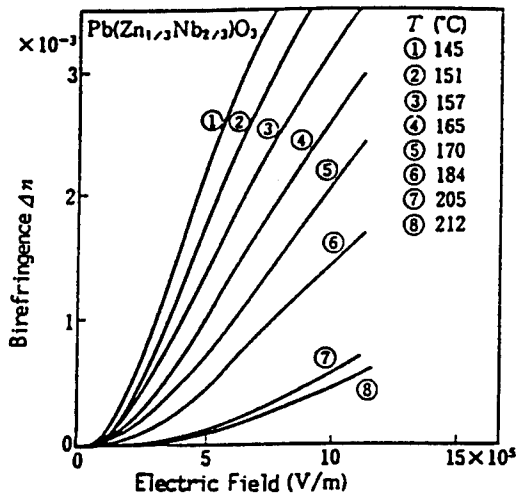

FIGURE 2
Birefringence vs. field in the paraelectric $Pb(Zn_{1/3}Nb_{2/3})O_3$.

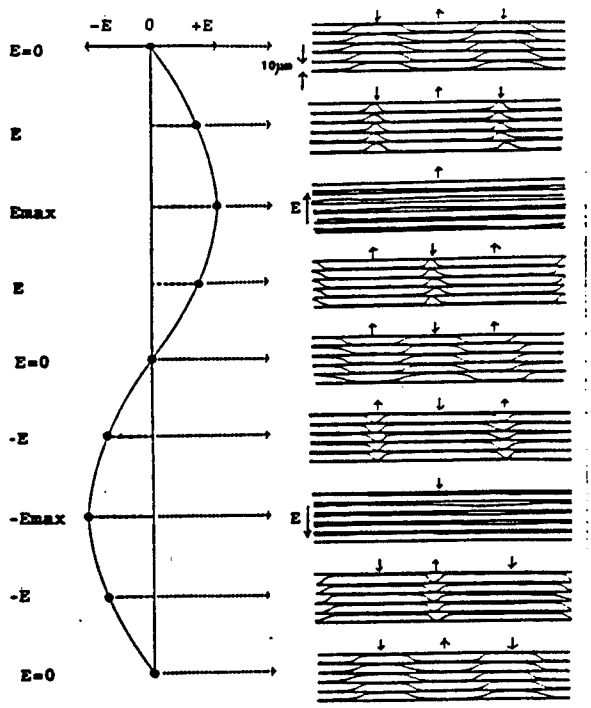

FIGURE 3
Domain reversal mechanism in $Pb(Zn_{1/3}Nb_{2/3})O_3$.

Lines to bottom single-spacing (for footnotes)

Lines to bottom single-spacing

2.2. $(Pb,La)(Zr,Ti)O_3$

Famous transparent ceramics PLZT, i. e. $(Pb_{1-x}La_x)(Zr_yTi_z)_{1-x/4}O_3$, are also an example of relaxor ferroelectrics, which exhibit large electooptic effect ($R = 9.1 \times 10^{-16}\ m^2V^{-2}$) near the composition 9/65/35 and are applicable to practical light shutters, displays etc.

However, care must be taken for grain size control. Figure 4 shows the grain size dependence of the electrooptic coefficients, R and g (defined as $\Delta n = -(1/2)g\, n^3P^2$), in PLZT 9/65/35.[4] The samples were prepared by hot-press sintering starting from coprecipitated PLZT powders. The electrooptic response is drastically decreased below 2 μm, which corresponds approximately to the critical grain size below which the sample exhibits paraelectric properties.[5] Therefore, relatively large grain size is necessary to reveal the reasonable electrooptic effect.

On the other hand, a serious problem arises in fracture toughness or durability for particularly large grain size samples, probably due to the deficient (B-site vacancy) crystal structure. A normally sintered transparent PLZT ceramic with an average grain size more than 6 μm has fracture toughness of $K_{IC} = 0.9\ MNm^{-3/2}$,[5] which corresponds roughly to 10^8 cycles durability under repeating operation. This means only 2 months durability when the PLZT is used for an image display (TV)driven at 30Hz.

2.3. $Pb(Mg_{1/3}Nb_{2/3})O_3$-$PbTiO_3$

Discovery of a new ceramic electrooptic material with higher fracture toughness as well as larger electrooptic coefficients will be an urgent necessity for image display applications. The following conditions should be satisfied for the ceramic: 1) ceramic transparency requires almost zero birefringence in the original state (i. e. a pseudo-cubic structure) to suppress light scattering, 2) large fracture toughness may be obtained in a sufficiently packed structure, 3) large electrooptic effect is realized in relaxor ferroelectrics.

The $Pb(Mg_{1/3}Nb_{2/3})O_3$-$PbTiO_3$ system which is known as a superior electrostrictive (secondary effect) material with very high fracture toughness ($K_{IC} = 1.7\ MNm^{-3/2}$) may be a good candidate to investigate from an electrooptic viewpoint. Samples of the (1 - x)Pb $(Mg_{1/3}Nb_{2/3})O_3$- x $PbTiO_3$ system were prepared by hot-press sintering starting from the oxide mixtures. Note that the Curie temperature increases gradually with the $PbTiO_3$ content, passing room temperature around x = 0.12, and the crystal structure is pseudo-cubic in the region below x = 0.4. Figure 5 shows the composition x dependence of light transmittance (λ = 633 nm) of a 0.5 mm thick sample in the (1 - x) $Pb(Mg_{1/3}Nb_{2/3})O_3$- x $PbTiO_3$ system. The transmittance is reduced drastically above x = 0.14, probably due to the scattering caused by the spontaneous birefringence. The best transmittance 49 % is still smaller than 62% in the conventional PLZT; this suggests that more sophisticated powder preparation technique will be required for the PMN-PT. The refractive index n (λ = 633 nm) change with x is plotted in Fig. 6, which shows a small maximum around x = 0.12. The values are slightly larger than n = 2.49 in PLZT 10/65/35. The most intriguing data can be found in electrooptic measurements. Figures 7(a) and 7(b) show the electrooptic R coefficient and its corresponding hysteresis for λ = 633 nm, respectively, plotted as a function of composition x. The maximum electrooptic R coefficient of $22 \times 10^{-16}\ m^2V^{-2}$ for x = 0.12 is more than twice larger than $9.1 \times 10^{-16}\ m^2V^{-2}$ in the famous PLZT

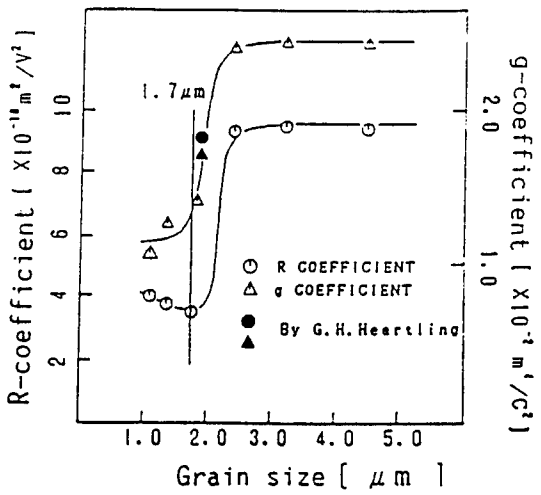

FIGURE 4
Grain size dependence of the electrooptic coefficients, R and g, in PLZT 9/65/35.

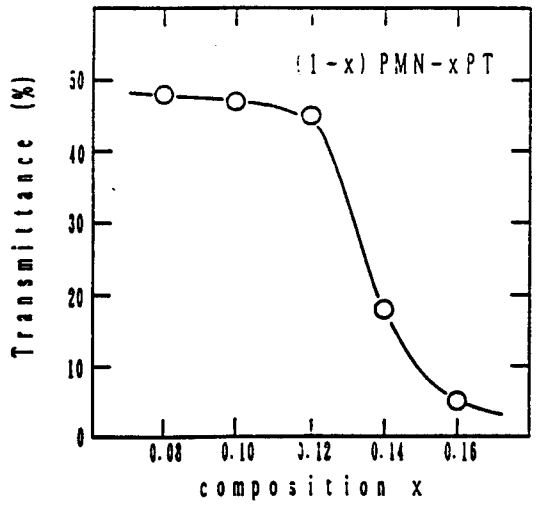

FIGURE 5
Transmittance of a 0.5 mm thick sample for $\lambda = 633$ nm in (1 - x) $Pb(Mg_{1/3}Nb_{2/3})O_3$- $xPbTiO_3$.

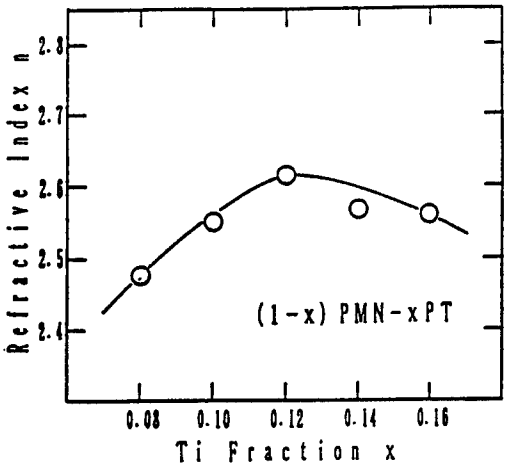

FIGURE 6
Refractive index change in (1 - x) $Pb(Mg_{1/3}Nb_{2/3})O_3$- $xPbTiO_3$.

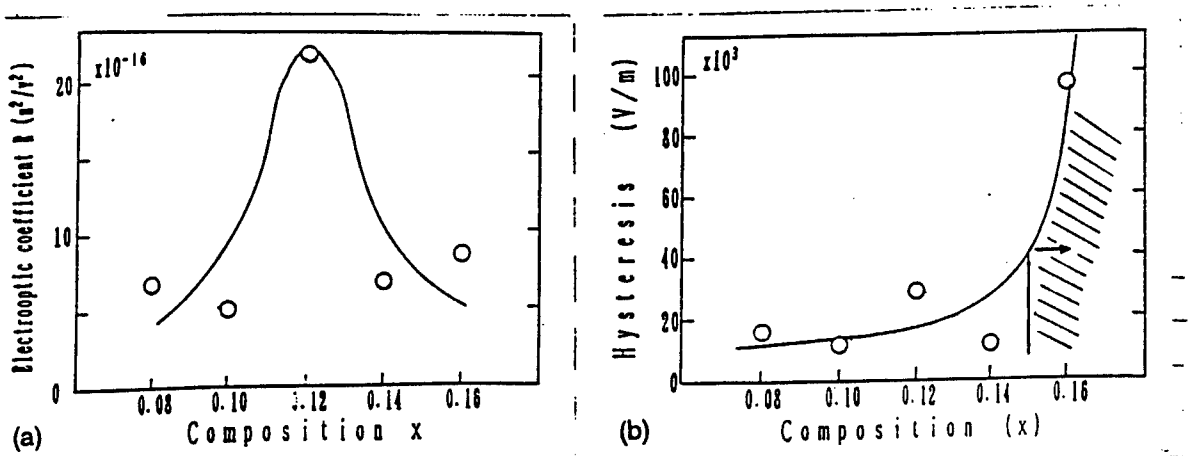

FIGURE 7
Changes in the electrooptic coefficient R (a) and the corresponding hysteresis (b) in (1 - x)$Pb(Mg_{1/3}Nb_{2/3})O_3$- $xPbTiO_3$.

9/65/35. The hysteresis, defined as an equivalent bias electric field to fit the experimental Δn curve by the quadratic relation of E, increases drastically above x = 0.16, the samples in which region can not be used practically.

In conclusion, $0.88Pb(Mg_{1/3}Nb_{2/3})O_3$-$0.12PbTiO_3$ will be the better electrooptic ceramic with high mechanical toughness, if the better light transmission is obtained by improving the preparation technology.

3. TWO-DIMENSIONAL DISPLAYS

This section deals a concept of a projection type TV utilizing two-dimensional PLZT displays. The development of a simple mass-production process and the designing of electrode configurations with a narrow gap are the key factors for the PLZT displays. A newly developed design as shown in Fig. 8 presents a very bright image w ith a slight crosstalk-related problem and is easy to produce.

3.1. Fabrication Process of the 2-D Display

The fabrication process of the two-dimensional PLZT light valve array is outlined in Fig. 9.[6] Coprecipitated PLZT 9/65/35 powders were mixed with organic solvent and binder and formed into a green sheet. Platinum internal electrodes were printed on the green sheets. The electroded sheets were then laminated alternately in 90 different orientations under a pressure of 3000 psi, so as to make plate-through and separate electrodes. The laminated body was sintered in an oxygen-controlled atmosphere, and the bulk was cut and polished. Finally the external connecting electrodes were applied to make vertical and horizontal addressing.

Figure10(a) shows the electrode configuration of a (10x10) matrix light valve. The shaded portion of the device in the figure represents one image unit (pixel). The vertical separate internal electrodes were connected by external electrodes printed on the surface of the device. The horizontal plate-through electrodes were embedded 100 μm deeper from the opticcal surface to avoid shorting with the vertical electrode connectors. Figure 10(b) shows a picture of the newly fabricated display. Note that the layer thickness is about 0.35 mm.

3.2. Characteristics of the light valve array

The optical transmittance of the PLZT device fabricated by the tape casting technique was62 % at λ = 633 nm, which is in good comparison with 63 % for the ideal sample prepared by hot-pressing. The brightness for red, green and blue light was measured as a function of applied voltage (Fig.11), where the electrode gap was 0.45 mm.[6] The contrast ratio defined by a ratio of brightness on the screen under the application of half-wavelength voltage over brightness under zero volt (220 cd/m^2/2.8 cd/m^2), was about 80, rather superior to the values for the conventional cathode ray tubes or liquid crystal displays. The response time associated with a single pixel of the display was less than 10 μsec for both rising and falling processes, which is rapid enough to drive this shutter array at a raster frequency of the conventional CRT's.

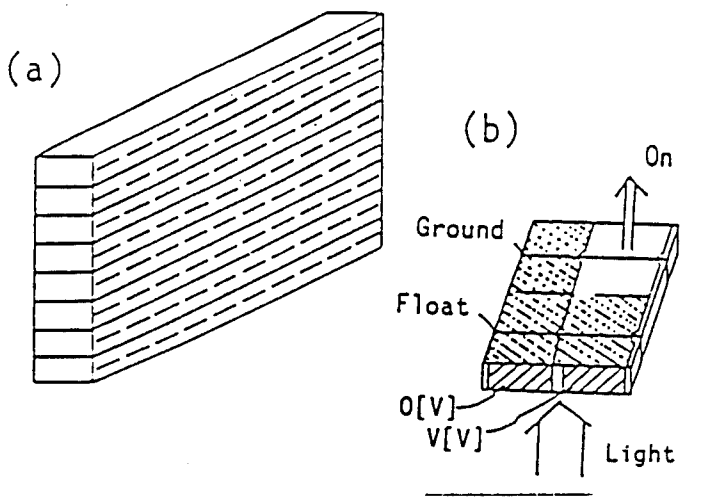

FIGURE 8
Newly developed design of a 2-dimensional display.

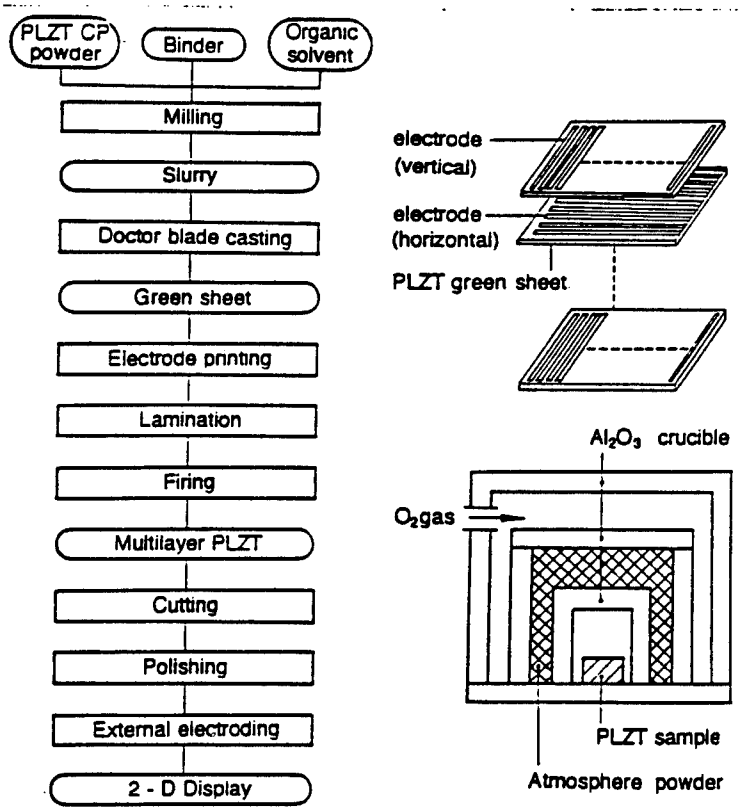

FIGURE 9
Fabrication process of the new 2-D display.

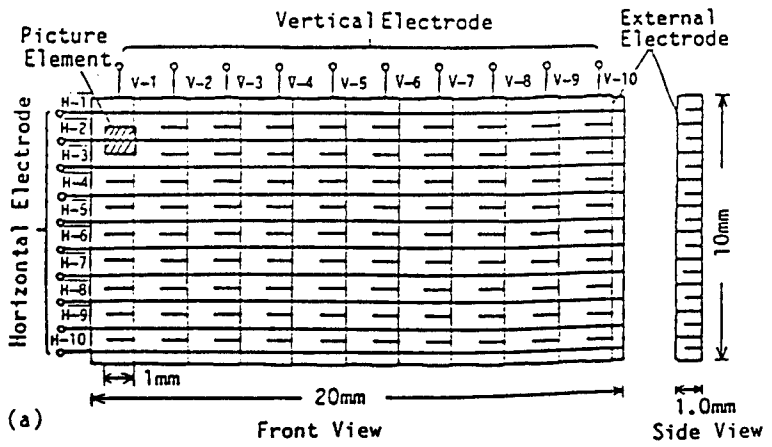

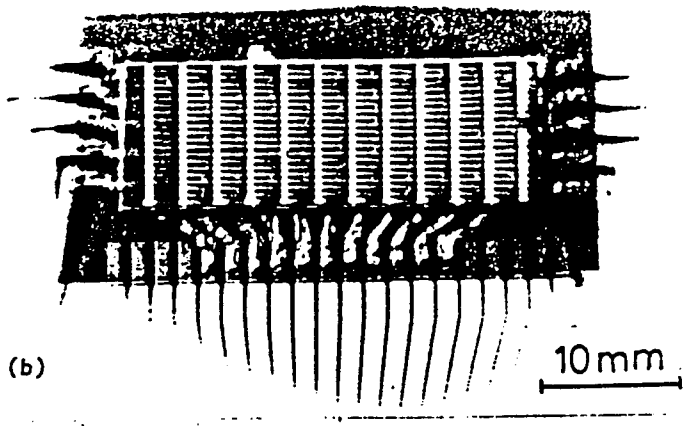

FIGURE 10
(a) Schematic electrode configuration of a (10x10) matrix PLZT light valve.
(b) Top view photograph of a PLZT light valve with external electrodes.

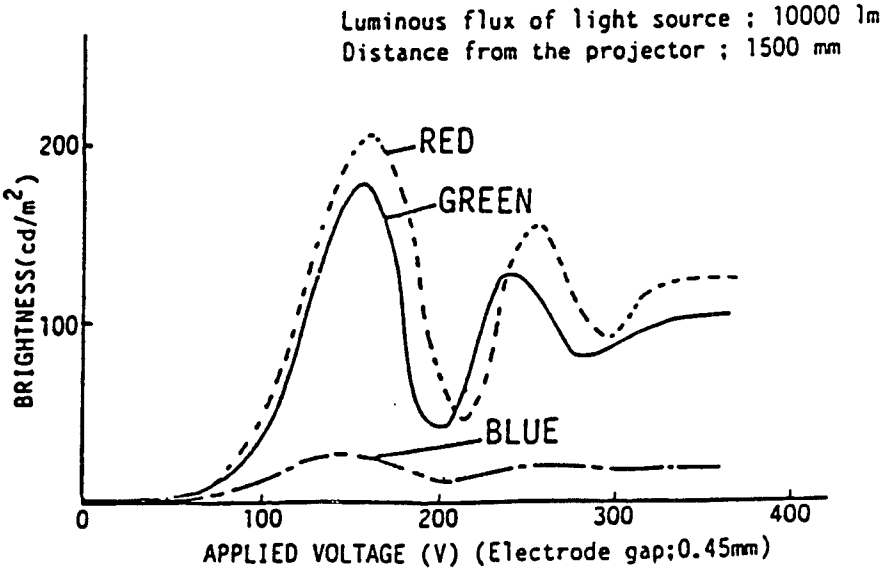

FIGURE 11
Brightness on the screen vs. applied voltage for red, green or blue light.
Note that the half-wavelength voltage differs for these three lights.

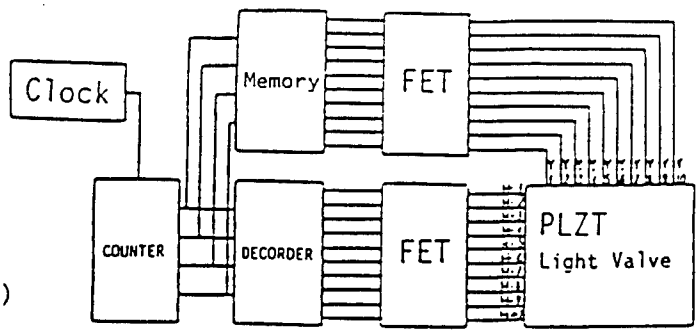

(a)

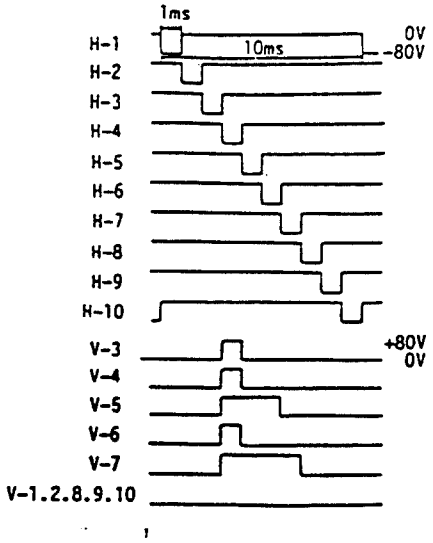

(b)

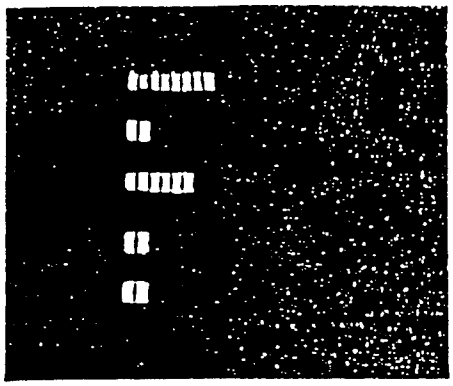

(c)

FIGURE 12
(a) Driving circuit of the 2-D display. (b) Example wave forms of the driving signal.
(c) An example image "F" on the screen illuminated from the PLZT projector.

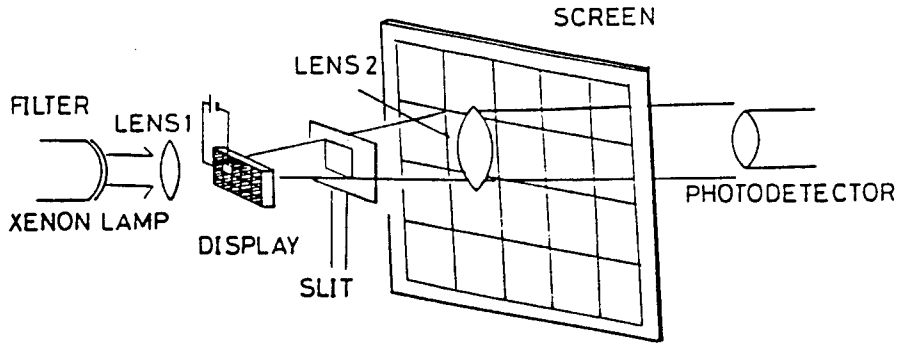

FIGURE 13
Crosstalk test system. The light through a slit focused on the screen is measured.

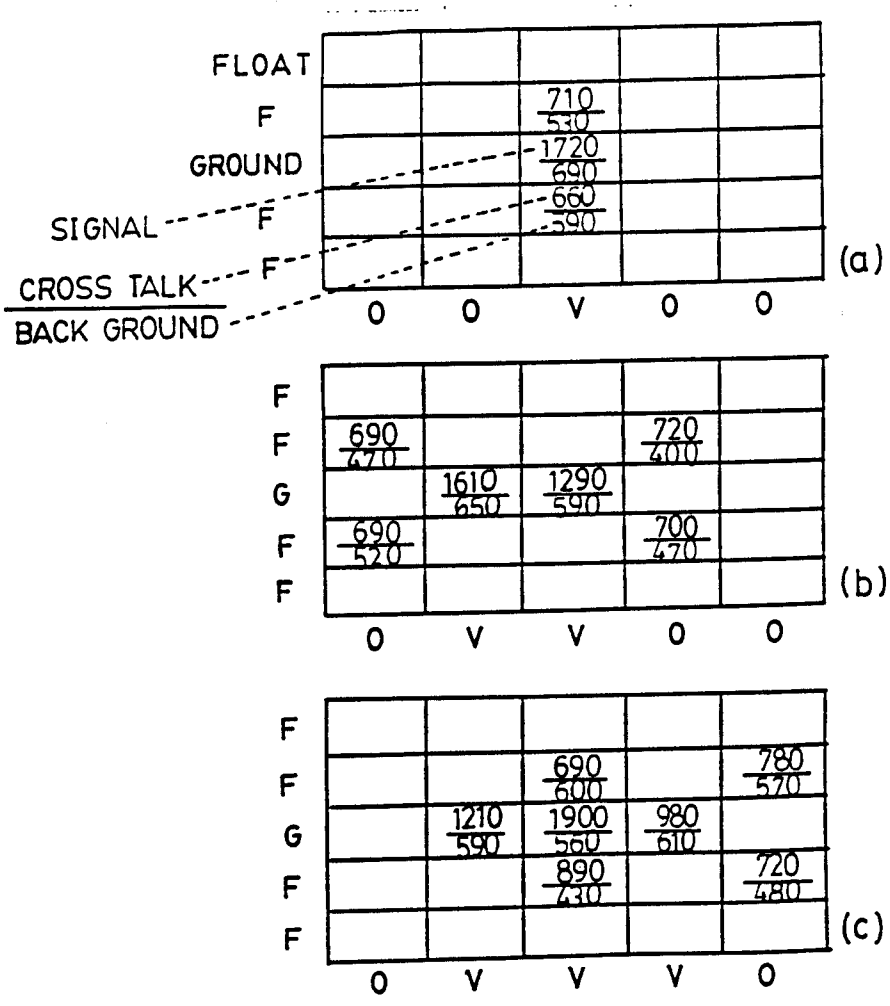

FIGURE 14
Crosstalk patterns for different signal addressing:
(a) vertical type, (b) oblique type and (c) complex type.

3.3. Construction of the Image Projector

The driving circuit of the display is represented schematically in Fig. 12(a). When the terminals of the device are addressed as shown in Fig. 12(b), the image appearing in Fig. 12(c) (alphabet "F") is generated on the screen.[6)]

Crosstalk phenomenon was checked on the 2-D display using a setup as illustrated in Fig. 13 with monochromatic light. The test was made with keeping one vertical terminal on (Ground) and applying high voltage on mutiple horizontal terminals. There are three different cross talk patterns: vertical, horizontal and oblique types. The results are shown in Fig. 14(a)-(c) for the different input number of horizontal terminals, where the top and bottom of a pair of figures indicate the light intensity in μW unit on the screen in ON state and OFF state, respectively. The leakage light intensity associated with the vertical or horizontal crosstalk is 20 -30 % or 10 - 20 % of the main peak intensity, which does not affect the image contrast significantly. On the contrary, the oblique type crosstalk causes unnegligible leakage up to 50 % depending on the applied voltage and the number of horizontal addressing input signal (combination type crosstalk). Modification of the internal electrode configurations will be necessary to avoid the crosstalk problem completely.

4. CONCLUSIONS

1. Relaxor ferroelectrics are widely applicable to electrooptic light valves/displays etc. Superior characteristics of these materials are mainly attributed to the easy poling of the ferroelectric micro-domains.

2. A new electrooptic ceramic $0.88Pb(Mg_{1/3}Nb_{2/3})O_3$-$0.12PbTiO_3$ with high mechanical toughness may provide a breakthrough for long-term display applications.

3. A new type of PLZT 2-dimensional light valve fabricated by a tape casting technique has been developed, and a prototype image projector was investigated. It is easy to mass-produce, leading to a low manufacturing cost. This light valve exhibits bright image with a negligible crosstalk-related problem. It can be driven in quick response (10 μsec) by a relatively low drive voltage (100 V/ 0.35 mm gap) in comparison with the conventional PLZT devices. The applicative feasibility to a high definition image projector was verified.

REFERENCES

1) F. Kojima, J. Kuwata and S. Nomura, Proc. 1st. Mtg. on Ferroelectric Mater. & Appl. (Kyoto, 1977) 155.

2) J. Kuwata, K. Uchino and S. Nomura, Ferroelectrics 22 (1979) 863.

3) R. Ujiie aand K. Uchino, Proc. IEEE Ultrasonic Sympl (Hawaii, 1990) 725.

4) K. Tokiwa and K. Uchino, Ferroelectrics 94 (1989) 87.

5) K. Uchino and T. Takasu, Inspec. 10 (1986) 29.

6) K. Uchino, K. Tokiwa, J. Giniewicz, Y. Murai and K. Ohmura, Ceramic Transactions 14 (Electro-Optics and Nonlinear Optic Materials) (1990) 297.

APPENDIX 51

Sensors and Materials, 5, 4 (1994) 231–240
MYU, Tokyo

S & M 0140

Humidity-Sensitive Properties of Nb_2O_5-Doped Pb(Zr, Ti)O_3

Duckchool Lee, Jaeho Yuk, Neungheon Lee[1] and Kenji Uchino[2]

Department of Electrical Engineering, Inha University, 253 Yonghyun-dong, Nam-gu, Inchon 402-751, S. Korea
[1]Department of Electronic Engineering, Kyungwon University, San 65, Bokjung-dong, Soojung-gu, Seongnam, Kyunggi-do, 461-701, S. Korea
[2]International Center for Actuators and Transducers, Materials Research Laboratory, Pennsylvania State University, University Park, Pennsylvania 16802 U.S.A.

(Received February 15, 1993; accepted October 25, 1993)

Key words: humidity sensitivity, open porosity, proton

Humidity-sensitive devices of $Pb(Zr_{0.52}Ti_{0.48})O_3$ + 4 mol% Nb_2O_5 were fabricated and their sensitivity was measured. The change of electrical conductivity with water adsorption is caused by ionic conduction in which the conducting carriers are protons. Humidity sensitivity is affected by the open porosity of the ceramic, and the open porosity and the adsorption rate decrease with increasing sintering temperature. The sensitivity is stable in a wide temperature range, and the hysteresis in one humidity cycle is negligible.

1. Introduction

Humidity sensors utilize the change of electrical parameters with humidity adsorption, and have been made of materials such as electrolytes,[1] organic polymers[2,3] and ceramics. Among them, ceramic humidity sensors form a majority because ceramics are essentially more stable physically, chemically and thermally than other materials.[4–6]

In this study, humidity sensitivity has been investigated in Nb_2O_5-doped Pb(Zr, Ti)O_3 ceramics, which were originally developed as a monomorph device (semicon-

ductive piezoelectrics).[7]

2. Experimental

The specimens were prepared by means of a solid-state reaction method, which

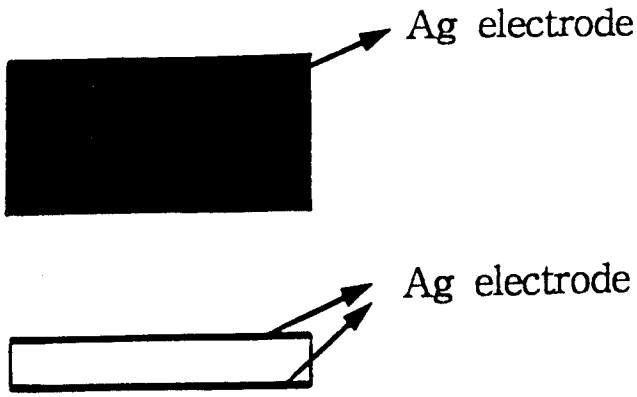

Fig. 1. Schematization of electrode geometry.

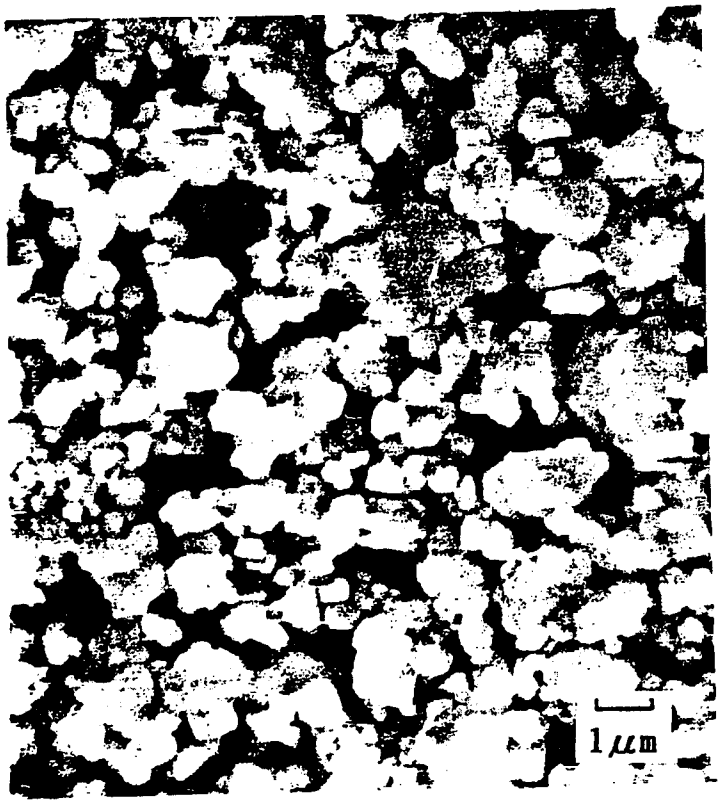

Fig. 2. Microstructure of the specime· d at 1000 for 2 h.

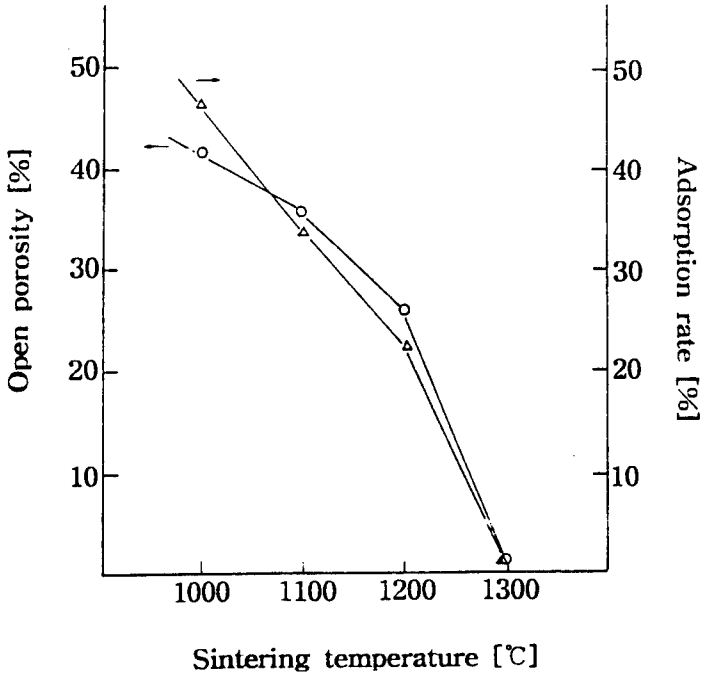

Fig. 3. Open porosity and adsorption rate as functions of sintering temperature.

is easy in terms of process control and conducive to mass production. The raw materials of PbO, ZrO_2, TiO_2 and Nb_2O_5 were ball-milled in ethyl alcohol for 24 h. The mixed powders were then dried and calcined at 850°C for 2 h. The calcined powders, $Pb(Zr_{0.52}Ti_{0.48})O_3$ doped with 4 mol% Nb_2O_5, were remilled in distilled water for 12 h, redried and sieved through a 170-mesh screen. Pressed into plates under a pressure of 1 ton/cm^2, the specimens were sintered in air at various temperatures ranging from 1000°C to 1300°C for 2 h.

The microstructures of the specimens were observed by means of scanning electron microscopy. Ag paste was painted on each side of specimens of 12 mm (length) × 6 mm (width) × 0.7 mm (thickness) and fired at 600°C for 10 min.

The resistance and capacitance change with adsorption of water were determined using an LF impedance analyzer (HP4192A). The ambient atmosphere (temperature and relative humidity) was controlled by a thermostatic humidity generator (HC7005, Heraeus Vötsch). The open porosity and the adsorption rate were calculated using eqs. (1) and (2):[8]

$$\text{Open porosity (\%)} = \frac{W_3 - W_1}{W_3 - W_2} \times 100 \tag{1}$$

and

$$\text{Adsorption rate (\%)} = \frac{W_3 - W_1}{W_1} \times 100, \tag{2}$$

where W_1, W_2 and W_3 represent dry weight (g), water-saturated weight in water (g) and water-saturated weight in air (g), respectively.

3. Results and Discussion

3.1 *Microstructure*

The microstructure of the specimen sintered at 1000°C for 2 h is shown in Fig. 2. The specimen is very porous, which is essential for humidity sensing.[9] The doping of Nb may inhibit grain growth.[7] The variations of the open porosity and the adsorption rate with sintering temperature are shown in Fig. 3. Both the porosity and adsorption rate decrease with increasing sintering temperature, as expected.

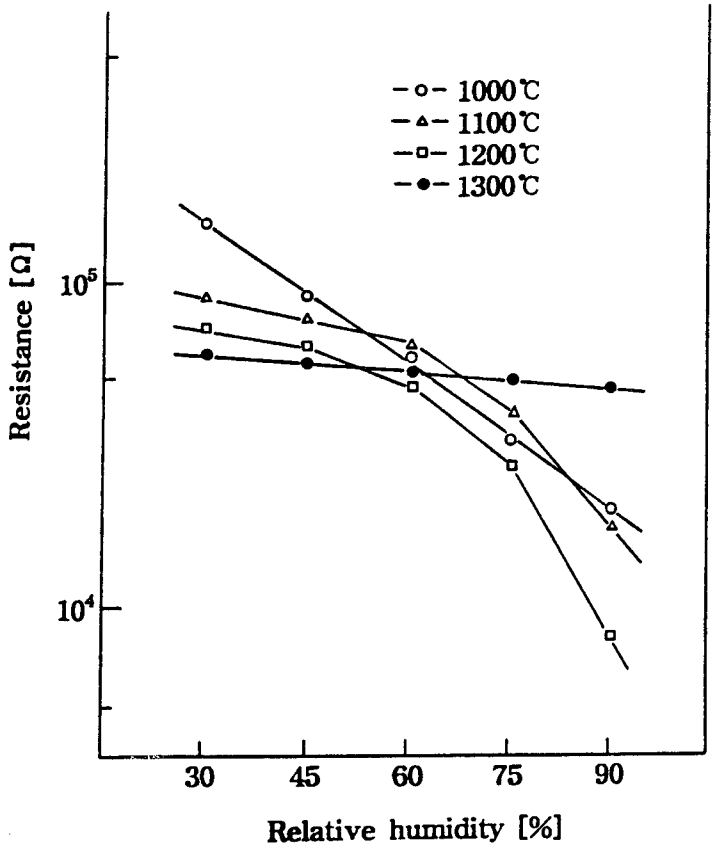

Fig. 4. Dependence of resistance on relative humidity for samples sintered at various temperatures.

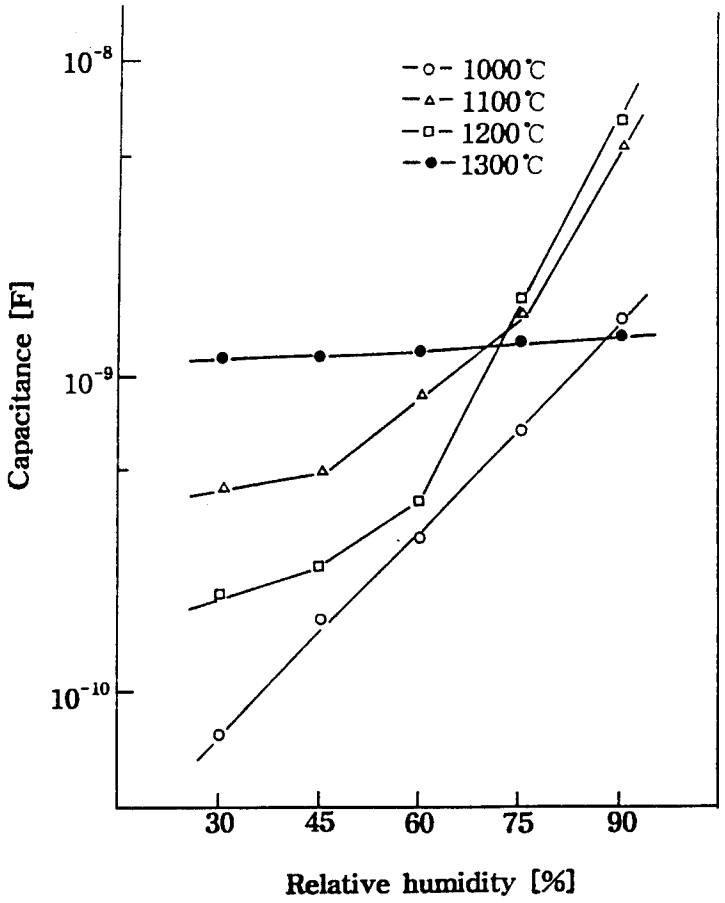

Fig. 5. Dependence of capacitance on relative humidity for samples sintered at various temperatures.

3.2 *Humidity sensitivity*

3.2.1 *Dependence on sintering temperature*

The resistance at 1 kHz and 25°C was measured as a function of relative humidity for several specimens sintered at 1000°C, 1100°C, 1200°C and 1300°C (Fig. 4). The resistance of the specimens decreases with increasing relative humidity; this is explained in terms of the model proposed by Anderson and Parks.[10] The humidity-sensing mechanism is as follows.

When a few water molecules are adsorbed, a water molecule will be physically adsorbed to form a hydroxyl group on the grain surface and a proton may be transferred from a surface hydroxyl group to a water molecule to form H_3O^+. When more water is adsorbed, clustering of the water molecules takes place forming patches of a liquidlike network of hydrogen-bonded water molecules. Since hydration of H_3O^+ into H_2O and H^+ is energetically favored in liquid water, the dominant charge carrier in high-humidity atmosphere is H^+.

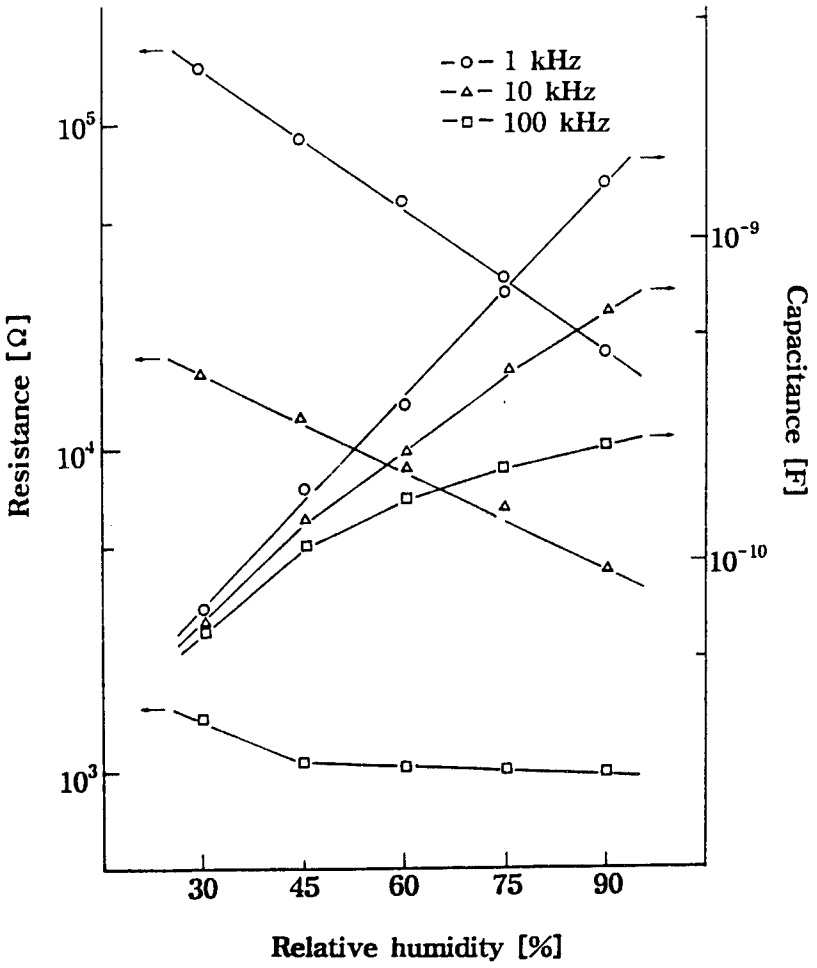

Fig. 6. Dependence of resistance and capacitance on relative humidity measured at various frequencies.

In the specimen sintered at 1000°C, the resistance decreases linearly with increasing relative humidity. On the other hand, in the specimens sintered at 1100°C and 1200°C, the resistance change in the low-humidity region is small, and the specimen sintered at 1300°C exhibits little resistance change over the entire range. The physisorption of water vapor through the pores becomes difficult because the pores disappear with increasing sintering temperature.

The capacitance of the above specimens, which was measured at 25°C and 1 kHz, is also plotted in Fig. 5. The capacitance change with the humidity is opposite that of the resistance change, but the sensitivity variation with the sintering conditions is very similar.

3.2.2 *Dependence on frequency and temperature*

The resistance and the capacitance of the specimen sintered at 1000°C were

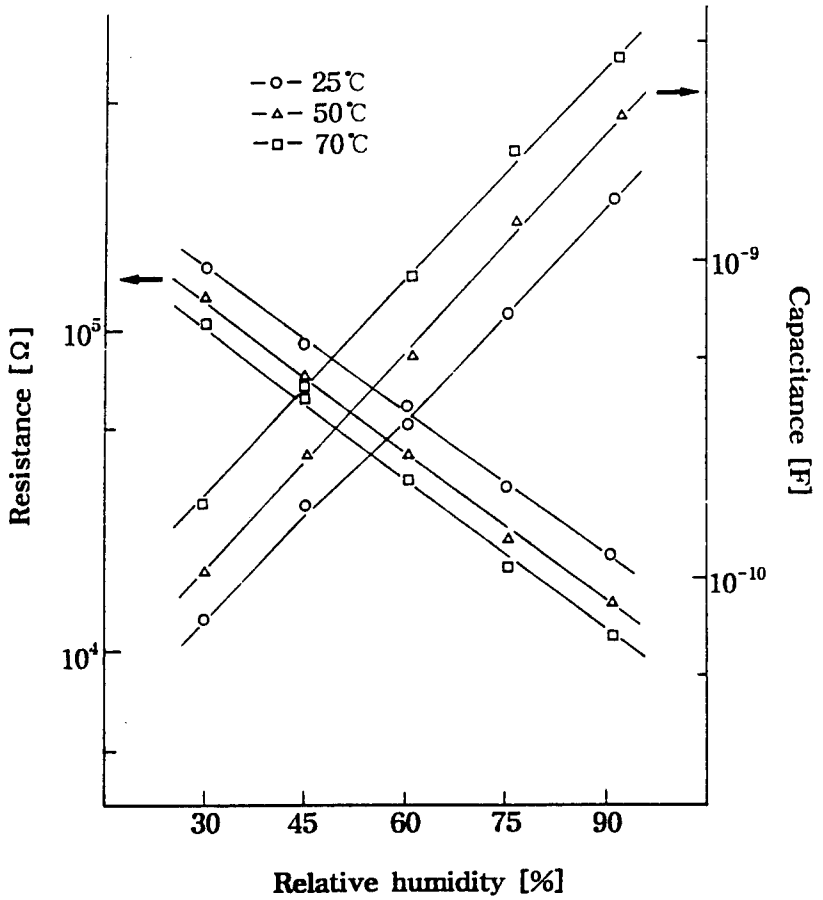

Fig. 7. Dependence of resistance and capacitance on relative humidity measured at various temperatures.

measured at 25°C for various frequencies (Fig. 6). Humidity sensitivity is higher at lower frequencies.

The temperature characteristics were also measured at 1 kHz for the specimen sintered at 1000°C (Fig. 7). Both the resistance and capacitance change show good linearity, and the slopes do not change significantly with temperature.

3.2.3 *Hysteresis and aging*

The characteristics of the resistance and capacitance with increasing and decreasing relative humidity are shown in Fig. 8. The specimen sintered at 1000°C was measured at 25°C and 1 kHz. Each point was measured 2 min after the relative humidity had stabilized. Hysteresis is negligible in both the resistance and capacitance.

This may be attributed to the fact that the effect of the variation of surface free energy of adsorbed water is negligible.[11] Furthermore, the adsorption response time (50% r.h. → 90% r.h.) and desorption response time (90% r.h. → 50% r.h.)

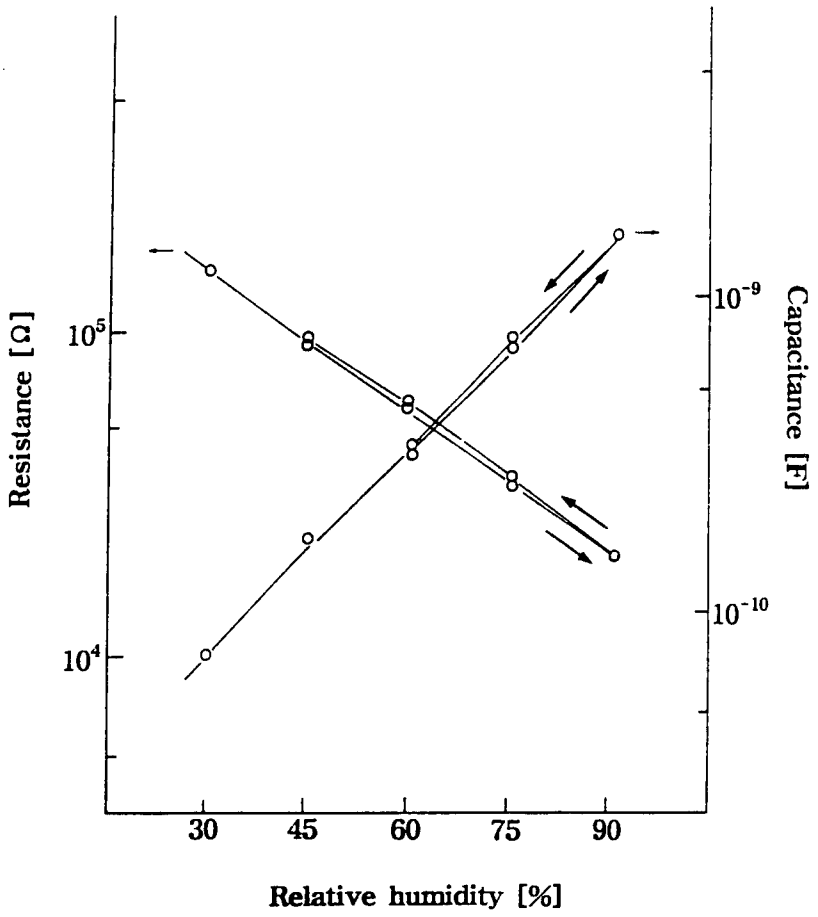

Fig. 8. Hysteresis characteristics.

for the above specimens are 40 s and 1 min, respectively.

The resistance and capacitance variations with aging time are shown in Fig. 9. The aging was performed by exposing the specimens in air for 15 days and 60 days. The aging effect proceeds at a rate of 3%/month, which is in the practical allowance range of commercial devices.

4. Conclusions

The specimens of $Pb(Zr_{0.52}Ti_{0.48})O_3$ + 4 mol% Nb_2O_5 were fabricated and their humidity sensitivity was investigated. The results are summarized as follows.

1) The specimens sintered at 1000°C showed the best humidity sensitivity, and the open porosity calculated by means of Archimedes' method was as high as 41%. High porosity was also confirmed with SEM.

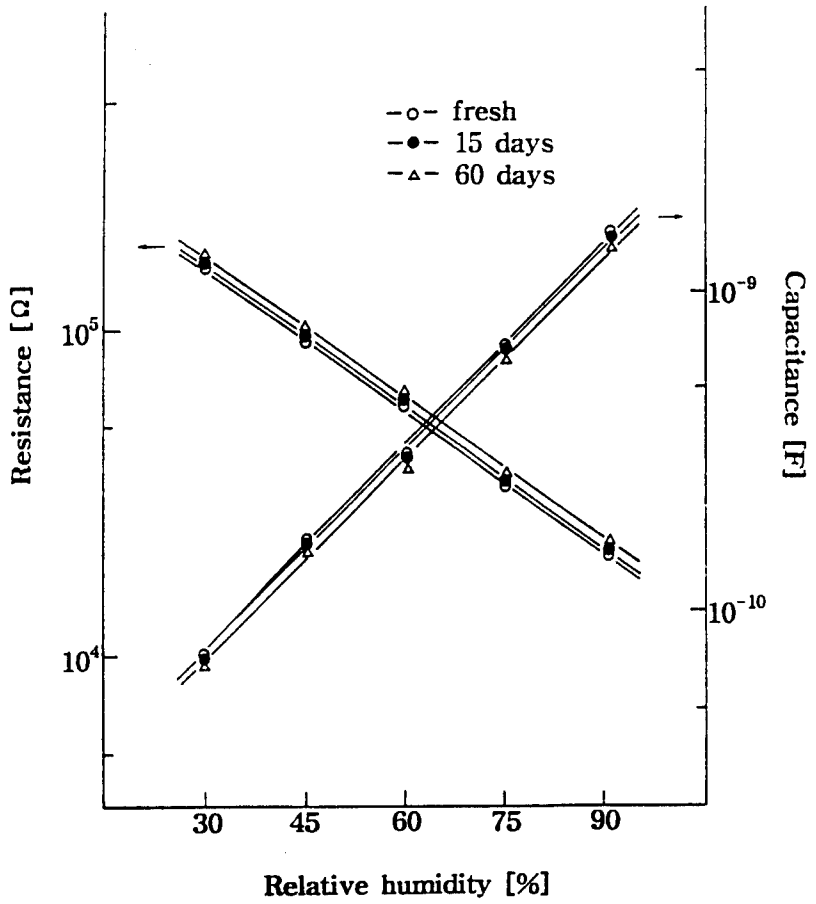

Fig. 9. Drift of hymidity sensitivity with time.

2) The open porosity and the adsorption rate decrease with increasing sintering temperature, and the humidlty sensitivity is highly dependent on the open porosity.

3) The capacitive sensitivity was higher than that of the resistance, and the humidity sensitivity was higher in the low-frequency region with good temperature stability and negligible hysteresis under cyclic humidity changes.

4) The resistance increases and the capacitance decreases at each value of relative humidity with aging, but the humidity sensitivity (slope) is constant.

Acknowledgment

The authors wish to thank the STRC (Sensor Technology Research Center) for financial support.

References

1 F. W. Dunmore: J. Res. Nat. Bur. Stand. **23** (1939) 701.
2 P. E. Thomas, J. O. Colla and R. Stewart: IEEE Trans. CHMT **2** (1979) 231.
3 K. Otsuka, S. Kinoki and T. Ushi: Denshi-Zairyo **19** (1980) 68 (in Japanese).
4 T. Nitta, Z. Terada and S. Hayakawa: J. Am. Ceram. Soc. **63** (1980) 295.
5 T. Seiyama, N. Yamazoe and H. Arai: Sensors and Actuators **4** (1983) 85.
6 Y. C. Yeh and T. Y. Tseng: J. Am. Ceram. Soc. **73** (1990) 1992.
7 H. Asakura, H. Yamamura and K. Uchino: Ferroelectrics **93** (1989) 205.
8 M. Wakamatsu: Ceramic Experimental Manual (N. K. Newspaper Company, Japan, 1989) Chap. 3.
9 N. Yamazoe and Y. Shimizu: Sensors and Actuators **10** (1986) 379.
10 J. H. Anderson and G. A. Parks: J. Phys. Chem. **72** (1968) 3662.
11 K. Suzuki: T. IEE Japan **112-A** (9) 782.

APPENDIX 52

Pb/Ti Ratio of RF-Magnetron Sputtered $PbTiO_3$ Thin Films

Nam-Yang LEE,* Narikazu USUKI, Hideaki ABURATANI,*♦
Yukio ITO,† and Kenji UCHINO*♦

Department of Physics, Sophia University, Kioi-cho 7-1,
Chiyoda-ku, Tokyo 102, JAPAN,

†Central Research Laboratory, Hitachi, Ltd., Kokubunji,
Tokyo 185, JAPAN, and

♦Materials Research Laboratory, Pennsylvania State University,
University Park, PA 16802, USA

<ABSTRACT>

Lead titanate ($PbTiO_3$) thin films have been deposited on Pt coated fused quartz substrates by rf-magnetron sputtering to investigate the effect of sputtering conditions on the Pb/Ti ratio of sputtered films. The thin films on Pt coated fused quartz were polycrystalline and did not have preferred orientation of the crystallites. It was found that the Pb/Ti ratio decreases with increasing oxygen content in sputtering gas and target-substrate distance, while it increases with rf-power. The ratio was varied in a wide range between 0.7-3.0 with sputtering conditions. The variation of Pb/Ti ratio could be explained by the variation of thermalization distance with sputtering conditions and the difference in diffusion coefficients of Pb and Ti atoms. By controlling the sputtering conditions, a single phase $PbTiO_3$

Presented at the 95th Annual Meeting of the American Ceramic Society, Cincinnati, OH, April 21, 1993 (Electronic Division, Paper No. E-76-93).
*Member, American Ceramic Society.

thin films were obtained. The films showed the phase transition from tetragonal to cubic at about 500 °C.

Key words; $PbTiO_3$ thin film, Pb/Ti ratio, thermalization, virtual source, diffusion

I. Introduction

Ferroelectric lead titanate ($PbTiO_3$) and lead zirconate titanate (PZT) thin films have been widely investigated because of the increasing demand for these materials in the applications of microactuators, nonvolatile random access memory capacitors, and pyroelectric detectors.[1-3] There are many kinds of methods for fabricating these ferroelectric thin films, such as sputtering, chemical vapor deposition, and sol-gel processing.[4-6]

Among these methods, sputtering is well known as one of the best deposition technique because of adhesion between the thin film and substrate, and epitaxial growth. However, it has some disadvantages such as damage by energetic species at the substrate, low deposition rate, and compositional change of the film compared to the target.[7] The compositional change is one of the most important factors that must be improved, since it affects the electrical properties of the thin films directly. The compositional change becomes more severe especially when the binding energy difference of the target components is great.

For example, when $PbTiO_3$ or another composition from its family is sputtered, the control of Pb content is difficult. There are two cases concerning the Pb content of sputtered thin films: one is excess Pb due to the higher sputtering yield of Pb over the other components; and the other is Pb deficiency due to the low sticking coefficient at higher substrate temperatures and resputtering phenomena by the energetic neutrals and/or negative particles.[1,8] The difficulty in controlling the lead content has been a main reason why these films have not been utilized practically. This problem could be solved if we understand more precisely the behavior of sputtered particles with sputtering conditions.

In this work, we tried to find the relationships between Pb/Ti ratio and sputtering conditions systematically, such as rf-power, sputtering gas pressure, gas composition, and target-substrate (T-S) distance.

II. Experimental Procedure

1. Sample preparation

$PbTiO_3$ thin films were prepared by an rf-magnetron sputtering system (Anelva, SPF-430HS). The sputtering target was $PbTiO_3$ ceramic with 100 mm in diameter and 5 mm in thickness. It had a stoichiometric composition of $PbTiO_3$ with purity of 99.9 %. The substrates were Pt coated fused quartz with the dimensions of 10 mm ×10 mm ×1 mm in size. The Pt film coated on fused quartz had (111) orientation. All the substrates were cleaned by using trichloroethane and acetone, and then placed in a stainless steel holder by clips prior to film deposition. The sputtering conditions are summarized in Table I. At a higher rf-power over 300 W the $PbTiO_3$ ceramic target was damaged by thermal heating, and hence the sputtering was conducted at or below 200 W. The deposition rate of the sputtered films was varied in the wide range of 30-250 Å/min. with sputtering conditions.

2. Measurement

X-ray diffraction (Jeol, JDX-11PA) was employed to examine the crystallographic properties. Pb/Ti ratio was obtained from the EPMA (electron probe micro-analyzer, Horiba, EMAX-1500) data. The integrated intensity of Pb-Mα and Ti-Kα was normalized by the value of ceramic target used for sputtering. SEM (scanning electron microscopy) was used to observe surface morphology and film thickness. The deposition rate was calculated from the film thickness and sputtering time. High temperature X-

ray diffractometer (Rigaku, D-Max3B) was used to observe the phase transition.

III. Review of the Sputtering Mechanism

Sputtering conditions such as power, sputtering gas pressure, gas composition, substrate temperature, and target-substrate (T-S) distance are known to affect the deposition profiles. In this section, the effect of these conditions on the Pb/Ti ratio and the deposition rate is discussed.

Sputtered particles lose their initial energy and direction by collisions with sputtering gas during their transport to the substrate, and after n collisions their energy reduces to the thermal energy (kT).[9,10,11] In this case, the sputtered particles are said to be thermalized and this region is called the thermalization region or cooling region. At the end of this region, a virtual source with relatively high density of sputtered particles forms. The thermalization distance is expressed by the mean free path and the average collision number required to thermalize. This thermalization distance depends on the mass and the initial energy of the sputtered particles, and the sputtering gas pressure.[8,11]

The transport of the sputtered particles from the virtual source to the substrate is by diffusion under the material concentration gradient. Thus the particle diffusion current density (J_{diff}) of sputtered particles can be expressed by Fick's law, $J_{diff} = -D(\partial n / \partial x)$, and will be inversely proportional to the distance, x, between the virtual source and the substrate. In multicomponent sputtering, there would be m virtual sources formed between the target and substrate, where m is the number of constituents of the target.[9] As a result, the composition of the deposited film may not be the same as that of the targets, particularly when the mass difference

between the components of target is significantly different. No virtual source may exist for certain sputtering conditions of low gas pressure or short target-substrate distance.

For the sputtering of $PbTiO_3$, it can be assumed that the region between the target and the substrate is divided into three regions by the difference in the thermalization distance of Pb and Ti atoms as shown in Figure 1. Although Pb and Ti can be ejected from the target in various types, for example, ions, neutrals, and oxides, they are assumed as neutral atoms in this study based on previous reports.[11,14] In region I, none of Pb and Ti atoms are thermalized. Therefore, the Pb/Ti ratio and deposition rate may be almost constant depending on the sputtering yield of each element, if resputtering effect is not considered. At region II, the Pb atoms are in state of thermalization, while the Ti atoms are not fully thermalized because of longer thermalization distance.[8] In this region, the Pb/Ti ratio and deposition rate may be low compared to the value obtained in region I due to previous thermalization of Pb. In region III, both Pb and Ti atoms are in state of thermalization. Therefore, the Pb/Ti ratio will depend on the diffusion process, especially, the diffusion coefficient. The deposition rate will decrease inversely proportional to the diffusion length.

IV. Results

1. Gas pressure change

Sputtering gas pressure is known as the most important parameter which affects the sputtering profile. Initially, the effect of gas pressure on the film composition and crystal structure was investigated.

Figure 2 shows the variation of Pb/Ti ratio with sputtering gas pressure for different rf-power and gas compositions. With increasing gas pressure,

the Pb/Ti ratio decreases irrespective to the other sputtering conditions. In case of 200W (O_2/Ar: 10/90), the ratio approaches 1.0 above 1.0 Pa. In case of 300W (O_2/Ar: 10/90) and 100W (O_2/Ar; 20/80), however, it is expected that very high gas pressure is necessary to obtain stoichiometric films.

Figure 3 shows the X-ray diffraction patterns of thin films sputtered at various sputtering gas pressures. The film sputtered at 0.1 Pa shows $PbTiO_3$ peaks and strong Pb_2O_3 peak at 29.4° (2θ) which indicates excess Pb. The Pb_2O_3 peak becomes weak with increasing gas pressure, and only the peaks due to $PbTiO_3$ remain at 1.0 Pa. This result agrees well with the results shown in Figure 2. The color of the thin films was reddish brown indicating a lead excess at lower gas pressure and changed to pale yellow with increasing gas pressure. The above results shown in Figures 2 and 3 imply that the sputtering gas pressure is an important factor in controlling the lead content.

However, it is not clear if the decrease in lead content is due to the total gas pressure or oxygen partial pressure since the oxygen partial pressure changes with total gas pressure. To confirm this, the deposition was performed at various gas pressures of Ar atmosphere. Figure 4 shows the effect of Ar gas pressure on the Pb/Ti ratio and deposition rate. The deposition rate decreases with increasing Ar gas pressure, while the Pb/Ti ratio shows almost a constant value near 3 in the experimental range. The decrease in deposition rate with increasing Ar gas pressure is probably due to the increase of scattering between sputtered particles and Ar gas particles. It is thought that the excess Pb in thin films is attributed to the higher sputtering yield of Pb than Ti. It has been reported that the sputtering yield of Pb is about 4 times higher than that of Ti for the metal target.[8] Therefore, it is also expected that the sputtering yield of Pb is higher than that of Ti even if the ceramic target is used. Considering this result under the assumption

mentioned in III. Pb and Ti atoms transport to the substrate before being fully thermalized in a given Ar pressure range, and the sputtering yield of Pb is approximately three times higher than that of Ti. The constant Pb/Ti ratio implies that the decrease of Pb/Ti ratio with sputtering gas pressure can be due to the increase of oxygen partial pressure.

2. Gas composition change

Figure 5 shows the variation of Pb/Ti ratio and deposition rate with oxygen content in the sputtering gas. The total gas pressure was fixed at 1.0 Pa. By introducing oxygen to the sputtering gas, the deposition rate decreased linearly, while the Pb/Ti ratio decreased rapidly, then saturated as it approached 1.0 near an oxygen content of 50 %.

It is well known that the introduction of oxygen is indispensable to compensate oxygen deficiency even though oxide ceramic target is used. Many studies have reported the decrease in deposition rate as oxygen is introduced to the reactive sputtering system.[8,15] This phenomenon has been explained by the oxidation of the target surface. Although the same tendency has been reported for the rf-sputtering using the oxide ceramic target, the reason is still not clear.

The oxygen partial pressure probably affects both the sputtering yield and initial energy of sputtered particles. The target surface was changed by the oxygen partial pressure during sputtering. For example, at oxygen free or lower oxygen partial pressure, the color of target surface changed black indicating reduction due to oxygen deficiency, and it returns to the original color at higher oxygen partial pressures. It is thought that the sputtering yield of Pb is suppressed in the oxidation state compared with reduction state. The introduction of oxygen may reduce the secondary electron by forming

negative ions near the target surface, and consequently a self-bias potential decreases. This results in the decrease of the sputtered particles' initial energy and thermalization distance, which causes the diffusion region to elongate.

We can expect the decrease of Pb/Ti ratio with increasing oxygen. Figure 6 shows the X-ray diffraction patterns for the films used in Figure 5. When the oxygen is not introduced to the sputtering gas, α-PbO peaks probably due to the excess Pb and small peak due to TiO appear. As the oxygen is introduced, the intensities of lead oxide peaks decrease and the peaks due to $PbTiO_3$ begin to appear. Above an oxygen content of 50 %, lead oxide peaks disappear and only the $PbTiO_3$ peaks exist. This result agrees well with the result shown in Figure 5. The peak intensity due to Pt substrate increases with oxygen content. This is probably due to the decrease in film thickness.

3. Rf-power change

Figure 7 shows the effect of rf-power on the Pb/Ti ratio at different oxygen contents. As the rf-power increases, the Pb/Ti ratio increases. However, the tendency is quite different with gas composition. The slope is very steep for the oxygen free atmosphere, while it is small when oxygen is introduced in the sputtering gas. Again the oxygen plays an important role on the lead content in thin films. This is contrary to the result by K. Torii et al. in PZT thin films.[1] They have reported the decrease of Pb/(Zr+Ti) ratio with increasing rf-power and explained it by the selective resputtering of Pb due to the impingement of accelerated negative ions. The resputtering effect was considered because the surface binding energy and sticking coefficient of Pb are low.[8]

However, according to D. J. Kester et al.[16] who has investigated the resputtering phenomena for various titanate perovskite, the evidence of resputtering phenomena in $PbTiO_3$ is not so obvious. Although the target material is different, S. Srivastav et al.[17] reported that they also did not find any resputtering phenomena in rf-sputtered ZnO thin films. Therefore, generally, the resputtering phenomena is not observed in rf-sputtering, but occurs only under limited sputtering conditions.

We have not observed a significant resputtering effect on the surface of the films. In addition it is difficult to explain by selective resputtering that the lead content increases with rf-power. Consequently, it is considered that the increase in Pb/Ti ratio with increasing rf-power in this study must be related to another phenomenon. The variation of Pb/Ti ratio with rf-power can be understood by the relationship between thermalization distance and rf-power. As the rf-power increases, the self-bias potential increases the initial energy of the sputtered particles. The self-bias potential increases because the initial energy of the sputtered particles is proportional to the energy of sputtering gas particles. This causes the thermalization distance of sputtered particles to become elongated. As a result, the Pb/Ti ratio of the thin films becomes close to the sputtering yield of Pb and Ti.

4. Target-substrate distance change

Figure 8 shows the variation of Pb/Ti ratio with the target-substrate (T-S) distance for various sputtering conditions. Although the value is different for the sputtering conditions, it decreased linearly with the T-S distance. This suggests that the virtual sources of Pb and Ti exist closer than 3 cm from the target.

V. Discussions

In order to establish a relationship between the Pb/Ti ratio and the sputtering conditions. sputtering yield, thermalization distance and diffusion coefficient of Pb and Ti should be estimated. Although the sputtering yield of Pb and Ti for the ceramic $PbTiO_3$ target is not known exactly, it is assumed from the result in Figure 4 that the value for Pb is more than three times higher than that for Ti. Sreenivas *et al.*[8] calculated the thermalization distance of Pb and Ti atoms by taking account of the chemical nature of the target element and the corresponding binding energies. The distance for Pb is calculated to be slightly shorter than that for Ti; therefore, the variation of Pb/Ti ratio with total gas pressure (oxygen partial pressure) or rf-power should be mainly due to the differences in the diffusion factor.

Next, the diffusion coefficient of Pb and Ti was calculated as a function of gas pressure by the following equation[12];

$$D_{12} = \frac{3}{32\,(n_1 + n_2)\,\sigma_{12}^2}\left\{\frac{8kT}{\pi}\left(\frac{1}{m_1} + \frac{1}{m_2}\right)\right\}^{1/2}, \qquad (1)$$

and the result is plotted in Figure 9. Here, D_{12} is the diffusion coefficient of gas 1 in gas 2, n_1 and n_2 are the number of atoms or molecules of the two gases per unit volume, m_1 and m_2, the molecular masses of the two gases, σ_{12}, the collision diameter, k, the Boltzmann constant, and T is the absolute temperature of the gas. The gas 1 and gas 2 correspond to Pb or Ti, and Ar, respectively, and the temperature T is assumed to be 500 $^{\circ}$K in our case. Figure 9 shows that the diffusion coefficient decreases with increasing gas pressure and the value for Ti is about 1.5 times higher than Pb. The particle diffusion current density of Pb decreases more rapidly than that of Ti in the diffusion region. As a result, Pb/Ti ratio decreases as the diffusion length is

elongated. The effect of sputtering conditions can be understood by the relationships between thermalization distance and diffusion region.

The phase transition of the $PbTiO_3$ thin film having a stoichiometric composition was observed by a high temperature X-ray diffractometer and the result is shown in Figure 10. The phase transition from tetragonal to cubic occurs near 500 °C which is almost the same as single crystal or ceramic $PbTiO_3$. The lattice constants at a room temperature were 3.90 and 4.14 Å, which are slightly smaller than the target $PbTiO_3$ values of 3.90 and 4.15 Å. Further investigations on electrical properties are now in progress.

VI. Conclusion

The effect of sputtering conditions on the lead content in rf-magnetron sputtered $PbTiO_3$ thin films was investigated. The Pb/Ti ratio was varied by the sputtering conditions in a wide range of 0.7-3.0. The excess lead in thin films is probably attributed to the higher sputtering yield of Pb than Ti. It is considered that the sputtering yield of Pb is three times higher than that of Ti for the ceramic $PbTiO_3$ target.

As the total gas pressure increases, the Pb/Ti ratio decreases. This ratio also decreases with increasing oxygen content at constant gas pressure, while it is almost constant with Ar pressure. The rf-power also affects lead content. When oxygen is introduced into the sputtering gas, rf-power effect decreases remarkably. These results reveal that oxygen plays an important role on the lead content of thin films.

The effect of sputtering conditions are explained well by the variation of thermalization distance and the difference in diffusion coefficient of Pb and Ti. Diffusion coefficient of Ti is 1.5 times larger than that of Pb. By controlling the sputtering conditions, stoichiometric and well-crystallized

$PbTiO_3$ thin films were obtained, which showed the phase transition from tetragonal to cubic near 500 °C.

Acknowledgements

The authors wish to thank Ms. Maureen L. Mulvihill for her critical reading of the manuscript and general support.

References

1. K. Torii, T. Kaga, K. Kushida, H. Takeuchi, and E. Takeda, "Single-Target Sputtering Process for Lead Zirconate Titanate Thin Films with Precise Composition Control," *Jpn. J. Appl. Phys.*, 30 [12B] 3562-66 (1991)
2. R. Takayama, Y. Tomita, K. Iijima, and I. Ueda, "Preparation and Characteristics of Pyroelectric Infrared Sensors Made of *c*-Axis Oriented La-Modified $PbTiO_3$ Thin Films," *J. Appl. Phys.*, 61 [1] 411-15 (1987)
3. E. Yamaka, H. Watanabe, H. Kimura, H. Kanaya, and H. Ohkuma, "Structural, Ferroelectric, and Pyroelectric Properties of Highly *c*-Axis Oriented $Pb_{1-x}Ca_xTiO_3$ Thin Film Grown by Radio-Frequency Magnetron Sputtering," *J. Vac. Sci. Technol.*, A6 [5] 2921-28 (1988)
4. T. Katayama, M. Fujimoto, M. Shimizu, and T. Shiosaki, "Growth and Properties of $PbTiO_3$ Thin Films by Photoenhanced Chemical Vapor Deposition," *Jpn. J. Appl. Phys.*, 30 [9B] 2189-92 (1991)
5. T. Kawano, T. Sei, and T. Tsuchiya," Preparation of Ferroelectric (Pb, La)(Zr, Ti)O_3 Thin Films by Sol-Gel Process and Dielectric Properties," *Jpn. J. Appl. Phys.*, 30 [9B] 2178-81 (1991)
6. J. Kang, T. Yuko, and S. Sakka, "Preparation of Lead-Based Perovskite Films by Sol-Gel Method and Their Properties," *Jpn. J. Appl. Phys.*, 30 [9B] 2182-85 (1991)
7. L. I. Maissel and R. Glang, *Handbook of Thin Film Technology;* McGraw-Hill, New York, 1970
8. K. Sreenivas and M. Sayer, "Characterization of Pb(Zr,Ti)O_3 Thin Films Deposited from Multi-Element Metal Targets," *J. Appl. Phys.*, 64 [3] 1484-93 (1988)

9. A. R. Nyaiesh, "Target Profile Change During Magnetron Sputtering," *Vacuum*, 36 [6] 307-9 (1986)

10. A. Gras-Marti and J. A. Valles-Abarca, "Slowing Down and Thermalization of Sputtered Particle Fluxes: Energy Distributions," *J. Appl. Phys.*, 54 [2] 1071-75 (1983)

11. W. D. Westwood, "Calculation of Deposition Rates in Diode Sputtering Systems," *J. Vac. Sic. Technol.*, 15 [1] 1-9 (1978)

12. C. E. Morosanu,*Thin Films by Chemical Vapour Deposition*: Chap. 5, Elsevier, Amsterdam, 1990

13. T. Ogawa, "Application of Nickel Alloy Electrode to Characterization of Crystal Oriented PbTiO3 Thin Films," *Integrated Ferroelectrics*, 1, 99-110 (1992)

14. T. Ogawa, A. Senda, and T. Kasanami, "Preparation of Ferroelectric Thin Films by RF Magnetron Sputtering," *Jpn. J. Appl. Phys.*, (1989) Suppl. 28-2, 11-14

15. C. V. R. Vasant Kumar and A Mansingh, "Effect of Target-Substrate Distance on the Growth and Properties of rf-Sputtered Indium Tin Oxide Films," *J. Appl. Phys.*, 65 [3] 1270-80 (1989)

16. D. J. Kester and R. Messier, "Predicting Negative Ion Resputtering in Thin Films," J. Vac. Sci. Technol. A 4 (3), 496-99 (1986)

17. S.Srivastav, C. V. R. Vasant Kumar, and A. Mansingh, "Effect of Oxygen on the Physical Parameters of RF Sputtered ZnO Thin Film," *J. Phys. D: Appl. Phys.*, 22, 1768-1772 (1989)

Figure Captions

Figure 1. Schematic diagram of the transport of sputtered Pb and Ti particles based on the differences in thermalization distance.

Figure 2. Effect of sputtering gas pressure on the Pb/Ti ratio. (substrate temperature; 750 °C, T-S distance; 50 mm)

Figure 3. X-ray diffraction patterns of as-grown films sputtered under various gas pressures. (rf-power; 200 W, O_2/Ar; 70/30, substrate temperature; 750 °C, T-S distance; 50 mm)

Figure 4. Variation of Pb/Ti ratio with Ar gas pressure. (rf-power; 200W, substrate temperature; 750 °C, T-S distance; 50 mm)

Figure 5. Effect of oxygen content on the Pb/Ti ratio and deposition rate. (rf-power; 200 W, substrate temperature; 750 °C, sputtering gas pressure; 1.0 Pa, T-S distance; 50 mm)

Figure 6. X-ray diffraction patterns of as-grown films sputtered at various oxygen contents. (rf-power; 200 W, substrate temperature; 750 °C, sputtering gas pressure; 1.0 Pa, T-S distance; 50 mm)

Figure 7. Effect of rf-power on the Pb/Ti ratio. (substrate temperature; 750 °C, sputtering gas pressure; 1.0 Pa, T-S distance; 50 mm)

Figure 8. Effect of Target-Substrate (T-S) distance on the Pb/Ti ratio. (substrate temperature; 750 °C, O_2/Ar; 70/30)

Figure 9. Calculated diffusion coefficient of Pb and Ti in Ar as a function of sputtering gas pressure.

Figure 10. Lattice constants of single phase $PbTiO_3$ thin film as a function of temperature. (rf-power; 200 W, sputtering gas pressure; 1.0 Pa, O_2/Ar; 70/30, substrate temperature; 750 °C, T-S distance; 50 mm)

Table I. Sputtering conditions of $PbTiO_3$ thin films

Target	$PbTiO_3$ ceramic disc
Substrate	Pt coated F.Q.
Substrate temperature	750 °C
Gas pressure	0.1 ~ 3.0 Pa
$O_2/(Ar+O_2)$	0 ~ 100 %
Rf-power	50 ~ 200 W
T-S distance	30 ~ 70 mm
Sputtering time	2 hrs.

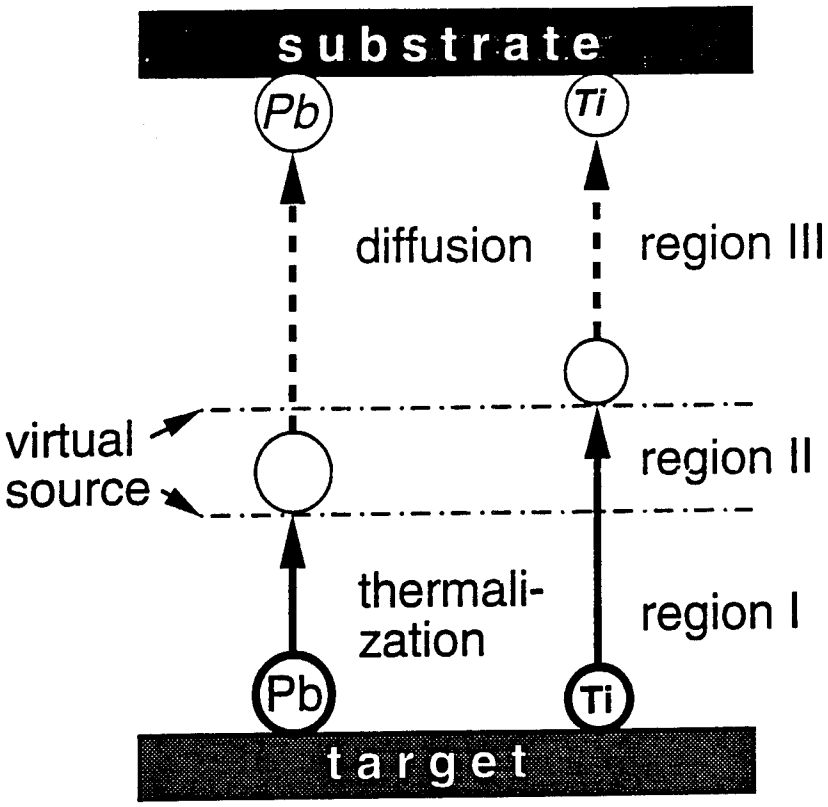
substrate
Pb
Ti
diffusion
region III
virtual
source
region II
thermali-
zation
region I
Pb
Ti
target

Figure 1

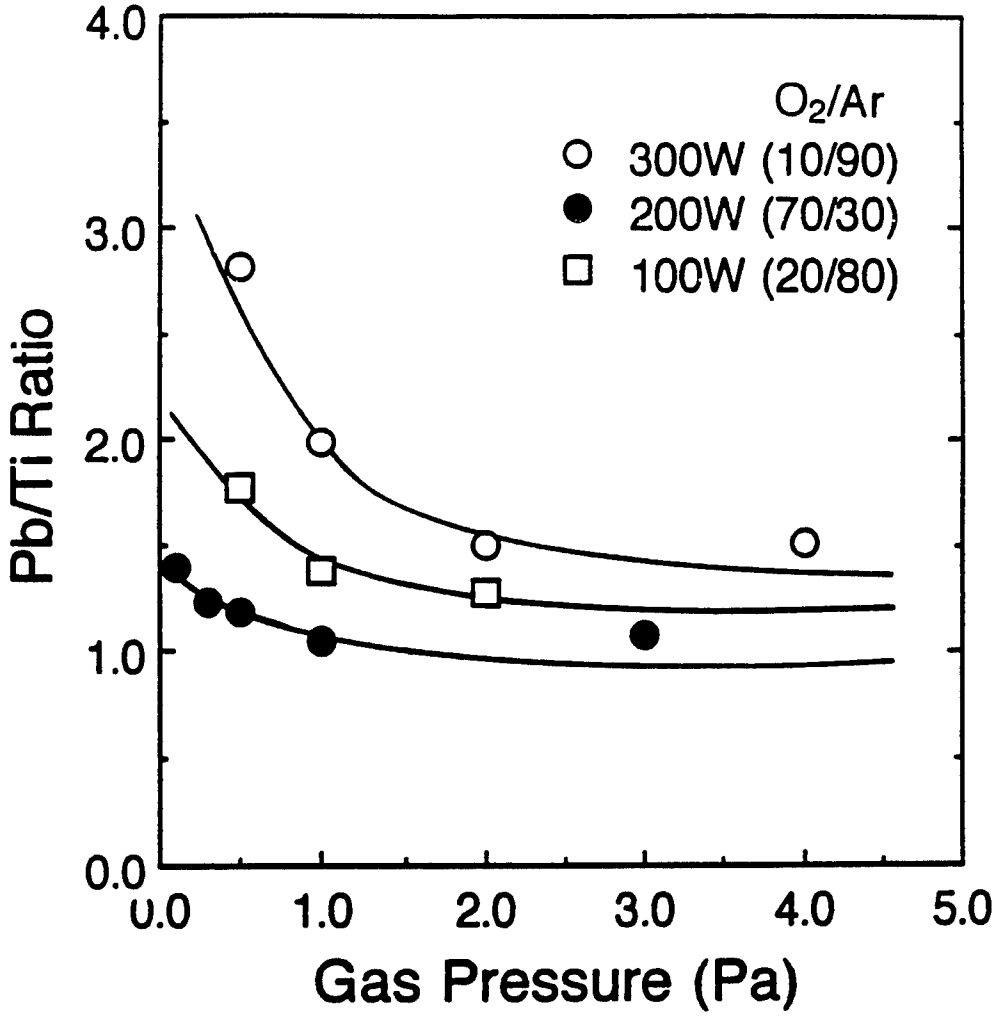
4.0
3.0
2.0
1.0
0.0
Pb/Ti Ratio
O2/Ar
300W (10/90)
200W (70/30)
100W (20/80)
0.0
1.0
2.0
3.0
4.0
5.0
Gas Pressure (Pa)

Figure 2

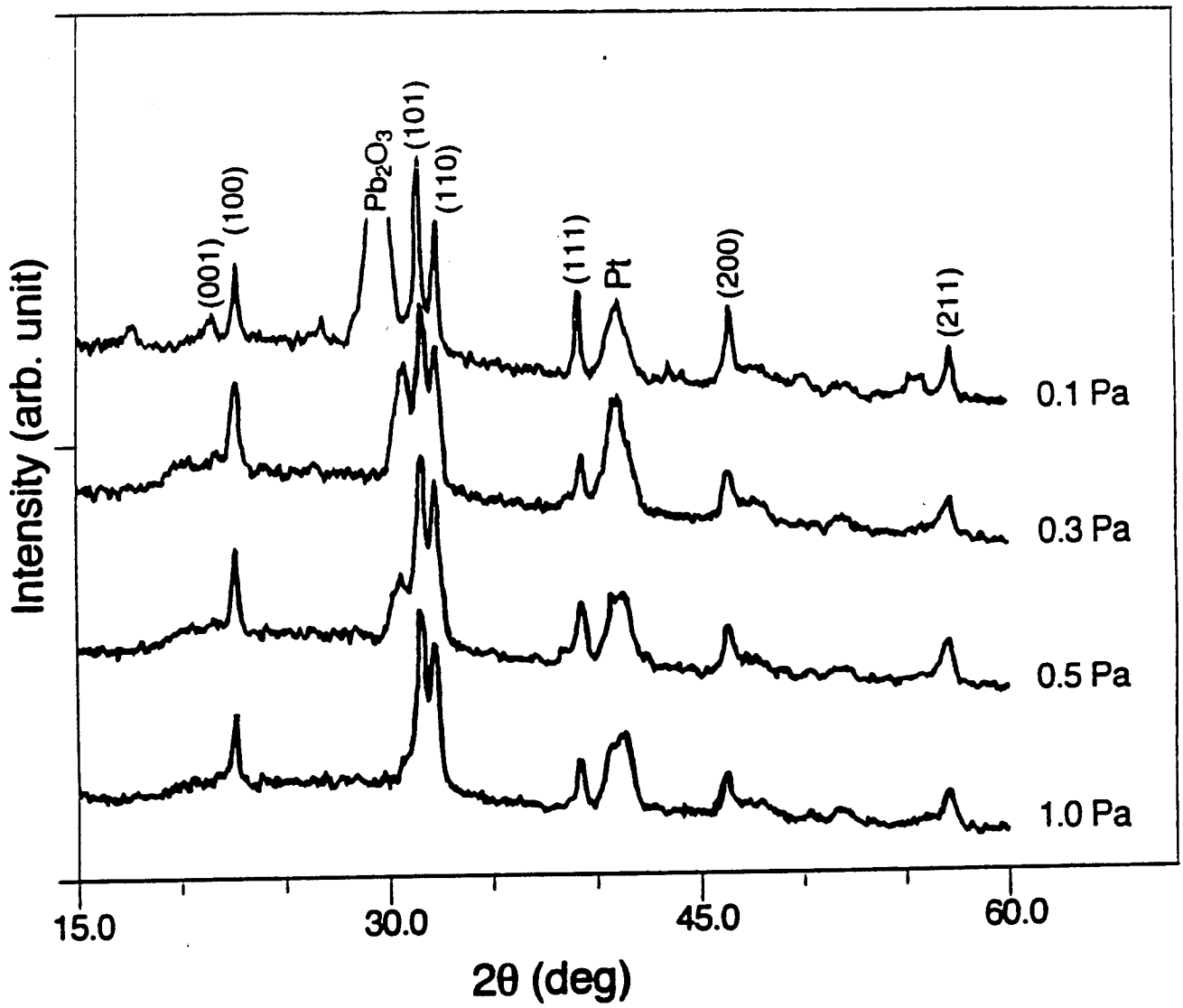
Intensity (arb. unit)
(001)
(100)
Pb2O3
(101)
(110)
(111)
Pt
(200)
(211)
0.1 Pa
0.3 Pa
0.5 Pa
1.0 Pa
15.0
30.0
45.0
60.0
2θ (deg)

Figure 3

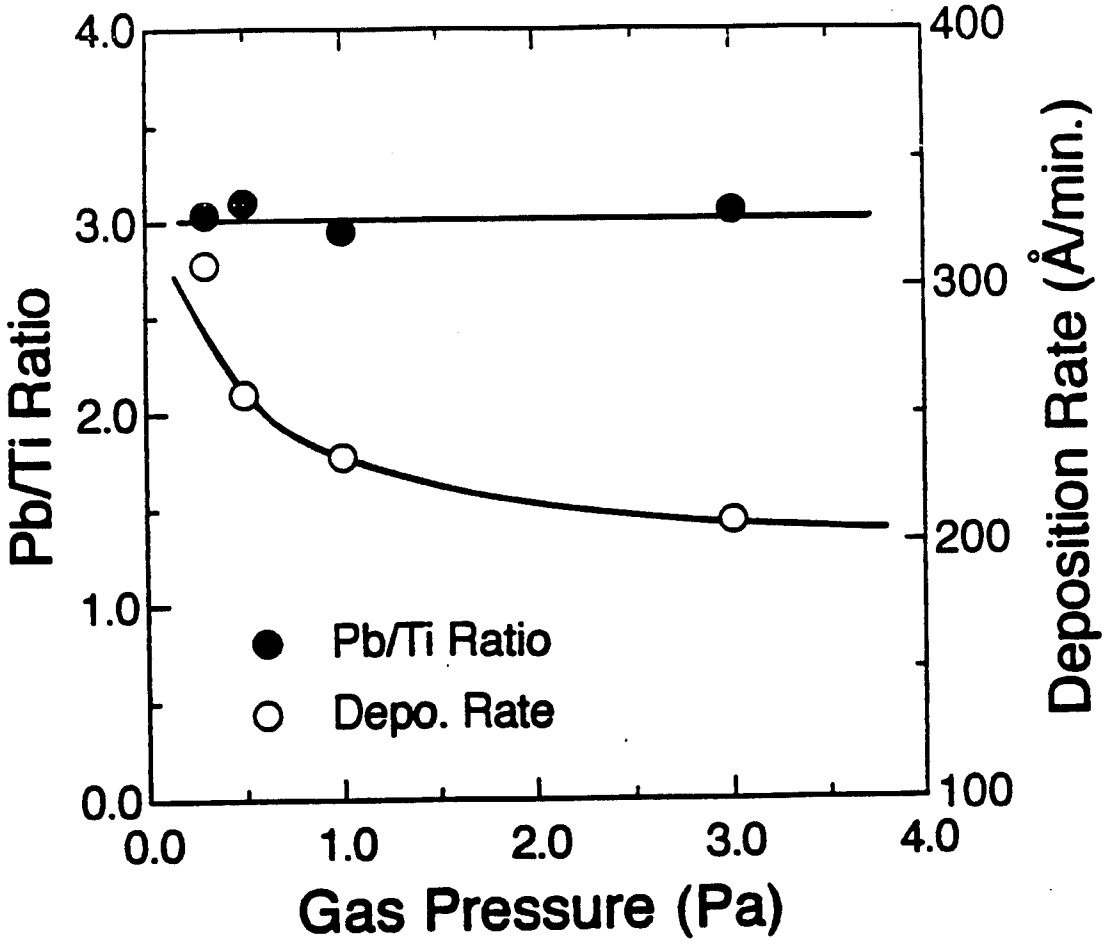
4.0
3.0
2.0
1.0
0.0
Pb/Ti Ratio
400
300
200
100
Deposition Rate (Å/min.)
Pb/Ti Ratio
Depo. Rate
0.0
1.0
2.0
3.0
4.0
Gas Pressure (Pa)

Figure 4

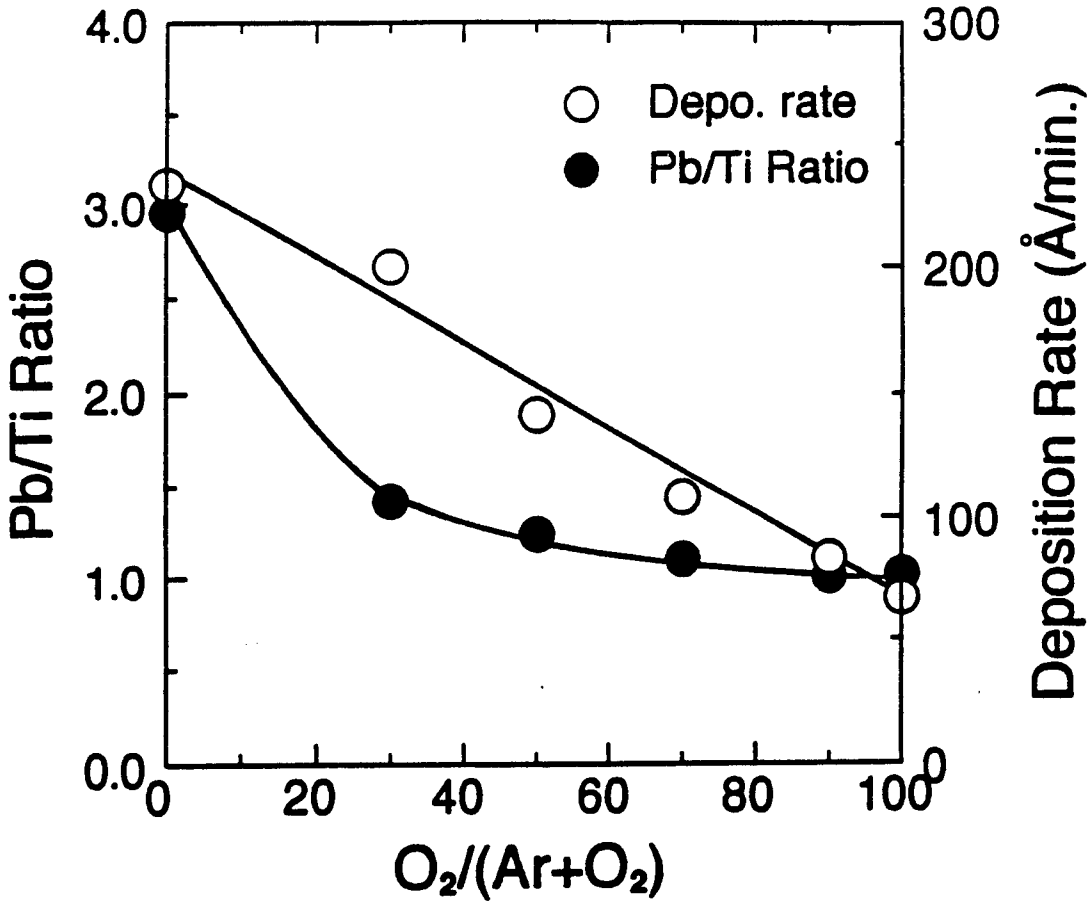
4.0
3.0
2.0
1.0
0.0
Pb/Ti Ratio
300
200
100
0
Deposition Rate (Å/min.)
Depo. rate
Pb/Ti Ratio
0
20
40
60
80
100
O2/(Ar+O2)

Figure 5

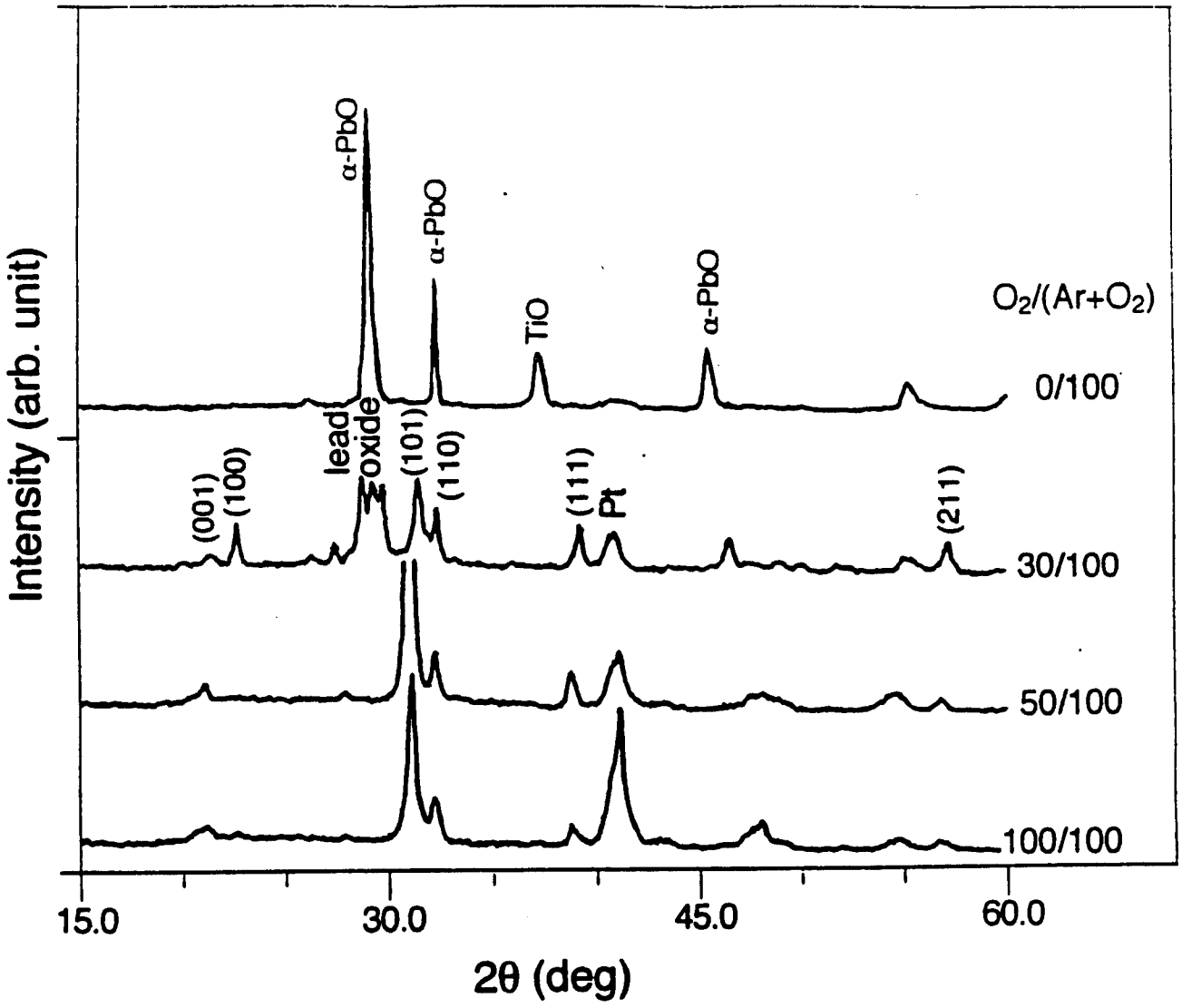
Intensity (arb. unit)
α-PbO
α-PbO
TiO
α-PbO
O2/(Ar+O2)
0/100
lead oxide
(001)
(100)
(101)
(110)
(111)
Pt
(211)
30/100
50/100
100/100
15.0
30.0
45.0
60.0
2θ (deg)

Figure 6

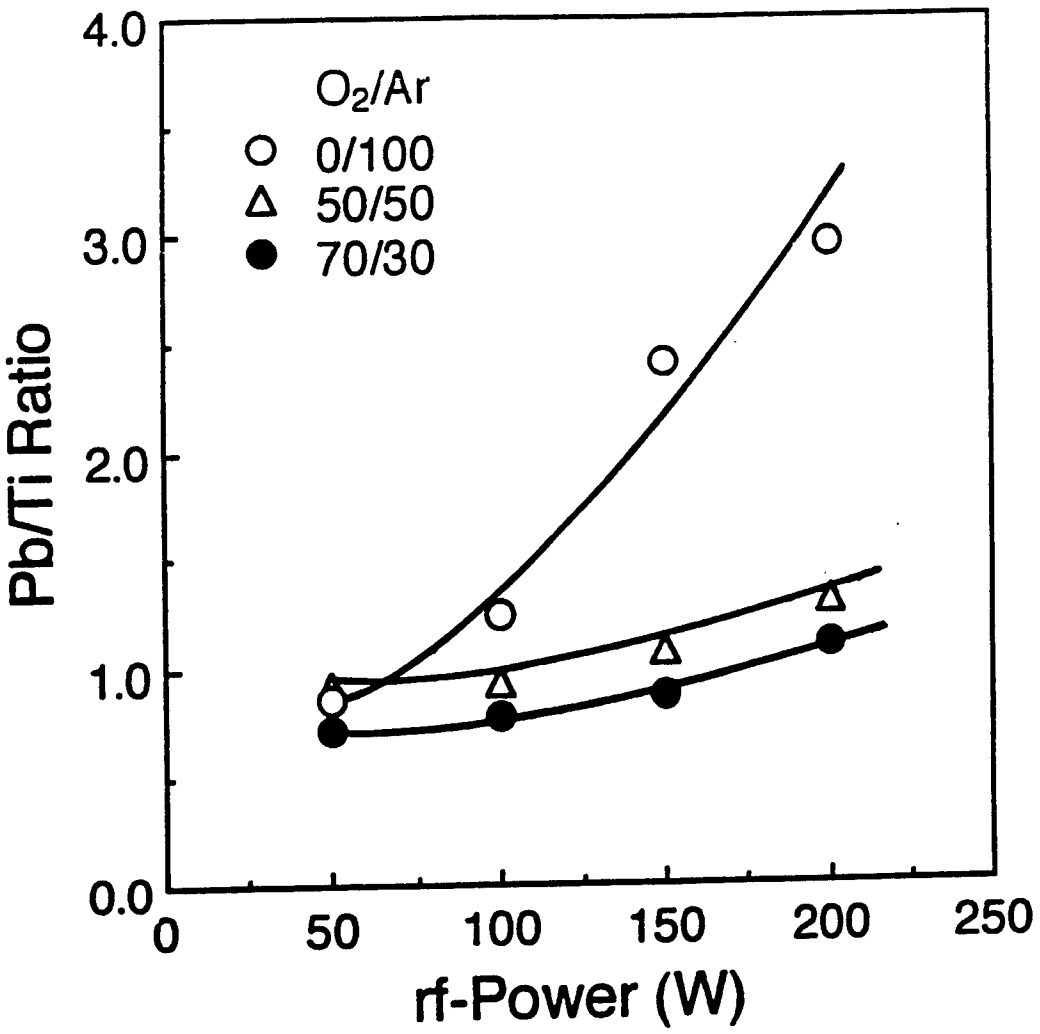
4.0
3.0
2.0
1.0
0.0
Pb/Ti Ratio
O2/Ar
0/100
50/50
70/30
0
50
100
150
200
250
rf-Power (W)

Figure 7

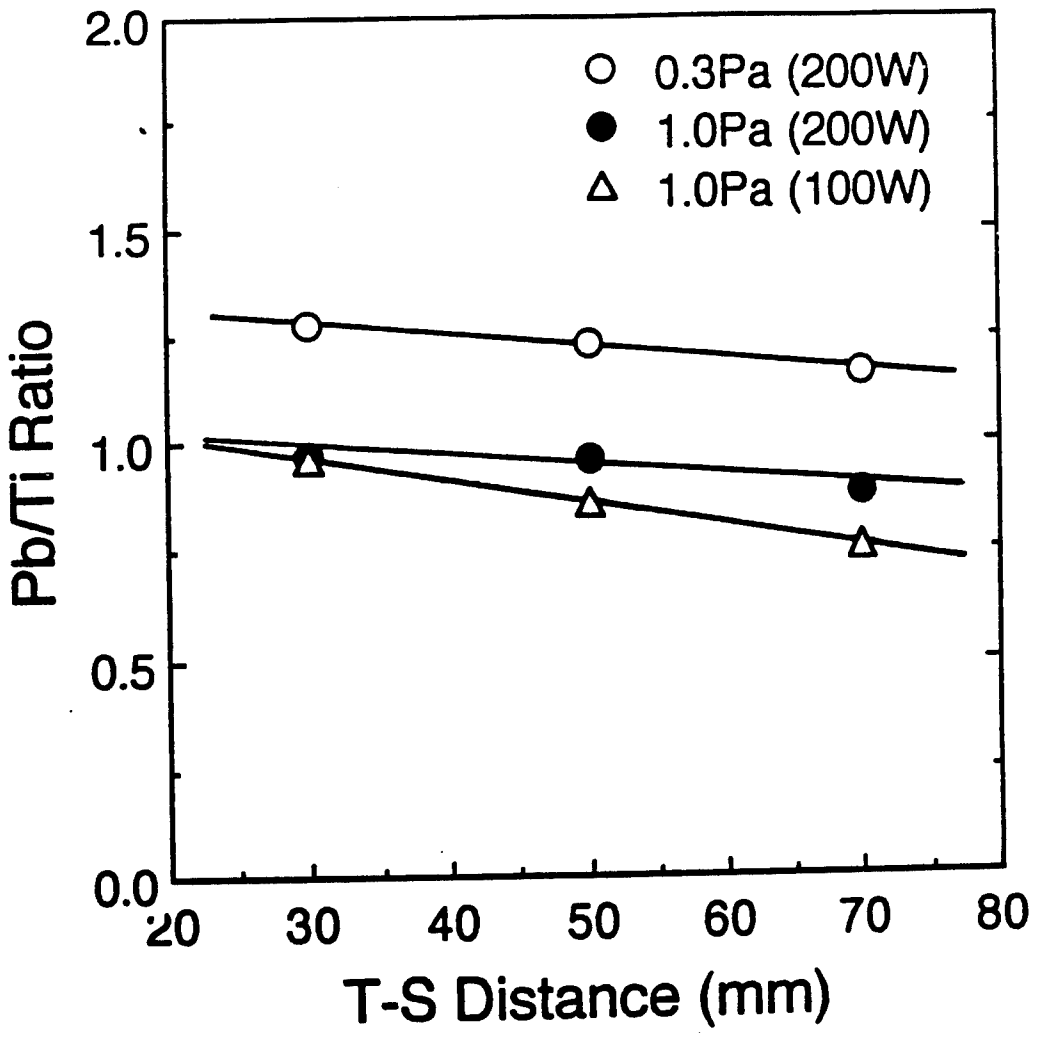
2.0
1.5
1.0
0.5
0.0
Pb/Ti Ratio
0.3Pa (200W)
1.0Pa (200W)
1.0Pa (100W)
20
30
40
50
60
70
80
T-S Distance (mm)

Figure 8

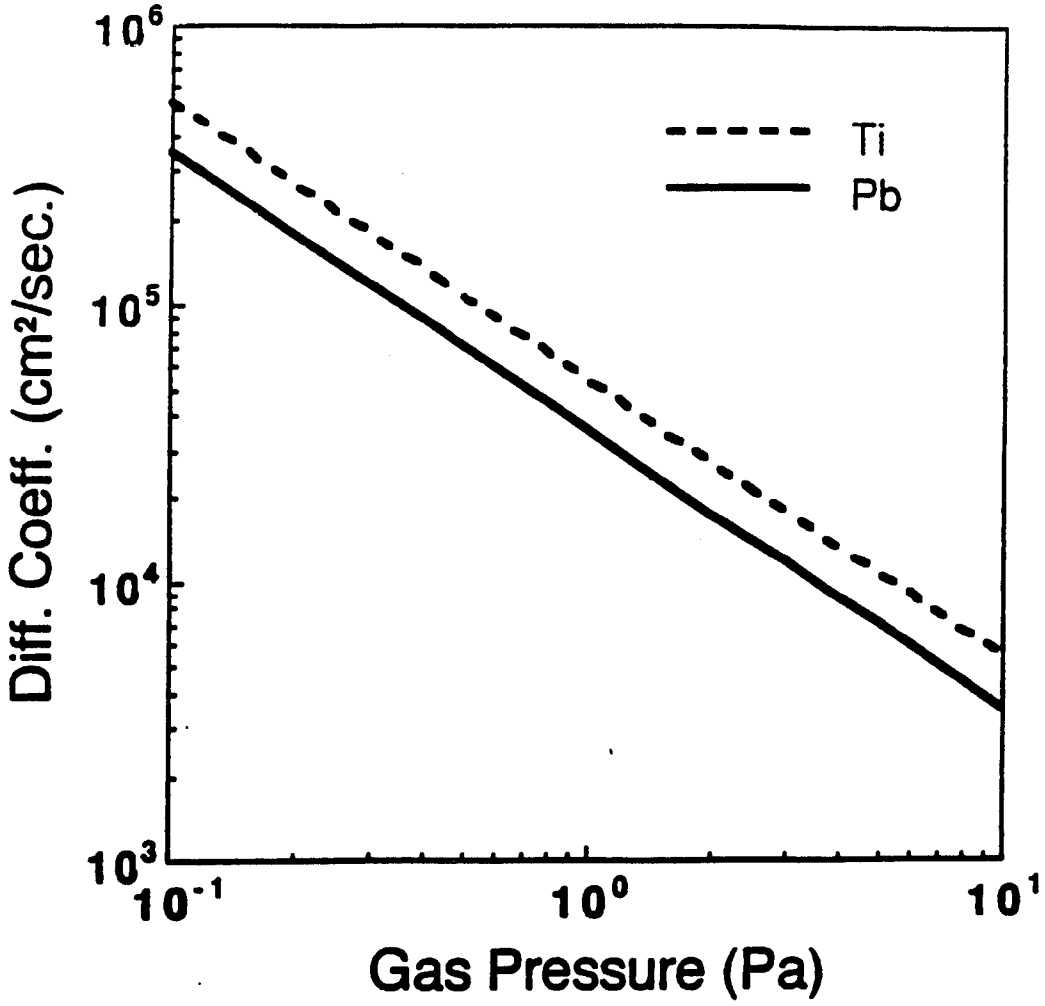
Diff. Coeff. (cm²/sec.)
10⁶
10⁵
10⁴
10³
10⁻¹
10⁰
10¹
Gas Pressure (Pa)
Ti
Pb

Figure 9

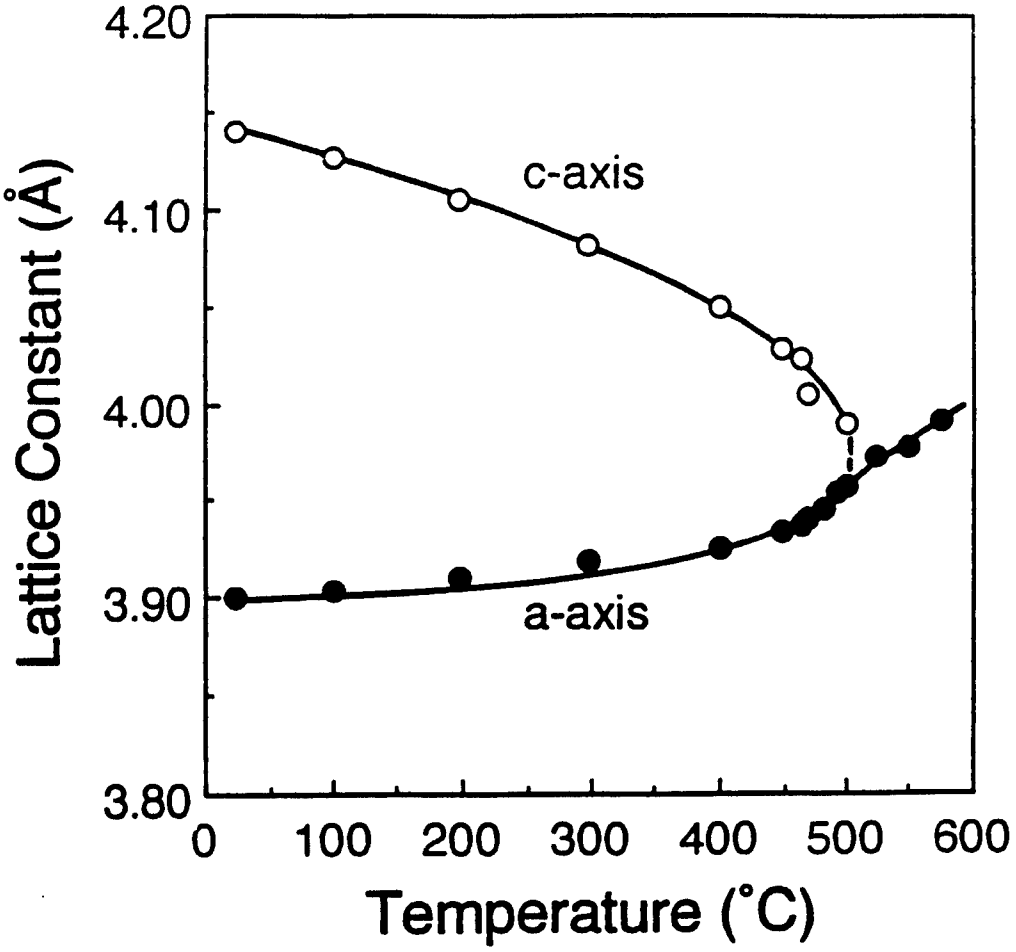
4.20
4.10
4.00
3.90
3.80
Lattice Constant (Å)
c-axis
a-axis
0
100
200
300
400
500
600
Temperature (°C)

Figure 10

INTEGRATION ISSUES

APPENDIX 53

Tailoring Materials for Smart Applications

J. P. DOUGHERTY AND Y. CHEN

ABSTRACT

An improved method has been developed for preparing piezoelectric composite materials. The piezoelectric ceramic phase loading in the piezoelectric composites was increased up to 85 volume percent. The piezoelectric efficiencies of the cured composite materials were found to be superior to those of the best composite 0-3 piezoelectrics that have been reported. The electrical and mechanical properties of the composites indicate the possible applications of these materials as transducers and sensors in smart systems.

INTRODUCTION

Piezoelectric materials are widely used in transducer and sensor manufacture. One newer application of the piezoelectric phenomenon is the "smart system". The "smart system" is a structure composed of sensor, processor and actuator network, and is capable of performing simultaneously both sensing and actuating functions. Figure 1 schematically shows an example of the "smart system". When the system is driven by an external vibration, the sensor embedded in the structure senses the vibration and gives an output signal to drive a controller which in turn drives the transducer to give feedback to the structure.

Tailoring materials to provide the desired properties for application such as the "smart system" has become an increasingly important subject in the materials research field. During the past years, the combination of piezoceramics with polymers as composites in various different connectivity patterns has proved to be a valuable and versatile processing technique for optimizations of a wide range of piezoelectric parameters (Skinner, Newnham and Cross, 1978; Newnham et al., 1980; Newnham, 1987). The 0-3 connectivity, in which the piezoelectric ceramic particles are dispersed in the 3-dimensionally connected polymer matrix, is one of the simplest patterns that have made it possible to produce flexible thin film sheets, with large areas, in various shapes.

The piezoelectricity describes the generation of an electrical polarization P_i in certain ceramic or composite materials by the application of a mechanical stress σ_{jk}. The direct piezoelectric effect is defined by the relation:

J. P. Dougherty, Center for Dielectric Study, 144 Intercollege Materials Research Laboratory, Pennsylvania State University, University Park, PA 16802

Yan Chen, 142 Intercollege Materials Research Laboratory, Pennsylvania State University, University Park, PA 16802

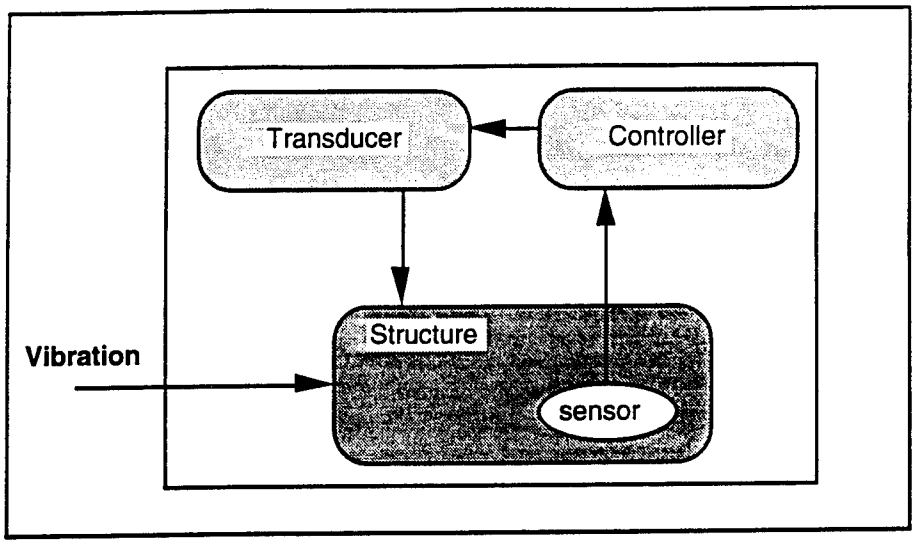

Figure 1. Schematic picture of an example of the "smart system".

$$P_i = d_{ijk}\sigma_{jk} \quad (1)$$

where the d_{ijk} is the piezoelectric constants. The converse piezoelectric effect can be expressed by:

$$S_{ij} = d_{ijk}E_k \quad (2)$$

where S_{ij} is the strain developed in the material when the electric field E_k is applied to it. In a ceramic or composite material polarized along the z-axis, the piezoelectric strain coefficient d_{33} and piezoelectric voltage coefficient g_{33} ($g_{33} = d_{33}/\varepsilon$) coefficient determine the transmitting and receiving characteristics of the transducer, respectively. It is desirable, therefore, to have high values of d_{33} and g_{33} in transducer applications.

Although the high g_{33} constant can be obtained by decreasing dielectric constant ε, the small capacitance due to the low dielectric constant requires a high impedance amplifier in close proximity to the transducer to raise the output to a sufficient level for transmission. It is obvious that the performance of the materials can be optimized if higher d_{33} and moderate dielectric constant ε can be obtained without degrading the voltage output. Since most organic polymers do not exhibit significant piezoelectric properties, a large piezoceramic volume fraction is needed to obtain strong piezoelectricity for a polymer/ceramic composite system.

This paper reports a unique approach towards preparation of 0-3 composite materials consisting of a polymer matrix and PZT powder. Up to 85 vol% of ceramic phase loading in the composites was achieved, and improved piezoelectric properties were obtained.

EXPERIMENTAL PROCEDURE

The polymer used in this work was a low viscosity Spurr epoxy purchased from Polysciences Inc. The piezoceramic powder used was PZT 501 from PKI. These

Figure 2. The SEM picture of the fracture surface of the composite sample 85PZT/15epoxy.

powders had a wide distribution of particle size from 1μm to 150 μm. The particles are mixed with epoxy matrix and the mixtures were transferred into a die and pressed into pellets at 25°C under various pressures. The samples were then cured at 70°C for 8 hours. After cooling down to room temperature, the cured samples were polished to an even thickness and both surfaces of the pellet were electroded with air-dry silver paint for poling and measurement.

RESULTS AND DISCUSSIONS

DENSITY

The various loadings of PZT phase in the composites were obtained following the previously described procedure. Microscopic analyses indicated that the PZT particles were closely packed with one another and evenly coated by the epoxy polymer. Figure 2 shows the SEM micrographs of the fracture surfaces of the composite sample with a composition of PZT/epoxy = 85/15 (by volume). The density of the cured composites was calculated directly from their measured volume and weight. By assuming that the composite samples were free from voids, the actual volume fractions of PZT and the epoxy were calculated using the equation:

$$\rho = \rho_1 v_1 + \rho_2 v_2 \tag{3}$$

where ρ, ρ_1 and ρ_2 are the densities of the composite, phase 1 and phase 2, respectively. The volume fractions of two phases are represented by v_1 and v_2, respectively. To test the assumption (samples were free from voids) a thermal gravimeter analysis (TGA) was performed. The data obtained from TGA results were also used to calculate the density of the sample, which was in good agreement with that obtained from equation (3). Figure 3 shows the density of the materials as a function of

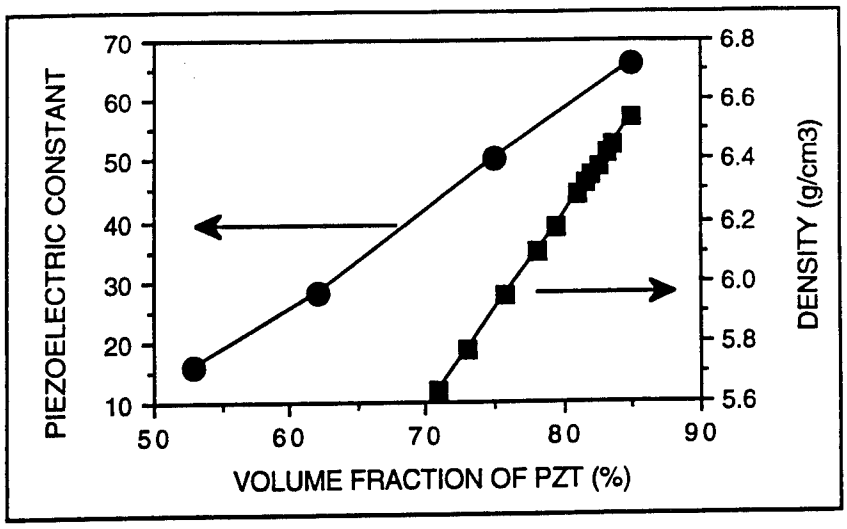

Figure 3. The density and the piezoelectric constant d_{33} of the materials as function of the volume fraction of the PZT loading in the composite.

the volume fraction of PZT phase in the composite. The results show the linear relation between the density of the composite and the volume fraction of the PZT particle. Up to 85 vol% PZT particle loading in the composite materials has been achieved.

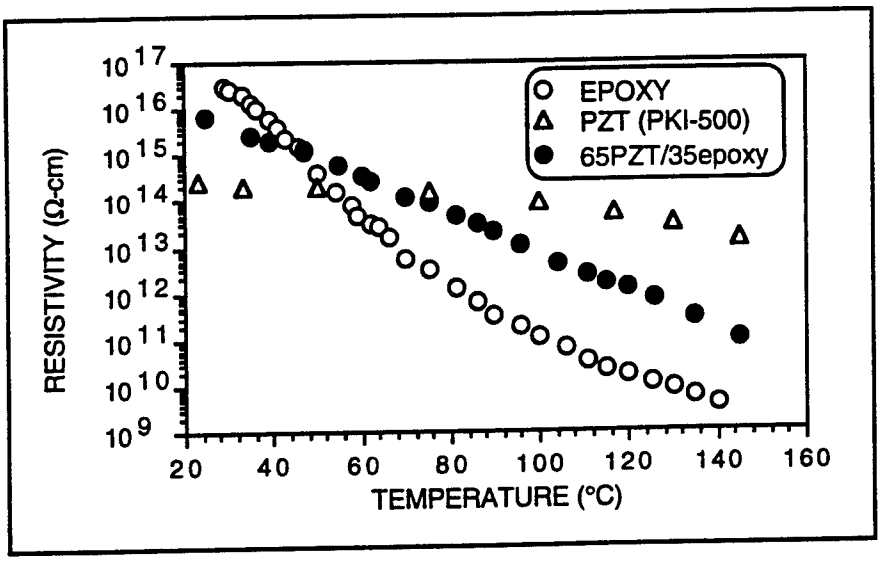

Figure 4. The resistivity of 65PZT/35epoxy, hard Spurrs epoxy and PZT (PKI-500) ceramic as functions of temperature.

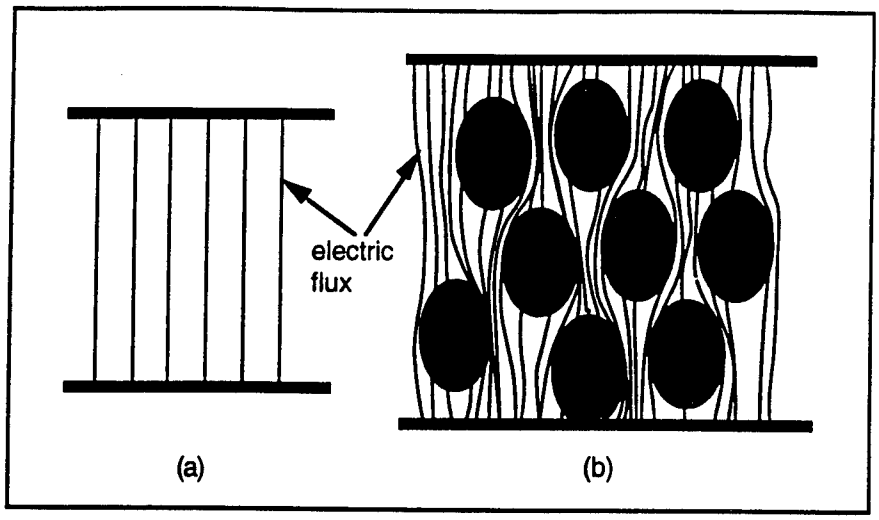

Figure 5. Electric flux in (a) single uniform medium and (b) diphasic composite medium. The shaded regions are the higher permitivity particles.

PIEZOELECTRIC PROPERTY

In order to produce macroscopic piezoelectricity in a ceramic or a composite the sample must be "poled" for aligning the polarization preferentially. Poling of the composites was accomplished by using a conventional poling technique. The apparatus was composed of a heated oil bath and a high voltage power supply. After poling, the piezoelectric constant d_{33} was measured using a Berlincourt Piezo d_{33}-meter. The piezoelectric constants d_{33} for composites with different composition were measured as a function of poling temperature under a poling field of 50KV/cm and a poling time of 20 minutes. The optimum poling temperature is found to be around 80°C. This result is believed to be related, in a certain degree, to the resistivities of both the composites and the composite constituents, which is shown in Figure 4. For a 0-3 composite, the particles dispersed in the matrix get the largest voltage on them when the resistivity of the particle equals to that of the polymer matrix (impedance match) because at this point the 0-3 composite can be treated as a single uniform medium in terms of electric flux. At higher temperatures, where the resistivity of the polymer becomes much lower than that of the particle phase, parts of the electric flux will by-pass the particles resulting in a lower voltage to the particles possibly producing a insufficient poling. Figure 5 shows the electric flux in a single uniform dielectric medium (a) as well as in a diphasic composite medium (b).

The measured d_{33} value for composite materials poled at 50 KV/cm and 80°C for 20 minutes is also plotted as a function of volume fraction of piezoelectric ceramic in Figure 3. The figure shows an almost linear relationship between the d_{33} constant and the volume fraction of the PZT phase.

The high piezoelectric constant clearly indicates that these materials may be used to make effective transducers and sensors. The transducers or sensors may be surface-bonded or embedded in the structure base on the design of actively controlled structures. Figure 6 shows the geometry of such a metal structure in which sensors can be either bonded on the surface or embedded inside the structure to sense a local vibration. Similar structures can also be applied to composite materials.

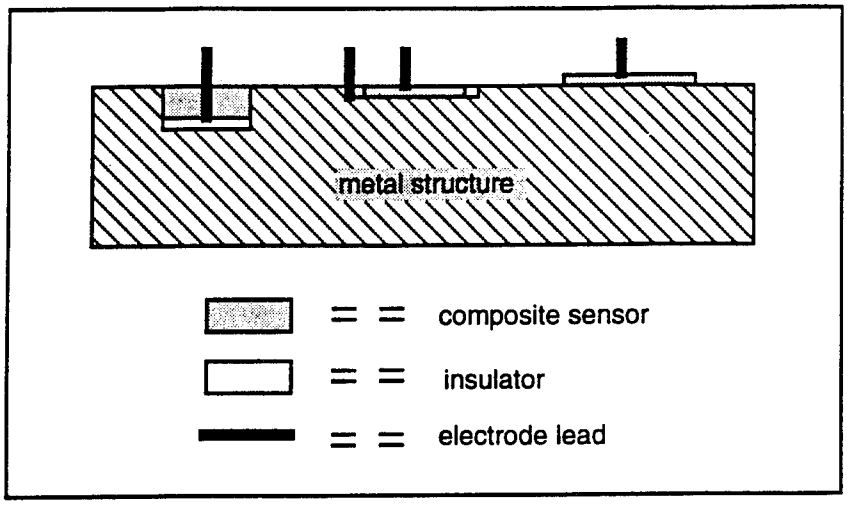

Figure 6. Geometry of a metal structure in which sensors are either bonded on the surface or embedded in the structure.

To evaluate the sensor performance, an 85PZT/15epoxy composite sample was used in a sensor/actuator combination with a "moonie" structure (Xu et al., 1991). When the "moonie" actuator was driven by a electric field E = 125V/mm, the sensor response was measured as a function of frequency. The result is shown in Figure 7. A standard PZT (PKI-500) ceramic sensor is also tested and the result is included for comparison. It can be seen that the composite material has adequate signal output and wider bandwidth which should improve the overall system performance.

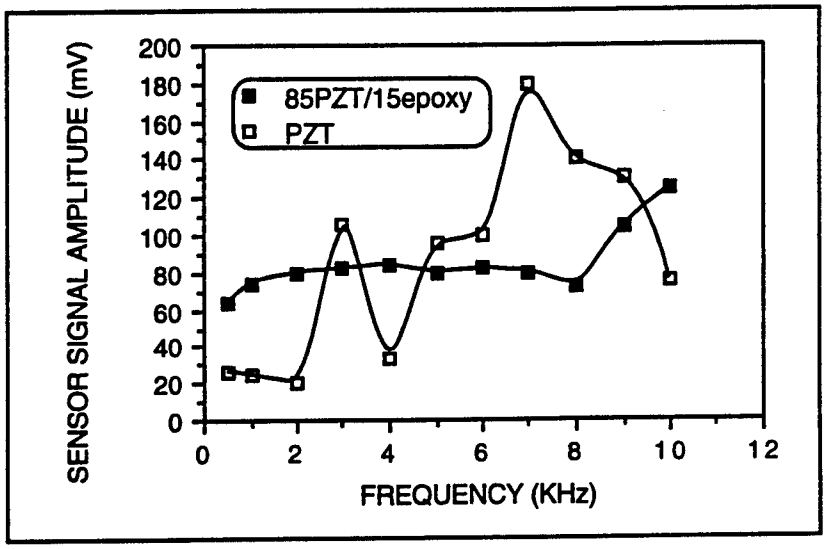

Figure 7. The signal response of sensor under driving field E = 125V/mm.

TABLE I. DIELECTRIC PROPERTIES OF COMPOSITE MATERIALS

MATERIALS	DENSITY(g/cm^3)	K (before poling)	tanδ	K (after poling)	tanδ
PZT (PKI500)	7.8	1300	0.024	1800	0.018
Spurrs Epoxy	1.1	3.2	0.010		
85PZT/15Epoxy	6.8	174	0.014	195	0.012
75PZT/25Epoxy	6.1	109	0.015	109	0.015

DIELECTRIC PROPERTY

The dielectric constant and loss of the composites were measured as a function of both temperature and frequency using a Hewlett-Packard 4274A Multi-frequency LCR Meter. The data obtained at 25°C are listed in Table I. The dielectric constant and dielectric loss are plotted in Figure 8 as a function of temperature for 85PZT/15epoxy composite material. The solid lines represent the dielectric constants and the dashed lines are dielectric losses. Both dielectric constant and dielectric loss decrease as increasing frequencies. A similar variation pattern of the dielectric properties is also observed for the 75PZT/25epoxy composite sample except that the dielectric constant for the

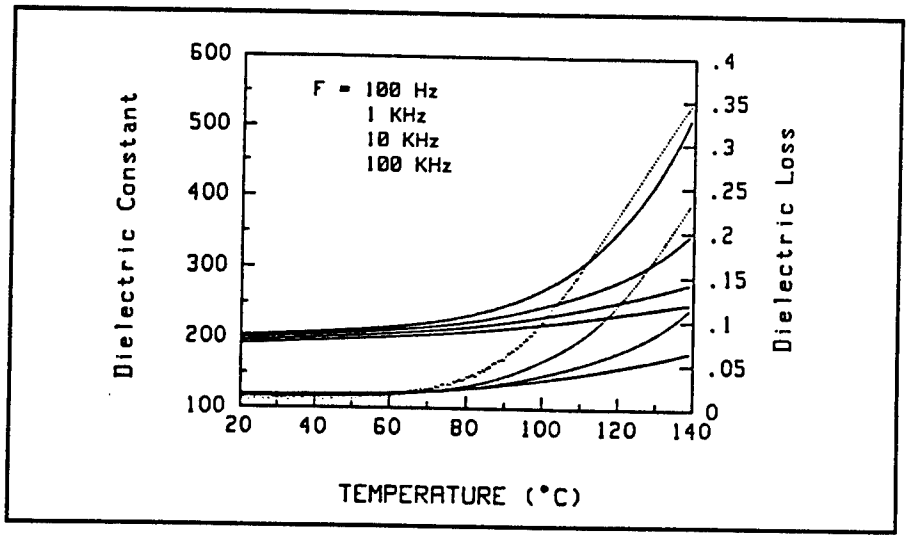

Figure 8. The dielectric constant and loss of the 85PZT/15epoxy composite as a function of temperature and frequency.

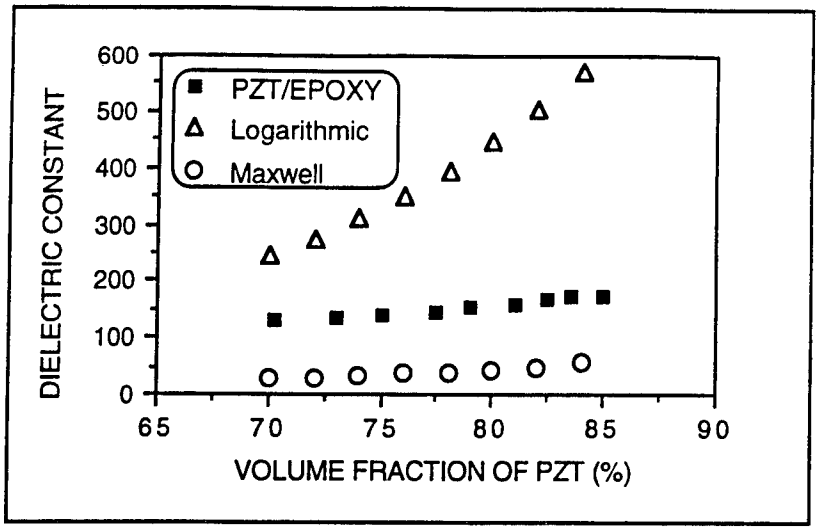

Figure 9. Dielectric constants of PZT/epoxy composites as a function of volume fraction of PZT together with both Logarithmic and Maxwell mixing rules.

85PZT/15epoxy are significantly higher than those for 75PZT/25epoxy and the dielectric loss for the former are consistently lower than that of the later, which are expected. The similarity of the dielectric properties for these samples suggests that the structures of the composite materials may be similar despite the difference in composition.

Figure 9 shows the plots of dielectric constants of the composites as a function of the volume fraction of the PZT phase together with both Logarithmic (3-3) and Maxwell (0-3) mixing rules. The values of the dielectric constant of the composites are between that

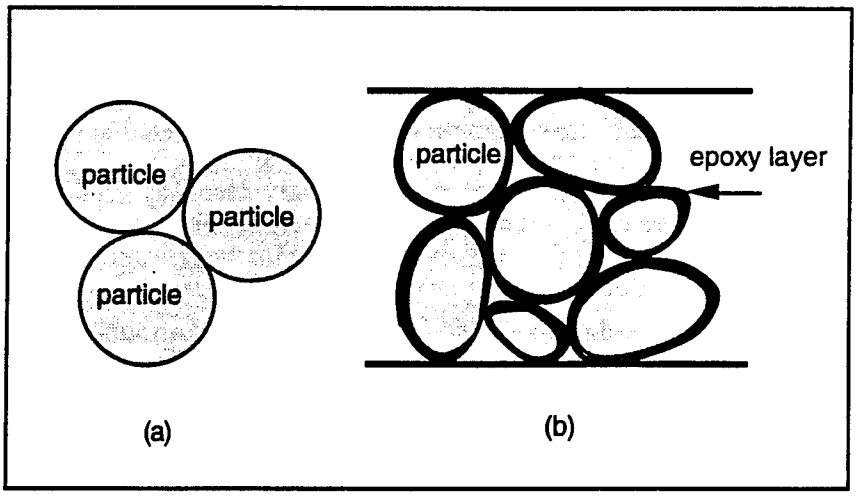

Figure 10. Geometry of diphasic model One. The epoxy layer is not to scale.The layer thickness is enlarged for clarity in the drawing.

of two mixing rules. Because none of these models could be applied to these materials, the following two new models were developed to explain the dielectric properties and the structure of the composite materials.

1) MODEL ONE

Figure 10 (a) illustrates an ideal packing structure of spherical ceramic particles in ceramic. Since the particles prepared are all coated with the epoxy, it is reasonable to introduce a model, shown in Figure 10 (b), representing the composite materials. In this model, each particle is coated with a thin layer of polymer and the "triple points" between the particles are filled with polymer (it has been shown previously virtually that no porosity exists in the composite). Based on this model, the particles and the coating polymers form a 0-3 connectivity, then these coated particles and the polymers in the triple points arrange in a 3-0 connectivity. The values of measured dielectric constant are used to calculate the amounts of the polymer forming the coating layer and in the triple point areas. The equations used for each composition in the calculation are:

$$\frac{1}{K_m} = \frac{v_{PZT}}{K_{PZT}} + \frac{v_c}{K_{epoxy}} \tag{4}$$

$$K = \frac{v_m K_m \left(\frac{2}{3} + \frac{K_{epoxy}}{3K_m}\right) + \left(v_{epoxy} - v_c\right) K_{epoxy}}{v_m \left(\frac{2}{3} + \frac{K_{epoxy}}{3K_m}\right) + \left(v_{epoxy} - v_c\right)} \tag{5}$$

where K_m: dielectric constant of coated particle phase;
K_{PZT}: dielectric constant of PZT particle;
K_{epoxy}: dielectric constant of epoxy;
v_{PZT}: total volume fraction of PZT phase in the composite;
v_{epoxy}: total volume fraction of epoxy in the composite;
v_c: volume fraction of epoxy in the coating layers;
$v_{epoxy} - v_c$: volume fraction of epoxy in the "triple points";
K: dielectric constant of composite sample.

Equation (4) is for series mixing and represents the mixing of the PZT particles with the coating epoxy because the range between the values of the dielectric constants of two phases are very large. Equation (5) is the one for the Maxwell mixing rule (3-0) and represents the mixing between the coated particles and the epoxy in the "triple points". The calculation results are listed in Table II. It is found that the amount of the epoxy in the triple points increases linearly with increasing amount of the epoxy in the composite samples.

2) MODEL TWO

In this model, we assume that parts of the ceramic particles are dispersed in the epoxy matrix and other portions of the particles are connected in 1- dimension along the direction of electric flux. Figure 11 is the geometric representation of the model. The dispersed particles in the epoxy matrix together with the surrounding epoxy are treated as

TABLE II. CALCULATED VOLUME FRACTIONS (%) OF EACH PHASE

		MODEL ONE		MODEL TWO	
TOTAL PZT	TOTAL EPOXY	EPOXY in coating layer	EPOXY in "triple points"	PZT dispersed in epoxy	PZT connected in 1-D path
53.0	47.0	4.1	42.9	51.3	1.7
62.0	38.0	3.6	34.4	59.7	2.3
70.3	29.7	1.5	28.2	63.7	6.6
73.0	27.0	1.5	25.5	66.3	6.7
75.0	25.0	1.4	23.6	67.8	7.2
77.5	22.5	1.4	21.1	70.2	7.3
79.0	21.0	1.4	19.6	71.2	7.8
81.0	19.0	1.4	17.6	73.0	8.0
82.5	17.5	1.3	16.2	74.1	8.4
83.6	16.4	1.3	15.1	75.1	8.5
85.0	15.0	1.3	13.7	76.4	8.6

a 0-3 mixing, and due to the large differences in the values of the dielectric constant of the two phases, the relation between these two phases can be represented by the series mixing rule. Then the 1- dimension connected particle phase mixes with this combination in a 1-3 connectivity and can be represented by the parallel mixing rule. Again, The values of measured dielectric constant are used to calculate the amounts of the PZT dispersed in the epoxy matrix and that of the 1- dimension connected region. The equations used for each composition in the calculation are:

$$\frac{1}{K_m} = \frac{v_d}{K_{PZT}} + \frac{v_{epoxy}}{K_{epoxy}} \tag{6}$$

$$K = (v_{PZT} - v_d) K_{PZT} + (v_{epoxy} + v_d) K_m \tag{7}$$

where K_m: dielectric constant of dispersed particles with the surrounding epoxy;

v_d: volume fraction of PZT dispersed in the epoxy matrix;

$v_{PZT} - v_d$: volume fraction of PZT forming 1-D path;

$v_{epoxy} + v_d$: volume fraction of the dispersed PZT and the epoxy matrix;

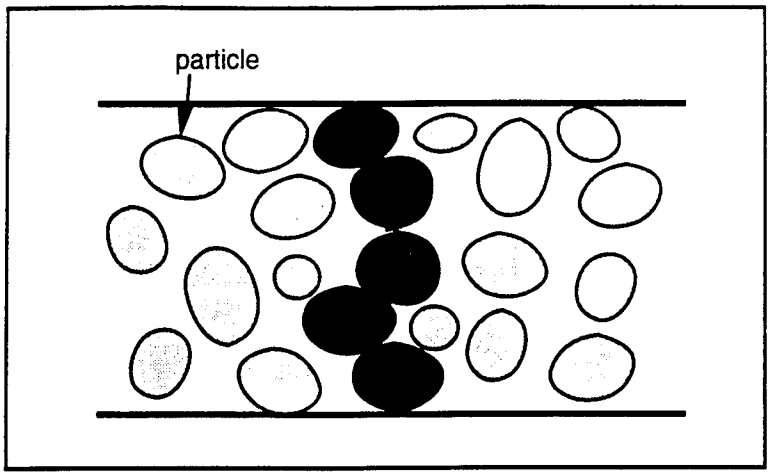

Figure 11. Geometric representation for model Two. The dark shaded particles show the 1-D connectivity. The matrix region is a (0-3) connected composite.

The values of the calculation result are also listed in Table II. A linear relation was also found between the volume fraction of PZT dispersed in the epoxy matrix and the amount of PZT forming 1- dimension path in the high loading region of the PZT particles. It can be seen from Table II that this model predicts that most of the particles are dispersed in the epoxy matrix and only small portions of the particles are interconnected forming the 1- dimension path through the sample.

It is noted that the models introduced are only applied to the high particle loading case for the composite materials. For low particle loading the existing mixing rules such as the Maxwell mixing rule are still valid. Based on (Newnham and Trolier-Mckinstry, 1990), heating a connected particle phase in a polymer can convert (3-3) to (0-3) connectivity. However, the dielectric constant vs. temperature (Figure 8) for our materials shows no evidence of conversion of a (1-3) to a (0-3) connectivity. By comparing the above two models and the temperature behavior of the dielectric properties, we believe that the first model may be more applicable to these particular composite materials. More work may be needed to determine the real internal structure of these composite materials.

CONCLUSION AND FUTURE WORK

1. We have demonstrated that the piezoelectric ceramic phase loading in the composite samples can be increased up to 85% volume percent by using a unique preparation method developed in our laboratory.

2. An almost linear relation was found between the piezoelectric constant d_{33} and the volume fraction of ceramic phase in the composite materials. As a result of the high PZT volume fraction, both dielectric and piezoelectric properties of these composites are better than those reported in the literature for the same class of materials.

3. Two new models were suggested to explain the structure of the materials and the dielectric properties of the composites.

4. The rather high piezoelectric constant, superior sensor performance and the ability to tailor the sensor shape and properties indicate the applications of these materials as transducers in smart systems.
5. Further optimization of the composite properties may be achieved by choosing different ceramic and polymer phase combinations. The poling process may also be further optimized to obtain desired properties.
6. Further evaluation of electrical performance in "smart system" is underway.

REFERENCES

Newnham, R.E., D.P. Skinner, K.A. Klicker, A.S. Bahalla, B. Hardiman and T.R. Gururaja. 1980, Ferroelectrics 27, 49.

Newnham, R.E. 1987, Chemtech, January.

Newnham, R.E. and S. Trolier-Mckinstry, 1990, J. Appl. Cryst. 23, 447-457.

Skinner, D.P., R.E. Newnham and L.E. Cross. 1978, Mater. Res. Bull. 13, 599.

Xu, Q.C., A. Dogan, J. Tressler, S. Yoshikawa and R.E. Newnham. 1991, IEEE Ultrasonic Symposium Proceedings (Florida).

APPENDIX 54

THE EFFECT OF DIFFERENTIAL SHRINKAGE ON MICROSTRUCTURAL DEVELOPMENT IN LTCC MULTILAYER SUBSTRATES

W. S. Hackenberger, T. R. Shrout, and J. P. Dougherty
Center for Dielectric Studies
The Pennsylvania State University
University Park, PA 16802
Phone: (814) 865-9931; Fax: (814) 865-2326

R. F. Speyer
Materials Engineering
Georgia Institute of Technology
Atlanta, GA 30332-0245
Phone: (404)-894-6075

ABSTRACT

The microstructural development of a multilayer substrate during co-firing was investigated using a combination of Environmental Scanning Electron Microscopy and sinter/quenching experiments. The multilayer samples were composed of a low temperature co-fireable ceramic substrate with buried silver thick films. At low heating rates the film was found to delaminate from the substrate during initial stage sintering of the silver. This delamination was healed as soon as the film's glass frit softened and flowed to the substrate and no further damage occurred. For heating rates greater than 25 °C/min delamination occurred above 800 °C and was facilitated by porosity at the film/substrate interface. This porosity was due to residual gases from the binder burnout process.

Key Words: Environmental Scanning Electron Microscopy, differential shrinkage, delamination.

1. INTRODUCTION

Low temperature co-fireable ceramics (LTCC's) have found use in the microelectronics industry as ceramic packaging for integrated circuits. LTCC electronic packages combine tape cast and

thick film technologies, and in general the materials used consist of ceramic-glass or metal-glass composites.

The advantages of this technology over co-fired alumina packaging include the low sintering temperature of the materials (850 to 1000 °C), the high conductivity of the co-fireable conductors, and the low dielectric constant (< 10) of LTCC substrates [1]. However, the co-firing process even for LTCC's is complex and not well understood. Problems such as differential shrinkage [2], noble metal migration (especially silver), and substrate/component reactions [3] continue to be major challenges to the technology.

Of all these problems differential shrinkage is fundamental to all co-fired systems, and the most common resulting defect is delamination [4]. In the case of buried metallization, void formation is also possible. The causes of these defects can be related to transient stresses which arise due to the shrinkage rate differential between the co-firing components [3 - 6].

In order to better understand differential shrinkage in the context of industrial manufacturing practice, a series of experiments were performed to determine the effect of temperature and heating rate on the microstructural development of a typical LTCC multilayer substrate. The specific objective of this work was to determine the critical segments of a sintering cycle during which the most damage is likely to occur. To do this work some novel experimental tools were used. Sintering at low heating rates (<10 °C/min) was observed at the microscopic level in real time using an environmental scanning electron microscope (ESEM). The effects of higher heating rates were studied by sintering multilayers in a special fast fire furnace that provides highly accurate and reproducible temperature profiles.

The ESEM (an Electroscan ES-30) allows one to observe insulating samples without the need for a conductive coating. Its sample chamber can support atmospheres of almost any gas at pressures up to 2500 Pa (see figure 1). The instrument is equipped with a hot stage that can reach 1000 °C and a video cassette recorder for continuous collection of microstructure data. These features make the ESEM ideal for observing the sintering of real materials in real time.

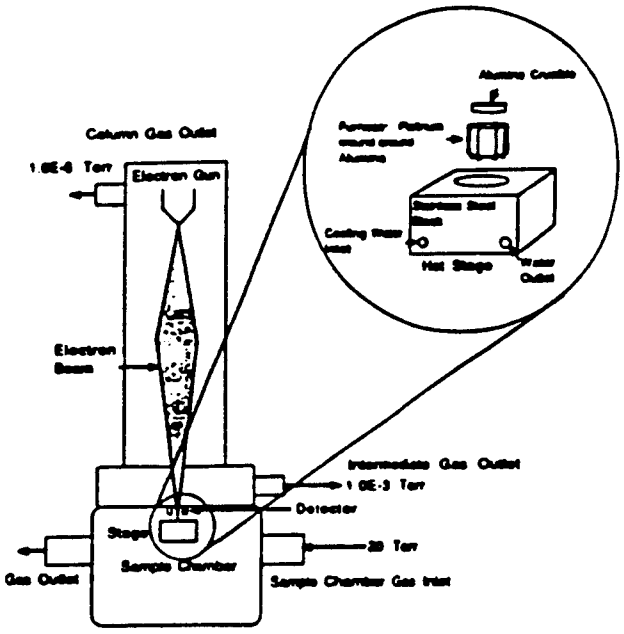

FIGURE 1. Schematic of the ESEM and its hot stage.

2. EXPERIMENTAL PROCEDURE

The materials chosen for this study were E. I. Du Pont de Nemours' 851AT Green Tape™ and 6142D silver thick film conductor. The Green Tape is a tape cast LTCC substrate material that is a composite of Pb-Ca-aluminoborosilicate glass, alumina , and quartz [7]. The 6142D silver thick film consists of silver particles and a glass frit. The 6142D is made specifically to be co-fired as a buried conductor film in a Green Tape substrate.

Two series of ESEM experiments were performed. First, the sintering of a 6142D silver film on an alumina substrate was observed to determine the effect of a planar constraint on the film microstructure. Second, Green Tape/silver multilayer co-firing was observed to determine those critical portions of a sintering profile where delaminations occur. The thick film sample was made by simply printing a 2.22 cm x 2.22 cm pad on 2.54 cm x 2.54 cm 96% alumina substrates using a 325 mesh screen. The films were about 7 - 10 μm thick. The Green Tape-silver multilayers used for the ESEM observations consisted of 10 Green Tape layers two of which were screen printed with 6142D silver paste. The stacking was such that the silver layers were all buried, and lamination was done by uniaxially pressing the stack under a pressure of 34 MPa and at a temperature of 75 °C for 15 minutes.

The ESEM multilayer samples were prepared by breaking the green multilayers and shaving off the resulting fracture surfaces with a hot razor blade. The fracture surfaces were perpendicular to the tape casting direction. The shaving was than pasted, with the fracture surface up, to the bottom of the alumina crucible used in the ESEM's hot stage (the crucible was approximately 0.635 cm in diameter and 0.159 cm deep). 6142D silver paste was used to insure good thermal contact between the sample and the bottom of the crucible. For silver thick films printed on alumina, the ESEM samples were prepared by simply breaking the substrate into pieces small enough to fit into the crucible. Sintering observations were made of the films' top surfaces. In all cases the samples' binders were burned out at 400 °C in a box furnace with flowing air.

The ESEM trials were done in an oxygen atmosphere at a pressure of 658 Pa. This was the maximum pressure that could be used below 850 °C without significantly degrading the image. The heating rate was controlled manually by means of a potentiometer that controlled the current flow to the hot stage. The average heating rates for the ESEM trials presented in this paper were approximately 5 to 7 °C/min.

To determine the effect of higher heating rates on the microstructural development of Green Tape-silver multilayers, samples were sintered in a fast fire furnace and then subjected to microstructure analysis with an ISI DS-130 SEM. The multilayers consisted of 10 layers of Green Tape three of which were printed. The printed layers were all buried. The rest of the multilayer preparation was the same as for the ESEM case. The sample sizes were about 1.2 cm x 0.7 cm.

The furnace used to sinter these samples was a tube furnace with an alumina sample holder connected to a stepper motor. The stepper motor pushes the sample into the furnace at a rate required to achieve a desired heating rate. In this way very accurate and reproducible heating and cooling rates as high as 100 °C/min can be achieved. Multilayer samples were sintered to various temperatures in the sintering range of both Green Tape and silver. The samples were held at temperature for 2 minutes and then quenched. Quenching was done by pulling the sample out of the furnace at the maximum stepper motor speed.

3. RESULTS AND DISCUSSION

3.1 ESEM Results Figure 2a and b show micrographs from the ESEM of a 6142D silver film on alumina. Figure 2a shows the film in its green state (some sintering of the silver occurred during binder burnout) while figure 2b shows the same portion of the film at 850 °C. ESEM observations showed that the silver powder begins to sinter at about 400 - 450 °C, and diffusional sintering and coarsening of the silver continues to about 650 °C. Around this temperature the glass frit softens and begins to wet and flow over the silver. By 750 °C sintering and coarsening of the silver is greatly enhanced due to liquid phase sintering through the glass frit. It is at this point that the large pores seen in figure 2b begin to form (note that some of these pores extend down to the alumina substrate).

Because the film is printed on a rigid substrate, it is constrained within the plane of the substrate, and during sintering the film can only shrink along its thickness. This constraint results in a tensile stress in the plane of the film which counteracts the effective sintering stress driving the densification [8]. The stress opposing densification is transient and depends on the amount of porosity in the film and on the film's free densification rate (i.e. the densification rate the film would have if it were unconstrained) [8]. Furthermore, materials subjected to stress at high temperatures will undergo creep, and if the stress is not overly large,the creep and sintering mechanisms will be similar (diffusional flow in the case of silver) [9].

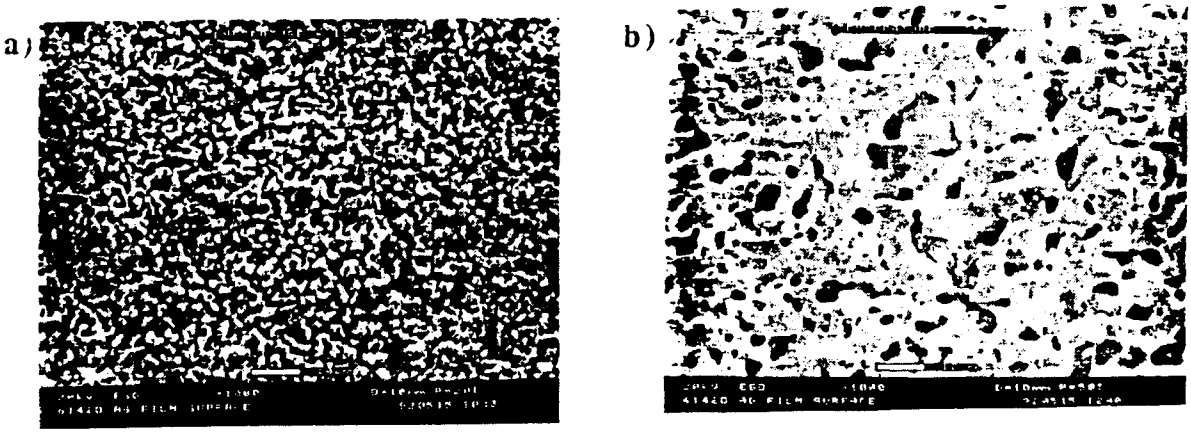

FIGURE 2. ESEM micrographs of 6142D silver films printed on alumina at temperatures of a) 450 °C and b) 850 °C. The scale bars represent 10 μm.

This then leads to an explanation of the pore growth that occurs after the frit softens. The densification rate will increase due to liquid phase sintering (dissolution/precipitation) of the silver through the glass. As mentioned above this will tend to increase the transient stress. By the same token, creep deformation by cavity growth, which is governed by surface and grain boundary diffusion [10,11], will be enhanced by the presence of a liquid solvent. Because the transient stress will be concentrated at the grain boundaries due to the porosity, large, crack-shaped pores will tend grow rapidly once easy diffusion through a liquid phase is possible [10,11].

In the case of multilayers the transient stresses arise in both the film and the substrate and depend on the difference in their free densification rates [3]. Figures 3a - d are micrographs from an ESEM observation of Green Tape/silver co-firing. These micrographs show an edge view of a buried film in a multilayer where the silver film runs nearly vertically across the center

of each figure and is sandwiched between two layers of Green Tape. The film is buried so that its plane extends back into the page and its thickness is in the plane of the page.

Figure 3a shows the multilayer at 470 °C. By this time the film has already undergone a considerable amount of sintering by diffusional transport of the silver, but the substrate has not yet begun to densify. It is also evident in this micrograph that there is a large amount of porosity at the film substrate interface. This porosity was not seen when the multilayer was in its green state and indicates that the film was able to pull away from the substrate and shrink within its plane. Thus, this initial stage delamination allowed the film to sinter relatively unconstrained compared to the case of a film printed on a rigid substrate.

Figure 3b shows the same multilayer at 652 °C. By this temperature the silver film has almost completely densified by solid state sintering and the substrate has begun to sinter by viscous flow of the glass phase (the large irregularly shaped particles in figure 3b; the smaller equiaxed particles are alumina). Also the glass frit in the film has just begun to soften. The fact that the film has almost completely densified before the frit softened is further evidence that it was able to pull away from the substrate. The porosity at the interface with the substrate is also becoming reduced indicating that the initial stage delamination is being healed as the substrate shrinks in around the film.

In figure 3c the multilayer is at 759 °C. The substrate has densified as much as possible by simple viscous flow and further shrinkage requires that the glass flows over the alumina and infiltrates the alumina interparticle spacing [12,13]. The glass frit in the film has thoroughly wetted the silver and the initial stage delamination has been healed. The glass in both the film and the substrate has flowed to fill in the porosity at the interface.

Finally, figure 3d shows the microstructure of the multilayer at about 850 °C, the nominal sintering temperature of these materials. The substrate has almost completely densified and the action of dissolution/reprecipitation of silver through the glass frit has homogenized the cross section of the film. That is areas of convex curvature have thinned while regions of concave curvature have thickened. The fact that no more damage has occurred in the film or the substrate, even though the substrate for most of its sintering range has been shrinking around a dense film, is largely due to stress relaxation in the substrate. Since the substrate consists mostly of glass, it responds to stress by bulk flow [14]. It should be noted that these experiments were carried out at relatively low heating rates (~ 5 °C/min). As will be shown, the situation at high heating rates (≥ 25 °C/min) is very different.

3.2. High Heating Rate Experiments Figures 4a - d and 5a - d show conventional SEM micrographs of multilayers sintered in the fast fire furnace at various heating rates and temperatures. The micrographs are all fracture surfaces and the view is the same as in the ESEM micrographs: an edge view of a buried silver pad. Note that all micrographs are of different samples. The high degree of temperature accuracy and heating rate reproducibility of the fast fire furnace ensures microstructural consistency from sample to sample.

Figures 4a and b show multilayers that were heated, respectively, at 25 and 100 °C/min to 600 °C, held for 2 minutes, and quenched. In both cases the silver in the film has sintered to some extent by diffusional flow but the glass in the film and the substrate has not yet softened. It is instructive to compare these micrographs with figure 3b. One can easily see that at the higher heating rates the sintering of silver is greatly delayed so that a significant amount of porosity persists in the film above a temperature of 600 °C. Also there is very little, if any, initial stage delamination between the substrate and the film at the higher heating rates.

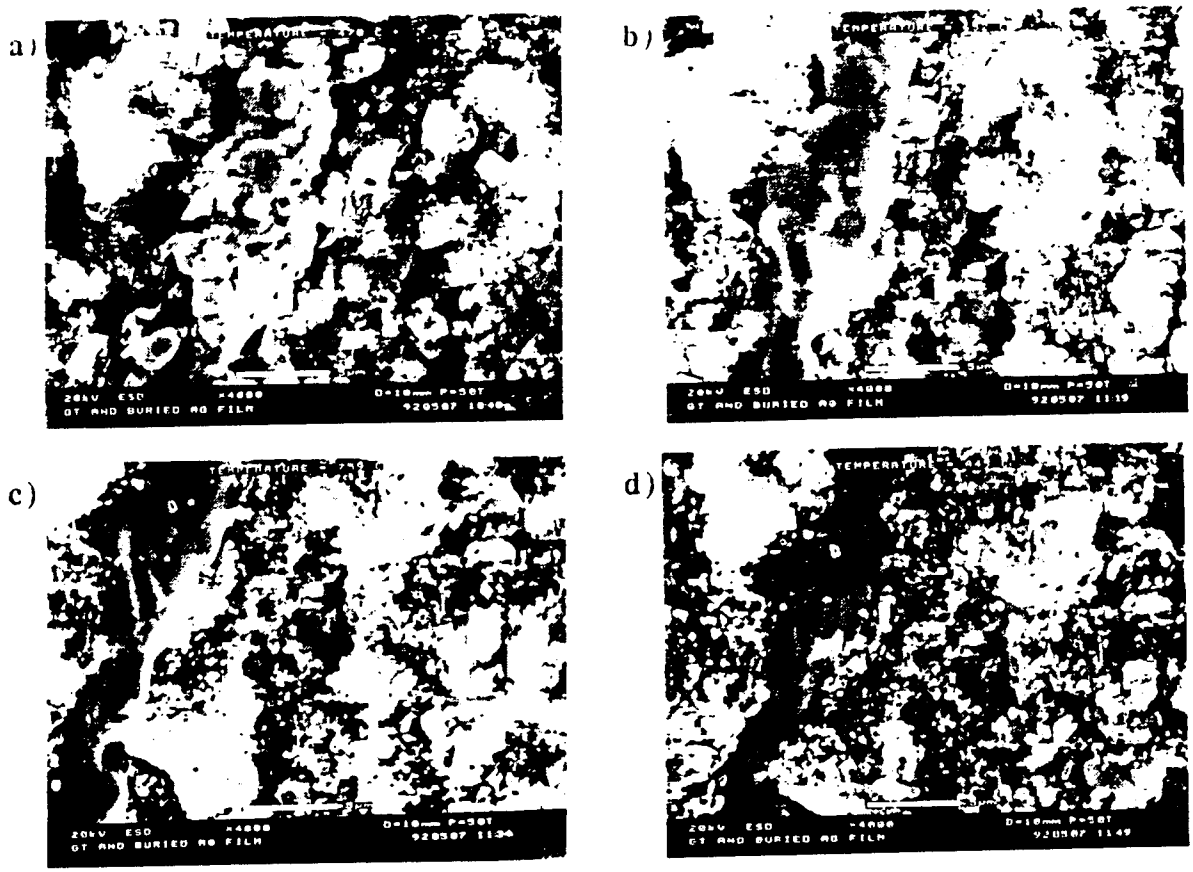

FIGURE 3. ESEM micrographs of a Green Tape/silver multilayer at a) 470 °C, b) 652 °C, c) 759 °C and d) 845 °C. The scale bars represent 5 μm.

Figures 4c and d show multilayers heated to 750 °C again at 25 and 100 °C/min. By this temperature considerable sintering of both the substrate and the film has taken place and the glass frit in the film has softened. The interface between the film and the substrate is excellent with no evidence of delamination. The delayed silver sintering due to the high heating rate is still quite apparent in the microstructure from the large amount of porosity. As expected the delayed sintering is more evident in the sample sintered at 100 °C/min.

The next set of micrographs (figures 5a - d) show multilayers sintered at 800 °C and above. Figures 5a and b show samples sintered at 800 °C at heating rates of 25 °C/min and 100 °C/min, respectively. In figure 5a the film and substrate appear to have a similar level of relative porosity. The interface is still very good, but there is a small degree of delamination in some areas. At the higher heating rate (figure 5b) this delamination is considerably more severe. As the sintering temperature is increased to 850 °C (figures 5c and d) the delamination worsens for both heating rates. Inspection of the interface between the film and the substrate reveals the existence of a large number of spherical pores.

The spherical pores are most likely due to entrapped gasses from binder burnout. A conservative burnout schedule was used for all these samples (3 hours at 400 °C in flowing air), but residual carbon from the burnout process will tend to persist and slowly form carbon oxides up to temperatures of about 800 °C. High heating rates would tend to delay the oxidation of residual carbon to temperatures were there is no open porosity in the multilayer, thus, entrapping the resulting gasses. Since thick film pastes contain a large amount of organic

compounds most of the porosity is at the film/substrate interface. These pores will greatly weaken the interface by reducing its load bearing area.

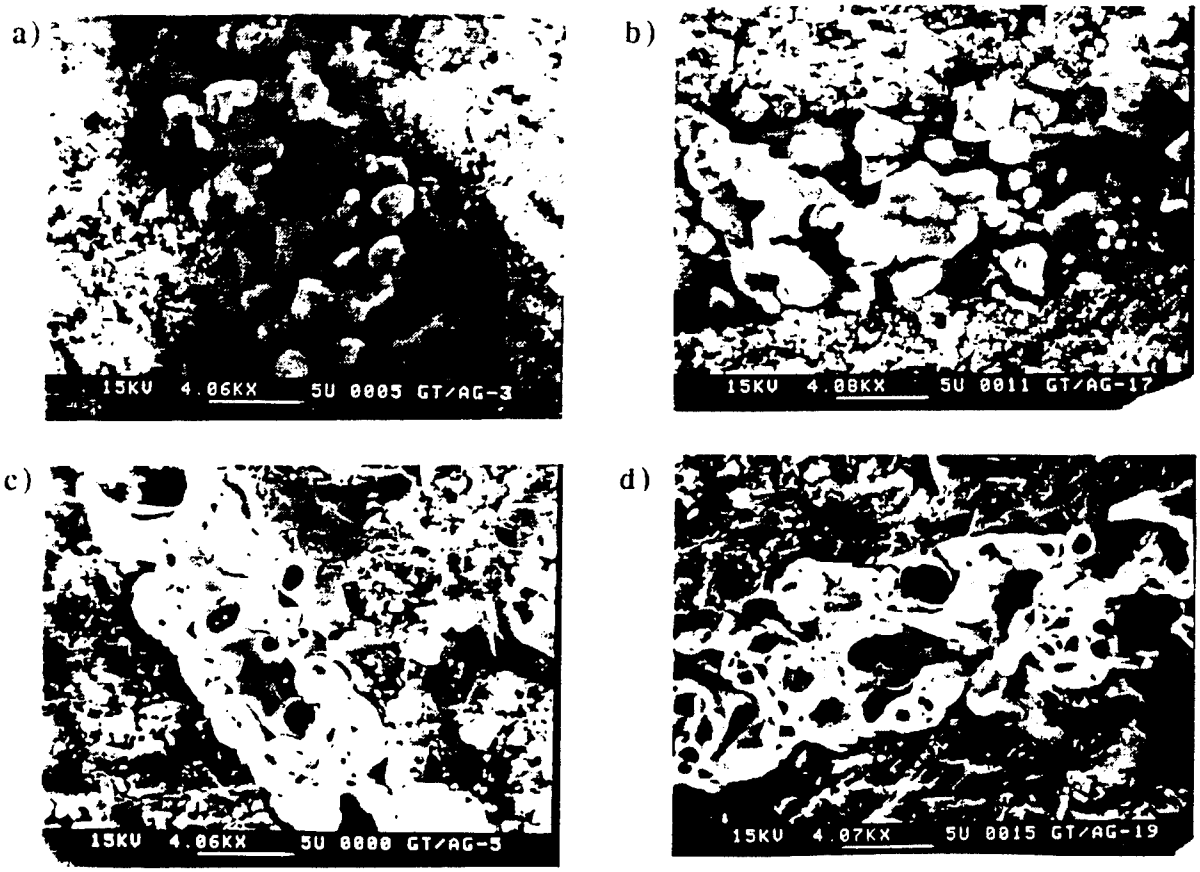

FIGURE 4. Green Tape/silver multilayers sintered at a) 25 °C/min to 600 °C, b) 100 °C/min to 600 °C, c) 25 °C/min to 750 °C and d) 100 °C/min to 750 °C. The scale bars represent 5 μm.

The high heating rates also delayed the sintering of silver so that at high temperature there was still a differential shrinkage between the film and the substrate resulting in stress being exerted on the interface. At the same temperature for samples heated at low heating rates, the film was already densified so that the substrate simply compressed in around it. But at high heating rates the differential shrinkage provides a driving force for the film to separate from the substrate, a process which is facilitated by the weakened interface.

The above results were found to be independent of cooling conditions indicating that the observed damage was due to differential shrinkage and not thermal expansion mismatch. Also samples sintered to 850 at 25 °C/min after an additional burnout step at 600 °C showed less delamination. There are actually two effects at work here: 1) the longer, higher-temperature burnout provided for more residual carbon removal before the onset of closed porosity and 2) more silver sintering would have occurred during burnout limiting the differential shrinkage at high temperature.

4. CONCLUSIONS

A combination of ESEM and sinter/quenching studies have been used to observe the effect of differential shrinkage on the microstructure of an LTCC multilayer substrate. It was found that at low heating rates (~ 5 - 10 °C/min) buried silver films almost completely densified before the onset of sintering in the substrate. The prominent defect in these samples was an initial stage delamination which healed once the substrate began sintering. In contrast the prominent defect in films printed on a dense, rigid substrate is void formation due to local creep deformation.

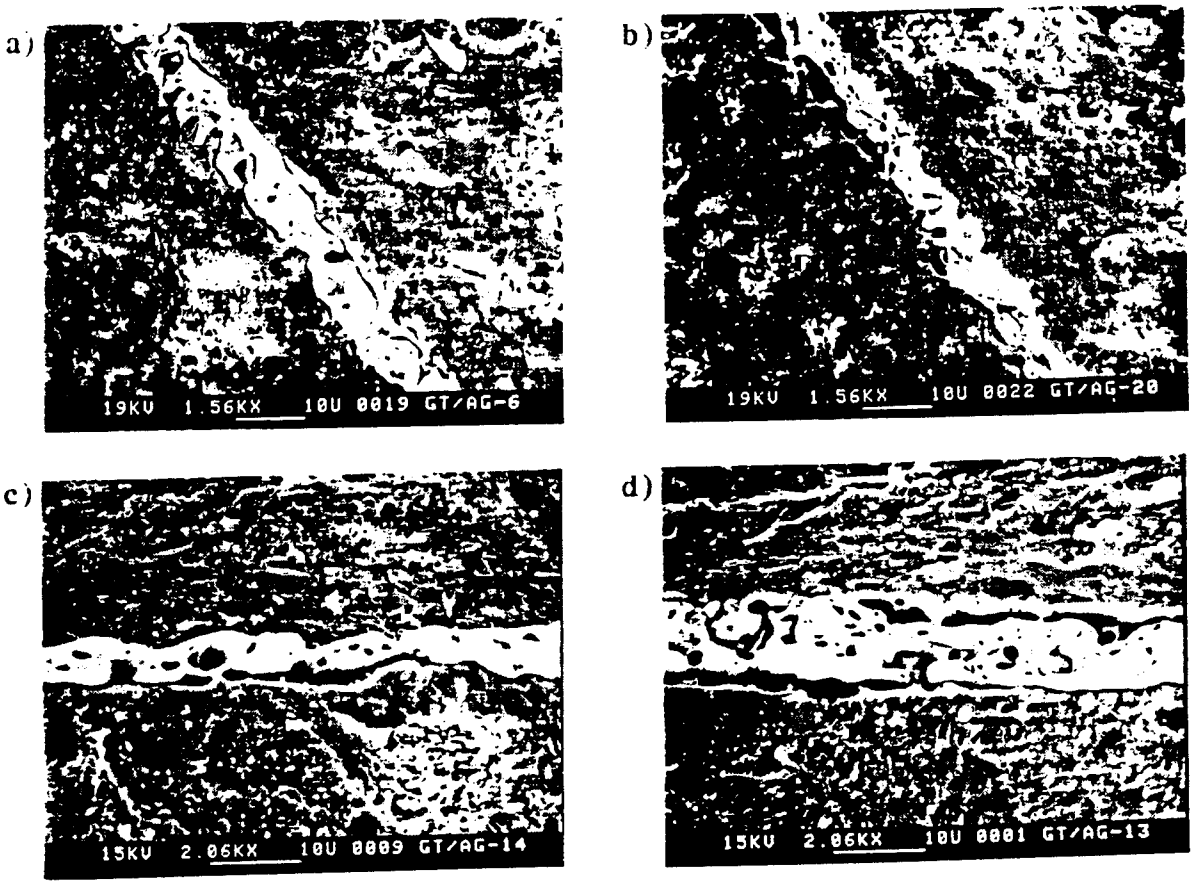

FIGURE 5. Multilayers sintered at a) 25 °C/min to 800 °C. b) 100 °C/min to 800 °C, c) 25 °C/min to 850 °C, and d) 100 °C/min to 850 °C. The scale bars represent 10 μm.

For multilayers sintered at high heating rates (25 - 100 °C/min), the sintering of the silver film was greatly delayed so that the film and the substrate sintered concurrently. Above 800 °C the differential shrinkage between the film and substrate lead to delamination which was facilitated by porosity at the interface. The porosity was due to entrapped gases resulting from insufficient carbon removal before the onset of closed porosity.

These observations suggest that low heating rates (at least at temperatures below 700 - 650 °C) are best for LTCC multilayer sintering where the buried metallization is silver. Lower heating rates facilitate almost complete densification of the silver before the onset of sintering in the substrate. Once the substrate does sinter it shrinks in around a dense silver film healing any initial stage delamination. Even though the film would tend to act like a rigid inclusion with

respect to the substrate, further sintering damage is prevented through stress relaxation by viscous flow of the glass (note that stress relaxation would not necessarily occur if the substrate were a sintering ceramic, and thus further sintering damage would be possible). Higher heating rates could be resumed above 650 °C to limit silver migration which in other work was found to be more severe at high temperatures and low heating rates [15].

5. REFERENCES

1. J.I. Steinberg, S.J. Horowitz, and R.J. Bacher, 5th European Hybrid Microelectronics Conference, (1985).

2. T. Cheng and R. Raj, J. Am. Ceram. Soc., 72, (9) 1649 (1989).

3. R.C. Sutterlin, Thick Film Resistor Interactions in Integrated Ceramic Packaging, M. S. Thesis, The Pennsylvania State University, University Park, PA 1990.

4. R.K. Bordia and R. Raj, J. Am. Ceram. Soc., 68, (6), 287 (1985).

5. A.G. Evans, J. Am. Ceram. Soc., 65, (10), 497 (1982).

6. C.H. Hsueh, A.G. Evans, R.M. Cannon, and R.J. Brook, Acta Metall., 34, (5), 927 (1986).

7. U. S. Patent 4,654,095 (Mar 31, 1987) J.I. Steinberg (to E.I. Du Pont de Nemours, Inc.).

8. G.W. Scherer and T. Garino, J. Am. Ceram. Soc., 68, (4), 216 (1985).

9. M.N. Rahaman, L.C. De Jonghe, and R.J. Brook, J. Am. Ceram. Soc., 69, (1), 53 (1986).

10. J.R. Porter, W. Blumenthal, and A.G. Evans, Acta Metall., 29, 1899 (1981).

11. C.H. Hsueh and A.G. Evans, Acta Metall., 29, 1907 (1981).

12. W.S. Hackenberger, T.R. Shrout, J.P. Dougherty, and R.F. Speyer, 1992 Proc. International Symp. on Microelectronics, 82 (1992).

13. D.H.R. Sarma and R.W. Vest, J. Am. Ceram. Soc., 68, (5), 249 (1985).

14. G.W. Scherer, J. Non-Crystalline Solids, 34, 239 (1979).

15. W.S. Hackenberger, T.R. Shrout, J.P. Dougherty, and R.F. Speyer, 1993 Proc. International Symp. on Microelectronics, 215 (1993).

APPENDIX 55

journal

Silver-Palladium Thick-Film Conductors

Sea Fue Wang* and Joseph P. Dougherty*

Center for Dielectric Studies, Materials Research Laboratory, The Pennsylvania State University, University Park, Pennsylvania 16802

Wayne Huebner*

Ceramic Engineering Department, University of Missouri-Rolla, Rolla, Missouri 65401

John G. Pepin*

DuPont Electronics, Research Triangle Park, North Carolina 27709

The trends in integrated circuit packaging technology are toward high speed, high density, reliability, and low cost. These demand the improvement of material formulations and processing technology. Among the thick-film materials systems, conductor materials generally represent an important and the most expensive element. Therefore, attention has been centered on the performance of the fired metal film and its cost. Silver and palladium (Ag/Pd) conductors are important components of thick-film paste technology. Thick-film Ag/Pd conductors find applications in many aspects of electronics and electronic packaging, such as hybrid microcircuits, multichip modules, packaging for integrated microcircuits, and in passive electronic components such as multilayer capacitors, varistors, and inductors. In this paper, the performance and properties of fired Ag/Pd films are discussed through their physical and chemical aspects. The final film properties are correlated to a number of factors, including thermodynamics and kinetics of Pd oxidation during burnout and firing; chemical and physical reaction of the Ag/Pd with the ceramic substrate, organic vehicle, and solder; Ag diffusion and migration; inorganic and organic additives; powders characteristics; and paste properties.

I. Introduction

DURING the past 30 years, electronics system requirements have demanded higher circuit speeds, device densities, and reliability, along with lower costs for integrated circuit packaging technology. These demands have accelerated the progress of materials development and processing technologies of both active and passive components, such as capacitors, resistors, conductors, substrates, varistors, thermistors, and semiconductors.[1-5] A common element of nearly all of these components is a thick-film conducting phase, although its configuration, purpose, and performance may vary widely. Importantly, these thick-film conductors often contain precious metals and thus represent a major fraction of the materials cost. In this paper we review thick-film conductor technology, using the Ag/Pd metallization system as the primary example.

II. Characteristics of Metal Conductors

Controlling the properties of thick-film metal conductors used in electronic packaging is not a simple matter and dictates a thorough understanding of structure ⟷ property ⟷ processing relationships. Indeed, most metals used for conductors are not utilized in their pure state. Instead, they may be alloyed with other metallic components or have oxide components added to control properties such as adhesion or densification

B. B. Ghate—contributing editor

Manuscript No. 194446. Received July 9, 1993; approved September 26, 1994.
*Member, American Ceramic Society.
Author to whom correspondence is to be addressed. Present address: Vitramon Incorporated, P.O. Box 544, Bridgeport, CT 06601-0544.

rate. Figure 1 is a schematic overview of the many interrelated factors which can affect the final desired properties. Throughout this paper we will be working within this general framework, pointing out the important issues which impact the use of thick-film metal conductors in different applications.

A good place to start is an overview of the properties intrinsic to individual metals in their pure state. Table I summarizes several properties of commonly used pure metal conductors. Figure 2 classifies their use depending upon the relative firing temperature and atmosphere.[7] In general, high electrical conductivity metals are favorable for high-frequency, low-loss, hybrid circuit applications, since the skin effect is minimized. For multilayer ceramic devices, a high conductivity for the internal metallization is important to reduce the dissipation factor, especially at high frequencies.[8,9] The best electrical conductors are elements residing in Groups I, II, and III of the periodic table. The elements of Group IB (Cu, Ag, and Au) have a valence of one. They are among the best conductors known and the most widely used in electronics.[10] However, due to their low melting temperatures, these metals and their alloys are used only at low firing temperatures (<1000°C). Metals with valences of two or three, such as Al, Pd, Pt, Ni, and W, are also good conductors, although not as good as those of Group IB. When used in thick-film compositions with added glass frits, these metals can be fired at low temperatures.

The thermal expansion coefficients (TECs) of these metals range from $\approx 4.5 \times 10^{-6}$/°C for W up to $\approx 29 \times 10^{-6}$/°C for Pb. As shown in Fig. 3, the TEC varies inversely with melting temperature. Strongly bonded metals have high melting temperatures and low TECs.[11] The bond strength is also reflected by an increase in Young's modulus with melting temperature, which is also shown in Fig. 3. These differences in elastic compliance and TEC, along with the resultant interfacial shear stresses, can be the source of metallization ⟷ ceramic delaminations and cracks, in particular for applications which involve repeated temperature or mechanical cycling.[12-15]

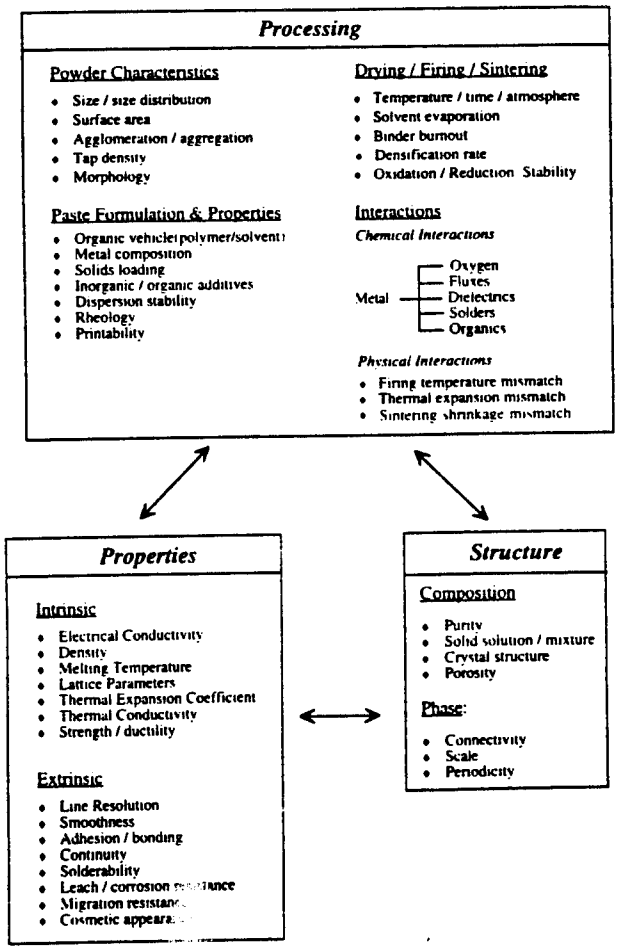

Fig. 1. Structure — property — processing relationships of thick-film, metallic conductors.

Since thermal conduction in a metal is carried primarily by the conduction electrons, most metals with a high electrical conductivity also have a high thermal conductivity. Hence, as seen in Table I, Ag, Cu, and Au are the best thermal conductors. For thick-film technology, the thermal conductivity of metals is usually not a major concern. However, for high-field multilayer ceramic devices, thermal breakdown is an important failure mechanism; hence, any improvement in the thermal conductivity is beneficial. In addition, a higher thermal conductivity can reduce the thermal shock imparted to a multilayer ceramic structure during soldering. The large differences in thermal conductivity between the metal and ceramic can introduce thermal anisotropy into a 2-2 composite structure.[16]

The oxidation/reduction stability of metals is another important factor in processing thick-film compositions. Oxidation and reduction reactions during cofiring may adversely affect the ultimate electrical conductivity of the metal phase, result in the formation of structural defects, and cause chemical reactions between the metal and the ceramic. Figure 4 shows the thermodynamic oxidation stability of a number of metals used in thick-film technology.[17] Table II gives their volume expansion on oxidation, assuming no porosity.

It is clear that only noble metals are thermodynamically stable in air over the temperature range commonly used for processing electronic ceramics containing thick-film materials. Whenever the metal is oxidized, the associated large volume change can generate internal stresses and mechanical defects. In the cases of Ag, Au, and the other semiprecious and precious metals used in thick-film compositions, the reduction of metal powder surface area on sintering acts to eliminate oxidation as a factor in the performance of thick-film pastes containing these metals.[18] In the case of Ni and Cu, inexpensive base metals, oxidation is a key factor, since these metals oxidize and remain oxidized during the firing process rather than sinter to lower effective surface areas. In thick-film technology, Cu conductors are usually fired in a nitrogen atmosphere in a belt furnace. However, Cu is thermodynamically stable in a nitrogen atmosphere only above its melting point.[4] The fast firing profile used and the frit, however, allow only limited oxidation during firing. Moreover, slight oxidation is desirable sometimes, since it can enhance adhesion due to the presence of copper oxides.[19]

In the cofiring of multilayer structures, a longer firing schedule is sometimes needed, requiring that the oxygen partial pressure be kept lower than the metal/metal oxide equilibrium value of Fig. 4 to prevent excessive oxidation. Typical atmospheres used include H_2O-H_2, CO_2/CO, NO_2/NO, Ar, or their combinations.[4,20] Unfortunately, RuO_2 or pyrochlore structure-type ruthenates, typical thick-film resistor components, are not stable under the reducing conditions required for firing Cu. Nickel has a higher melting temperature than that of Cu, so it has the potential to be used in high-fire systems. However, the lower oxidation resistance of Ni dictates a reducing firing atmosphere ($p_{O_2} < 10^{-8}$ atm at 1100°C). This requirement places tight restrictions on the formulation of the dielectric. In addition to RuO_2, PbO, and Bi_2O_3, other common constituents in ceramic packaging should not be used when Ni metallizations are fired. A further problem with Ni conductors is the paramagnetic skin effect which reduces electrical conductivity at high frequencies.

III. Comparison of Thick-Film Conductors

Table III provides some general performance characteristics related to extrinsic properties of the various metals used in thick-film conductor technology.[21,22] Most thick-film conductors are noble metal-based; the most common are Au, Pd, Pt, Ag, and binary or ternary alloy combinations of these metals. These conductor systems do not oxidize when fired in air.[23-25]

Table I. Properties of Common Electrode Metals

Metal	Density (g cm⁻³)	Melting temperature (°C)	Lattice parameter (Å)	Electrical resistivity (×10⁻⁶ Ω cm, 298 K)	Thermal expansion coefficient (×10⁻⁶ K⁻¹)	Thermal conductivity (W m⁻¹ K⁻¹, 300 K)	Young's modulus (GPa)
Silver	10.5	961	4.0857 (fcc)	1.59	19.2	429	76
Gold	19.3	1063	4.0783 (fcc)	2.35	14.2	317	80
Platinum	21.4	2045	3.9240 (fcc)	10.6	9	71.6	147
Palladium	12	1825	3.8839 (fcc)	10.8	11.2	71.8	112
Copper	8.96	1083	3.6147 (fcc)	1.7	16.5	401	110
Lead	11.4	327	4.9500 (fcc)	0.6	29.1	35.3	14
Nickel	8.9	1453	3.5238 (fcc)	6.84	13.3	90.7	207
Molybdenum	10.2	2610	3.1470 (bcc)	5.2	5.43	138	324
Tungsten	19.3	3410	3.1652 (bcc)	5.65	4.59	174	407

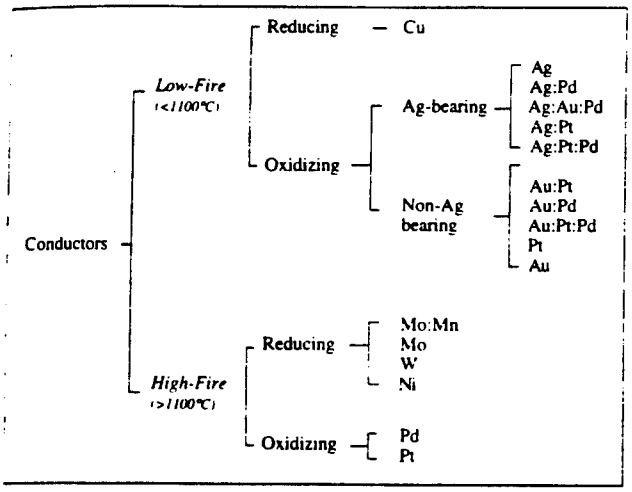

Fig. 2. Classification of common thick-film conductors.

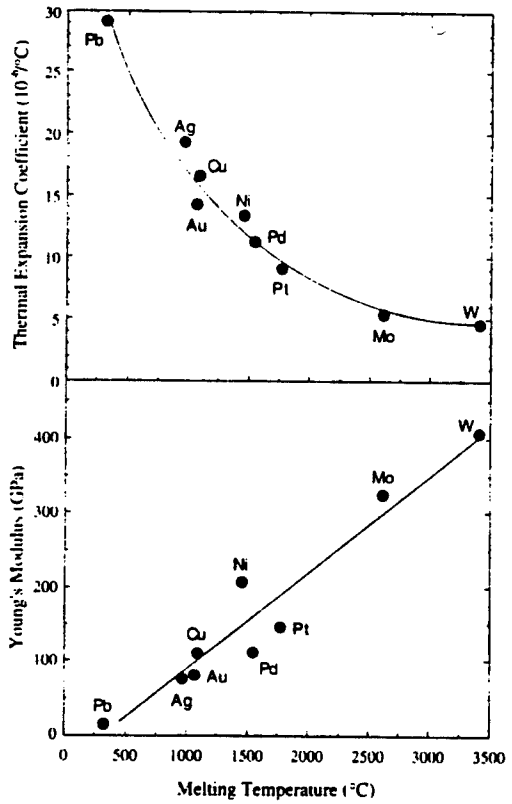

Fig. 3. Relationship of thermal expansion coefficient and Young's modulus with melting temperature for common electrode metals.

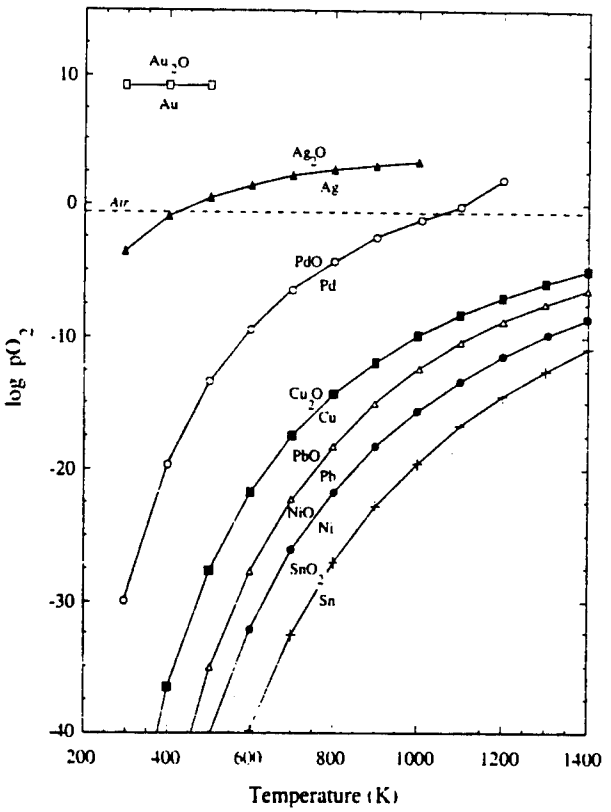

Fig. 4. Oxidation stability with temperature and partial pressure oxygen for common electrode metals.

Table II. Volume Expansion due to the Oxidation of Common MLC Internal Electrode Metals

Metal	Oxide	V_{ox}/V_{met}
Pd	PdO	1.68
Ag	Ag_2O	1.56
Ni	NiO	1.66
Cu	Cu_2O	1.65
Pb	PbO	1.28
Sn	SnO_2	1.33

Gold and Pt are high in cost. Gold exhibits the highest conductivity and excellent wire bondability and migration resistance, but cannot withstand Sn/Pb solder.[5,26] Additions of Pt or Pd to form Au/Pt and Au/Pd alloys circumvent the solderability problem, but result in a lower electrical conductivity and higher cost.[25,27-29] Au/Pt systems also have the problem of fissuring in the fired film. Partial replacement of Au by less expensive Pd yields the Au/Pt/Pd alloys,[29-31] which increase the density of the film as well as the solder leaching resistance. The ternary

Table III. Performance of Conductors in Thick-Film Microelectronics

Metal	Solderability	Solder leach resistance	Corrosion resistance
Au	Poor	Poor	Excellent
Pt:Au	Excellent	Good	Excellent
Pd:Au	Good	Good	Excellent
Ag	Good	Poor	Poor
Pt:Ag	Good	Good	Good
Pd:Ag	Good	Good	Good
Pd:Pt:Ag	Good	Good	Good
Cu	Excellent	Excellent	Poor
Ni	Good	Excellent	Excellent
Polymeric	Poor*	Poor*	Good
W, Mo, Mo:Mn	†	†	Good

*Usually not formulated to be soldered. †Usually not soldered.

alloy also reduces the dependence of the fissuring on the Pt sources. However, Au, Au/Pd, and Au/Pt systems result in a high contact resistance when used with doped glazed resistors. Partial substitution of Au by Ag, Au/Ag, Au/Pd/Ag, or Au/Pt/Ag substantially lowers the cost and the contact resistance.[32-34]

Although Ag has the highest conductivity among these conductors, it has the problem of electromigration in humid conditions under bias. Silver also has poor solder leach resistance. Additions of Pd or Pt to Ag, i.e., the Ag/Pd and Ag/Pt, as well as Ag/Pd/Pt alloy systems, help minimize these problems,[35-38] but at the expense of increased cost and lower electrical conductivity.

The addition of Pt or Pd to Au or Ag increases the electrical resistivity. Therefore, in the fabrication of multilayer substrates, pastes of these alloys are used only for the top conductor layer or for the solder pads. The inner conductor layers are formed from the unalloyed Au or Ag paste.

Copper, Ni, W, Mo, and Mo/Mn systems are used only when firing in a reducing or neutral atmosphere. Low-cost conductors based on Cu and Ni are available for some applications.[39] However, Ni does not have the high electrical conductivity of Cu, Ag, or Au, and thus its application to electronic circuits is limited. Thick-film Cu metallization, in addition to high electrical conductivity, exhibits advantages that include low solder leaching, no cation migration, low material cost, and a high thermal conductivity almost equal to that of Ag.[4] However, increased processing costs often outweigh raw material savings. A major drawback for using base metals in thick-film technology is the inefficient removal of the organic binder associated with the dielectric material in the low oxygen, inert gas atmosphere of the furnace. In addition, there is a tendency toward surface corrosion, and the industry has a limited availability of reliable and compatible thick-film dielectric and resistor systems.[40]

Refractory metals, Mo, W, and Mo/Mn, have been used for conductors for many years in high-temperature cofired systems such as Al_2O_3-based, multichip modules,[41-43] but they are nonsolderable. In order to become solderable, they must be plated with a solderable metal or alloy, such as Ni.

IV. Comparison of Various Internal Electrodes

Internal electrodes are the very important parts of the multilayer ceramic components such as actuators, transducers, inductors, varistors, capacitors, monolithic multilayer substrates, and chip carriers.[2,44-48] Here, we focus on multilayer ceramic capacitors. Figure 5 is a schematic diagram of a multilayer ceramic capacitor. The performance of the internal electrode directly affects the electrical performance, including the permittivity, dissipation factor, and insulation resistance.[8,49] For high-voltage applications, it also impacts the breakdown strength and the fatigue behavior.

In the early days of multilayer ceramic capacitors (MLCs), internal electrodes of the Au/Pt/Pd ternary were used in high firing temperature ("high-fire") $BaTiO_3$-based dielectrics.[50,51]

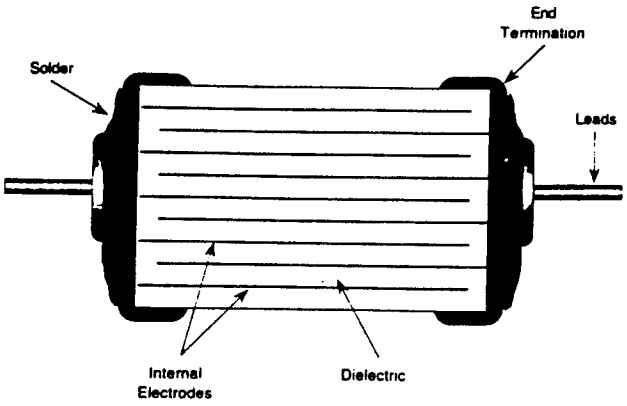

Fig. 5. Schematic diagram of a multilayer ceramic capacitor.

Although metals in this ternary do not create problems due to detrimental reactions, such as metal oxidation, Au- and Pt-containing electrodes are now used only in specialty capacitors, due to the high metal costs.

During the last decade, much MLC materials research and development concentrated on reducing internal electrode costs, which can account for a major portion of the materials cost in an MLC part.[2] The high and variable price of noble metals that have traditionally been used as electrode materials have forced the MLC capacitor industry to replace them with less expensive metals, such as Pd/Ag, Cu, Ni, and Pb.[23] In order to use these less expensive electrodes, it is necessary to either substantially reduce the sintering temperature of the dielectric, fire components in a reducing atmosphere, or inject electrodes made of solder alloy into the MLC structure after densification of the dielectric has been achieved.[51-55] These approaches to lowering the overall cost of a MLC without sacrificing performance are summarized in Fig. 6.

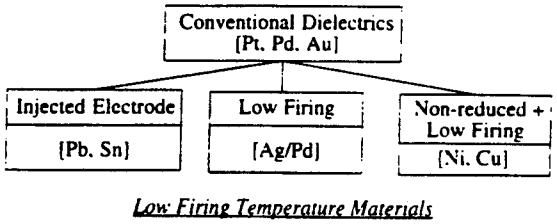

Low Firing Temperature Materials

- New Materials [relaxor ferroelectrics]
- Fluxed Systems [liquid phase sintering]

Fig. 6. Evolution of electrode utilization in multilayer capacitors.

Copper has a low melting temperature relative to most MLC dielectrics.[56,57] It can be used as an internal electrode only for dielectrics with a sintering temperature < 1000°C. Currently, many low-fire relaxor compounds have been developed using Cu as an internal electrode.[57] On the other hand, Ni could be used in high-fire systems; however, similar to Cu, the sintering atmosphere must be precisely controlled to keep the metal from oxidizing.[55,58] The low oxygen partial pressure required during firing elminates the use of Ni in Pb-based materials, due to metallic Pb formation.[59] Many dielectrics based on $BaTiO_3$ were developed to be cofired with Ni internal electrodes. These nonreducible dielectrics were formulated with stoichiometry control in order to prevent them from becoming semiconducting in reducing/neutral firing atmosphere.[55] The low cost of the base metal is traded off by the expensive costs of processing and equipment maintenance.[2] In addition, the electrical properties of most nonreducible dielectrics are strongly dependent on the sintering temperature, time, and atmosphere.

Another approach used to reduce electrode cost is the use of injected Pb/Sn alloys.[54] This method eliminates the troublesome reactions between metal and ceramic during firing at high temperatures. The injection process for making multilayer ceramic capacitors involves making MLC parts with a "fugitive electrode" (e.g., carbon black) which is removed during the burnout and firing process. The resulting empty electrode spaces are backfilled with a solder alloy injected under high pressures. The lead injection method is not widely used. Due to the high contact angle of the metal on dielectrics,[60] the method requires careful control in order to have a complete penetration of the molten metal into the electrode channel between the dielectric layers and to obtain a continuous electrode film.[48] The electrodes are usually thicker than those printed directly onto the unfired dielectric in order to ensure the formation of good connections between the plates. The thicker electrode associated with the presence of ceramic pillars in the electrode cavities reduces the volumetric efficiency.

Ag/Pd systems are widely used as internal electrodes in the MLC industry because they can be fired in air. Another reason is their melting temperature, and therefore the sintering temperature of MLC, which can be varied with simple changes in the Ag/Pd ratio. The system Ag/Pd is one of complete solid-solution formation, with the solidus and liquidus increasing in temperature monotonically from Ag to Pd (T_m^{Ag} = 692°C, T_m^{Pd} = 1552°C). Figure 7 shows this system.[61] For $BaTiO_3$-based dielectrics sintered at 1100°C, 70Ag/30Pd is usually used as the electrode. These dielectrics sometimes contain inorganic additives, such as PbO, Bi_2O_3, ZnO, B_2O_3, or SiO_2, which serve as sintering aids. The lower firing, relaxor type dielectrics can use 85% Ag/15% Pd or 100% Ag internal electrodes, although relaxor dielectric technology is not widely used in MLCs.

Copper and Ni may eventually replace noble and semiprecious metals in some applications in thick-film as well as MLC technology. However, noble metals are better suited for a wider variety of applications, do not require unique control of the firing atmosphere, and will probably continue to be incorporated into new applications, especially with new dielectric systems for which base metal compatibility has not been researched.

In the next few sections we will discuss applications of Ag/Pd thick-film conductors. We will relate the applications to the properties of oxidation of Pd in the presence of Ag, chemical interactions of Ag/Pd with other components, and the formulation and processing aspects of thick-film Ag/Pd conductors.

V. Application of Thick-Film Ag/Pd Conductors

Silver, palladium, and solid solutions or mixtures of them are an important class of thick-film conductors used in thick-film hybrid microelectronic systems and as internal electrodes and end terminations for multilayer ceramic capacitors, transducers, varistors, actuators, chip carriers, etc.[5,25,26,62-65] These systems offer substantial cost benefits over Au alloys, pure Pd, or Pd/Pt alloys.

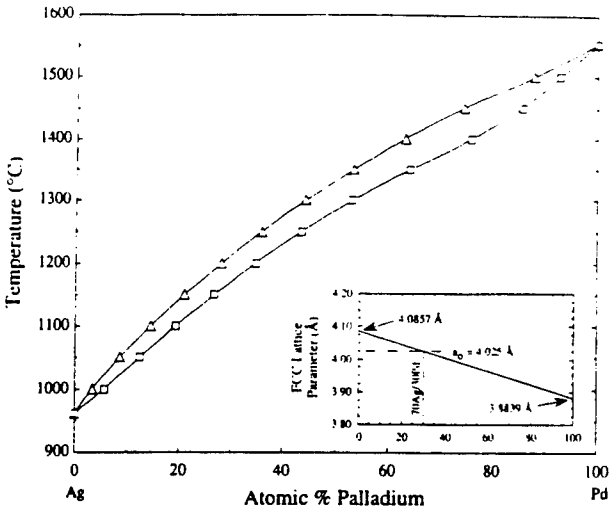

Fig. 7. Phase diagram and room-temperature lattice parameters for the Ag/Pd system.

Thick-film technology uses screen printing techniques to deposit patterned conducting, resistive, and insulating films to form passive electronic components and circuits. A thick-film conductor generally requires the incorporation of three main functional components in the paste: a metal or metal alloy to provide conductivity and joinability, an inorganic additive, usually a glass or oxide to promote adhesion to the substrate, and organic-based vehicles, dispersants, and other additives to produce a screen-printable paste. The additive phases in Ag/Pd thick-film conductors are significantly different, depending upon the particular purpose of the thick-film ink.[5,26,27]

(1) Ag/Pd Electrodes for Thick-Film Hybrid Microelectronic Technology

In thick-film hybrid circuits, conductors function primarily as bonding sites for discrete active and passive devices and as electrical interconnections between these discrete devices, printed passive elements, and leads or pins for connection to external circuitry.[66] Superior thick-film conductors have high electrical conductivity, high migration resistance, compatibility with other components and other thick-film deposits in the circuit, ease of producing solder or wire interconnection bonds that have good electrical and mechanical integrity, good adhesion to the ceramic on which the conductors were printed and fired, good line definition, and firability in air at 1000°C or less.[5]

Usually, Ag/Pd thick-film conductors are fritted with borosilicate or similar glass phases which are used to bond the metal particles to the surface of the alumina substrate on firing.[26,27] As fluxing aids for sintering and adhesion, intermediates and modifiers such as Bi_2O_3, PbO, Al_2O_3, CdO, ZnO, CuO, BaO, and CaO are often included in the glass, even though they may cause other problems such as reduced conductor adhesion to the substrate when solder tracks are stored at elevated temperatures.[5] Flux additives should also possess proper viscosity, surface tension, thermal expansion, and environmental inertness so as to contribute to the overall properties of the fired thick-film conductor.[68,69]

The presence of Pd serves to inhibit solder from leaching Ag out of conductors, and it also reduces Ag migration in hot or humid environments, especially when high electric field biases are present between closely adjacent conductor tracks held at different electric potentials. The addition of Pd does, however, add cost. For less stringent applications where cost is of greater importance, the ratio of Ag/Pd can be as high as 12:1. Pure Ag can be used in hermetically sealed environments. For applications where high reliability is required in adverse environments, the ratio of Ag to Pd is usually reduced.[24] Any further decrease

in Ag/Pd ratio usually leads to lower solderability and a reduction in electrical conductivity.

(2) Ag/Pd Electrodes for MLC Terminations

In MLCs, the termination (or the external electrode) functions as a low electrical resistance connection for the stacked dielectric layers connected electrically in parallel.[65,70] Terminations have similar compositional makeup of fired-on thick-film conductors used in hybrid microcircuitry, except that different fritted formulations are used to match to the capacitor body chemistry, surface roughness, and thermal properties.[12,13] Functional requirements of the fired-on termination are solderability, solder leach resistance, thermal shock resistance, adhesion to the ceramic, and, in some cases, electroplatability.[71] The most common end termination materials for MLCs are Ag or Ag-rich Ag/Pd alloys.[36] The balance between solderability and solder leach resistance rests primarily on the Ag/Pd ratio. Silver dissolves rapidly in the Sn/Pb solder used in hybrid microcircuitry, while Pd solubility is negligible. The composition and quantity of glass frit used to bond termination to the ceramic dielectric are also important factors which influence the thermal shock and thermal cycle performance of MLCs.[12,71,72] Thermal shock resistance increases with the addition of glass frit, even though it has a thermal conductivity of about 1 W/m·K compared to about 400 W/m·K for Ag.[73]

Termination pastes are applied either by hand-dipping or by a variety of machines. Accordingly, one of the most important property requirements of the composition is rheology control relative to the method of application. There are three types of terminations: the leaded termination, the hybrid chip termination, and the surface mount termination.

The leaded mount termination is used for solder connection to wire leads. The composition of a leaded mount termination is typically a solderable, 100% Ag metallurgy, because the soldering and lead attachment processing is done with appropriate allowances for and control of solder leach, such as using Pb/Sn/Ag solders.[74]

Hybrid chip terminations are used when mounting the MLC onto a hybrid electronic circuit, typically by using a solder reflow technique. The solder on the termination may undergo several reflows during assembly of the microcircuit. Thus, the terminations require a higher degree of solder leaching resistance, and subsequently a higher Pd/Ag ratio (typically 1:3 or 1:4) is used.[65]

Surface mount terminations are used when the MLC is connected directly to the printed circuit board, usually by wave soldering. Due to the aggressive nature of this process, with regard to termination leaching, very high resistance to solder leaching is required. This is obtained by Ni-coating the Ag termination or, alternatively, by using a ternary metallurgy termination (Pt/Pd/Ag).[65]

(3) Ag/Pd Electrodes for MLC Internal Conductors

The function of the internal electrode is to provide the electrical conductor for each active plate in the multilayer stack.[44,48] The basic thick-film electrode composition comprises a conductive metallization phase and a vehicle plus various additives for rheology and sintering control of the metal phase. Since these electrodes are entirely buried in the dielectric layers except for the exposed ends, strong adhesion of the metallization to the ceramic is not needed. Therefore, a glass phase for adhesion of the conductor is usually not necessary. However, particulate additives such as dielectric materials and other oxides (ThO_2, Gd_2O_3, NiO, etc.) are often incorporated in the metallization to minimize shrinkage mismatch with the dielectric during cofiring by delaying the early sintering of the metallization to higher temperatures so as to more closely match that of the dielectric.[75,76] In some cases organo-metallic compounds of Ru, Rh, Re, Ir, or Pt are added to produce better shrinkage matches.[76,77]

The metals used in MLC electrodes are usually based on either pure Pd or mixtures of Pd and Ag. Solid solutions or physical mixtures of the metals can be used. As dielectric technology has improved, MLC manufacturers have been able to use lower firing dielectric compositions to manufacture MLCs. Lower firing temperatures for the dielectrics allow the incorporation of more Ag into the electrodes, resulting in significant cost savings.[51,77] A common sintering temperature for low firing dielectrics is 1100°C, enabling use of 70Ag/30Pd electrodes.[56]

An ongoing challenge for future developments in high-performance ceramic multilayer capacitors is to reduce the internal electrode cost and the fired thickness of the dielectric without sacrificing finished part performance, yield, or reliability.[47,78,79] One way to reduce cost is to deposit less metallization so as to make the electrodes thinner. However, as electrodes become thinner, problems associated with electrode continuity become greater. Combined with the push toward the use of lower firing temperature dielectrics (fluxed systems) and relaxor ferroelectrics, potential interactions between the electrode and dielectric become more critical. The interaction problem is particularly acute for low-cost base metal electrode systems (e.g., Cu and Ni), because the relationships between the oxidation behavior and potential chemical interactions with the dielectric have not been thoroughly characterized.

VI. Oxidation of Pd in Ag/Pd Systems

Although the Ag/Pd system is widely used in the thick-film paste industry, it unfortunately also exhibits a unique problem. Specifically, volume expansion due to the oxidation of Pd ($Pd + \frac{1}{2}O_2 \longrightarrow PdO$) and contraction during reduction of PdO ($PdO \longrightarrow \frac{1}{2}O_2 + Pd$) can have a detrimental impact on microstructure development of not only the metal, but also of surrounding components during sintering and densification.[80]

In the thick-film hybrid microelectronics industry, the Ag/Pd system was originally studied for use with both thick-film resistor components and simple conductors.[81–88] The electrical resistivity in Pd/Ag thick-film resistors was formed by the partial or complete oxidation of the Pd to PdO. Early studies revealed that O_2 evolving during the reduction of PdO was responsible for bubble formation in resistor compositions,[81] porosity in conductors,[89,90] and blistering of conductor ⟷ resistor/capacitor interfaces.[86] Resultant decreases in interfacial bond strengths,[88] degraded solderability,[87,91,92] and low-density conductors limited the widespread use of Ag/Pd in thick-film applications and eventually led to their replacement by other thick-film resistor technologies.[81]

During the processing of MLCs, not only does the volume expansion associated with Pd oxidation result in internal stress, but also the reduction of PdO back to Pd creates O_2 evolution. This occurs during the initial stages of dielectric sintering when the multilayer structure is fragile. This volume expansion and contraction, with the accompanying gas evolution, may result in delaminations, porosity, or microcracking.[88,93–95]

In their pure state, the oxides of both Ag and Pd are thermodynamically stable in air at room temperature. For example, Ag_2O is the thermodynamically stable form of Ag in air below 250°C.[96,97] However, due to kinetic limitations and reducing conditions during burnout of organics, and rapid densification of the metallic film during the low-temperature stage of sintering, Ag_2O is not observed in thick-film conductors. In comparison, PdO is stable below 800°C (Fig. 4) and is often present during some stage of the firing process. The temperature at which Pd oxidizes during heating depends on the local oxygen partial pressure, heating rate, sintering, the presence or absence of Ag, and its particle size and surface area, which control the reactivity.[18,89,97] Figure 8 shows a thermogravimetric analysis (TGA) plot of a pure Pd powder heated from room temperature to 1000°C in an air atmosphere. It shows that significant Pd oxidation begins to occur at about 300°C, with almost complete oxidation by 600°C. At 800°C the PdO quickly reduces back to Pd.

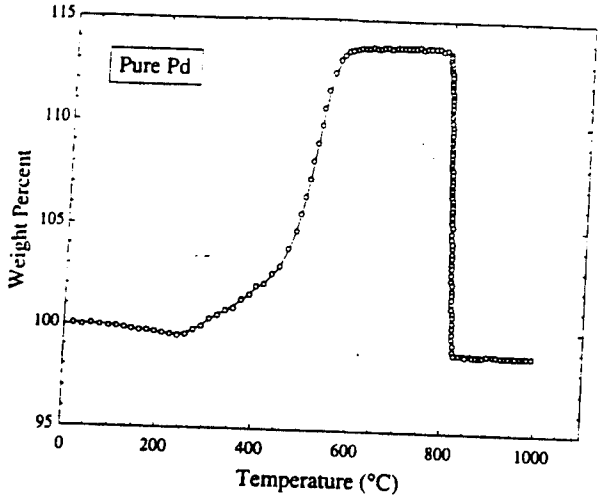

Fig. 8. TGA analysis of pure Pd powder (10°C/min, flowing air).

(1) Ag-Pd-O Phase Relations

The oxidation behavior of Pd changes significantly in the presence of Ag,[80,95,98] such as in Ag/Pd physical mixtures or solid solutions thereof. In general, the presence of Ag increases the temperature at which Pd oxidizes and decreases the temperature at which PdO is reduced. Hoffman pointed out in his paper on Pd/Ag resistors[81] that PdO decomposes over a broad temperature range (690° to 800°C), depending on the amount of Ag present. Similarly, Cole[98] found that increasing the relative amount of Ag in two-phase powders up to ≈60 mol% continuously reduced the onset temperature of reduction from 800°C to as low as 450°C. Pepin[80] used thermogravimetric analysis to construct the phase diagram for the system Pd/Ag/O in air. Further work was done on this system by Wang and Huebner[99] using thermodynamic calculations and high-temperature X-ray diffraction (XRD) phase analysis.

The Pd oxidation in Ag/Pd alloys is strongly dependent on the nonlinearity of the thermodynamic activity of the Pd, $a_{Pd(Ag)}$, in Ag/Pd solid solutions, as well as the Gibbs free energy of the formation of PdO.[100-104] With respect to ideal behavior, the activity of Pd deviates positively in the Pd-rich region and negatively in the Ag-rich region (Figure 9).[105-107] This difference has been ascribed to nonconfigurational contributions to the thermodynamic properties that are associated with changes in the electronic structure upon alloying.[105,108,109]

Figure 10 shows the temperature at which a specific Ag/Pd alloy will be in equilibrium with PdO for a given p_{O_2}.[99] These phase relations show that for a Ag/Pd solid solution the maximum equilibrium temperature at which PdO is stable in a given p_{O_2} depends on the initial Ag/Pd ratio of the alloy. For example, if a 10Ag/90Pd alloy were heated to ≈400°C in air, it would oxidize. If equilibrium were established, the alloy would be composed of nearly pure Ag mixed with a relatively large amount of PdO. Upon further heating to temperatures ≥ ≈500°C, the PdO would begin to reduce back to Pd, with a continuous decrease in the Ag/Pd ratio as predicted by the p_{O_2} = 0.21 atm curve of Fig. 10. At >795°C the last of the PdO would disappear, and the original ratio of Ag/Pd would be established once more. Therefore, the departure point from the curve depends upon the initial Ag/Pd ratio. This means that as the amount of Ag in a Ag/Pd alloy composition is increased, the maximum temperature at which PdO is stable continuously reduces. In addition, for alloy compositions with ≥60% Ag, the reduction of PdO occurs over a broad temperature range. But for more-Pd-rich compositions, the reduction occurs over a much narrower temperature range. This is directly related to the rapid change in the $a_{Pd(Ag)}$ that occurs at about the 55Ag/45Pd composition (see Fig. 9). As also shown in Fig. 10, small changes in the p_{O_2} decrease the stability temperature of PdO.

(2) Oxidation Reduction Kinetics and the Volume Change of Ag/Pd Powders

The equilibrium subsolidus phase relations for Ag/Pd/O describe the influence of Ag on the oxidation/reduction behavior of Pd and quantitatively predict the phases present at any given temperature and p_{O_2}.[99] However, with regard to problems encountered while using Ag/Pd in microelectronic systems, the reaction kinetics, i.e., the path to the equilibrium state, are the most important factor which must be considered.[110-111] The oxidation/reduction kinetics depend on the form of the Ag/Pd powders (alloyed or coprecipitated powders), heating rate, initial Ag/Pd ratio, and surface area of the powders. In this paper, we define the term "alloy" to mean a mixture of Ag and Pd which is a single-phase solid solution. "Coprecipitate" refers to a two-phase mixture of Ag and Pd formed by either coprecipitation and/or mechanical mixing of separate Ag and Pd powders.

The importance of the initial state of Ag and Pd is clearly seen in Fig. 11,[109] which shows the difference in TGA results for 70Ag/30Pd coprecipitated and alloyed powders for a heating rate of 3°C/min in air. The theoretical weight gain for full oxidation of Pd in 70Ag/30Pd is 4.5%. The alloyed powder doesn't oxidize nearly as much as the coprecipitated powder.

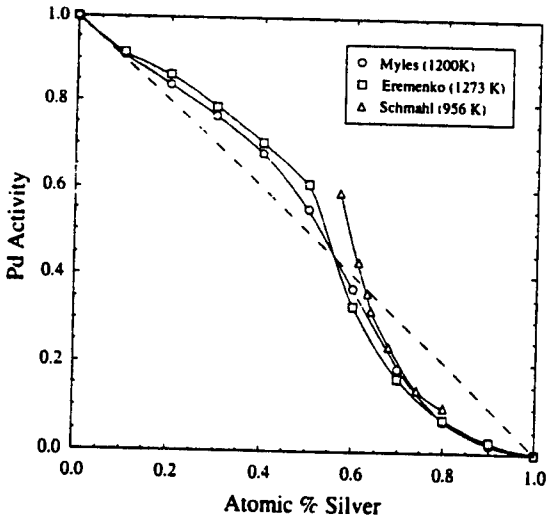

Fig. 9. Thermodynamic activity of Pd in Ag/Pd solid solutions.

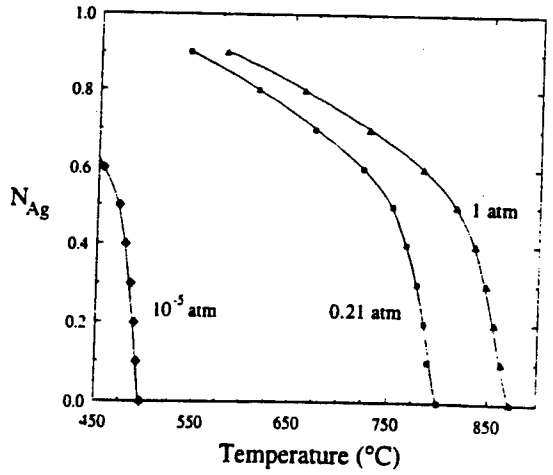

Fig. 10. Calculated phase stability of the Pd(Ag)–PdO system for p_{O_2} = 1, 0.21, and 10^{-5} atm.

Several studies have shown that the oxidation of Pd is controlled by oxygen diffusion through the PdO layers.[18,109] However, for both the coprecipitated and alloyed powders, full oxidation usually does not occur, due to kinetic limitations.

The overall oxidation and reduction behavior of a 70Ag/30Pd coprecipitated powder can be described by the schematic shown in Fig. 12.[110] Pd oxidation is negligible below 250°C (region 1). In region 2 the major constituents of the powder are Ag, Pd, and PdO. Alloying in this region is negligible, due to kinetic limitations (unless the Ag and Pd were mixed at the atomic scale). The extent of PdO formation depends on the heating rate, the initial Ag/Pd ratio, the particle size, and the powder surface area.[18,93,110,112] Increasing the heating rate decreases the total amount of Pd oxidation. Significant amounts of Pd begin to alloy with Ag above 450°C, with concurrent reduction of PdO. In region 3, for temperatures >500°C, equilibrium is achieved rapidly, and the reaction proceeds along the equilibrium curve between regions 3 and 4; the Ag/Pd ratio decreases concurrently with PdO reduction. This proceeds until all of the PdO reduces back to Pd, resulting in an alloy with the original 70/30 Ag/Pd ratio. The onset temperature of PdO reduction depends on the extent of Pd oxidation in region 2. When the heating rate is slow, complete oxidation of Pd occurs, and the onset temperature of Pd reduction is the temperature at which point alloying begins, ≈450°C. If Pd oxidation is not complete in region 2 due to rapid heating, then alloy formation will consume the unoxidized Pd first, resulting in a higher onset temperature of reduction.

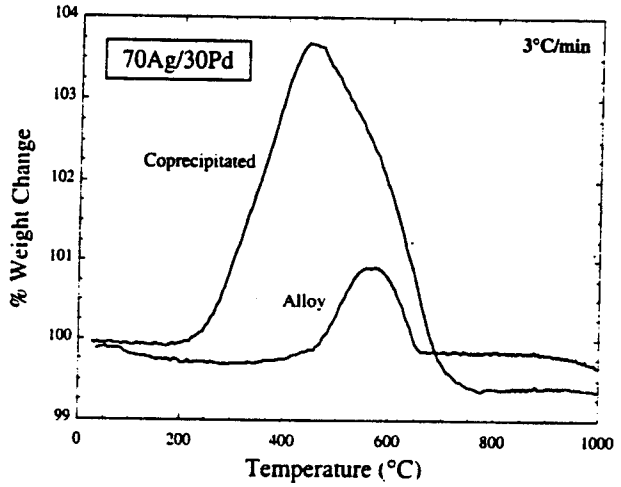

Fig. 11. TGA analyses of coprecipitated and alloyed 70Ag/30Pd powders.

Figure 13 shows the corollary schematic describing the oxidation and reduction behavior of Ag/Pd alloyed powders.[110] Due to the low diffusivity of Pd in Ag/Pd alloys,[113] the oxidation rate is much slower than those of coprecipitated powders and is only detectable for temperatures >350°C (region 2). The extent of oxidation in region 2 depends on the heating rate, the surface area of the powders, and the equilibrium ratio of the Ag/Pd alloy. Due to the kinetic limitations at low temperatures and the equilibrium phases present (Ag(Pd)–PdO) at high temperatures, complete oxidation of Pd does not occur. Therefore, under identical conditions, the maximum amount of PdO formation for alloyed (or solid solution) powders is much smaller than that of coprecipitated powders. At higher temperatures, as the PdO reduces, the Ag/Pd solid solution becomes richer in Pd as more Pd from the oxide is incorporated, and the equilibrium phases follow the equilibrium line separating regions 2 and 3. From these considerations it can be seen that the onset temperature of PdO reduction for alloyed powders is higher than that of coprecipitated powders.

The expansion of the Ag/Pd film associated with PdO formation is dependent on not only the extent of PdO formation but also the green density of the powder compact. For the same PdO formulation, higher green densities of the screen-printed material will result in a larger expansion of the film. Before the PdO completely reduces back to Pd, no significant sintering shrinkage occurs due to surface diffusion. Also, gas evolution and the lack of significant structural rearrangement cancels out the anticipated shrinkage associated with reduction. After the PdO reduces back to Pd, sintering and pore coalescence result in rapid shrinkage of the film. If the heating rate is too fast, the rapid generation of oxygen may result in local blistering, and the subsequent rapid sintering may result in a large shrinkage mismatch between the metal and ceramic. Several studies have also shown that additions of various materials can inhibit the densification of high surface area alloyed powders and hence minimize the shrinkage mismatch with the surrounding dielectric.[63,64,112] This powder additive also has the additional benefit of retaining an open porosity structure for the metal, which will allow O_2 to escape as the last traces of PdO decompose.

Since heating rate is an important kinetic factor which affects Pd oxidation,[98] a heating rate of 50°C/min (similar to the firing profile that is used for making microcircuit hybrids) allows less Pd oxidation than the 2°C/min heating rate (typical of the firing schedules used in multilayer capacitor fabrication). Heating rates in excess of 100°C/min are often used to manufacture hybrid microcircuits today (infrared furnace profiles are capable of heating rates over 600°C/min). Under such conditions, PdO formation is certainly kinetically limited. However, in MLC manufacturing, the slow heating rates used during multilayer burnout and cofiring require careful control of the

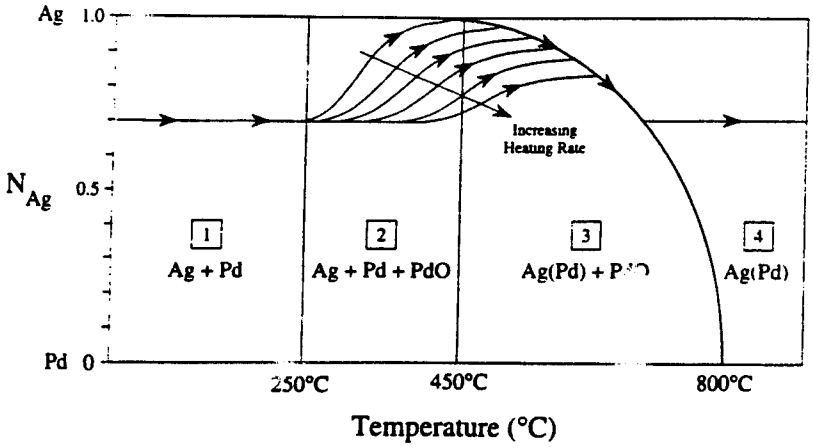

Fig. 12. Schematic diagram of the oxidation/reduction behavior of coprecipitated Ag/Pd powders.

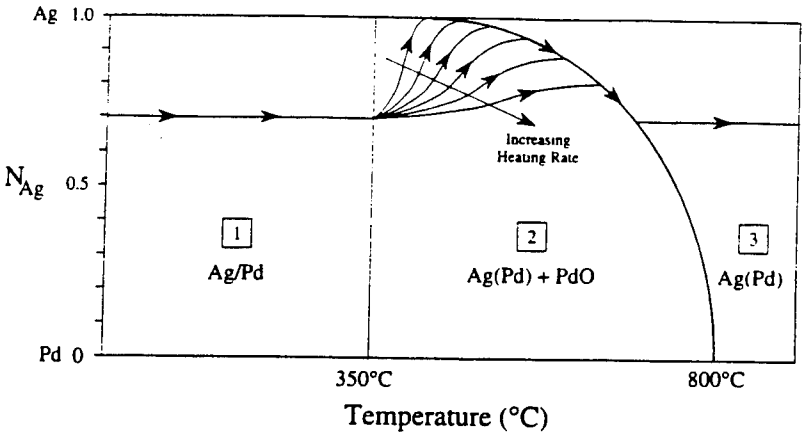

Fig. 13. Schematic diagram of the oxidation/reduction behavior of alloyed Ag/Pd powders.

PdO formation to minimize physical defects such as delaminations and cracks.

VII. Interaction of Ag/Pd with Surrounding Components

A trend in hybrid microcircuits is toward miniaturization. The proximity of the Ag/Pd metallization with the surrounding components increases the potential for mechanical and chemical interactions during cofiring. The influence of the interactions on the electrical performance must be carefully considered.[58,114–116]

Mechanical considerations include expansion and contraction due to the oxidation/reduction of Ag/Pd conductors, shrinkage mismatch during firing, and differing coefficients of thermal expansion (ΔTEC) during cooling and operation. With regard to chemical interaction, the formation of undesirable phases at the interface and interdiffusion of components of the metallization and the dielectric are the major concerns.[117,118]

(1) Chemical Reaction of Ag/Pd with Bi_2O_3, PbO, or Bi- and Pb-Compounds

Bi_2O_3 and lead oxides such as PbO are two common constituents in thick-film materials as well as MLC formulations.[5,51,119] In MLCs, they are present in the fluxes which are used to promote low-temperature densification and to tailor the final, fired dielectric properties by entering into solid solution with the dielectric phases during firing at higher temperatures.[119] For terminations and fired-on thick-film conductor applications, Bi_2O_3 and PbO are present in the inorganic glass or oxide binder phase to enhance adhesion to substrates and are also a sintering aid to allow the low firing temperatures needed to use Ag/Pd conductors.[5,119] In addition, Bi_2O_3 is also a common additive in ZnO varistors.[120] Therefore, understanding the chemical interactions between Ag/Pd and Bi_2O_3 and Ag/Pd and PbO during firing is very important for manufacturing reliable, high-performance electronic ceramics.[121,122]

Several studies have shown that reaction between Pd and Bi_2O_3 results in the so-called "Bismuth reaction."[123–127] Wang and Huebner[17] have proposed the phase relations of Ag/Pd–Bi_2O_3 and Ag/Pd–PbO systems, as shown in Figs. 14 and 15, respectively. For region 1 in both systems, PdO and $PdBi_2O_4$ or $PdPbO_2$ are stable. $PdBi_2O_4$ is a semiconducting material and crystallizes in the tetragonal structure, with lattice parameters $a = 8.62$ Å and $c = 5.89$ Å.[124] The density of $PdBi_2O_4$ is 8.93 g/cm^3, corresponding to four $PdBi_2O_4$ formula units in the unit cell. Muller and Roy[127] have tentatively indexed $PdPbO_2$ on the basis of a hexagonal unit cell with $a = 10.90$ Å and $c = 4.65$ Å. The kinetics of both $PdBi_2O_4$ and $PdPbO_2$ formation are slow. Taking 70Ag/30Pd as an example, the reaction sequences below 700°C can be described as follows:

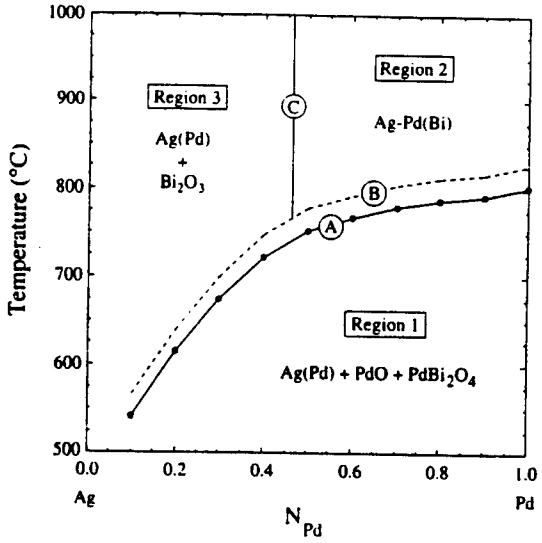

Fig. 14. Phase relations for the Ag/Pd–Bi_2O_3–O_2(air) system.

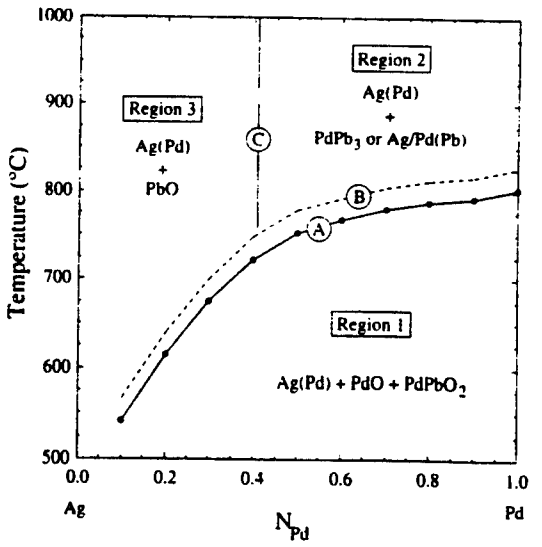

Fig. 15. Phase relations for the Ag/Pd–PbO–O_2(air) system.

Overall oxidation reaction

$$70Ag/30Pd + \tfrac{1}{2}O_2 \longrightarrow PdO + (Ag, Pd) \quad (1)$$

For Ag/Pd ⟷ Bi_2O_3

$$PdO + Bi_2O_3 \longrightarrow PdBi_2O_4 \quad (2)$$

For Ag/Pd ⟷ PbO

$$PdO + PbO \longrightarrow PdPbO_2 \quad (3)$$

The temperature of PdO reduction (line A) and $PdBi_2O_4$ and $PdPbO_2$ decomposition (line B) both depend on the Ag/Pd ratio. The decomposition temperatures of $PdBi_2O_4$ and $PdPbO_2$ are ≈35°C higher than that of PdO reduction.

In region 2, Ag/Pd(Bi) forms in Ag/Pd–Bi_2O_3 systems and Pd(Pb) or $PbPd_3$ (an intermetallic compound) forms in Ag/Pd–PbO systems. Formation of these phases will result in oxygen evolution. Ag/Pd(Bi), Ag/Pd(Pb), and $PbPd_3$ all have melting temperatures lower than that of the initial Ag/Pd. In the Ag/Pd–Bi_2O_3 system, ≈16 at.% (28 wt%) Bi can be dissolved into the Ag/Pd alloy. However, in the Ag/Pd–PbO system, the maximum solubility of Pb is ≈14 at.% (26 wt%). Increasing the PbO content (>25 at.%) results in $PbPd_3$ formation and the subsequent increase in the Ag/Pd ratio of the remaining alloy. Importantly, this higher Ag/Pd ratio has a lower melting point. Taking pure Pd as example, the reaction sequence could be described as follows:

For Ag/Pd ⟷ Bi_2O_3

$$PdO + Bi_2O_3 \longrightarrow Pd + Bi_2O_3 + \tfrac{1}{2}O_2 \quad (4)$$

$$Pd + \tfrac{1}{2}Bi_2O_3 \longrightarrow Pd(Bi) + \tfrac{1}{4}O_2 \quad (5)$$

For Ag/Pd ⟷ PbO

$$3PdPbO_2 \longrightarrow 3PdO + 3PbO \longrightarrow$$

$$3Pd + 3PbO + \tfrac{1}{2}O_2 \longrightarrow PbPd_3 + 2PbO + 2O_2 \quad (6)$$

$$0.14PbPdO_2 + 0.72PdO \longrightarrow$$

$$0.14PbO + 0.86PdO \longrightarrow 86Pd{:}14Pb + \tfrac{1}{2}O_2 \quad (7)$$

In region 3 (the Ag-rich region), no reactions occur in either the Ag/Pd–Bi_2O_3 or Ag/Pd–PbO systems. The boundaries (line C) are located at 45 at.% Pd and 40 at.% Pd. Taking pure 70Ag/30Pd as example, the reaction sequence could be described as follows:

For Ag/Pd ⟷ Bi_2O_3

$$PdBi_2O_4 \longrightarrow PdO + Bi_2O_3 \longrightarrow Pd + Bi_2O_3 + \tfrac{1}{2}O_2 \quad (8)$$

$$Pd + (Ag, Pd) \longrightarrow 70Ag/30Pd \quad (9)$$

For Ag/Pd ⟷ PbO

$$PdPbO_2 \longrightarrow PdO + PbO \longrightarrow Pd + PbO + \tfrac{1}{2}O_2 \quad (10)$$

$$Pd + (Ag, Pd) \longrightarrow 70Ag/30\,Pd \quad (11)$$

These reactions can have a severely detrimental impact on the electrical performance of a component. For high-permittivity dielectrics used in multilayer capacitors (MLCs), the formation of low-permittivity phases at the interface will result in a series capacitance which can significantly reduce the effective dielectric constant. The formation of low melting temperature phases and the interdiffusion of components can reduce yield or reliability by resulting in a metallic phase which is lower melting and perhaps will form discontinuous metallizations due to melting during the firing process.[131]

Wang and Huebner[128] also showed that similar reactions of Pd with various Bi-compounds, including $Bi_4Ti_3O_{12}$, $Bi_2Ti_2O_7$, $Bi_2(SnO_3)_3$, $Bi_{12}TiO_{20}$, and $(Bi_2O_3)_{0.8}(BaO)_{0.2}$, form either $PdBi_2O_4$ or a Pd(Bi) alloy. The Pd(Bi) alloy exhibits the maximum solubility of Bi at 16 at.%.[129] The Bi-compounds with the lowest thermodynamic stability react with Pd at the lowest temperatures. If the reaction proceeds at $T < 835$°C, then $PdBi_2O_4$ forms, since it is stable up until this temperature. Wang and Huebner[128] also showed that there is a reaction of pure Pd with Pb-based electroceramics used for capacitor and transducer applications. Materials such as $Pb(Zr,Ti)O_3$, $Pb(Mg_{1/3}Nb_{2/3})O_3$ (PMN), or $PbTiO_3$ lose Pb from their structure as they react to form a Pd(Pb) alloy. All cases exhibit the maximum solubility of the Pb, i.e., 14 at.%.[130] The formation of this solid solution indicates that not only will the conductivity and melting temperature of the electrode be decreased ($T_m \approx 1200$°C for this alloy) but, more importantly, that the stoichiometry of the ceramic will be altered. The change in stoichiometry at the electrode–dielectric interface can significantly reduce the effective dielectric constant in capacitor and actuator applications.

Similar to the reaction of Pd with Bi_2O_3 and PbO, the reactivity of Pd with Bi- and Pb-compounds is also dependent upon the Ag/Pd ratio. For Ag/Pd ratios >60/40, the lower activity of Pd will greatly diminish the reactivity of the electrode with Pb or Bi-based dielectrics.

These studies indicate that Ag-rich Ag/Pd compositions will diminish the extent of the interaction between Ag/Pd metallizations and flux systems or Bi- and Pb-compounds present as an oxide additive to a thick-film paste or in the dielectric layer of MLCs. However, high Ag/Pd ratios can be deleterious, due to Ag migration and lower solder leach resistance, as observed in thick films in hybrid microcircuits.[67,131] In the case of Ag/Pd electrodes for MLCs, there is a fundamental limitation to the amount of Ag which can be used, due to the firing temperature required by the dielectric. Also, the Ag/Pd ratio after firing may not be the same as the initial ratio, due to diffusion and/or evaporation of Ag.[126] Another consideration is the local Pd activity, which may be very high at an interface in which $PdBi_2O_4$ or $PdPbO_2$ decomposes to form PdO, which immediately reduces to Pd.

Finally, it is worthwhile to note that Ag/Pd also reacts with both bismuth-containing (Bi–Sr–Ca–Cu–O systems) and non-bismuth-containing superconductors (YBCO systems) at high temperatures.[132–134] For bismuth-containing superconductors, the reactions of Bi and Pd are expected to proceed similar to the reactions as mentioned. For non-bismuth compounds, the Ba and Cu of the YBCO compound were reported to react with the Pd to form a body-centered cubic phase Ba(Pd,Cu)O_2. CuO was also found as a product of the reaction. Also, Ag and Pd have been reported as common dopants of the superconductors, which increase the critical current density of the sintered bodies.[135,136]

(2) Interaction of Ag/Pd with Sn/Pb Solders

Thick films are widely used in hybrid microelectronics. Solder joint reliability between the thick-film conductor and solder joint is crucial. Three important parameters must be considered: (a) thick-film solderability, (b) solder leaching resistance, and (c) aged adhesion.[36,131]

Generally, Ag/Pd thick-film conductors are solderable. However, poor solder wetting may occur when the metal surface has been contaminated externally or internally, such as with organic residues, inorganic salts, or through Pd oxidation (when the Pd/Ag ratio is high).[91,92] Thick-film conductors that contain large amounts of glass frit are also difficult to solder.[131]

Silver will dissolve in Sn/Pb solders. Silver leaching is more serious with increasing Sn content in the solder. For this reason, Ag is sometimes present in the solder composition to decrease Ag loss from the thick film. Thick-film conductors with higher Pd/Ag ratios have higher solder leaching resistance, but at the expense of reduced electrical conductivity and, in the case of extreme levels of Pd, decreased solderability.[67,74] Thus, in the fabrication of multilayer substrates, higher Pd/Ag ratios are used as a top conductor or for the solder pads. For higher conductivity, the inner conductor layers generally contain Ag paste.

The solderability and solder leach resistance can also be modified by varying the inorganic binder level.[16]

A significant degradation in the adhesion strength between solder and metal as well as metal and ceramic interfaces occurs after thermal aging at temperatures greater than 125°C. The failure mechanisms have been studied by several researchers in the past two decades.[68,137–41] They concluded that the failures were due to two sources: (1) the interdiffusion between the solder and the Ag/Pd conductor during soldering, with subsequent formation of intermetallics (Pd_3Pb), and (2) formation of other phases during thermal aging such as Pd_3Sn, Pd_2Sn, Pd_3Sn_2, PdSn, Ag_3Sn, and Ag_3Sn.[140,141] The swelling in the conductor film due to the volume change associated with intermetallic compound formation (Table IV) decreases the adhesion strength between Pb/Sn solder and Ag/Pd termination. Additional decreases in the adhesion may be due to the redox reaction that occurs at the conductor grain boundary:[131]

$$3Bi_2O_3 + 3Sn \longrightarrow 3SnO_2 + 4Bi \qquad (12)$$

This reaction weakens the glass network within the sintered metal and disrupts the bond between conductor and substrate.

(3) Metal-Organic Interactions

Among the transition metals, Ag and Pd are well-known catalysts and hence are used to catalyze oxidation, decomposition, or hydrogenation reactions used for synthesizing for many organic chemicals.[142–145] Since both metals and organics are major constituents in thick-film conductors, possible metal-organic catalysis reactions are another factor which must be considered when formulating and firing Ag/Pd thick-film conductors. This mechanism of failure and detrimental reactions can usually be considered negligible, however, owing to the low surface areas of the metal powders used in the thick-film formulation. However, in some cases additions of small amounts of high surface area Pd and/or Ag may be done, and catalysis during burnout and firing becomes a factor in overall thick-film composition performance. Catalysis of the organics by the Ag/Pd during burnout is detrimental to the cofired multilayer structure, because it can generate hot spots from the exothermic reactions in the electrode regions and cause rapid evolution of gases through the decomposition of the resins.[145,146] These can rupture the metallization–ceramic interface, especially since the multilayer structure is still weak during burnout.[147]

Catalysts usually act by chemisorbing one or more of the reactants, and it is the subsequent perturbation of the electronic and geometric structure of the molecule which leads to the catalytic enhancement in the reaction rate. The catalytic action of the metals is dependent on particle size, surface area, and surface structure of the metal. These factors determine the area of virgin metal surface available for reactant adsorption and change the effective heat of adsorption for the reactant. The more active the sites on the surfaces, the higher the metal-organic reactivity.[142] Therefore, the metal-organic catalysis reaction can be minimized or eliminated by tailoring the particle morphology parameters. In Ag/Pd thick-film production, several methods are generally used to minimize metal-organic catalysis. These are (1) avoiding extremely small particle size and high surface area Ag/Pd powders, (2) passivating the metal surface to reduce the metal-organic reactivity,[145,147] (3) reducing the amount of residual organic resins contained in the paste vehicle, and (4) reducing the p_{O_2} at low temperatures during firing, which can limit the reaction.

(4) Diffusion and Loss of Ag During Firing

Silver diffusion and silver volatilization during firing can occur in cofired thick-film systems as well as in MLC electrode systems.[126,148] This is especially true for pure Ag or high Ag/Pd ratio metallizations. In a thick-film multilayer package, bulk diffusion of Ag can occur if the multilayer dielectric is porous and undergoes many firing cycles. The penetration of Ag into the ceramic can be detrimental to the electrical performance of the dielectric layer. As a termination for thick-film resistors, Ag or Ag/Pd may result in a lower resistance compared with other terminations.[149,150] This is due to Ag diffusion into resistor materials (oxide and glass binder) and precipitates as metallic Ag particles. It is known from the literature that Ag is quite soluble in a wide variety of glasses and oxides and that it often can be precipitated from solution by thermal treatment.[151] Silver has much higher solubility in borosilicate glasses (≈0.45 wt%) than that of Pd (≈0.03 wt%). Most of the Pd exists in the insoluble metal form, with only a small fraction of the Pd present, because the Pd^{2+} ion dissolves in the melt. However, studies have shown that Ag and Ag^+ coexist in borosilicate glass melts.[69,152–155]

In the cofiring of MLC capacitors, Ag is known to interdiffuse with perovskites, thereby affecting microstructure development and electrical performance.[156] Chu and Hodgkins[115] reported that diffusion of Ag into the ceramic affects grain growth. Maher[157] and Ikushima and Hayakawa[158] reported that a small percentage of Ag was soluble in $BaTiO_3$ and PLZT, substituting onto the A site. When $BaTiO_3$-based ceramics were cofired with buried Ag-containing electrodes, the Ag was found to behave as an acceptor dopant and hence improved the stability of capacitance with temperature and applied voltage, but decreased the dielectric constant. Several studies found that Ag preferentially migrates along the porosity or grain boundary of PZT,[159,160] and Murty *et al.*[161] showed that Ag substitution into PZT at high temperatures resulted in diminished piezoelectric properties. All of these reactions will effectively reduce the

Table IV. Calculated Volume Changes due to Conductor/Solder Interactions

Component	Structure	Lattice parameters (Å)	Density (g/cm^3)	% vol change with respect to pure Ag or Pd
Ag	Cubic	a = 4.0857	10.50	
Pd	Cubic	a = 3.8839	12.01	
Pd_3Sn	Cubic	a = 3.88	12.45	32.3
Pd_2Sn	Orthorhombic	a = 8.110	9.10	111.8
		b = 5.662		
		c = 4.234		
Pd_3Sn_2	Hexagonal	a = 4.390	9.79	112.9
PdSn	Orthorhombic	a = 3.86	10.03	152.4
		b = 6.12		
		c = 6.31		
Pd_3Pb	Cubic	a = 4.024	13.41	47.7
Ag_3Sn	Orthorhombic	a = 2.995	9.94	23.3
		b = 5.519		
		c = 4.781		
Ag_3Sn	Hexagonal	a = 2.966	10.03	36.7
		c = 4.782		

Ag/Pd ratio, making the electrode richer in Pd and therefore more susceptible to detrimental Pd-based reactions.[5]

The vapor pressure of Ag (P_{Ag} = 0.1 mmHg, at 1100°C) is very high compared with that of Pd (P_{Pd} = 0.00001 mmHg).[162] In MLC capacitors, loss of Ag during processing is from diffusion along internal electrodes followed by evaporation through the edge, or from diffusion directly through the edges. The silver loss changes the Ag/Pd ratio, especially near the edge.[126] If the metallization is thin, then compensation of Ag from the inner central region may not be sufficient. The result is that the excess silver volatilization increases the resistance of the electrodes due to enrichment in Pd and creates poor electrode-to-termination contacts. This can result in lowering of component capacitance and higher dissipation factors, especially at high frequencies where the electrical resistance of the electrode is a key factor in electrical losses. Additional degradation can come from electrode discontinuity and a reaction of Pd with bismuth or lead oxides as discussed previously.

The diffusion and loss of Ag can be minimized by decreasing the Ag/Pd ratio. Larger Pd/Ag ratio alloys have higher melting temperatures and reduced silver mobility. Since the vaporization of Pd is four orders of magnitude smaller than that of Ag, both the bulk diffusivity and vapor pressure can be greatly reduced by Pd addition, but with higher costs for the metals portion of the conductor. Another approach is to design the dielectric or glass composition to limit the Ag solubility level. For instance, some critical components, such as boron oxide, can be minimized; B_2O_3 forms solid solutions with Ag. In some cases, the glass-ceramic could be designed to crystallize rapidly on firing to give high levels of crystallized filler. This crystallized glass reduces the dissolution tendency of Ag due to the low residual glass concentration.[163]

(5) Electrolytic Ag Migration

Silver migration can occur between closely spaced conductor lines on a microelectronic circuit, or between interdigitated electrode layers in multilayer ceramic substrates. Silver migration causes reduction of the insulation resistance, an increased leakage current, and eventual electrical shorting or dielectric breakdown.[164–166] The failure mechanism is electrolytic diffusion of Ag ions under the influence of an electric field. This diffusion causes the growth of acicular or dendritic Ag at the cathode, which migrates through the ceramic grain boundaries or ceramic surfaces and eventually causes a short on contact with the anode.[166,167] A water-drop test is the most effective and common method to determine the rate of Ag migration. Several factors which may affect the rate of Ag migration are indicated in Table V.[131]

Several techniques are used to minimize silver migration. One is to avoid the use of pure Ag or high Ag/Pd ratio alloys in the thick-film pastes. The rate of Ag migration generally decreases with increasing Pd content in the Ag/Pd conductors.[165,168] However, the glass components in the thick-film conductor, as well as the processing of the paste, can have a significant influence on metal migration susceptibility, regardless of Pd content. An additional method is to encapsulate the fired film with an organic coating or a glaze layer to prevent the moisture condensation or ionic contamination on the surface.[168–170] Since surface migration of Ag is the main failure mode in dielectric crossover structures, this failure mechanism can be avoided by completely covering the bottom conductor with a dielectric layer.[5] Glaze-coated and sealed MLC capacitors not only isolate the component from outside contamination, but also inhibit the gas formation at the electrode that accompanies oxygen vacancy transport. With the electrolytic reaction suppressed by the hermetic sealing, oxygen vacancy migration is minimized. A final method is to make the fired dielectric microstructure as dense and pore-free as possible.[148] This not only electrically isolates the internal Ag conductors from each other, but also protects them from the external environment.

Table V. Factors Which Affect the Rate of Silver Migration

Level of relative humidity
Presence of ionic or hydroscopic contaminants
Porosity of the dielectric or substrate
Spacing between the conductor lines or electrodes
Nature of the encapsulant
Time under bias
Magnitude of the dc field gradient

(6) Battery Effect

Many of the components in a hybrid circuit need to be wire bonded on the top layer. This necessitates the use of Au for the top layer, while Ag or Ag/Pd is used for the inner layers of the circuit. Using these dissimilar metals in a hybrid circuit can lead to the so-called "battery effect,"[171,172] which can result in a delamination or blistering of one of the conductor layers during firing. Although the exact mechanism has not been established, consensus is that the structure mimics a galvanic cell consisting of a gold anode, a silver cathode, and the "molten" (ionically conducting) dielectric as the electrolyte. The observed result of the battery effect is blistering or delaminations. This suggests that gas is formed at interfaces, most likely O_2, during cofiring as a result of the electrolysis from the generated EMF. The gases, however, do not escape before densification occurs and are trapped within the multilayer structure, resulting in the bloating of the thick film as seen in the dilatometer work described earlier. The battery effect is usually not observed if the top layer and inner layer metallization are connected by a vias.[172]

VIII. Sintering Behavior of Ag/Pd Metallizations

Several researchers have investigated the sintering of pure Ag. Similar to other face-centered cubic metals, self-diffusion of Ag at high temperatures takes place by a lattice vacancy mechanism.[173] Based on the diffusion coefficients and activation energies, the rate-controlling mechanism changes from lattice diffusion to grain boundary diffusion at ≈750°C.[174]

The sintering of pure Pd in air is more complicated than that of Ag, because of the formation of PdO surface layers on the Pd powders between 300° and 800°C.[175–179] The oxide surface layer influences the mass transport process during sintering. Below the PdO dissociation temperature, Pd sinters with a dominant surface diffusion mechanism. With the presence of an oxide layer, Pd sintering is characterized by neck formation, lack of densification, retarded grain growth, and an activation energy of 58.9 kJ/mol.[176–178] When Pd sinters under vacuum or in a reducing atmosphere (below the p_{O_2} for PdO surface layer formation) at temperature <800°C, it sinters by grain boundary diffusion with an activation energy of 132.9 kJ/mol. For the temperatures between 800° and 1000°C, Pd sinters by grain boundary diffusion independent of the atmosphere. At high temperatures, lattice diffusion with an activation energy of 266 kJ/mol controls the sintering.[179]

For Ag/Pd alloys, Nachtrieb[180] found that when up to 20% Pd was added into Ag, the activation energy was virtually constant and only the preexponential constant of the Arrhenius expression was changed. This condition predicts that the initial sintering of Ag/Pd powders will follow a grain boundary diffusion model below 750°C. They also found that the self-diffusion rate of Ag declines with Pd additions, but that the diffusion rate of Pd in Ag/Pd is an order of magnitude lower.[113] Hence, it can be expected that Pd particles will consume Ag particles, resulting in Pd particle growth and voids formed when the Ag is removed.

The sintering of termination and fired-on thick-film Ag/Pd conductors proceeds along very different lines than for internal metallizations.[39,90,181,182] The formulations of termination and fired-on thick-film conductors incorporate glass to form a bond between the ceramic and the metal film.[39] The addition of oxides components which may or may not react with the glass

phase to alter the glass composition is also common. The glass phase in pure Ag or Ag/Pd conductors acts as a liquid phase during sintering. The sintering process, thus, is regarded as liquid-phase sintering.[183,184] In addition, the solution–reprecipitation of Ag or Ag/Pd in the glass enhances the densification. The sintering mechanism may be complex if the glass extent exceeds certain limits or the glass is inhomogeneously distributed. In such cases, viscous sintering, liquid-phase sintering, and solid-state sintering must be taken into account.

Yamaguchi, Chung, and co-workers[89,185–90] performed a detailed sintering study of Ag thick films with glass added. Borosilicate glass systems, common glass in the thick-film industry, were used. They concluded that, compared with pure Ag, the densification of Ag glass thick film takes place at lower temperatures. The Ag particles grow in glass by the Ostwald ripening mechanism controlled by diffusion between 600° and 900°C.[186] For extremely high glass contents (>30 vol%), the Ag particles became separated during sintering, and the final film resistivity increased due to poor connectivity of the Ag particles.[189] Addition of Pd retards the Ostwald ripening of Ag.[187] This is due to the decrease in solubility of Ag in glass caused by the formation of Ag/Pd solid solutions. The densification behavior of Ag is strongly dependent on the particle size, surface area, and degree of agglomeration of the Ag powders. In addition, it is also affected by the viscosity, softening point, and wettability of the glass.

Cole[89,90] studied the sintering behavior of 80Ag/20Pd film and concluded that the sintering also proceeds according to solution precipitation at metal sites containing lead bismuth borosilicate glass. At sites with no glass, grain boundary diffusion controlled the sintering. He also reported that a typical glass wets the ceramic far better than it wets the metal. This knowledge provides the information needed to largely understand the final structure of a glass-added film. The small Ag/Pd particles form agglomerates and sinter rapidly into larger particles forming grain boundaries with their neighbors. While this grain growth is occurring, the glass begins to migrate from the inside of the film to the free surface or to the film/ceramic interface. The glass both wets the metal and the ceramic and forms a bonding zone between metal particle and ceramic.[191,192] The migration of glass must be precisely controlled. Otherwise, glass on the surface may retard solderability in the case of conventional thick-film conductors or cause plating problems in the case of MLC termination compositions.[193] In addition, excess glass migrating into the interface may result in a series resistance. Sometimes, the glass may also penetrate into the ceramic along grain boundaries or through porosity. Glass infiltration is usually detrimental to the electrical performance.

Sintering of Ag/Pd films on Al_2O_3 substrates as well as on multilayer ceramic structures proceeds differently from simple bulk sintering due to the constraint of a rigid substrate.[194–197] Understanding the phenomenon of constrained-film sintering is very important for eliminating the problem of registration retention in thick-film hybrid circuit during firing and reducing the flaws in the multilayer ceramic structures during cofiring. In both cases, the particle characteristics of the powders, the uniformity of the green microstructure, and the glass or oxide additives in the film have overwhelming effects on controlling the densification process and evolution of the sintered microstructure.

For constrained sintering of a Ag/Pd film attached to a substrate, shrinkage can occur in the direction perpendicular to the plane of substrate if the film remains attached to the substrate and does not crack. The substrate exerts a tensile stress on the Ag/Pd film at the interface between them, which balances the sintering stress acting to produce in-plane shrinkage in the film.[174] The tensile stresses generated reduce the driving force for sintering. Therefore, the densification rate of the constrained film is always less than that of the free film. The stress developed in the plane is relaxed by creep or high-temperature deformation due to the presence of the glassy phase. Process defects such as cracks are not observed. Due to the low green density of the compact, the onset temperature at which grain growth begins for the Ag/Pd film is lower than that for bulk materials.

For constrained sintering of metal–ceramic multilayer structure, the laminated body shrinks in the X–Y directions as well as the Z direction. Minimizing the sintering shrinkage mismatch between the Ag/Pd and ceramic is very important for controlling the multilayer dimension and eliminating process flaws, such as delaminations, bowing, blistering, and crazing.[195,196] The shrinkage mismatch may include the mismatch in the onset of sintering temperature, the densification rate, and the total shrinkage between the Ag/Pd and the ceramic. Usually the metal film starts to sinter at lower temperatures, and its densification rapidly reaches a considerable extent. However, the ceramic tape generally sinters at higher temperatures, and most shrinkage occurs at soaking temperatures. The total shrinkage of the ceramic is generally larger than that of metal. The shrinkage mismatch can potentially create a tensile stress in the region which sinters faster and shrinks more. Therefore, the stress can be developed in the early stage of sintering. As stress in the film exceeds a critical level, process flaws will be generated.

IX. Parameters Which Affect the Final Film Properties

Depending on the application, requirements for good conductor film properties generally involve a high conductivity, good line resolution, smoothness, a high density, low metal consumption rates, good fired adhesion, good unfired strengths and toughness, and good bondability.[119,198] All of these requirements must be met in a film that also has matched thermal expansion and sintering shrinkage. These film properties are controlled by several parameters, including constituents of the paste, physical characteristics of the metal and additive powders, paste rheological properties, overall processing procedures, oxidation of the metal, and interaction of the Ag/Pd with surrounding components. Many of these factors are interrelated. The last two parameters are determined when the other parameters are fixed. In the following section, the initial parameters will be discussed.

(1) Constituents of the Ink

The three general types of thick-film Ag/Pd pastes can be classified by their end use: internal metallizations, end terminations, and fired-on thick-film conductors. Regardless of their application, all pastes consist of four generic ingredients: the Ag/Pd which serves as the functional conductor, a solvent, a temporary binder, and a permanent binder.[199]

(A) Ag/Pd Powders: Two kinds of Ag/Pd powders are used: (1) coprecipitated or physical mixtures, and (2) alloyed or solid solutions. Coprecipitated powders are usually a physical mixture (two phases) of distinguishable pure Ag and pure Pd, with only slight solid solution between the phases. These powders are usually produced simultaneously by chemical coprecipitation from an aqueous solution of Pd and Ag salts.[200] Alloyed powders can be produced by similar chemical coprecipitation followed by heating in an inert atmosphere. Therefore, a Pd-coated Ag powder, another form of two-phase Ag/Pd powders, was developed to ensure good dispersion. This power is prepared by growing Ag nuclei from an Ag salt solution, followed by precipitating Pd onto these nuclei in a Pd salt solution. Figure 16 shows the SEM micrographs of mono-size pure Pd and 70Ag/30PD powders (Pd-coated Ag powders).

The ratio of the Ag/Pd which is used is dependent on the conductivity desired, the firing temperature, and the soldering characteristics.[91] With increased Pd content, the melting temperature and the solder leaching resistance are increased. The conductivity of the film depends on the Ag/Pd ratio, as indicated in Fig. 17, and the glass extent.[201–203] Higher Pd contents also increase the Pd oxidation tendency as well as the Bi and Pb reactions previously discussed.

Formation of PdO during firing can result in blistering and delamination due to gas evolution and volume changes, respectively. PdO also inhibits the densification and grain growth pro-

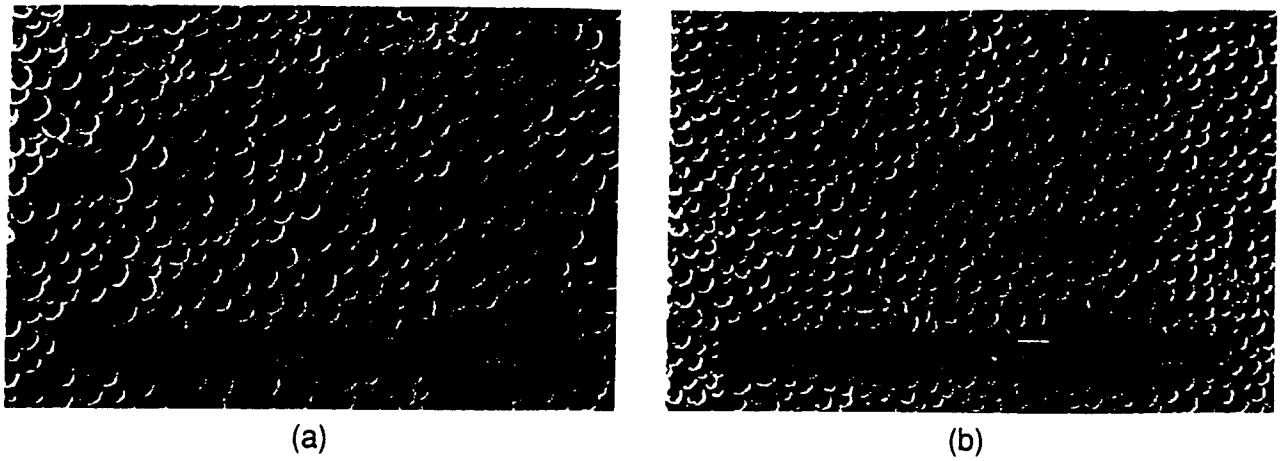

Fig. 16. SEM micrographs of (a) pure Pd and (b) 70Ag/30Pd (Pd-coated Ag) powders.

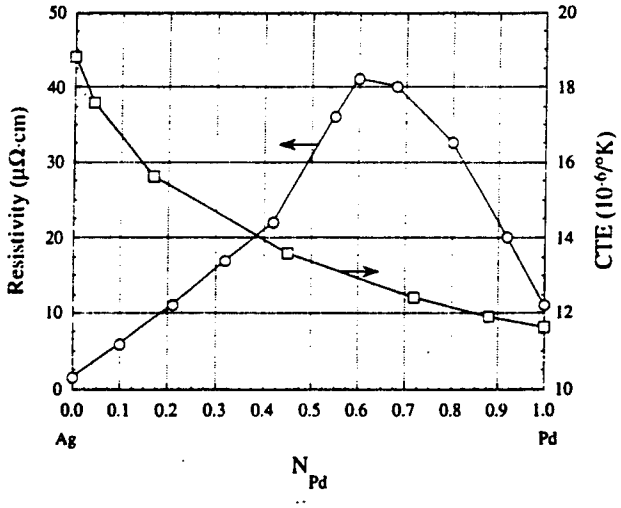

Fig. 17. Bulk electrical conductivity and linear thermal expansion of the Ag/Pd system.

cess during sintering of Ag/Pd powders. Therefore, it is often necessary to avoid or at least control the oxidation and reduction process. However, Maher[94,95] suggested a possible advantage to preoxidation of an alloy powder prior to its use as an internal metallization. A continuous PdO coating is formed which could decrease the shrinkage mismatch and the change in weight during multilayer ceramic cofiring.

(B) Inorganic Binders: The main functions of the glasses or fluxes used as inorganic binders are to enhance the adhesion between the metal and ceramic, provide lower sintering temperatures for the metal, and control (or usually minimize) the metal sintering shrinkage in firing and thermal expansion mismatch.[75] Adhesion is not often a problem for internal conductors in MLC capacitors and multichip modules; the purpose of an inorganic binder is to minimize the shrinkage mismatch.[112] since the metal powders generally densify at a much lower temperature than that of the cofired dielectrics, and to increase the performance of the fired film.

For internal metallizations, incorporation of refractory oxides, such as ThO_2 and Gd_2O_3, as reported in the patent literature,[76] not only inhibits excessive sintering of metallization during firing but also enables reduction of the thickness of electrode with acceptable capacitance parts. Addition of oxides or the same dielectric powder used in the body of the capacitor (<15%) into the electrode paste has the benefit of better sintering shrinkage and thermal expansion match, easier burnout of organics, and better mechanical integrity.[75,112] To enhance the dispersion of oxide additives in the electrode paste, they can be added either as ceramic coating on electrode particles or as metal coating on dielectric particles. Using a small amount of nonprecious metals or their oxide as additives (such as NiO),[204,205] the metallization was shown to have better electrical conductivity and stability. However, the high reactivity of these oxides with the dielectrics at high temperature is deleterious to the electrical performance of dielectrics. In some cases, organometallic compounds of Ru, Rh, Re, Ir, Pt, Al, Si, Mg, Pb, Ca, and Zn with an alkyl or aryl organic moiety are added to produce a highly dense metal surface structure and better shrinkage match.[206]

All of the Ag/Pd thick-film conductors used as terminations as well as fired-on conductors for microcircuits contain glasses to provide adhesion and lower the firing temperature.[207] Almost any low melting glass with a low alkali content can be used. High-lead glasses are common. The glass must also be chemically and thermally compatible with the adjacent components, such as thick-film resistors, crossovers, and dielectrics.[208] When good solderability is required, bismuth oxide and borosilicate glass is used, since it is compatible with Sn/Pb solder.[27,131]

Depending on the chemistry of the glasses, three types of bonding can occur between Ag/Pd and the ceramic.[5,27,209] These are glass bonding, reaction bonding, and flux bonding. For glass-bonded systems, typically 2–10 wt% lead borosilicate, the glass generally migrates to the ceramic/metal interface during firing due to wetting.[210,211] In addition to chemical bonding, the glass provides a mechanical interlock between the different phases. However, good adhesion must be made without introducing an appreciable thickness between the metal and ceramic. At excessively high firing temperatures or long soak times, in addition to forming a continuous film between the glass and ceramic, the glass may also float to the conductor surface. The glass on the surface can result in poor solderability. The continuous glass film in the interface may mechanically provide a propagation path for cracks and, from that, electrically form a blocking contact.[193] In addition, high loading of this type of glass also produces line spreading and ultimately poor line densities.[212]

Reaction-bonded system[illegible]e adhesion using additives such as CuO and CdO (0.[illegible]%) added to the paste. They form intermediate compo[illegible]th Al_2O_3 at the peak firing temperature.[213–216] An adva[illegible], that a lesser amount of additive is typically needed. To achieve optimum adhesion, it is often necessary to fire reaction-bonded conductors at higher temperatures than glass-bonded conductors. However, if the additive dissolves in the glass, its effectiveness will decrease drastically, because it will become more difficult for the additive to reach the substrate. In addition, if the oxide melts before

the peak firing temperature, these additives will not work well. The additive must be stable in the sintering atmosphere at the firing temperature.

For a flux-bonded system, 1–5 wt% of an oxide is added, which can form a liquid phase with the ceramic. For instance, Bi_2O_3 is often used because of the eutectic liquid formation of Bi_2O_3–Al_2O_3 at 820°C.[217] Good adhesion is provided if the liquid phase wets the metal. However, this type of glass may also generate line spreading and weaken the substrate.

Interactions between the glass and the ceramic may not always be desirable. For instance, the reaction of Bi_2O_3 in a Ag paste with TiO_2 ceramic results in the formation of $Bi_2Ti_2O_7$ at temperatures as low as 600°C. This interfacial layer reduces the dielectric constant and dissipation factor of TiO_2 ceramics.[218] It may also act as a nonohmic barrier layer between the Ag electrode and *n*-type TiO_2 or semiconducting $BaTiO_3$ ceramic. Alternatively, if the substrate is fired numerous times due to the complexity of the circuit, the Bi_2O_3 may react with the binder, crossover, or resistor pastes to cause open circuits in resistors or short circuits in crossovers.[208]

An important consideration when choosing a glass formulation is the softening point. A high softening point is desirable so that all of the organics from the paste vehicle are burned out before the glass melts.[219] If an organic remains, it will be trapped by the glass when it softens. Entrapped carbon often leads to the formation of blisters in the final film.[220] A high softening point glass can also help match the thermal expansion of the ceramic. On the other hand, a low softening point allows for glass to wet the metal particles and begin sintering at lower temperatures.[67,221] In this manner the metal particles are bound to the ceramic, which can minimize the *X–Y* shrinkage and the open porosity in the film.

Other desirable properties of a thick-film conductor glass include a low viscosity, high density, and low surface tension. Low viscosities result in good capillary soaking of the particles. A high density helps the glass flow downward to the substrate to aid in bonding to it. A low surface tension promotes good wetting of the metal particles and ceramics. Wetting of the ceramic surface is a key factor involved in good conductor adhesion. Low wetting angle oxide additions (e.g., Cu_2O, V_2O_5, and WO_3) are usually added in lead or bismuth borosilicate glasses.[211]

(C) Vehicle: The chief function of the screening vehicle is to maintain the inorganic particulates in a desirable state of dispersion and to allow easy transfer of the paste through the screen and onto the substrate without paste spreading.[27] In general, it requires a polymeric binder and a solvent. Other organics, such as wetting agents, defoaming agents and viscosity modifiers can aid in processing. Thick-film conductor ink compositions are formulated to exhibit pseudoplastic flow behavior.[5] These repond to shear with a decrease in viscosity and recover to high viscosity on cessation of shear.[222]

General considerations for resin and solvent systems include rheological response, paste operation lifetime, drying rate, long shelf life, low toxicity, chemical inertness (to preclude reactions with the screen or solids), a small change in viscosity with change in temperature, and solubility and compatibility with other solvents for easy cleanup.[5] Other criteria for the selection of the vehicle systems may be used to optimize the thick-film paste for specific applications. For fired-on thick-film paste, print-line resolution and high squeegee speed capability are the critical factors. For MLC terminations, important issues include conformal coating thickness (including edge, side, and corner coverage), dipped band shape and appearance (peaking or sagging), and chip wetting by the paste. The pseudoplastic nature of the termination compositions is often modified with flow control agents to obtain better edge coverage and cosmetics. For internal electrodes, the vehicle in the paste has a direct effect on the tendency of the electrode to cause delamination. A good vehicle should have easy organic removal during burnout, minimum or zero reactivity with the binder in the dielectric substrates, minimum metal-organic catalysis reaction, and lower tendency toward delamination.

The solvent of the vehicle serves to disperse the other organics homogeneously throughout the paste. The solvent should evaporate slowly at ambient temperatures to ensure long residence times on the screen during use, but must dry easily at elevated temperatures to provide films with sufficient green strength to withstand normal handling. Solvents with a vapor pressure of <0.2 mm Hg at 20°C and boiling points in the range of 200° to 300°C at 760 mmHg are generally used in vehicle formulations.[27] Common solvents include terpineol, pine oil, dibutyl carbitol, turpentine oil, 2,2,4-trimethylpentanediol-1,-3-monoisobutyrute, 1-methylethylene glycol butyl ether, butyl carbitol acetate, dibutyl phthalate, aromatic hydrocarbons, ethylene glycol ethers, diethylene glycol ethers, and their ester derivatives.[223–28]

The binder gives the film mechanical integrity after solvent evaporation. A binder with polar groups on the polymer chain helps maintain adequate dispersion of metal and glass particles. The binder should provide good viscosity build at low concentrations and burn out cleanly during the early stages of the thick-film firing circle. Common binders include ethyl cellulose, hydrogenated wood rosin, polyacrylates, polymethacrylates, methacrylic acid ester, polyesters and polyolefins.[226,229–31] Among these, cellulose and cellulose derivatives are the most widely employed, since they are readily soluble in hydroxylic and some aromatic type solvents. One of the simplest vehicle systems is a cellulose derivative in terpineol.[86,232,233]

The binder content of the paste has a direct effect on the tendency of MLC electrodes to cause delaminations. Reduction of the amount of resin in dried electrode prints has a number of benefits. Less binder in the dried electrode print results in easier organic removal during burnout and of course also reduces the amount of resin available for metal-organic catalysis reaction.[147]

Viscosity modifiers are added to the ink to alter the viscosity level of the organic mixture to that desired for screen printing. Common viscosity modifiers are castor oil derivatives.[228] Wetting agents help the organic mixture coat the collection of powders and help to achieve good metal powder dispersability. Wetting agents are also used to achieve a good bond between the inorganic particulates between the composite and substrate. Typical wetting agents are soya lecithin, triethanolamine, cyanoquanidine, phospholipids, and phosphate esters.[234]

Surfactant agents prevent agglomeration and assure a good particulate dispersion through surface charges. Examples of surfactants are amine soap amphoteric surfactant, linoleic acid, oleylamine, N-alkyl-1 3-diaminopropane dioleate, carboxylic acid salts, and mono- and dialkylethoxylate esters of phosphoric acid.[228,235] In termination inks, hardening additives are sometimes added. They are usually low molecular weight, brittle materials such as those derived from wood extraction.

In addition to metal-organic catalytic reaction, another chemical reaction must be considered during selection of any organic additives. For instance, if terephthalic or furoic acid are used as flow-controlling agents, they would react with basic metal oxides (inorganic additives) such as Bi_2O_3 in the paste. This reaction will result in an increasing viscosity over time.[5]

Any organics used in the internal electrode must be compatible with those used in the dielectric ceramic green tapes. Organic solvent-binder systems are commonly used in both dielectric slurries and thick-film pastes. The major advantage of organic solvents is the wide range of vapor pressures and boiling points of solvents available, which allows for tailoring of the rheological characteristics to match any application. Despite the narrower range of water-soluble binders, the use of water-based binder systems for the tape casting of dielectrics used in MLCs is of increasing interest due to economic, safety, and environmental reasons.[236,237] Thus, development of vehicle systems which are water-based is going to be a potential research area.

(2) Characteristics of Metal Powders

Palladium and Ag powders can be prepared by several methods, such as chemical precipitation, powder metallurgy, and electrolytic reduction. Usually they are prepared by precipitation from aqueous solutions of Pd and Ag salts (e.g., $AgNO_3$ and $PdCl_2$). The precipitation conditions and any postprecipitation treatments determine the powders morphology, surface area, particle size distribution, and tap bulk density.[200] These parameters directly and indirectly affect the ink's properties and thus the ultimate performance of the thick-film conductors.[238] For example, the Pd particle size and surface area affect resistivity, aged adhesion, and solderability of thick-film conductors. These effects are attributed to the alteration of the rate of PdO formation; i.e., coarse Pd oxidizes more slowly.

(A) Morphology: The Ag/Pd morphology directly affects the sintering of the film, but also indirectly affects final film properties such as solderability, adhesion, and electrical properties.[63] Surface morphologies for the Ag/Pd powders include spherical, flake, nodular, acicular, and dendritic powders.[238] Among them, spherical and flake are the most common accepted for use as thick-film materials. Nodular powders usually have a low surface area. However, the surface irregularity and wide particle size distribution promotes uneven sintering during the firing stages, which ultimately leads to poorly defined conducting layers. Dendritic powders can have good sintering characteristics and lead to strong coherent layers due to the formation of mat-type structures during printing. However, these mats can result in screen blockage, which makes the powder of little practical use.

Flake powders are commonly used in termination inks and thick-film conductors.[239,240] They can be prepared by ball-milling or fluid-energy-milling the Ag/Pd powders or can be directly precipitated as flake morphology from the solution. Flake powders are known to produce low-viscosity formulations and allow for high solid loading of thick-film paste compared with that of spherical particles. Flake powders can provide good rheology for termination to prevent sagging as well as peaking. But flake powders tend to produce gelation, which reduces the screenability. Powder morphology also affects the sintering of the Ag powder with or without glass addition. For pure Ag, flake powders densify at temperatures higher than that of spherical powders. With addition of glass frits, the densification of flaky Ag starts only above the softening temperature of the glass, but the Ag-glass wetting is more difficult in flaky Ag powders.

(B) Surface Area: The surface area of Ag/Pd powders indirectly affects solder leach resistance, rheology, shrinkage during firing, film density, and conductivity. There are a broad variety of chemically coprecipitated Pd, Ag, and Ag/Pd powders for use in different applications. Surface areas range from 0.1 to 10 m^2/g for pure Ag, from 0.5 to 30 m^2/g for pure Pd, and from 0.5 to 15 m^2/g for Ag/Pd. Typically Pd can be made with higher surface areas than Ag, although Ag powders with surface areas of up to 15 m^2/g are possible and known in thick-film compositions.

The surface area must be within an optimum range. The surface area should be relatively low to permit high solid loadings which yield high metal powder green densities in the dried prints and therefore lead to high electrical conductivity.[63] However, powders having too low a surface area often result in either poor reproducibility and/or open circuits. On the other hand, the greater the surface area of powder, the finer the fired film, but the resistivity is higher due to microcrack formation and the presence of more grain boundaries.[63] Powders having a high surface area also result in higher viscosity pastes which cannot be screen printed easily.[238] Powder finer than 20 m^2/g also has a tendency to "cake" and catalytically react with the vehicle and/or substrate.

Decreasing the surface area decreases the rate at which Pd oxidizes and slows the shrinkage rate during firing.[18,93] However, this has an adverse effect on later metal densification and results in thicker fired films. Constantine[112] showed that increases in the surface area result in low densities due to densification prior to reduction of PdO and subsequent entrapment of PdO at high temperatures.

For internal metallization applications, surface area is a very important parameter to control the shrinkage mismatch. High surface area (>10 m^2/g) materials are of little use in MLC applications, since the metal densities at lower temperatures worsens the shrinkage mismatch, and can increase the rate of internal catalytic reactions.[238] Differences in the temperature ranges over which the electrode and dielectric begin to densify can lead to internal stress and subsequent stress relief by formation of delaminations. In addition, catalyzed exothermic reactions due to the high surface area powder can generate local hot spots which can also result in delaminations.

(C) Particle Size and Particle Size Distribution: The particle size and particle size distribution directly affect the green packing density, final film density, and hence the electrical properties. The packing of the particles for maximum green density is a problem of great importance in ceramic processing and powder metallurgy, but it is even more critical for thick-film conductors because of the very low or negligible compacting pressures exerted during screen printing. The fired film density, and hence the electrical resistivity, are intimately related to the density of the metal compact which exists after the organic constituents of the ink have been removed in the early stage of firing.[103] Good packing density in thick films can be achieved by using powders that are well deagglomerated, have an optimum surface area, or have a multimodal particle size distribution (for dense random packing). However, powders with wide or multimodal particle size distributions usually result in uneven sintering during firing. This can lead to discontinuous metal layers due to the tendency of fine particles to align or stick together due to electrostatic forces or differences in sintering between small and large particles. Therefore, in practice, tighter distributions and smaller agglomerate size powders are used to achieve high green density.

Ag/Pd powders usually comprise primary particles that form agglomerates 1 to 10 μm in size.[200] Powders with excessively large particles tend to clog screens, leach in solder, produce poor adhesion, and tin poorly. However, using smaller particles requires considerably more vehicle to wet the pigment surface, leaving less vehicle for flow and viscosity control. Thus, screen clogging often occurs from inks or pastes made from very small particle powders. Very fine powders can also build up complex agglomerate structures and result in undesirable rheological dilatancy.

The powder particle size also affects the densification for solid-state sintering as well as liquid-phase sintering of the Ag/Pd. For pure Ag, densification starts at temperatures lower than that of coarse particles. For liquid-phase sintering, the effect of glass addition on the densification is more pronounced with small Ag powders. This is due to good wettability of Ag and the large Ag/glass interfacial area obtainable with fine Ag particles.

(D) Agglomeration: Deagglomerated powders result in better particle dispersions and, hence, reduced surface asperities or lumps in the dried prints. The resultant smooth surface of dried prints results in more-uniform and better-continuity fired films with higher electrical conductivities.[63] Usually the final agglomerate or aggregate size in the paste will control the packing in the dried prints and influence the fired film density. Also, the agglomerate particles can be the cause of pinholes and cracks in the fired film. The largest agglomerate or aggregate in a dispersion should be smaller than the thickness of the fired film in order to ensure fired uniformity. Thus, a key to formulating superior thick-film conductors is to improve their powder dispersion or to precipitate unagglomerated powders directly from solution. Otherwise, the Ag/Pd particles will not pack well, leading to discontinuous fired films. In many cases, manufacturers of the powders are using various dispersants and surfactants to coat the powder as part of the powder precipitation

process, or after precipitation, in order to prevent agglomeration and to improve powder properties.[63,64]

High green-state powder packing will also produce more rapid sintering rates at lower temperatures than agglomerated compacts because of the higher degree of coordination with other particles in the denser green film.[241] The green-state packing of the powder in a dried print is determined by the particle size distribution and bulk density of the powder; a finer particle size distribution and higher bulk density usually will lead to more rapid densification.

A general finding for thick-film pastes is that the quality of the powder dispersion and the ultimate performance are highly related. The paste with the better powder dispersion will allow manufacturers to print electrodes at lower metal deposition without sacrificing design performance. Pepin *et al.*[63,64] have shown (Fig. 18) that one advantage of using deagglomerated Ag/Pd powders is that typically 30% less metal powder is needed to achieve the identical capacitance of a MLC.[63,64] Improved powder dispersions also result in a much sharper capacitance cutoff, allowing tighter control on the distribution of fired part capacitance. In addition, the better overall electrical conductivity of MLCs made with deagglomerated powder gives them a lower dissipation factor, at higher frequencies, than MLCs made with agglomerated powder paste.[64] It is also shown that the level of MLC failure due to low insulation resistance is increased in proportion to the degree of agglomeration of the internal electrode.[30]

(E) Tap Bulk Density: The tap density is measured by compacting a known amount of powder in an automatic tapping machine for a preset time. Tap bulk density, combined with powder particle size distribution and surface area, defines the state of agglomeration of the powder. Tap bulk density is of interest to the thick-film manufacturer because it additionally can predict the powder's ability to be wet by the vehicle during milling. It is particularly critical for powders with a surface area less than 2 m^2/g.[200]

(3) Paste Properties

Paste properties, such as solids loading, dispersability, rheology, and printability, influence the quality of the print. As mentioned earlier, the maximum solids loading of the paste which can be achieved for a desired rheology depends on the surface area of the powders. Usually, the solids loading of the fired-on conductors and terminations are higher than that of internal metallizations. Increases in the green density usually improve the final film properties, yet cause problems with low-temperature shrinkage mismatch and high metal deposition.

In addition to loading, the dispersion of the powders in the vehicle also plays an important role in determining the final density.[64] The dispersion influences both the particle packing in the green state and the dried-to-fired shrinkage, though the latter is more strongly controlled by surface area.

Table VI summarizes the rheological behavior typically desired for Ag/Pd thick-film conductors used in different applications. Paste rheology is a critical concern for the screen printing step.[242] Paste viscosity should be low at high shear rates to allow for rapid printing, and high at low shear rates for good line resolution.[243] In general, fine powders can cause excessively high paste viscosity, especially at high solid loadings. Rheological optimization can be achieved by adjustment of the vehicle resin content, the solid loading in the ink, and usage of surface active materials. Rheology control is also very important for termination during the dipping process.[244] Some thixotropic behavior is generally required for a good termination. Too much can lead to a peaked end termination and thus result in increased length dimension. Too little can lead to an increasing degree of termination sagging, thus increasing the land length and rendering the component unusable for some surface mount applications.[245] Although paste materials for fired-on conductor and internal electrode also exhibit shear thinning behavior, the degree of pseudoplasticity is usually less than for a termination.

(4) Processing

During the manufacture of a thick-film material, components are blended together in the desired ratio and are usually milled on a three-roll mill (high shear rather than high impact) to achieve deagglomeration and homogenization without altering the morphological characteristics of the functional powders. In some cases, ball-milling is another choice for low-viscosity mixes, particularly for Ag-bearing terminations.[240,246] The metal powders are sometimes initially roll-milled without frit in order to measure the paste particle size distribution of just the metal

Table VI. Typical Rheology of Thick-Film Conductors

Application	Rheological characteristic
Internal electrodes	Newtonian or pseudoplastic
Terminations	Pseudoplastic and thixotropic
Fired-on conductors	Pseudoplastic and thixotropic

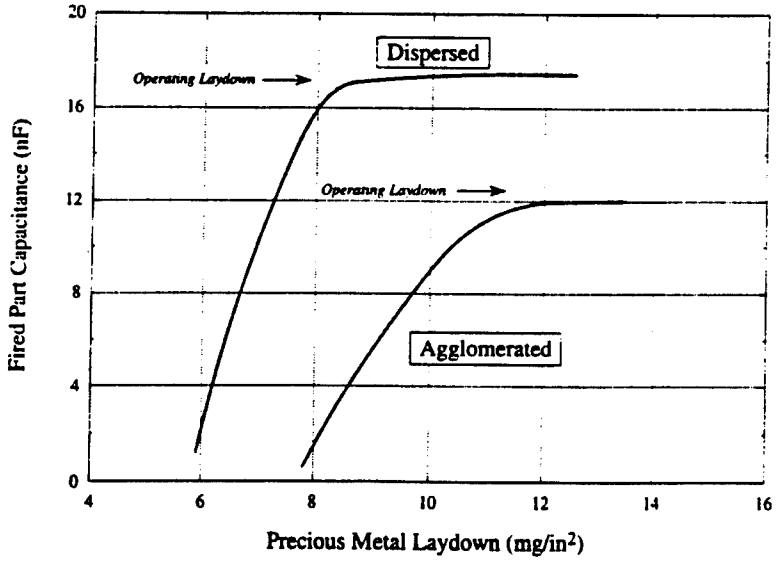

Fig. 18. Impact of the state of agglomeration on the capacitance and dissipation factor of multilayer capacitors.

particles. A separate frit paste can also be made and roll-milled. Final conductor compositions are obtained by combining the metal and frit pastes, with a final roll-milling step added to ensure intimate mixture.[63,200]

After the ink pattern is screen-printed, it is necessary to allow the paste to level, by viscous flow, to a uniform thickness before drying. Firing the hybrid circuit is a complex process which consists of (a) burning out of organic binders, (b) oxidation/reduction of the metallic elements, and (c) sintering of the metallic element and glass to anchor the film to the ceramic. The temperature, time, composition of atmosphere, and pressure are important parameters during firing for controlling the oxidation of Pd, the extent of the organic residue, the adhesion of metal to ceramic, and the sintering shrinkage mismatch between the multicomponents.[247] For example, the presence of excess O_2 in the burnout atmosphere can have detrimental effects. Pd can easily catalyze a strong exothermic pyrolysis of the binder. It is usually possible to suppress such an exotherm by monitoring the weight loss rate (dW/dt) through the heating rate or restrictions on the amount of O_2 in the atmosphere which can control the reaction.[248] When an exothermic reaction occurs, the rate of gas evolution can easily exceed the capability of the porosity in the green compact. This creates bubbles or bloating. To avoid this, one can use N_2 atmosphere burnout at temperatures below 500°C. But if the temperature is too high, burnout in N_2 results in excess carbonization of the binder residue.

X. Summary

Ag/Pd thick-film conductors are one of the most important metallizations in microelectronic circuitry. Materials development and process technology are very important for microcircuit design, since they directly affect the electrical performance, yield, reliability, and cost.

Pd oxidation and subsequent PdO reduction may influence many properties of Ag/Pd film such as solderability, continuity, density, and electrical conductivity. The Pd oxidation/reduction also impacts on the reactivity and sintering shrinkage mismatch between the metallization and ceramic substrates. Pd oxidation/reduction can be controlled using either thermodynamic or kinetic approaches. The thermodynamic approach includes atmosphere, firing temperatures, and Ag/Pd ratio; and the kinetic approach includes powder characteristics and heating rate.

Formulation design parameters include Ag/Pd ratio and inorganic and organic constituents. These determine the chemical and physical interaction between the Ag/Pd metallization and the adjacent compounds as well as the fired film properties such as electrical conductivity, thermal conductivity, adhesion/bonding, continuity, solderability, migration resistance, and solder leaching resistance.

Paste properties, such as rheology and dispersity of the inorganic powders, are critical issues that influence the line resolution, smoothness, or cosmetic properties of the film. Properties of an Ag/Pd thick-film paste can be controlled by tailoring the powder characteristics of the metal powders and inorganic components and by optimizing the paste mixing and milling process.

Therefore, powder characteristics, paste formulation, and processing control must all be optimized in order to reduce the Pd oxidation, to minimize the potential interaction between Ag/Pd and the other components, and to obtain the desired paste properties. These, in turn, determine the final film properties and the mechanical and thermal compatibility.

Acknowledgment: The authors would like to thank Dr. Dan V. Goia, technical manager of Degussa Corporation, for providing SEM micrographs and helpful discussions.

References

[1]R. R. Tummala, "Ceramic and Glass-Ceramic Packaging in the 1990s," *J. Am. Ceram. Soc.*, **74** [5] 895–908 (1991).
[2]R. R. Tummala, "Multichip Packaging—A Tutorial," *Proc. IEEE*, **80** [12] 1924–41 (1992).
[3]R. DellAcqua, "Non-conventional Applications of Thick Film Technology," *Hybrid/Circuits*, **12**, 10–21 (1987).
[4]A. H. Kumar and R. Tummala, "State of the Art, Glass-Ceramic/Copper, Multilayer Substrate for High Performance Computers," *Int. J. Hybrid Microelectron.*, **14** [4] 137–50 (1991).
[5]R. W. Vest, "Materials Science of Thick Film Technology," *Am. Ceram. Soc. Bull.*, **65** [4] 631–36 (1986).
[6]L. F. Miller, *Thick Film Technology and Chip Joining*, Gordon and Breach, New York, 1972.
[7]L. F. Miller, "Silver-Palladium Fired Electrode"; p. 52–64 in Proceedings of 1968 Electronic Component Conference, IEEE, New York, 1968.
[8]J. M. Herbert, *Ceramic Dielectrics and Capacitors*, Electrocomponent Science Monographs, Vol. 6, Gordon and Breach, New York, 1985.
[9]W. Noorlander, "Some Aspects of Multilayer Ceramic Chip Capacitors for Hybrid Circuits," *Electrocomponent Sci. Technol.*, **5**, 33–40 (1978).
[10]J. L. Sprague, "Multilayer Ceramic Packaging Alternatives," *IEEE Trans. Compon., Hybrids, Manuf. Technol.*, **13** [2] 390–95 (1990).
[11]*Metal Handbook*, 10th ed. ASM International, Materials Park, OH, 1990.
[12]L. A. Mann, S. P. Gupta, and L. G. Jones, "The Effects of Termination Composition on the Thermal Shock and Thermal Cycle Performance of SMD Ceramic Capacitors"; pp. 16–20 in Proceedings of 11th Capacitor and Resistor Technology Symposium, March 4–7, 1991, Components Technology Institute, Huntsville, AL, 1991.
[13]B. S. Rawal, R. Ladew, and R. Garcia, "Factors Responsible for Thermal Shock Behavior of Chip Capacitors"; pp. 145–56 in 37th Electronic Components and Technology Conference, 1987, IEEE, New York, 1987.
[14]R. O. Carlson, H. H. Glascock II, H. F. Webster, and C. A. Neugebauer, "Thermal Expansion Mismatch in Electronic Packaging," *Mater. Res. Soc. Symp. Proc.*, **40**, 177–90 (1985).
[15]R. Chanchani and P. M. Hall, "Temperature Dependence of Thermal Expansion of Ceramics and Metals for Electronic Packages"; pp. 94–102 in 40th Electronic Components and Technology Conference, 1990, IEEE, New York, 1990.
[16]G. Foster, "Solder Shock Jeopardizes SM Reliability," *Electron. Prod.*, **17**, 35–39 (1988).
[17]S. F. Wang and W. Huebner, "Interaction of Ag/Pd Metallization with Lead and Bismuth Oxide-based Fluxes in Multilayer Ceramic Capacitors," *J. Am. Ceram. Soc.*, **75** [9] 2339–52 (1992).
[18]Z. A. Munir and P. G. Coombs, "Role of Sintering on the Oxidation–Reduction of Palladium Powders"; pp. 301–307 in Advances in Ceramics, Vol. 7, *Additives and Interfaces in Electronic Ceramics*, American Ceramic Society, Columbus, OH, 1983.
[19]D. R. Sample, "The Effects of Glass Additions on Firing of Copper Thick Films"; M.S. Thesis, The Pennsylvania State University, University Park, PA, 1992.
[20]P. Palanisamy and D. H. R. Sarma, "Thermodynamics of Processing Copper Thick Film System in a Reactive Atmosphere," *Hybrid Circuits*, **13**, 13019 (1987).
[21]R. Tanabe and J. Chiba, "Properties of New Nitrogen Firable Resistor System for Thick Film Circuit"; pp. 92–97 in ISHM 1990 Proceedings, International Society for Hybrid Microelectronics, Reston, VA, 1990.
[22]R. L. Cadenhead, "Materials and Electronic Phenomena," *Inside ISHM* [June] 9–18 (1985).
[23]B. D. Rowen, "The Role of Previous Metal Powders in Electronics"; pp. 259–68 in *Precious Metal*, Pergamon Press, New York, 1982.
[24]N. M. Davey and R. J. Seymour, "The Platinum Metals in Electronics," *Platinum Met. Rev.*, **29** [1] 2–11 (1985).
[25]L. C. Hoffman, "Metallizing Compositions," U.S. Pat. No. 3 385 799, 1968.
[26]J. R. Larry, R. M. Rosenberg, and R. O. Uhler, "Thick Film Technology: An Introduction to the Materials," *IEEE Trans. Compon., Hybrids, Manuf. Technol.*, **CHMT-3** [2] 211–25 (1980).
[27]B. E. Taylor, J. J. Felten, and J. R. Larry, "Progress in and Technology of Low Cost Silver Containing Thick Film Conductors," *IEEE Trans. Compon., Hybrids, Manuf. Technol.*, **CHMT-3** [4] 504–17 (1980).
[28]J. C. Fu, "A Study of Structure of Gold-Platinum in Thick Film Conductors"; pp. 469–83 in *Precious Metal*, Pergamon Press, New York, 1985.
[29]S. Milkovich and L. F. Miller, "Metallizing Composition Conductor and Method," U.S. Pat. No. 3 537 892, 1970.
[30]O. A. Short, "Ceramic Capacitors with Noble Electrode Alloys," U.S. Pat. No. 3 798 516, 1974.
[31]O. A. Short, "Alloy Metallizations," U.S. Pat. No. 3 756 834, 1973.
[32]O. A. Short, "Elimination of Dielectric Degradation in Printed Gold/Dielectric/Palladium-Silver Structure," U.S. Pat. No. 3 770 496, 1973.
[33]H. H. Mones and K. Nessler, Jr., "Electrical Resistance Compositions, Elements and Methods of Making the Same," U.S. Pat. No. 3 248 345.
[34]O. A. Novikova and A. A. Rudintzkiy, "A Study of the System Gold-Silver-Palladium," *Zh. Neorg. Khim.*, **3** [3] 729–49 (1958).
[35]W. Borland, C. R. S. Needs, V. P. Siuta, and K. M. Nair, "High Conductivity Materials Systems for Advanced Hybrids"; in Proceedings of the 1989 Electronic Components Conference, IEEE, New York, 1989.
[36]S. Tong and C. E. Falletta, "Silver-Palladium Conductors with Excellent Lead Resistance and Solderability but Containing Less Than 1% Palladium"; pp. 8–10 in ISHM 1987 Proceedings, International Society for Hybrid Microelectronics, Reston, VA, 1987.
[37]S. J. Stein, C. Huang, L. Cang, and G. Schultz, "Recent Advances in Platinum-Silver Thick Film Conductors," *Solid State Technol.*, **18** [5] 25 (1975).
[38]H. L. Hvims, *Effects of Terminal Metallization on SMT Soldering*, ECR-202, Elektronik Centralen, Denmark, 1990.
[39]D. W. Hamer and J. U. Biggers, *Thick Film Hybrid Circuit Technology*, Wiley-Interscience, New York, 1972.

[40]R. R. Sutherland and I. D. E. Videlo, "A Comparison of the Reliability of Copper and Palladium-Silver Thick Film Crossovers," *IEEE Trans. Compon., Hybrids, Manuf. Technol.*, **CHMT-12** [4] 676–82 (1987).

[41]Y. H. Chiao and K. Yang, "Cofire Metallization of Aluminum Nitrade Substrates"; pp. 88–93 in ISHM 1992 Proceedings. International Society for Hybrid Microelectronics, Reston, VA, 1992.

[42]F. A. Bydash, "Molybdenum in the Electronic Industry," *IEEE Trans. Compon., Hybrids, Manuf. Technol.*, **CHMT-3** [2] 232–36 (1980).

[43]S. Nozaki, A. Kanda, S. Iio, Y. Nakayamn, and N. Kato, "Mo-Mn Metallization on AlN Substrate"; pp. 365–73 in Ceramic Transactions, Vol. 15, *Materials and Processes for Microelectronic Systems*. Edited by K. M. Nair, R. Pohanka, and R. C. Buchanan. American Ceramic Society, Westerville, OH, 1990.

[44]S. R. Winzer, N. S. Shankar, and A. P. Ritter, "Designing Cofired Multilayer Electrostrictive Actuators for Reliability," *J. Am. Ceram. Soc.*, **72** [12] 2246–57 (1989).

[45]S. Takahashi, A. Ochi, M. Yonezawa, T. Yano, T. Hanatsuki, and I. Fukui, "Internal Electrode Piezoelectric Ceramic Actuator," *Jpn. J. Appl. Phys.*, **22** [Suppl. 22-2] 157 (1983).

[46]J. Maxwell, N. Chan, and A. Templeton, "Multilayer Varistor"; pp. 107–12 in 1989 Proceedings of Capacitor and Resistor Technology Symposium, Components Technology Institute, Huntsville, AL, 1989.

[47]P. Ward, "Approaching the Limits: the Latest Developments in Multilayer Ceramic Capacitors," *Electron. Eng.*, **65**, 39–43 (1993).

[48]Y. Sakabe, "Recent Progress on Multilayer Ceramic Capacitors"; pp. 119–29 in Proceedings of Materials Research Society International Meeting on Advanced Materials, Vol. 10, Materials Research Society, Pittsburgh, PA, 1989.

[49]W. R. Buessem and T. I. Prokopowicz, "Electrode and Materials Problems in Ceramic Capacitors," *Ferroelectrics*, **10** [1–4] 225–30 (1976).

[50]O. A. Short, "Gold Alloy Metallizations for Capacitor Electrode," U.S. Pat. No. 3 817 758, 1974.

[51]I. Burn, "Flux-Sintered $BaTiO_3$," *J. Mater. Sci.*, **17** [5] 398–411 (1982).

[52]I. Burn and W. C. Porter, "Processing Multilayer Ceramics with Internal Copper Conductors"; see Ref. 43, pp. 385–90.

[53]S. Sumita, M. Ikeda, Y. Nakano, K. Nishiyama, and T. Nomura, "Degradation of Multilayer Ceramic Capacitors with Nickel Electrodes," *J. Am. Ceram. Soc.*, **74** [11] 2739–46 (1991).

[54]T. L. Rutt, "Ceramic Bodies with End Termination Electrodes," U.S. Pat. No. 4 071 880, 1978.

[55]Y. Sakabe, "Dielectric Materials for Base-Metal Multilayer Ceramic Capacitors," *Am. Ceram. Soc. Bull.*, **66** [9] 1338–41 (1987).

[56]I. Burn, "Temperature Stable Monolithic Ceramic Capacitor with Base Metal Electrode," U.S. Pat. No. 3 987 347, 1976.

[57]J. Kaqto, Y. Yokotani, H. Kagata, and H. Niwa, "Multilayer Ceramic Capacitor with Copper Electrode," *Jpn. J. Appl. Phys.*, **26**, 90–92 (1987).

[58]M. Kahn, D. P. Burks, I. Burn, and W. A. Schulze, *Ceramic Capacitor Technology*, Electrocomponent Science Monographs, Vol. 6, Gordon and Breach, New York, 1985.

[59]T. R. Shrout and A. Halliyal, "Preparation of Lead-Based Relaxor Ferroelectrics for Capacitors," *Am. Ceram. Soc. Bull.*, **66**, 704–11 (1987).

[60]S. Sugihara and K. Okazaki, "Interfaces of Electronic Ceramics/Electrodes and Wetting Properties"; pp. 130–33 in Abstracts of the Fifth U.S.-Japan Seminar on Dielectric and Piezoelectric Ceramic (Dec. 11–14, 1990, Kyoto, Japan).

[61]I. Karakaya and W. T. Thompson, "The Ag/Pd System," *Bull. Alloy Phase Diagrams*, **9** [3] 237–43 (1988).

[62]Y. Shimada, Y. Yamashita, and H. Takamizawa, "Low Dielectric Constant Multilayer Glass-Ceramic Substrate with Ag/Pd Wiring for VLSI Package," *IEEE Trans. Compon., Hybrids, Manuf. Technol.*, **11** [1] 163–70 (1988).

[63]M. H. LaBranche, J. G. Pepin, and W. Borland, "Silver/Palladium Thick Film Conductors and Multilayer Ceramic Capacitor Electrodes: Powder Technology and Fired Properties"; in Proceedings of the ASM Thick Film Conference (Atlanta, GA, June 8–9, 1988). American Society for Metals, Metals Park, OH, 1988.

[64]J. G. Pepin, "Multilayer Ceramic Capacitor Electrodes," *J. Mater. Sci.*, **2**, 34–39 (1991).

[65]R. A. Parr, W. A. Craig, J. G. Pepin, J. R. Brotzmann, R. J. S. Young, and A. Inaba, "High Reliability Terminations for Surface Mount Multilayer Ceramic Capacitors on Printed Circuit Boards"; pp. 192–97 in Proceedings of 5th European Capacitor and Resistor Technology Symposium, Components Technology Institute, Huntsville, AL, 1991.

[66]W. Borland, "Thick Film Hybrid"; pp. 332–53 in *Packaging, Electronic Materials Handbook*, Vol. 1, ASM International, Materials Park, OH, 1989.

[67]J. R. Larry and R. B. Amin, "High Adhesion, Thick Film Palladium-Silver Conductors"; pp. 161–70 in 23rd Electronic Components Conference (May 14–16, 1973), IEEE, New York, 1973.

[68]R. G. Loasby, N. Davey, and H. Barlow, "Enhanced Properties of Thick Film Pastes," *Solid State Technol.*, **15**, 46–54 (1972).

[69]H. Imai and T. Yamaguchi, "Science and Technology in Composite Materials—Sintering of Silver-Glass Thick Films," *Ceramics*, **27** [11] 1092–99 (1992).

[70]C. F. Smith, "End Termination Compositions for Multilayer Chip Capacitors: Platable Bases and Plating"; pp. 157–69 in Proceedings of Electronic Components Conference, Vol. 37, IEEE, New York, 1986.

[71]F. R. Anderson and H. C. Ling, "Interaction of PMN Ceramics with Silver Termination Inks"; pp. 136–47 in Ceramic Transactions, Vol. 8, *Ceramic Dielectrics: Composition, Processing, and Properties*. Edited by H. C. Ling and M. F. Yan. American Ceramic Society, Westerville, OH, 1990.

[72]D. Suvoroupv and J. Klobcar, "Interaction of MLC $BaTiO_3$ Based Ceramics with Silver Termination Ink"; pp. 143–62 in Proceedings of the Center for Dielectric Studies Symposium on Improvement of Multilayer Ceramic Reliability (May 1991), Pennsylvania State University, University Park, PA, 1991.

[73]B. S. Rawal, "Parameters Important for Surface Mount Applications of Multilayer Ceramic Capacitors"; see Ref. 43, pp. 329–45.

[74]Y. Kudoh, S. Sekihara, J. Ishigame, "Investigations of Resistance to Solder Leaching of 4Pd/96Ag Thick Film with Ag-Sn-Pb Solders"; pp. 51–56 in ISHM 1987 Proceedings, International Society for Hybrid Microelectronics, Reston, VA, 1987.

[75]J. W. Crownover, "Composition and Method for Electroding Dielectric Ceramics," U.S. Pat. No. 3 342 655, 1967.

[76]M. J. Popowwich, "Capacitor with Noble Metal Electrodes," U.S. Pat. No. 4 075 681, 1978.

[77]J. C. Constantine, "Modification of Sintering Rates of Palladium Silver Electroding Powders," European Pat. No. 0 394 037 (1990).

[78]P. Ward, "Multilayer Ceramic Capacitors Materials, Processing and Reliability"; pp. 51–61 in 1989 Proceedings of Capacitor and Resistor Technology Symposium, Components Technology Institute, Huntsville, AL, 1989.

[79]A. E. Dyson, "Improvements in Multilayer Ceramic Capacitors," *Electrocomponent Sci. Technol.*, **11**, 53–64 (1983).

[80]J. G. Pepin, "Subsolidus Phase Relations in the System Pd-Ag-O and Application to Multilayer Ceramic Capacitor Electrodes," *Adv. Ceram. Mater.*, 3 [5] 517–19 (1988).

[81]L. C. Hoffman, "Precision Glaze Resistors," *Am. Ceram. Soc. Bull.*, **42** [9] 490–93 (1963).

[82]A. Kusy, "An Investigation of the Relations between Technological Parameters, Phase Constitution and Electrical Characteristics of Thick Pd-Ag Resistive Films," *Thin Solid Films*, **17**, 345–61 (1973).

[83]Y. Taketa and M. Haradome, "The Basic Reactions, Compositions, and Electrical Properties of Pd-Ag Thick Film Resistors," *IEEE Trans. Parts, Hybrids, Packag.*, **9** [2] 104–14 (1973).

[84]A. Kusy, "On the Structure and Conduction Mechanism of Thick Resistive Films," *Thin Solid Films*, **37**, 281–302 (1976).

[85]I. Barycka and A. Misiuk, "Solid State Reactions in the Preparation of Thick Film Resistors and Conductors," *Proc. Int. Symp. React. Solids, 9th*, **2**, 831–35 (1982).

[86]B. E. Taylor and W. A. Craig, "Thick Film Palladium-Silver Conductors: A Processing and Performance Study"; pp. 124–31 in ISHM 1986 Proceedings, International Society for Hybrid Microelectronics, Reston, VA, 1986.

[87]T. Kubota and T. Shinmura, "Study of Surface Oxidation and Solderability on Silver Palladium Thick Film Conductor"; pp. 81–89 in 1969 ISHM Proceedings, International Society for Hybrid Microelectronics, Reston, VA, 1969.

[88]G. Tomandl and A. Stiegelschmitt, "Investigation of the Adhesion Mechanism between Metal Layers and Crystalline Ceramics for Metallization of Electroceramics. Also with Respect to the Electrical Properties," *Ber. Dtsch. Keram. Ges.*, **56** [11–12] 337–41 (1979).

[89]S. S. Cole, "Sintering of Ag-Pd in the Presence of a Reactive Glass," *J. Am. Ceram. Soc.*, **55** [6] 296–99 (1972).

[90]S. S. Cole, "The Sintering Mechanism in a Silver-Palladium Film"; pp. 2A-1-1–2A-1-6 in ISHM 1981 Proceedings, International Society for Hybrid Microelectronics, Reston, VA, 1981.

[91]E. C. Liang, "Solderability of Silver/Palladium End Terminations for Multilayer Capacitors"; pp. 45–49 in *Hybrid Circuit Technology*, September, 1984.

[92]T. Kubota and T. Shinmura, "Study of Surface Oxidation and Solderability on Silver Palladium Thick Film Conductors"; pp. 81–88 in ISHM 1983 Proceedings, International Society for Hybrid Microelectronics, Reston, VA, 1983.

[93]F. Makuta and T. Inokuma, "Effect of Specific Surface Area of Palladium and Silver-Palladium Mixed Powders on Inner Electrodes of Multilayer Ceramic Capacitors," *Int. J. Hybrid Microelectron.*, **6** [1] 74–78 (1983).

[94]G. H. Maher, "Ag/Pd Electroding Powder and Method of Making," U.S. Pat. No. 4 500 368, 1985.

[95]G. H. Maher, "Method for Making Ag/Pd Electroding Powders," U.S. Pat. No. 4 568 384, 1986.

[96]E. M. Otto, "Equilibrium Pressures of Oxygen over Ag_2O-Ag at Various Temperatures," *J. Electrochem. Soc.*, **113**, 643–45 (1966).

[97]P. J. Herley and E. G. Prout, "The Thermal Decomposition of Silver Oxide," *J. Am. Chem. Soc.*, **82**, 1540–43 (1960).

[98]S. S. Cole, "Oxidation and Reduction of Palladium in the Presence of Silver," *J. Am. Ceram. Soc.*, **68** [4] C-106–C-107 (1985).

[99]S. F. Wang and W. Huebner, "Thermodynamic Modeling of Equilibrium Subsolidus Phase Relations in the Ag-Pd-O_2 System," *J. Am. Ceram. Soc.*, **74** [6] 1349–53 (1991).

[100]J. Warner, "The Free Energy of Formation of Palladium Oxide," *J. Electrochem. Soc.*, **114** [1] 68–71 (1967).

[101]V. H. Kleykamp, "Free Energy of Formation of Palladium Oxide," *Z. Phys. Chem.*, **71**, 142–48 (1970).

[102]J. Fouletier, G. Vitter, and M. Kleitz, "Measurement and Regulation of Oxygen Content in Gases Using Solid Electrolyte Cells. III. Oxygen Pump Gauge," *J. Appl. Electrochem.*, **5**, 111–20 (1975).

[103]G. Bayer and H. G. Wiedemann, "Formation, Dissociation, and Expansion Behavior of Platinum Group Metal Oxides (PdO, RuO_2, IrO_2)," *Thermochim. Acta*, **11**, 79–88 (1975).

[104]I. Barin, *Thermochemical Data for Pure Substances*, VCH Publishers, New York, 1989.

[105]K. M. Myles, "Thermodynamic Properties of Solid Palladium-Silver Alloys," *Acta Metall.*, **13**, 109–13 (1965).

[106]V. M. Eremenko, G. M. Lukashenko, and V. L. Pritula, "Investigation of the Thermodynamic Properties of Silver-Palladium Solid Solutions by Vapour Pressure Measurements," *Russ. J. Phys. Chem. (Engl. Transl.)*, **42** [3] 346 (1968).

[107]N. G. Schmahl and W. Schneider, "Determination of the Palladium Activity in Palladium-Silver Alloys with the Aid of Oxidic Decomposition Pressures," *Z. Phys. Chem.*, **57**, 218–33 (1968).

[103]V. A. Levitski, P. B. Narchuk, M. L. Kovba, and Y. Y. Skolis, "Solid Electrolytes in Thermodynamic Properties of PdO," *Russ. J. Phys. Chem. (Engl Transl.)*, **56** [10] 1474–78 (1982).

[104]J. P. Chan and R. Hultgren, "The Thermodynamic Properties of Silver and Palladium Alloys," *J. Chem. Thermodyn.*, **1**, 45–50 (1969).

[105]S. F. Wang, W. Huebner, and C. Y. Huang, "Correlation of Subsolidus Phase Relations in the Ag-Pd-O System to Oxidation/Reduction Kinetics and Dilatometric Behavior," *J. Am. Ceram. Soc.*, 75 [8] 2232–39 (1992).

[106]J. G. Pepin, "High Fire Multilayer Ceramic Capacitor Electrode Technology"; pp. 7–15 in Proceedings of the Capacitor and Resistor Technology Symposium (March 4–7, 1991, Las Vegas, NV). Components Technology Institute, Huntsville, AL, 1991.

[107]J. C. Constantine, "Modification of Sintering Rates of Silver Palladium Powders"; see Ref. 71, pp. 185–99.

[108]R. L. Rowland and N. H. Nachtrieb, "Self-Diffusion of Palladium in Silver–Palladium Alloys," *J. Phys. Chem.*, **67** [12] 2817–21 (1963).

[109]B. E. Taylor and S. T. Joslin, "Dielectric/Conductor Interactions and Their Effect on Performance"; see Ref. 36, pp. 30–46.

[110]D. A. Chance and D. L. Wilcox, "Metal–Ceramic Constraints for Multilayer Electronic Packages," *Proc. IEEE*, **59** [10] 1455–62 (1971).

[111]G. J. Ewell and W. K. Jones, "Material Incompatibilities in Ceramic Chip Capacitors," *Int. J. Hybrid Microelectron.*, **1** [2] 77–86 (1978).

[112]A. Peigney, M. Marchal, and N. Gerard, "Interaction between Metallic Films and Dielectric Ceramic Substrates during Sintering of the Ceramics," *Ber. Dtsch. Keram. Ges.*, **55** [7] 351–52 (1978).

[113]M. H. Chu and C. E. Hodgkins, "Ceramic and Metal Oxide Interaction in Multilayer Ceramic Capacitors"; pp. 203–17 in Advances in Ceramics, Vol. 9, *Forming of Ceramics*. Edited by J. A. Mangels and G. L. Messing. American Ceramic Society, Columbus, OH, 1988.

[114]C. A. Harper (Ed.), *Handbook of Thick Film Hybrid Microelectronics*. McGraw-Hill, New York, 1974.

[120]K. Eda, "ZnO Oxide Varistors," *IEEE Trans. Electr. Insul.*, **5** [6] 28–41 (1989).

[121]R. B. Amin and M. A. Rosenberg, "Precious Metal Electrode Systems for Multilayer Ceramic Capacitors"; pp. 91–106 in *Report on the Workshop on the Reliability of Multilayer Ceramic Capacitors*. National Academy Press, Washington, D.C., 1983.

[122]R. E. Newnham, "Structure-Property Relations in Multilayer Ceramics"; see Ref. 121, pp. 53–66.

[123]B. G. Kakhan, V. B. Lazarev, and I. S. Shaplygin, "Subsolidus Part of the Equilibrium Diagrams of the Bi_2O_3–MO Binary Systems," *Russ. J. Inorg. Chem. (Engl. Transl.)*, **24** [6] 922–25 (1979).

[124]V. B. Lazarev and I. S. Shaplygin, "Reactions of Palladium Oxide with Oxides of Group V Elements," *Russ. J. Inorg. Chem. (Engl. Transl.)*, **19** [9] 1305–306 (1974).

[125]M. Hrovat, S. Bernik, and D. Kolar, "Phase Equilibria in the RuO_2–Bi_2O_3–PdO System," *J. Mater. Sci. Lett.*, **67**, 637–38 (1988).

[126]W. Borland, "Capacitance Loss Problems Associated with CL750 and BL152 Low Layer Designs"; presented at the 83rd Annual Meeting of the American Ceramic Society, Washington, D.C., May 4–6, 1981 (Paper No. 64-E-81).

[127]O. Muller and R. Roy, "Synthesis and Crystal Chemistry of Some New Complex Palladium Oxides," *Adv. Chem. Ser.*, **28**, 28–38 (1971).

[128]S. F. Wang and W. Huebner, "Interaction of Ag/Pd Electrodes with Lead and Bismuth-Based Electroceramics," *J. Am. Ceram. Soc.*, **76** [2] 474–80 (1993).

[129]P. M. Hansen, *Constitution of Binary Alloys*; pp. 41–42. McGraw-Hill, New York, 1958.

[130]W. G. Moffatt, *The Handbook of Binary Phase Diagrams*. Genium, New York, 1987.

[131]B. E. Taylor, J. J. Felten, and J. R. Larry, "Progress in and Technology of Low Cost Silver Containing Thick Film Conductors," *IEEE Trans. Compon., Hybrid, Manuf. Technol.*, **CHMT-3** [2] 504–17 (1980).

[132]R. Allem, F. Lavallee, and G. L. Esperance, "Interfacial Reactions between $YBa_2Cu_3O_{7-x}$ and Ag–Pd Alloys during High Temperature Heat Treatments," *J. Mater. Res.*, **7** [11] 2936–41 (1992).

[133]C. T. Cheung and E. Ruckenstein, "Superconductor-Substrate Interactions of Y-Ba-Cu Oxide," *J. Mater. Res.*, **4** [1] 1–15 (1989).

[134]J. L. Porter, T. K. Vethanayagam, R. L. Snyder, and J. A. T. Taylor, "Reactivity of Ceramic Superconductors with Palladium Alloys," *J. Am. Ceram. Soc.*, **73** [6] 1760–62 (1990).

[135]G. Kozlowski, S. Rele, D. F. Lee, and K. Salama, "Grain Growth Enhancement in Silver-Doped $YBa_2Cu_3O_{7-x}$ Superconductor," *J. Mater. Sci.*, **26**, 1056–60 (1991).

[136]Y. M. Shulga, E. N. Izakovich, V. I. Rubtsov, and B. E. Shklyaruk, "The Modification of Superconductors: Platinum Group Metals Confer Notable Properties," *Platinum Met. Rev.*, **37** [2] 86–96 (1993).

[137]W. A. Crossland and L. Hailes, "Thick Film Conductor Adhesion Reliability"; pp. 3.3.1–3.3.13 in ISHM 1970 Proceedings. International Society for Hybrid Microelectronics, Reston, VA, 1971.

[138]K. Yamada, F. Mukuta, and S. Chiba, "Degradation of Soldered Thick Film Conductor during Thermal Cycling"; see Ref. 41, pp. 725–31.

[139]J. Ishigame, S. Sikihara, K. Fujimura, and H. Hayata, "An Investigation of the Mechanism about the Adhesion Degradation of Ag-Pd Thick Film Conductor by Thermal Aging"; pp. 455–61 in Proceedings of the 4th International Microelectronics Conference, Kobe, Japan, May 1986.

[140]B. S. Chiou, K. C. Liu, J. G. Duh, and P. S. Palanisamy, "Intermetallic Formation on the Fracture of Sn/Pb Solder and Pd/Ag Conductor Interfaces," *IEEE Trans. Compon., Hybrid, Manuf. Technol.*, **13** [2] 267–74 (1990).

[141]K. C. Liu and J. G. Duh, "Microstructural Evolution in Sn/Pb Solder and Pd/Ag Thick Film Conductor Metallization," *IEEE Trans. Compon., Hybrid Manuf. Technol.*, **14** [4] 703–707 (1991).

[142]J. R. Anderson, *Structure of Metallic Catalysts*. Academic Press, New York, 1975.

[143]A. H. Haines, *Methods for the Oxidation of Organic Compounds*. Academic Press, New York, 1985.

[144]P. H. Emmett, *Catalysis Then and Now*. Franklin Publishing, Englewood NJ, 1965.

[145]R. B. Anderson and P. T. Dawson, *Characterization of Surface and Adsorbed Species*. Academic Press, New York, 1976.

[146]R. C. Hanold, "Process for Making Ceramic Capacitors," U.S. Pat. No 3 815 187, 1974.

[147]J. G. Pepin, W. Borland, P. O'Callaghan, and R. J. S. Young, "Electrode-Based Causes of Delaminations in Multilayer Ceramic Capacitors," *J. Am Ceram. Soc.*, **72** [12] 2287–91 (1989).

[148]D. J. Gasper, F. K. Patterson, and B. L. Iorfido, "Silver Reliability in a Multilayer Ceramic Package"; pp. 246–55 in ISHM 1988 Proceedings. International Society for Hybrid Microelectronics, Reston, VA, 1988.

[149]F. M. Collins and C. F. Parks, "Thallium Oxide Glaze Resistor"; p. 432 in Proceedings of 1967 IEEE Electronic Component Conference. IEEE, New York, 1967.

[150]J. R. Raiden and R. T. Girard, "Interactions between Thallium Oxide Thick Film Resistors and Thick Film Conductor Materials," *Am. Ceram. Soc. Bull.*, **50** [6] 536–40 (1971).

[151]A. Hornung, "Electrical Properties of a Silver Contaminated Borosilicate Glass"; in ISHM 1968 Transactions. International Society for Hybrid Microelectronics, Reston, VA, 1968.

[152]H. D. Schreiber, T. R. Harville, and G. N. Damron, "Redox-Controlled Solubility of Palladium in a Borosilicate Glass Melt," *J. Am. Ceram. Soc.*, **73** [5] 1435–37 (1990).

[153]G. Schulze, "Diffusion of Ag into Glass," *Ann. Phys.(Leipzig)*, **40**, 355 (1913).

[154]M. Maric, M. P. Brungs, and M. Skyllas-Kazacos, "Voltammetric and Chronopotentiometric Reactions of Silver Ions in Molten Sodium Disilicate Glass," *Phys. Chem. Glasses*, **30** [1] 12–18 (1989).

[155]H. D. Schreiber, G. B. Galazs, B. E. Carpenter, J. E. Kirkley, L. M. Minnix, and P. L. Jamison, "An Electromotive Force Series in Borosilicate Glass-Forming Melt," *J. Am. Ceram. Soc.*, **67**, C-106–C-108 (1984).

[156]G. H. Maher, T. I. Prokopowicz, and V. Bheemineni, "Properties of X7R MLC Capacitors Containing 70Ag/30Pd or 60Au/20Pd/20Pt Internal Electrode Composition"; pp. 23–28 in Proceedings of 1992 Capacitor and Resistor Technology Symposium. Components Technology Institute, Huntsville, AL, 1992.

[157]G. H. Maher, "Effect of Silver Doping on the Physical and Electrical Properties of PLZT Ceramics," *J. Am. Ceram. Soc.*, **66** [6] 408–13 (1983).

[158]H. Ikushima and S. Hayakawa, "Electrical Properties of Ag-Doped Barium Titanate Ceramics," *Jpn. J. Appl. Phys.*, **4** [5] 328–36 (1967).

[159]W. Wersing, H. Wahl, and M. Schnöller, "PZT-Based Multilayer Piezoelectric Ceramics with AgPd-Internal Electrodes," *Ferroelectrics*, **87**, 271–94 (1988).

[160]M. V. Slinkina, G. I. Dontsov, and V. H. Zhukovsky, "Silver Diffusion at Metallization of Piezoelectrics," *Mater. Sci. Forum*, **62–64**, 363–64 (1990).

[161]K. V. R. Murty, S. N. Murty, K. C. Mouli, and A. Bhanumathi, "Domain Orientation and Piezoelectric Properties of Ag Doped PMN-PZT Ceramics"; pp. 144–47 in Proceedings of IEEE 1992 International Symposium on Applications of Ferroelectrics, IEEE, New York, 1992.

[162]S. G. Kulkarni, C. S. Subbanna, V. Venugopal, and D. D. Sood, "Vapor Pressure of Pd(g) Measured Over Pd(s) by Knudsen Effusion Cell Mass Spectrometry," *J. Less-Common Met.*, **160**, 133–41 (1990).

[163]W. Borland, C. R. S. Needs, V. P. Siuta, and K. M. Nair, "High Conductivity Materials Systems for Advanced Hybrids"; pp. 704–13 in Proceedings of 39th Electronic Components Conference, IEEE, New York, 1989.

[164]H. M. Naguib and B. K. MacLaurin, "Reliability of Pd/Ag Conductors," *IEEE Trans. Compon., Hybrid. Manuf. Technol.*, **CHMT-2**, [2] 196–207 (1979).

[165]H. M. Naguib and B. K. Maclaurin, "Silver Migration and the Reliability of Pd/Ag Conductors in Thick Film Dielectric Crossover Structures," *IEEE Trans. Compon., Hybrids, Manuf. Technol.*, **CHMT-2** [2] 196–207 (1979).

[166]J. J. Paul Gagne, "Silver Migration Model for Ag-Au-Pd Conductors," *IEEE Trans. Compon., Hybrids, Manuf. Technol.*, **CHMT-5** [4] 402–407 (1982).

[167]A. Hornung, "Diffusion of Silver on Borosilicate Glass"; pp. 250–55 in Proceedings of 1968 Electronic Components Conference, IEEE, New York, 1968.

[168]P. E. Rogren, "Electro Migration in Thick Film Conductor Materials"; pp. 267–72 in ISHM 1976 Proceedings. International Society for Hybrid Microelectronics, Reston, VA, 1976.

[169]J. B. Dixon, D. T. Rooney, and N. T. Castello, "Metal Migration Failures in a Hybrid Devices: Interaction of Package Materials, Process Residues"; pp. 410–15 in ISHM 92 Proceedings. International Society for Hybrid Microelectronics, Reston, VA, 1992.

[170]A. H. C. Hendriks, "Atmospheric Corrosion Test on Pd/Ag Thick Film Conductors," *Hybrid Circuits*, **11**, 69–71 (1986).

[171]A. Maslowski, R. Senkalski, and S. Shahbazi, "A New High Reliability Silver-Compatible Dielectric System with Mixed-Metal Capability"; see Ref. 41, pp. 204–208.

[172]I. Steinberg and B. Kistler, "The Battery Effect in Thick Film Multilayer Circuits"; pp. 237–41 in ISHM 1989 Proceedings. International Society for Hybrid Microelectronics, Reston, VA, 1989.

[173]R. E. Hoffman and D. J. Turnbull, "Lattice and Grain Boundary Self-Diffusion in Silver," *J. Appl. Phys.*, **22** [5] 634–39 (1951).

[174]D. L. Johnson and T. M. Clarke, "Grain Boundary and Volume Diffusion in the Sintering of Silver," *Acta Metall.*, **12** [10] 1173–79 (1964).

[179]N. L. Peterson, "Isotope Effect in Self-Diffusion in Palladium," *Phys. Rev.*, **136** [2A] 568–74 (1964).
[180]P. K. Higgins and Z. A. Munir, "Modification of the Sintering Kinetics of Palladium by a Surface Oxide"; pp. 183–97 in Proceedings of Metal and Ceramic Powders. Edited by R. M. German and L. W. Lay. Metallurgical Society of AIME, Warrendale, PA, 1981.
[181]P. K. Higgins and Z. A. Munir, "Application of the Surface Oxide Model in the Sintering of Metallic Particles," *Powder Metall. Int.*, **14** [1] 26–29 (1982).
[182]Z. A. Munir, "Surface Oxides and Sintering of Metals," *Powder Metall.*, **24** [4] 177–80 (1981).
[183]H. U. Anderson, "Initial Sintering of Palladium Powder Compacts," *Sci. Sintering*, **6** [1] 45–58 (1974).
[184]N. H. Nachtrieb, "Self-Diffusion of Silver:Palladium Alloy," *J. Chem. Phys.*, **26** [1] 106 (1957).
[185]K. Nagashima, T. Himeda, and A. Kato, "Properties of Conductive Films Made from Fine Spherical Silver–Palladium Alloy Particles," *J. Mater. Sci.*, **26**, 2477–82 (1991).
[186]I. Barycka and A. Misiuk, "Some Physiochemical Aspects of Pd-PdO-Ag-Glass Mixture Sintering," *Mater. Sci.*, **7** [4] 467–74 (1981).
[187]W. D. Kingery, "Densification during Sintering in the Presence of a Liquid Phase, I Theory," *J. Appl. Phys.*, **30** [3] 301 (1959).
[188]W. D. Kingery and M. D. Narasimhan, "Densification during Sintering in the Presence of a Liquid Phase, II Experimental," *J. Appl. Phys.*, **30** [3] 307 (1959).
[189]K. Yata and T. Yamaguchi, "Effect of Temperature on Ostwald Ripening of Silver in Glass," *J. Am. Ceram. Soc.*, **75** [8] 2071–75 (1992).
[190]K. Yata and T. Yamaguchi, "Ostwald Ripening of Silver in Glass," *J. Mater. Sci.*, **27**, 101–106 (1992).
[191]K. Yata and T. Yamaguchi, "Effect of Additives on Ostwald Ripening of Silver in Glass," *J. Am. Ceram. Soc.*, **75** [10] 2910–14 (1992).
[192]K. I. Yajima and T. Yamaguchi, "Sintering and Microstructure Development of Glass-Bonded Silver Thick Films," *J. Mater. Sci.*, **19**, 777–84 (1984).
[193]Y. S. Chung and H. G. Kim, "Effect of Oxide Glass on the Sintering Behavior and Electrical Properties in Ag Thick Films," *IEEE Trans. Compon., Hybrids, Manuf. Technol.*, **11** [2] 195–99 (1988).
[194]T. Yamaguchi and H. Imai, "Sintering in Silver-Glass Electrode Systems"; see Ref. 43, pp. 347–54.
[195]V. K. Nagesh, A. P. Tomsia, and J. A. Pask, "Wetting and Reactions in the Lead Borosilicate Glass–Previous Metal System," *J. Mater. Sci.*, **18**, 2173 (1983).
[196]V. F. Zackay, D. W. Mitchell, S. P. Mitoff, and J. A. Pask, "Fundamentals of Glass-to-Metal Bonding: I, Wettability of Some Group I and Group VIII Metals by Sodium Silicate Glass," *J. Am. Ceram. Soc.*, **36** [3] 84–89 (1953).
[197]P. F. Becher and W. L. Newell, "Adherence-Fracture Energy of a Glass-Bonded Thick-Film Conductor: Effect of Firing Conditions," *J. Mater. Sci.*, **12**, 90–96 (1977).
[198]T. J. Garino and H. K. Bowen, "Kinetics of Constrained-Film Sintering," *J. Am. Ceram. Soc.*, **73** [2] 251–57 (1990).
[199]Y. Imanaka and N. Kamehara, "Influence of Shrinkage Mismatch between Copper and Ceramics on Dimensional Control of the Multilayer Ceramic Circuit Board," *J. Ceram. Soc. Jpn.*, **100** [4] 560–64 (1992).
[200]T. Cheng and R. Raj, "Flaw Generation during Constrained Sintering of Metal–Ceramic and Metal–Glass Multilayer Films," *J. Am. Ceram. Soc.*, **72** [9] 1649–55 (1989).
[201]H. T. Sawhill, "Materials Compatibility and Cosintering Aspects of Shrinkage Control in Low Temperature Cofired Ceramic Packages"; pp. 307–19 in Advances in Ceramics, Vol. 26, *Ceramic Substrates and Packages for Electronic Applications*. Edited by M. F. Yan, H. M. O'Bryan, Jr., K. Niwa, and W. S. Young. American Ceramic Society, Westerville, OH, 1987.
[202]M. L. Topfer, *Thick Film Microelectronics*. Van Nostrand Reinhold, New York, 1971.
[203]B. Walton, "Principles of Thick Film Materials Formulation," *Radio Electron. Eng.*, **45** [3] 139–43 (1979).
[204]M. Novotny, "Use of Previous Metal Powders in the Electronic Industry"; pp. 69–80 in *Precious Metal*. Pergamon Press, New York, 1983.
[205]R. W. Westerlund and M. E. Nicholson, "Effect of Plastic Formation on the Resistivity and Hall Constant of Silver–Palladium Alloys," *Acta Metall.*, **14** [5] 569–74 (1966).
[206]B. Svensson, "Magnetische Suszeplibilitat und Elektrischer Wiclerstand der Mischkristallreihen Pd-Ag and Pd-Cu," *Ann. Phys.*, **5** [13] 699 (1932).
[207]A. C. Bailey, N. Waterhouse, and B. Yates, "The Thermal Expansion of Silver–Palladium Alloy at Low Temperatures," *J. Phys. C*, **2** [2] 769–76 (1969).
[208]S. Prakash, "Capacitor with Electrode Containing Nickel," U.S. Pat. No. 4 055 850, 1977.
[209]J. L. Sheard, "Capacitors with Copper Containing Electrode," U.S. Pat. No. 3 763 409, 1975.
[210]J. P. Pepin, "Thick Film Conductor Composition," U.S. Pat. No. 4 954 926 (1990).
[211]C. E. Newberg and S. H. Risbud, "Binder Chemistry, Adhesion and Structure of Interface in Thick Film Metallized Aluminum Nitride Substrate," *J. Mater. Sci.*, **27**, 2670–76 (1992).
[212]P. J. Holmes and R. G. Loasby, *Handbook of Thick Film Technology*. Electrochemical Publications Limited, Scotland, 1976.
[213]H. C. Bheduar and H. T. Sawhill, "Ceramic Multilayer Package Fabrication"; pp. 360–69 in *Packaging, Electronic Materials Handbook*, Vol. 1. ASM International, Materials Park, OH, 1989.
[214]A. K. Varshneya and S. C. Cherukuri, "Low Firing Temperature Glasses for Electronic Applications"; pp. 387–95 in Ceramic Transactions, Vol. 20, *Glasses for Electronic Applications*. Edited by K. M. Nair. American Ceramic Society, Westerville, OH, 1991.
[215]R. A. Perecherla and R. C. Buchanan, "Role of Glass Frit in Thick Film Adhesion"; see Ref. 210, pp. 433–46.
[216]P. W. Bless, R. L. Wahlers, and S. J. Stein, "Application of Glasses in Thick Film Technology"; see Ref. 210, pp. 397–417.
[217]J. J. Licari and L. R. Enlow, *Hybrid Microcircuit Technology Handbook*. Noyes Publications, Park Ridge, NJ, 1988.
[218]B. Walton, "Thick Film Pastes and Substrate"; pp. 41–52 in *Hybrid Microelectronic Technology*. Edited by P. Moran. Gordon and Breach, New York, 1984.
[219]M. Wittmer, "Eutectic Bonding of Copper to Ceramic," *Mater. Res. Soc. Symp. Proc.*, **40**, 393–98 (1985).
[220]E. M. Levin, C. R. Robbins, and H. F. McCurdie; Fig. 2085 in *Phase Diagrams for Ceramists*. Edited by M. Reser. American Ceramic Society, Columbus, OH, 1969.
[221]E. M. Levin and H. F. McMurdie; Fig. 4365 in *Phase Diagrams for Ceramists*. Edited by M. K. Reser. American Ceramic Society, Columbus, OH, 1975.
[222]C. J. Chen and J. M. Wu, "The Effect of Ag Electrode Processing on (Nb,Ba) Doped TiO_2 Ceramics," *J. Mater. Res.*, **5** [7] 1530–37 (1990).
[223]A. N. Prabhu, K. W. Hang, and E. J. Conlon, "Thick Film Copper Conductor Inks," U.S. Pat. No. 4 880 567, 1989.
[224]D. Whitman, "Mechanisms of Char Formation in Nitrogen Fired Thick Film Materials"; pp. 421–25 in Proceedings of the International Microelectronics Symposium. International Society for Hybrid Microelectronics, Reston, VA, 1988.
[225]C. C. Y. Kuo, "Adhesion of Thick Film Copper Conductors," *Int. J. Hybrid Microelectron.*, **4** [2] 70–78 (1981).
[226]L. F. Miller, "Screenability and Rheology," *Solid State Technol.*, 54–60 (1974).
[227]K. M. Nair "Thick Film Conductor Compositions," U.S. Pat. 4 416 942, 1983.
[228]V. P. Siuta, "Copper Conductor Composition," U.S. Pat. No. 4 687 597, 1987.
[229]N. Nazarenko, "Flexible Screen-Printable Conductive Composition," U.S. Pat. No. 4 425 263, 1984.
[230]J. D. Grier, "Copper Thick Film Conductor," U.S. Pat. No. 4 072 771, 1978.
[231]P. Kaplan, J. Kelley, and L. Miller, *IBM Technical Disclosure Bull.*, **2** [5] 1864 (1978).
[232]A. N. Prabhu and K. W. Hang, "Thick Film Copper Conductor Ink," U.S. Pat. No. 4 874 550, 1989.
[233]L. F. Frazee, "Humidity Sensor, Materials Thereof and Method," U.S. Pat. No. 4 050 048, 1977.
[234]D. S. Janikowski and M. S. Shun, "Conductive Pigment-Coated Surfaces," U.S. Pat. No. 4 567 111, 1986.
[235]A. N. Prabhu, W. Hang, and E. J. Conlon, "Thick Film Copper Conductor Inks," U.S. Pat. No. 4 880 567, 1989.
[236]L. Hoffman, "An Overview of Thick Film Hybrid Materials," *Am. Ceram. Soc. Bull.*, **63** [4] 572–76 (1984).
[237]Y. Yamamoto and T. Kitagaki, "Conductive Paste Composition," U.S. Pat. No. 4 859 364, 1989.
[238]J. J. Felten, "Process for Producing Gold Conductor," U.S. Pat. No. 4 235 944, 1980.
[239]I. Burn, "Method for Making a Multilayer Ceramic Structure Having Internal Copper Conductors," U.S. Pat. No. 4 766 027, 1987.
[240]J. E. Schuetz, I. A. Khoury, and R. A. DiChisra, "Water-Based Binder for Tape Casting," *Ceram. Ind.*, **129**, 42–44 (1987).
[241]A. Hui, D. Bloomfield, A. Bell, and M. Chu, "Water Based Binder Systems for Tape-Casting of MLC Dielectrics"; pp. 78–85 in Proceedings of 3rd European Capacitor and Resistor Technology Symposium (Oct. 9–11, 1989). Components Technology Institute, Huntsville, AL, 1989.
[242]G. G. Ferrier, A. R. Berzins, and N. M. Davey, "The Production of Palladium Powders for Electronic Applications: Reaction Conditions Determine Surface Character," *Platinum Met. Rev.*, **29** [4] 175–79 (1985).
[243]T. Whiting and J. Tuffee, "The Fabrication of Silver Flakes for Use in MLCC Termination Inks"; pp. 42–53 in 1992 Proceedings of Capacitor and Resistor Technology Symposium. Components Technology Institute, Huntsville, AL, 1992.
[244]L. W. Tyran, "Flake Silver Powder with Chemisorbed Monolayer of Dispersant," U.S. Pat. No. 4 273 583, 1981.
[245]W. H. Rhodes, "Agglomerate and Particle Size Effects on Sintering Yttria-Stabilized Zirconia," *J. Am. Ceram. Soc.*, **64**, 19–22 (1981).
[246]R. E. Trease and R. L. Dietz, "Rheology of Pastes in Thick Film Printing," *Solid State Technol.*, **15**, 39–43 (1972).
[247]H. Baudry, "Rheology and Printing of High Definition Thick Film Inks," *Int. J. Hybrid Microelectron.*, **5**, 15–23 (1982).
[248]M. A. Wesselmann and D. Meagher, "Visual Illustration of the Dynamics of Pinhole Formation in MLCC End Terminations"; pp. 190–95 in 1990 Proceedings of Capacitor and Resistor Technology Symposium. Components Technology Institute, Huntsville, AL, 1990.
[249]M. Strawhorne and I. McAuley, "Characterization Techniques for Materials Used in the Manufacture of Multilayer Ceramic Capacitors"; in 1991 Proceedings of Capacitor and Resistor Technology Symposium, 1991. Components Technology Institute, Huntsville, AL, 1991.
[250]G. H. Maher, "Making an Electroding Ink for a Monolithic Ceramic Capacitor," U.S. Pat. No. 4 192 698, 1980.
[251]J. H. Beck, "Firing Thick Film Integrated Circuits"; pp. 29–32 in SCP and Solid State Tech., June 1967.
[252]H. Verweij and W. H. M. Bruggink, "Reaction-Controlled Burnout of Ceramic Multilayer Capacitors," *J. Am. Ceram. Soc.*, **73** [2] 226–31 (1990). □

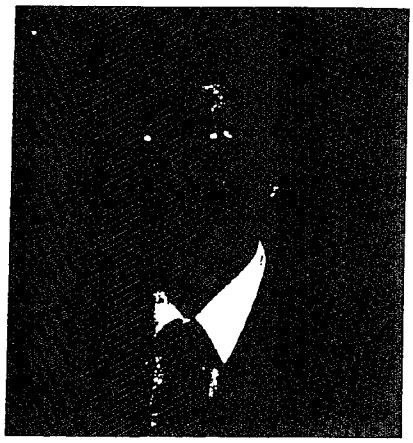

Sea Fue Wang is a Senior Research and Development Engineer at Vitramon Incorporated, a company of Vishay, Monroe, Connecticut. Prior to joining Vitramon in 19 he was a Research Associate at Materials Research Laboratory, Pennsylvania State University. He graduated from National Taipei Institute of Technology, Taiwan, R.O.C., 1979. He received his M.S. in Metallurgical Engineering from South Dakota School Mines and Technology in 1985 and his Ph.D. in Ceramic Science from Pennsylvania State University in 1991. His principal areas of interest are processing and characterization of electronic ceramics. He is a member of American Ceramic Society and ISHM

Joseph P. Dougherty is Associate Professor of Materials and Director, Center for Dielectric Studies at Pennsylvania State University, State College, PA (1988–). He received a B.E.E. from Villanova University and M.S.E.E. and Ph.D. from Penn State University. From 1973 to 1979 he was a research scientist at Philips Laboratories including $1\frac{1}{2}$ years at Philips' Central Research Labs in the Netherlands. He then joined Gulton Industries as the Piezoelectric Division Director of Engineering and laster was Director of Engineering for Electronic Products in the Electro-Voice division. In 198 he formed Advanced Materials Technologies, an electronic ceramics consulting firm Dougherty is a Fellow of the American Ceramic Society, a member of ISHM and IEEE and an Associate Editor of the UFFC Transactions. He holds four patents and has coauthored more than 40 papers and parts of five books.

John G. Pepin is a Research Associate with the Microcircuit and Component Materials Division of DuPont Electronics. A member of the American Ceramic Society, he graduated from the New York State College of Ceramics at Alfred University in 1977 with dual degrees in Physics and Ceramic Science. In 1981 he obtained his doctoral degree in Solid State Science from the Pennsylvania State University. With DuPont since 1981, his research interests are in the field of thick-film conductors for electronic components and hybrid microcircuit applications.

Dr. Wayne Huebner is an Associate Professor of Ceramic Engineering at the University of Missouri–Rolla. Dr. Huebner received his B.S. and Ph.D. in ceramic engineering from the University of Missouri–Rolla. He was an Assistant Professor of Ceramic Science and Engineering for five years at the Pennsylvania State University before returning to the University of Missouri. Dr. Huebner teaches short courses on Electronic Ceramics, and is currently the President-elect of the Ceramic Educational Council and an Associate Editor for the *Journal of the American Ceramic Society*. Dr. Huebner's research interests include the preparation, characterization, and theoretical understanding of electronic ceramics, in particular ferroelectrics and solid oxide electrolytes.

APPENDIX 56

The Microstructural Evolution of Copper Thick Films Observed by Environmental Scanning Electron Microscopy

David R. Sample, Paul W. Brown and Joseph P. Dougherty

The Materials Research Laboratory

The Pennsylvania State University

University Park, PA 16802

I. Abstract

A generic copper thick film ink system was formulated to be representative of the inks used currently in industry. The microstructural evolution of two of the copper-based inks based on the generic composition was investigated using an environmental scanning electron microscope (ESEM) equiped with a hot stage. The first ink, consisting of copper and organics, oxidized heavily during firing while an ink, consisting of copper, glass and organics, oxidized only slightly. The sequence of events observed in firing the ink comprised of copper, glass and organics is as follows: the burnout process reached completion by about 320 °C. Copper oxidation was observed to occur between 500 °C and 600 °C. The glass was observed to soften over the same temperature range. By 700 °C, the glass has softened and coated the copper particles. Prior to glass softening, oxidation occurs regardless of the presence of the glass. However, once the glass has softened, copper oxidation was retarded.

Cu_2O was found to be sufficiently soluble in the glass to allow it to be removed from the surfaces of the copper particles. Thus the presence of glass facilitates the formation of conductive paths by two mechanisms. It inhibits oxidation and it dissolveed the oxide that forms. Both processes allow effective sintering.

Supported by funding from the Center for Dielectric Studies at Penn State

II. Introduction

Superior properties, such as solderability, adhesion and conductivity, make copper based thick films ideal for applications in hybrid circuits [1]. Therefore, much can be found in the literature regarding the processing and properties of copper films [2,3,4,5,6]. Details about firing atmospheres, film compositions and film properties are widely published [3,6,7,8]. But for a few exceptions [9,10,11], little have been written regarding how the film composition affects the microstructural evolution during firing. One exception is a study by Kuo [9] which reported that the glass in the copper thick film penetrates into the glassy phase between alumina grains as a result of firing. In spite of this, there has been a lack of investigations that describe the manner in which glass or adhesion promoters affects the microstructural development during the firing of a copper film.

The aim of this study was to first establish generic copper thick film constituents that are representative of the constituents used in industry today. Simple copper film compositions were formulated and their microstructural evolution studied. Progressively more complex compositions were then formulated and studied once the microstructural evolution of the simple systems was established.

In addition to copper, copper thick films usually contain a glass frit, an adhesion promoter and organics; other additives may be incorporated for special applications. The proportions of components are generally in the following range:

- 70-90 wt% copper
- 1-10 wt% glass
- 0-5 wt% adhesion promoter
- 10-20 wt% organics

It has been empirically determined that the copper powder should be spherical and have particle sizes between 0.5 and 10 μm. Copper particles that are too large will not sinter well at low temperatures. Particles below 0.5 μm require an excessive amount of organic to achieve dispersion. [10]. The organic additives are necessary for screen printing. At a minimum, these

include a binder and a solvent (dispersants, wetting agents and viscosity modifiers are sometimes added to aid in processing). A very common combination is ethyl cellulose as the binder and terpineol as the solvent. It is important that all of the organics be burnt out between 300 and 550 °C otherwise film integrity will be compromised [12]. Residual carbon from improperly burnt out organics can lead to char formation and blisters in the final film [13].

There is much latitude in the composition of the glass frit that can be used. Lead borosilicates are common; however, any number of constituents can be used. One important parameter is the softening point of the glass. Two views have been expressed regarding the optimum softening point. Prabhu et al. [14] suggest using a glass of high softening point (>700°C) to insure that the organics are completely burnt out from the film before the glass melts and possibly entraps the organics. Alternatively, Kuo [9] suggest using a glass with a lower softening point (400-500°C). Since the softened glass creates a medium for liquid phase sintering, a lower softening point glass allows the copper particles to begin sintering at lower temperatures.

Common adhesion promoters are Cu_2O, PbO and CdO. These oxides form spinel-type compounds with the alumina substrate to aid adhesion. A way of predicting the utility of an adhesion promoter is to determine if it forms an intermediate compound with the substrate material. If for example, an intermediate compound exists with alumina, it is likely that the oxide will help adhesion [15].

Finally, other compounds may be used as additives to allow firing in air, to improve dimensional stability, or to improve solderability. For example, a boron paste screen printed on top of a copper film will oxidize preferentially to the copper allowing the film to be fired in air. The boron oxide can then be washed away after firing [8]. A refractory metal can be added to remove oxidation present on the copper or any oxygen present in the atmosphere [16]. Coating the copper particles with a metal oxide can control sintering and hence shrinkage rates [17]. Finally, a metal silicide or metal boride can be added to improve solderability by hindering grain growth [18].

III. Experimental Procedure

Two inks were studied in this investigation. The first ink contained only copper and organic constituents and will be referred to as the copper ink or film. The second contained 90 wt% copper and 10 wt% glass as the solid constituents and will be referred to as the copper + glass ink or film. In both cases, the ink composition consisted of 85 wt% solids and 15 wt% organics. The glass used consists of 63 wt% PbO, 25 wt% B_2O_3, and 12 wt% SiO_2. The organic composition consists of 9 wt% ethyl cellulose (binder) in terpineol (solvent).

Determination of a generic copper thick film ink composition also dictated the manner in which the film would be processed. The copper powder did not require any special processing before it was used in the ink. The organics were prepared by simply adding the ethyl cellulose powder to the terpineol solvent and stirring until the powder dissolved completely.

The glass was prepared by heating the suitable proportions of PbO, H_3BO_3, and SiO_2 in a platinum crucible to 1000 °C for one hour. The melt was quenched by pouring it into deionized water. Quenching the glass in water frits it into a coarse powder. After drying at 110°C for six hours, the glass was milled in acetone with alumina media for 24 hours and dried again. The resulting glass powder was sieved through a 400 mesh screen.

Mixing was carried out using a three roll mill in order to achieve a homogeneous paste. The inks were screen printed on 96% alumina substrates and dried at 110 °C for 10 minutes before they were fired.

The inks were fired in an environmental scanning electron microscope (ESEM). The ESEM was equiped with a hot stage and was used to investigate the microstructural evolution of the copper thick films during firing. The ESEM allows pressures as high as 100 torr above the sample while it is being imaged. The hot stage can achieve temperatures as high as 1000 °C. In this investigation, nitrogen containing 2-10 ppm oxygen (reported by vendor) was used as the atmosphere. The nitrogen pressure was maintained at 2.3 torr. The firing cycles (figure 1) consisted of a ramp of approximately 20 °C/min to a peak firing temperature of 900 °C and then a rapid quench.

The burnout characteristics of the organics were determined using thermal gravimetric analysis (TGA) for the weight loss versus temperature. Sixty-five mg of the ethyl cellulose/terpineol mixture was heated at 5 °C/min in a platinum pan to 500 °C in a nitrogen atmosphere containing 2-10 ppm oxygen. The glass was characterized using Differential Thermal Analysis (DTA). Approximately 40 mg of the glass was heated at 10 °C/min to 700 °C to determine the transformation range and softening point. The copper was characterized using sedimentary technique to determine the particle size distribution. The copper powder was dispersed using "sedisperse" oils and sonicated to insure thorough dispersion of the particles. The results of the sedigraph analysis of the copper powder show a mean particle size of 4.8 μm with the largest particles being 10 μm and the smallest being 1μm.

Finally, x-ray diffraction was performed on a mixture of 15 wt% Cu_2O in the glass before and after melting to determine the extent of the Cu_2O solubility. The Cu_2O powder and glass frit were mixed and heated to 900 °C at 20 °C/min and then quenched by pouring into deionized water.

IV. Results and Discussion

The firing cycles used in this study differ from those used in commercial operations. The heating rate used in this study is much slower, however, the same mechanisms should occur in the firing of commercial inks but at different rates.

The thermogravimetric analysis plot in figure 2 shows that solvent evaporation occurs over a temperature range of 85 °C to 250 °C and that the maximum rate of evaporation occurs at 150°C. These results show that the drying of the ink at 110 °C before firing will evaporate all of the solvent. The ethyl cellulose burns out over a range of temperatures from 250 °C to 400 °C. Differential thermal analysis (figure 3) shows the glass in our ink has a transformation range of 440-480 °C and a softening point of approximately 540 °C. Thus the glass softens after the binder has burned out minimizing the chance of entrapping organics that may result in carbon residue in the film.

Figure 4 shows the microstructural evolution observed in the ESEM for the two compositions studied. Because the dimensions of the specimen change considerably during heating the micrographs at each temperature are not of the exact same area of each film, however, an attempt was made to image the same particles throughout the firing cycle. A number of such particles can be observed in each micrograph throughout the firing cycle. Figure 4A shows the the screen printed films after drying and before firing. The glass particles are morphologically distinct from the copper particles. The glass particles have very sharp corners while the copper particles are equiaxed. A glass particle is labeled as B in figure 4. The particle sizes of the copper powder seen in the micrographs are in agreement with those seen in the sedigraph analysis. The microstructures of the films do not change until they are heated above 500 °C. As figure 4B shows, there is no change in the microstructure after heating to 500 °C. According to the TGA results all of the organics have volatilized by this temperature, therefore burnout occurs without any discernable variation in microstructure. There is no noticeable difference between the copper film and the copper + glass film other than the existence of the glass particles.

At 600°C (figure 4C), the microstructures become noticeably different. The copper particles in the copper film now have a "fuzzy" appearance which is the result of the onset of oxidation. Particle A has grown from 5 μm to 5.7 μm along its major axis and from 3.3 μm to 4.0 μm along its minor axis due to oxidation.

The corners of the glass particle labeled as B, in the micrograph of the copper + glass film at 600°C (figure 4C), have rounded, indicating that the glass has begun to soften. This observation is in accord with the DTA results that show that the glass has a softening point of 540°C. This micrograph also shows the glass wets the copper particles by this temperature. Once the glass softens, liquid phase sintering may begin and a continuous film is starting to form. The presence of oxidation at these temperatures is not noticeable in the copper + glass film.

Once 700 °C has been reached, the oxidation on the copper film is more extensive (figure 4D). The copper particle labelled as A in figure 4D has grown to 6.0 μm along the major axes, however no further measurable oxidation is seen along the minor axis. The oxidation microstructure has progressed from a fuzzy covering of the copper at 600 °C to fine scaled faceted particles. The glass in the copper + glass film has completely melted and coated the copper particles creating a 3-dimensionally connected microstructure that is the result of further liquid phase sintering. In addition, the copper + glass film has oxidized slightly. Evidence of oxidation is seen as the presence of submicron nodules on the copper particles.

At the highest temperature (900 °C - figure 4E) oxidation in the copper film is very extensive. The entire surface of the film consists of faceted copper oxide crystallites much larger than the fine particles seen at 700 °C. Particle A has oxidized to a final size of 6.7 μm along the major axis and 5 μm along the minor axis. It is difficult to discern the extent to which the copper particles have sintered beneath the oxidation layer. The copper + glass film shows further oxidation when compared to the 700 °C (figure 4D) but not nearly to the extent of the copper film. The existence of discrete copper particles can no longer be seen. Comparing the copper and copper + glass films illustrates the extent to which the glass addition inhibits oxidation.

The data does not suggest the mechanism by which the glass inhibits oxidation. There appears to be simultaneous processes occuring. The first is that the glass coats the copper particles after it has softened and is able to flow thereby isolating them from the small amount of oxygen in the nitrogen atmosphere preventing oxidation. However, although oxidation is retarded, it is still occuring in the copper + glass film as shown in figure 4E.

The second phenomenon is the dissolution of the Cu_2O by the glass. The viability of this mechanism was found using x-ray diffraction. Addition of crystalline Cu_2O to the glass and carrying out x-ray diffraction analysis before and after melting demonstrates that Cu_2O is soluble in the glass used for the copper + glass film. Figure 5 shows the XRD patterns before and after melting (peak temperature of 900 °C) the lead borosilicate glass with 15 wt% Cu_2O added to it. The Cu_2O peaks seen in the first XRD pattern can no longer be observed after melting. This demonstrates that Cu_2O is soluble in the glass used in this study indicating that the glass can dissolve a large amount of copper oxide as it forms in copper thick films during firing.

V. Summary

Direct observation of the microstructural evolution with temperature indicated that the presence of glass serves two functions. Glass facilitates sintering and improves oxidation resistance. No change in microstructure for either film is apparent until 600 °C. At 600 °C, the copper film began to oxidize and the glass in the copper + glass film softened. In addition, the copper + glass film shows signs of sintering while the copper film does not. The copper film continues to oxidize with further heating. Evidence of copper oxidation in the copper + glass film is observed at 700 °C but oxidation is not nearly as severe as the copper paste. At 900 °C the copper film consists of faceted Cu_2O particles while the copper + glass film shows only limited signs of oxidation. Solubility of Cu_2O in the glass shows that the dissolution of copper oxide in the glass is possible during firing to aid in sintering as well as improve oxidation resistance.

VI. References

[1] J. J. Licari, L. R. Enlow, *Hybrid Microcircuit Technology Handbook - Materials, Processes, Design, Testing and Production* ; pp. 118-125. Noyes, New Jersey, 1988.

[2] R. J. Bacher, and V. P. Siuta, "Firing Process-Related Failure In Thick-Film Copper Multilayers," *Proc ECC* , 471-480 (1986).

[3] J. B. Bradley, "Copper Thick Film Nitrogen Atmosphere Furnace Design and Firing Process Considerations," *Proc. of 1985 Int'l Microelectronics Symp.*, 435-440 (1985) .

[4] C.L. Fisher, D. L. Hankey, E.C. Liang, B. Bertsch, and D.K. Hinkle, "Infrared Firing of a Copper Multilayer System," *Proc. of the 1984 Int'l Microelectronics Symp.*, 259-267 (1984).

[5] R. D. Gardner, A. S. Shaikh, G. Sarker, and C. Bauer, "Materials Science Aspects of a Thick Film Copper/Dielectric System", *Proc. of the 1990 Int'l Microelectronics Symp.*, 285-294 (1990) .

[6] C. R. S. Needes and J. F. Knaak, "The Thermal-Cycled Adhesion of Thick-Film Copper Conductors," *Proc. ECC* , 618-628 (1988).

[7] V.P. Siuta,"Metal Oxide-Coated Copper Powder," U.S. Patent #4,594,181 (1986).

[8] C.C.Y. Kuo, "A New Air-Firable Thick Film Copper Conductor," *Proc. of the 1985 Int'l Microelectronics Symp.*, 472-477 (1985).

[9] C.C.Y. Kuo,"Adhesion of Thick Film Copper Conductors,"*The International Journal for Hybrid Microelectronics,* 4 [2] 70-78 (1981).

[10] J. Murayama, H. Ikezaka, N. Tanifuji, and T. Kato, "The Adhesion Mechanism of Copper Thick Film on Alumina Substrates," *Proc. Int'l Conf on Microelectronics,* 303-307 (1990).

[11] Y. Nakamura,"Alumina Substrate and Glass Interfacial Interactions,"*The International Journal for Hybrid Microelectronics,* 4 [2] 168-171 (1981).

[12] R. J. Bacher, and V. P. Siuta, "Firing Process-Related Failure In Thick-Film Copper Multilayers," *Proc. ECC* , 471-480(1986).

[13] D. Whitman,"Mechanisms for Char Formation in Nitrogen Fired Thick Film Materials," *Proc. of the 1988 Int'l Microelectronics Symp.*, 421-425 (1988).

[14] A.N. Prabhu, K.W. Hang, and E.J. Conlon,"Thick Film Copper Conductor Inks," U.S. Patent # 4,880,567 (1989).

[15] C.C.Y. Kuo,"Adhesion of Copper Conductors, Part II,"*Proc. of the 1987 Int'l Microelectronics Symp.*, 562-568 (1987).

[16] V.P. Siuta "Thick Film Conductor Compositions," U.S. Patent # 4,540,604 (1985).

[17] V.P. Siuta,"Metal Oxide-Coated Copper Powder," U.S. Patent #4,594,181 (1986).

[18] M. Suehiro, M. Echigo, M. Sakvhara and N. Kawamura,"Copper Conductor Composition," U.S. Patent # 4,937,016 (1990).

List of Figures

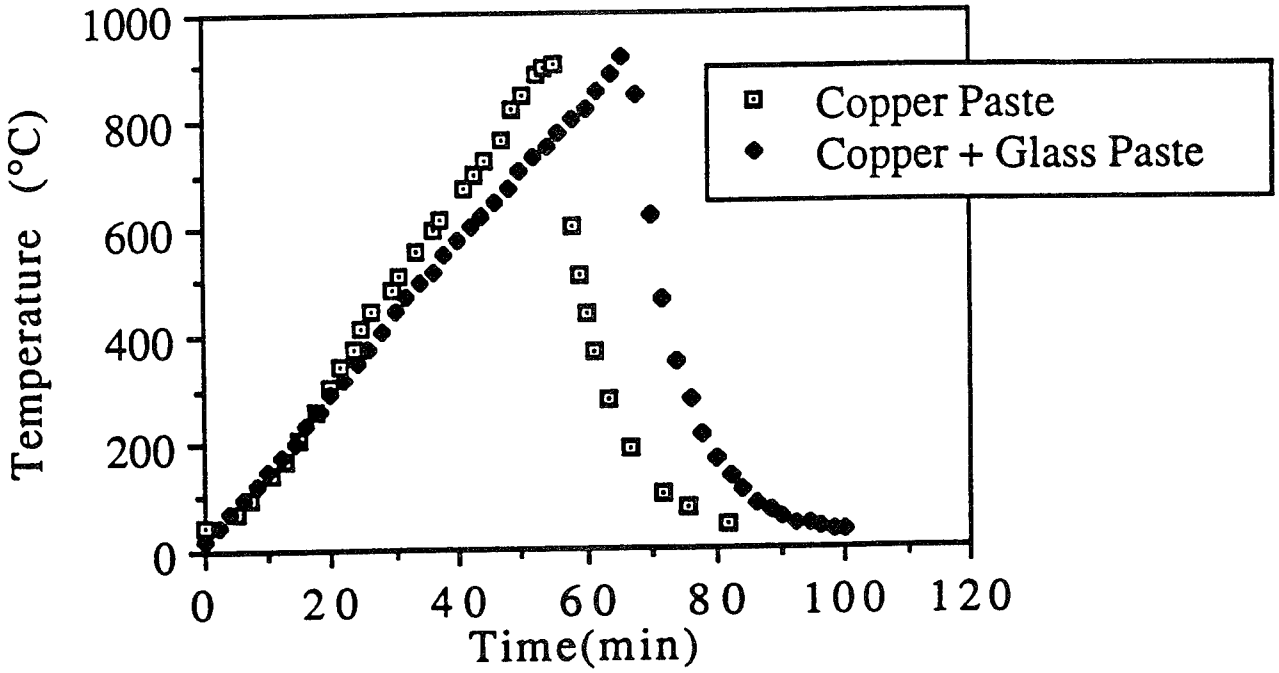

Figure 1. Heating rates used in the ESEM to fire the copper and the copper + glass pastes.

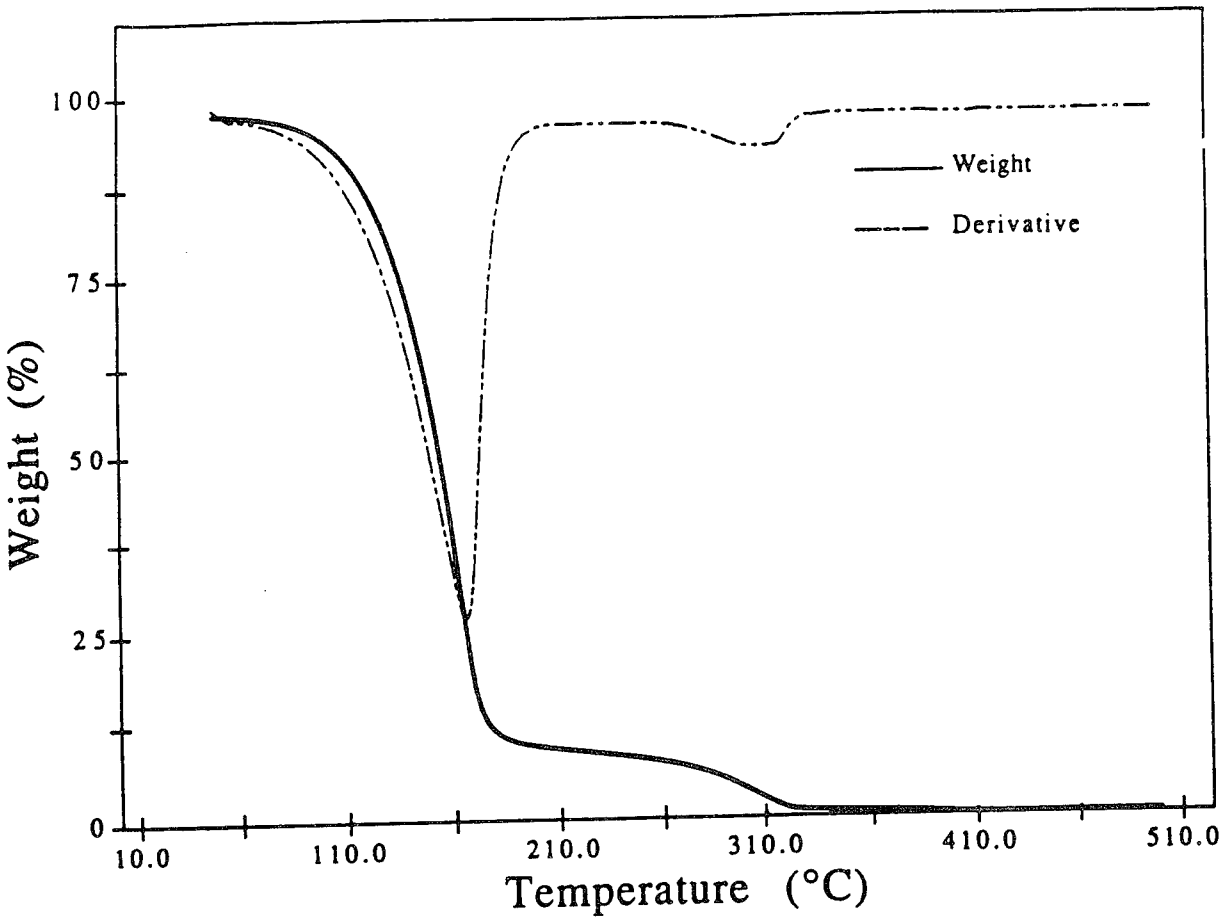

Figure 2. TGA plot showing weight loss versus temperature and the first derivative of weight loss versus temperature for the organics system used to form the pastes used in this study.

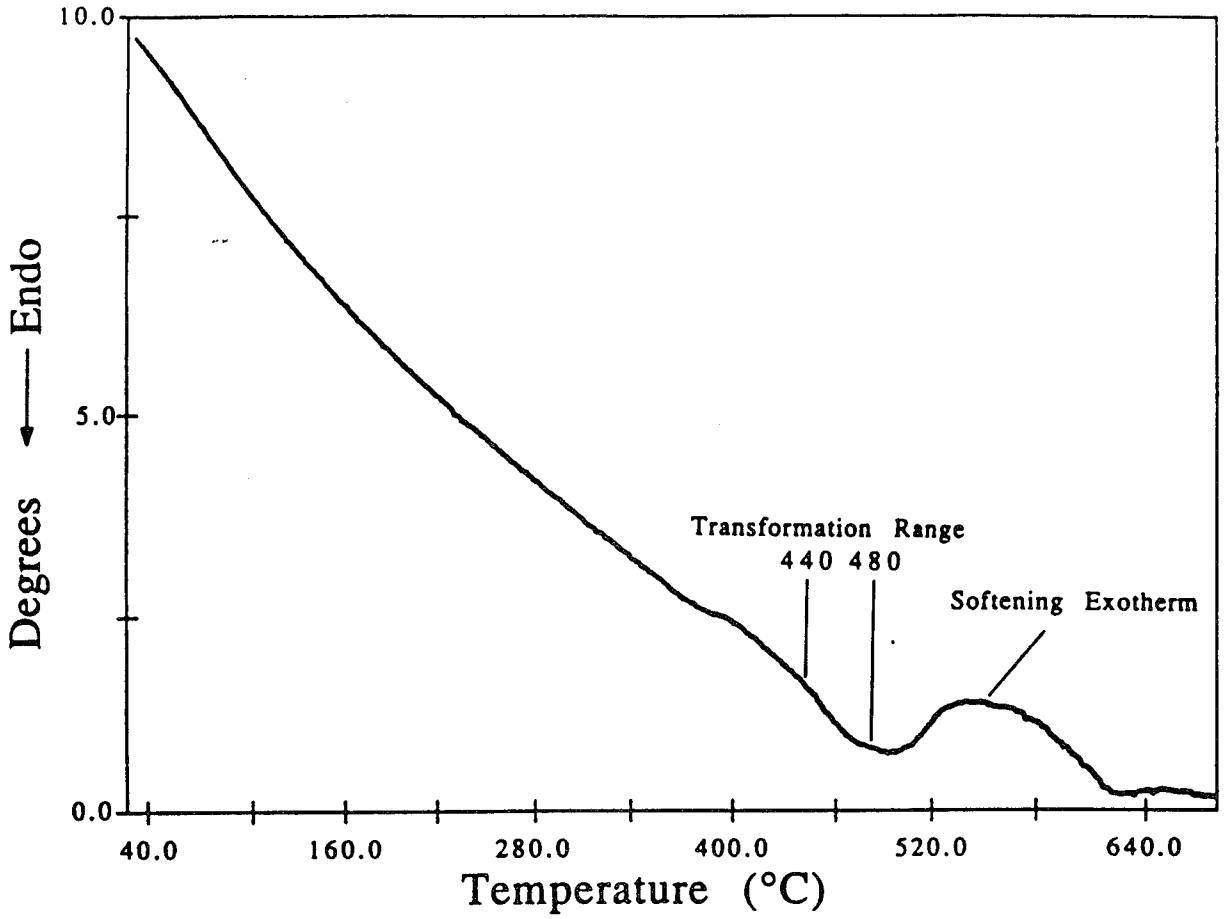

Figure 3. DTA plot of the glass used for the copper + glass paste formulated in this study.

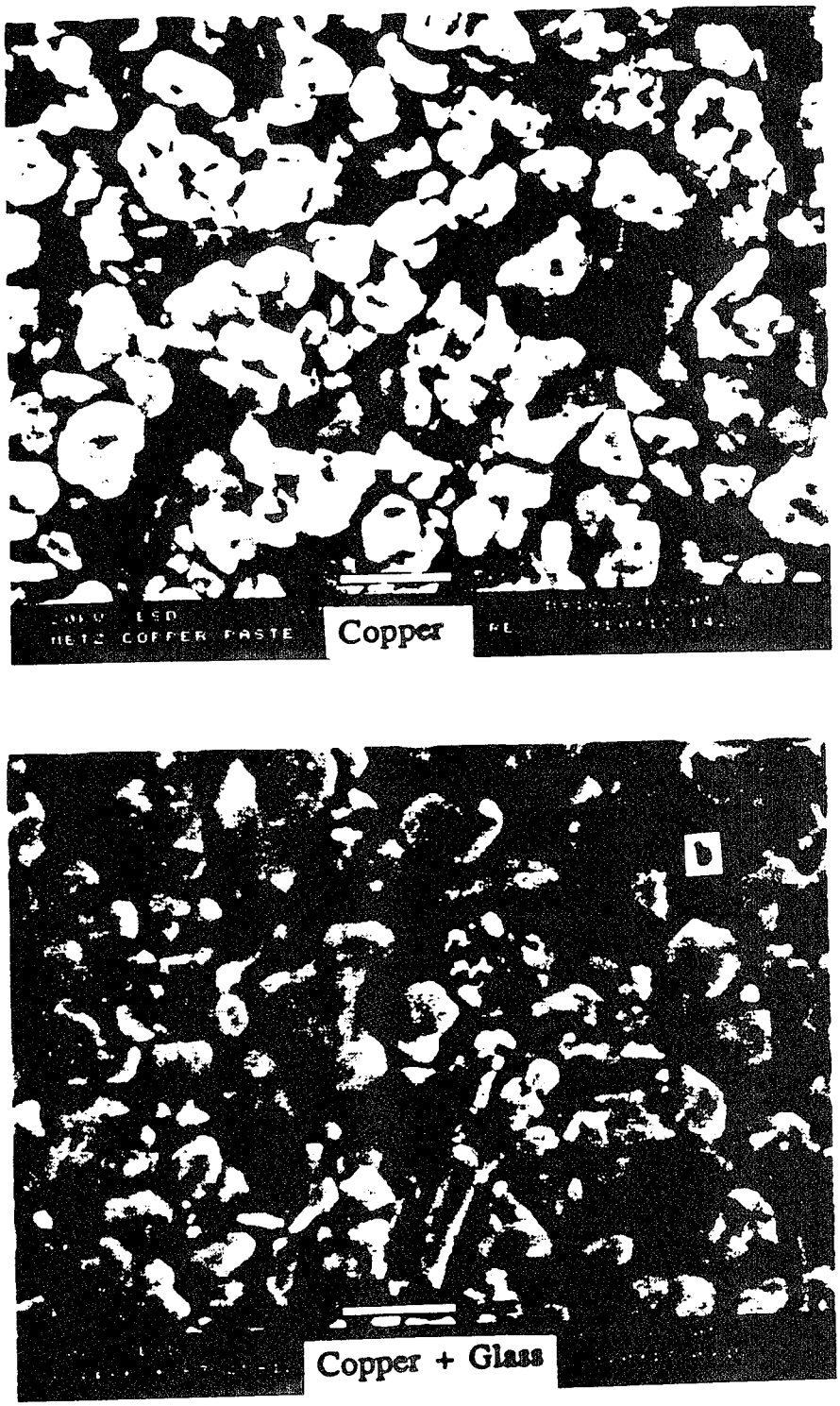

A

Figure 4. The micrographs of the pastes as a function of temperature during firing. A). Before firing. B). Heated to 500 °C. C). Heated to 600 °C. D). Heated to 800 °C. E). Heated to 900 °C. (The bar is 5 μm.)

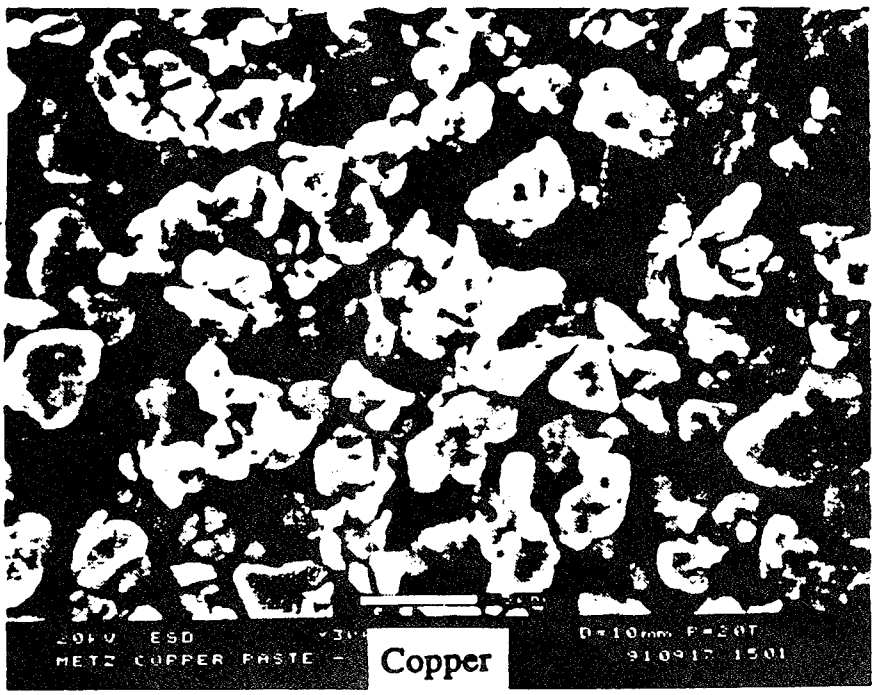

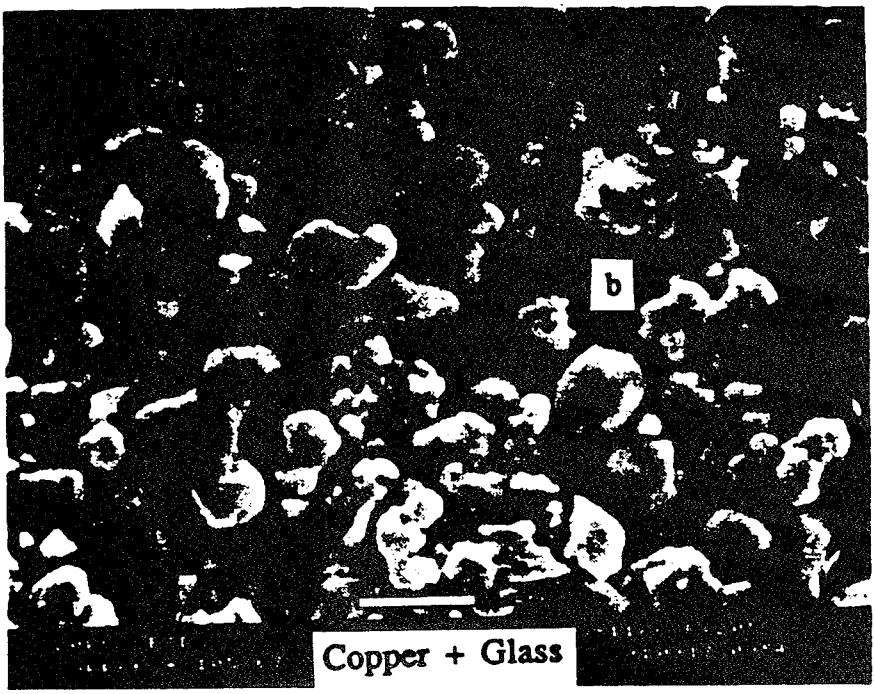

B

Figure 4 cont.

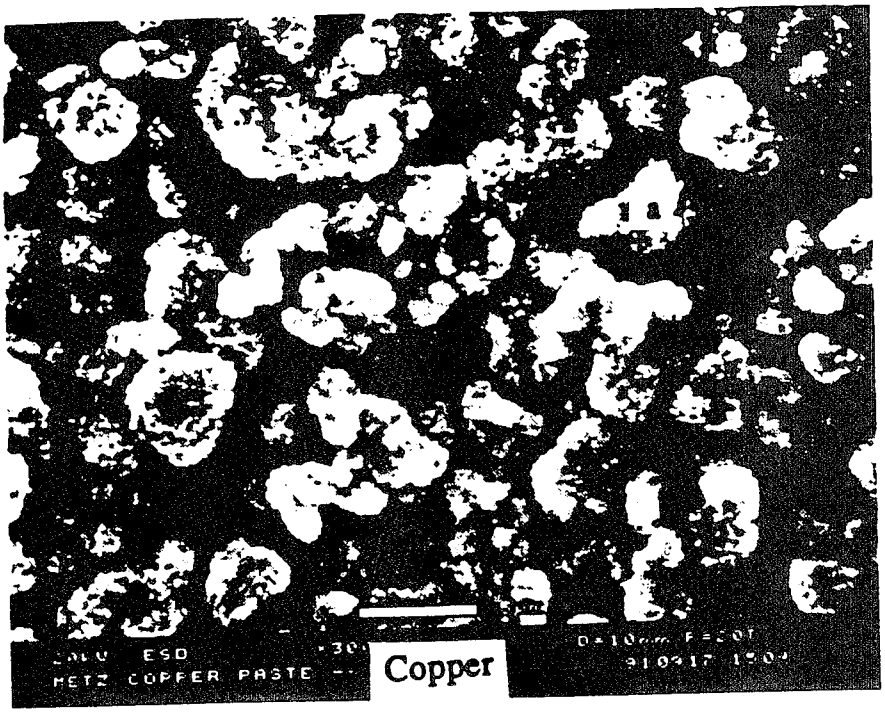

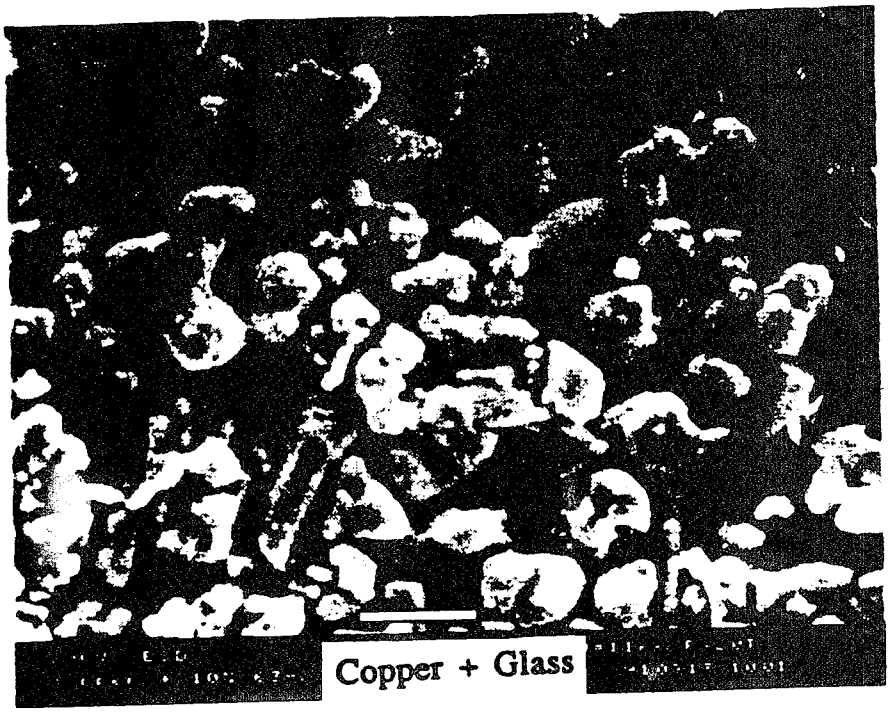

C

Figure 4 cont.

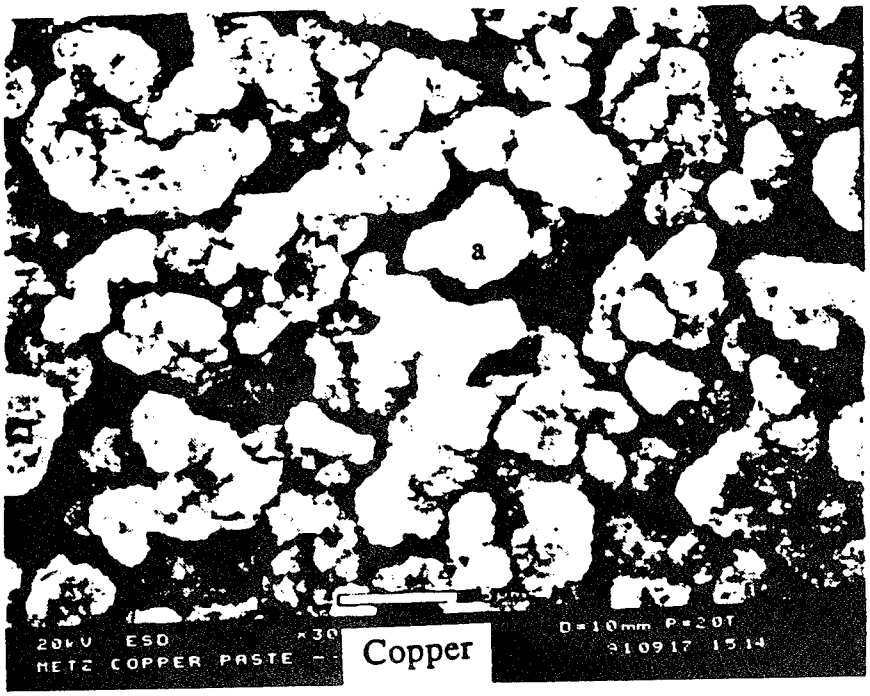

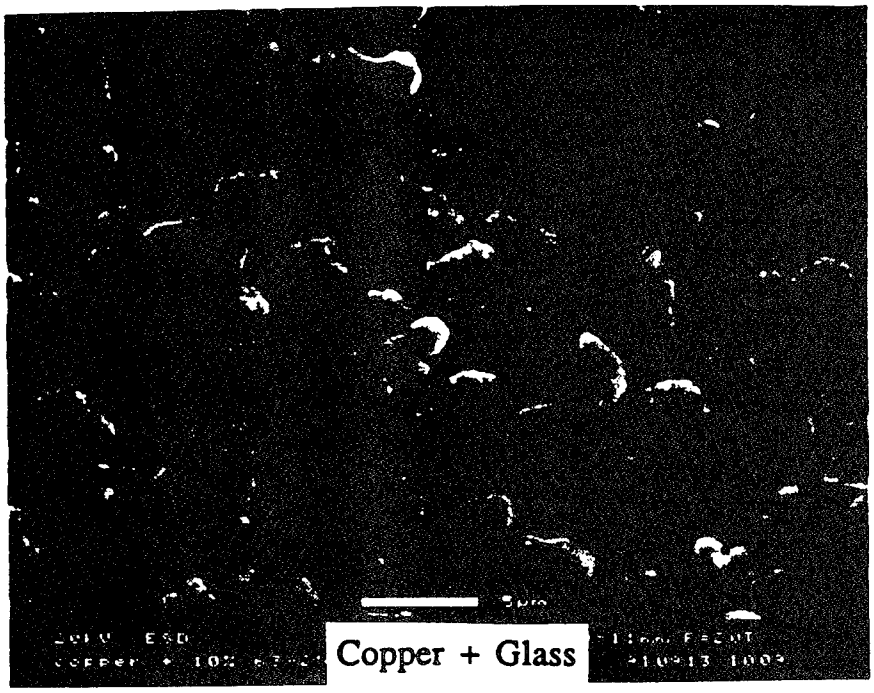

D

Figure 4 cont.

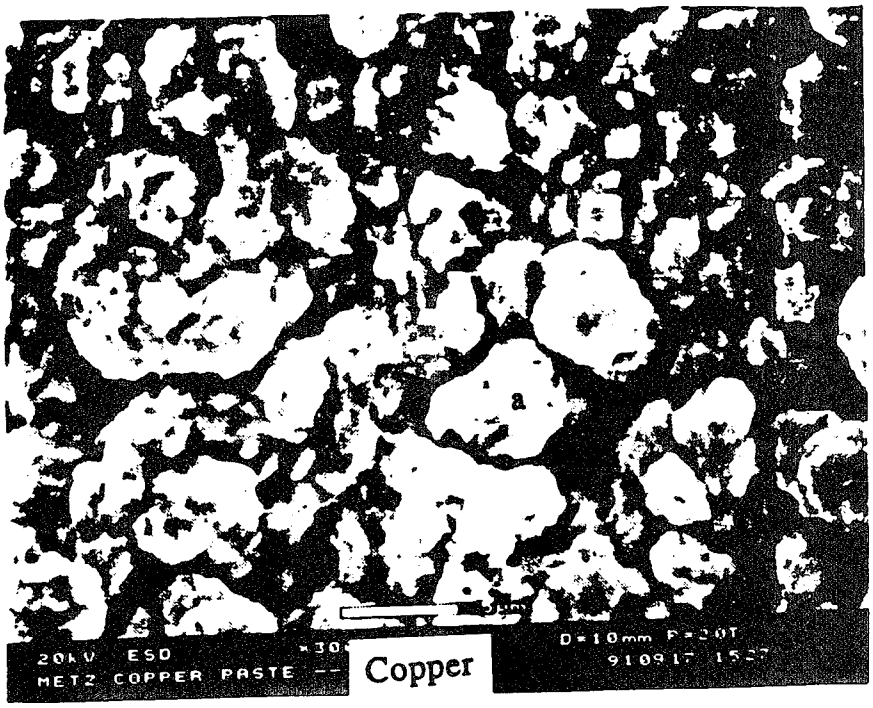

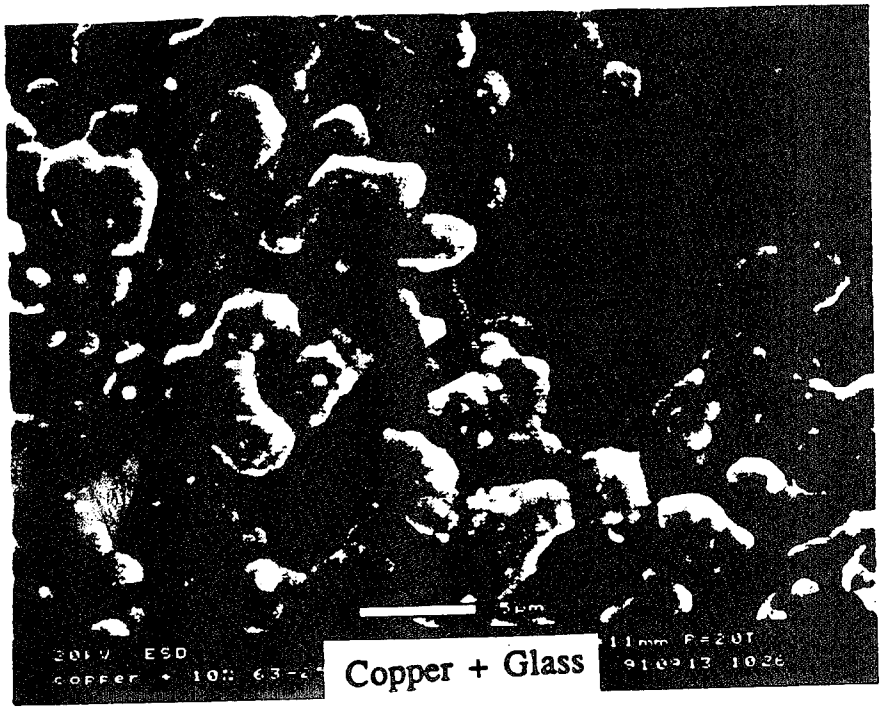

E

Figure 4 cont.

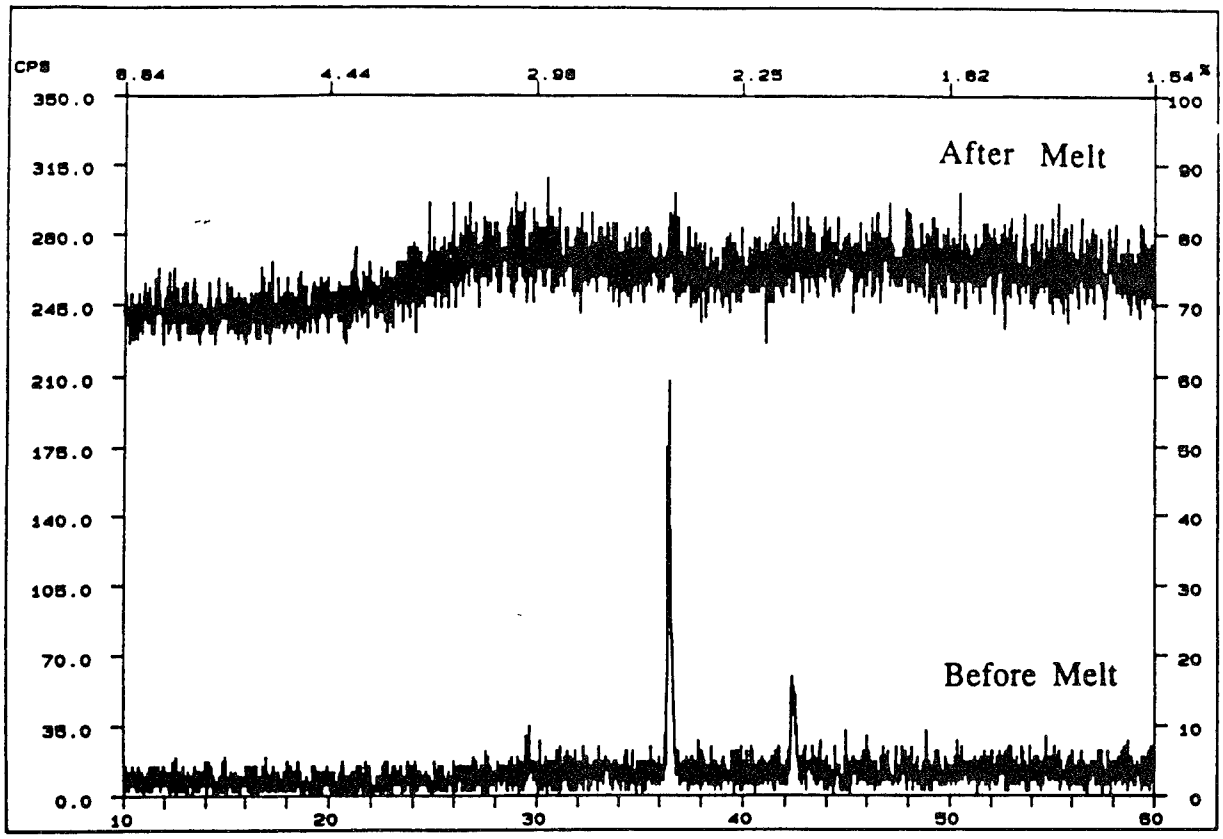

Figure 5. X-ray diffraction scan of a mixture of 15 wt% Cu_2O in the lead borosilicate glass before and after melting showing the ability of the glass to dissolve the Cu_2O.